

Surface Science Studies of Conversion Coatings on 2024-T3

Aluminum Alloy

by

ANISA SHERA AKHTAR

B.Sc., University of British Columbia, 2001

A THESIS SUBMITTED IN PARTIAL FULFILLMENT OF
THE REQUIREMENTS FOR THE DEGREE OF

DOCTOR OF PHILOSOPHY

in

THE FACULTY OF GRADUATE STUDIES

(Chemistry)

THE UNIVERSITY OF BRITISH COLUMBIA

(Vancouver)

April 2008

© Anisa Shera Akhtar, 2008

Abstract

The research in this thesis aims to develop new mechanistic knowledge for coating processes at 2024-Al alloy surfaces, ultimately to aid the design of new protective coatings. Coatings formed by phosphating, chromating, and permanganating were characterized especially by scanning Auger microscopy (SAM), X-ray photoelectron spectroscopy, and scanning electron microscopy. The objective was to learn about growth (nm level) as a function of time for different coating baths, as well as a function of lateral position across the different surface microstructural regions, specifically on the μm -sized Al-Cu-Mg and Al-Cu-Fe-Mn particles which are embedded in the alloy matrix. The research characterizes coating thickness, composition, and morphology.

The thesis emphasizes learning about the effect of different additives in zinc phosphating baths. It was found that the Ni^{2+} additive has two main roles: first, the rate of increase in local solution pH is limited by the slower kinetics of reactions involving Ni^{2+} compared to Zn^{2+} , leading to thinner zinc phosphate (ZPO) coatings when Ni^{2+} is present. Second, most Ni^{2+} deposition occurs during the later stages of the coating process in the form of nickel phosphate and a Ni-Al oxide in the coating pores on the alloy surface, increasing the corrosion resistance. Aluminum fluoride precipitates first during the initial stages of the coating process, followed by aluminum phosphate, zinc oxide, and finally ZPO.

When Ni^{2+} is present in the coating solution at 2000 ppm, ZnO predominates in the coating above the Al-Cu-Fe-Mn particle while ZPO dominates on the rest of the surface. The Mn^{2+} additive gives a more even coating distribution (compared with Ni^{2+}) across the whole surface. The Mn^{2+} -containing ZPO coating is similar to the chromate coating in terms of evenness, while there is more coating deposition at the second-phase particles for

permanganate coatings. The oxides on the Al-Cu-Fe-Mn and matrix regions are similar before coating, thereby confirming that a variety of observed differences in ZPO coating characteristics at these regions arise from the different electrochemical characteristics of the underlying metals. Upon exposure to a corrosive solution, the ZPO coating provides more protection to the second-phase particles compared to the matrix.

Table of Contents

Abstract.....	ii
Table of Contents.....	iv
List of Tables.....	ix
List of Figures.....	xi
List of Acronyms.....	xvii
Acknowledgements.....	xviii
Chapter 1 Introduction.....	1
1.1 Aluminum and its Alloys.....	1
1.2 Protection of Aluminum from Corrosion.....	5
1.3 Zinc Phosphate Conversion Coatings.....	9
1.4 Objectives of Research.....	12
1.5 Outline of Thesis.....	13
Chapter 2 Experimental Methods.....	14
2.1 X-ray Photoelectron Spectroscopy.....	14
2.1.1 Theory of Technique.....	14
2.1.2 Instrumentation.....	19
2.1.3 Quantitative Analysis.....	24
2.2 Scanning Auger Microscopy.....	29
2.2.1 Theory of Techniques.....	29
2.2.2 Instrumentation.....	31
2.2.3 Other Instruments for SEM.....	35
2.3 Energy Dispersive X-ray Spectroscopy.....	36

2.3.1	Theory of Technique.....	36
2.3.2	EDX Instrumentation.....	39
2.4	Electrochemical Polarization.....	40
2.4.1	Theory of Technique.....	40
2.4.2	Instrumentation.....	44
Chapter 3	The Effect of Ni ²⁺ on Zinc Phosphating of 2024-T3 Al Alloy.....	45
3.1	Introduction.....	45
3.2	Experimental.....	46
3.3	Results and Discussion.....	47
3.3.1	Coating Topography on 2024-Al.....	47
3.3.2	Electrochemical Characterization.....	47
3.3.3	Chemical Analysis - Spectroscopic Measurements.....	51
3.3.4	Effect of Microstructure – EDX Analysis.....	54
3.3.5	Approach to Measurements on Microstructure.....	57
3.3.6	Effect of Microstructure – SAM Analysis.....	58
3.3.7	Measurements on High-Purity Al.....	63
3.4	Concluding Remarks.....	65
Chapter 4	The Effect of pH and Role of Ni ²⁺ in Zinc Phosphating of 2024-Al alloy.....	67
4.1	Introduction.....	67
4.2	Experimental.....	69
4.3	Results and Discussion.....	70
4.3.1	Setting the Scene.....	70
4.3.2	Macroscopic Characterization.....	74
4.3.2.1	Coatings from ZPO Solutions Containing Ni ²⁺	74

4.3.2.2	Mechanistic Issues: Ni ²⁺ in Coating Solution.....	81
4.3.2.3	Coatings from ZPO Solutions with No Ni ²⁺	84
4.3.3	Analysis at Micro-Regions.....	87
4.3.3.1	Ni ²⁺ -Containing Coatings.....	87
4.3.3.1.1	Al-Cu-Mg Second-Phase Particle.....	87
4.3.3.1.2	Al-Cu-Fe-Mn Second-Phase Particle.....	91
4.3.3.1.3	Matrix.....	95
4.3.3.2	Coatings Not Containing Ni ²⁺	99
4.3.3.2.1	Al-Cu-Mg and Al-Cu-Fe-Mn Second-Phase Particles.....	99
4.3.3.2.2	Matrix.....	101
4.3.3.3	Comparison with XPS Observations.....	102
4.4	Concluding Remarks.....	103
Chapter 5	Effect of Mn ²⁺ Additive on the Zinc Phosphating of 2024-Al Alloy.....	106
5.1	Introduction.....	106
5.2	Experimental.....	107
5.3	Results and Discussion.....	108
5.3.1	Growth of Coating.....	108
5.3.1.1	Characterizations with XPS.....	108
5.3.1.2	Coating Morphology	112
5.3.2	Effect of Mn ²⁺ Concentration.....	113
5.3.2.1	Coating Topography.....	113
5.3.2.2	Chemical Analysis.....	116
5.3.3	Comparison of Effects of Mn ²⁺ and Ni ²⁺	118
5.3.3.1	Macroscopic Analysis.....	118

5.3.3.2	Microstructural Regions.....	119
5.3.4	Coating Adhesion	125
5.4	Concluding Remarks.....	127
Chapter 6 Microstructural Effects on the Formation and Degradation of Zinc Phosphate Coatings on 2024-Al Alloy.....		
6.1	Introduction.....	128
6.2	Experimental Details.....	130
6.3	Results and Discussion.....	131
6.3.1	2024-Al Before Dipping in ZPO Coating Bath.....	131
6.3.1.1	Oxide Thickness.....	136
6.3.2	2024-Al After Dipping in ZPO Coating Bath.....	137
6.3.3	Corroded ZPO Coating on 2024-Al.....	140
6.3.3.1	Initiation of Corrosion (3 h Immersion).....	140
6.3.3.2	More Extensive Degradation (48 h Immersion).....	143
6.3.3.3	Corrosion Protection Provided by ZPO Coating.....	145
6.4	Concluding Remarks.....	148
Chapter 7 Growth of Chromate and Permanganate Conversion Coatings on 2024-Al Alloy.....		
7.1	Introduction.....	150
7.2	Experimental Details.....	153
7.3	Results and Discussion.....	154
7.3.1	Chromate Coatings.....	154
7.3.1.1	Auger Spectra.....	154
7.3.1.1.1	Sample After 5 s Immersion.....	154
7.3.1.1.2	Sample After 30 s Immersion.....	162

7.3.1.2 Behaviour of Intermetallic Particles.....	166
7.3.2 Permanganate Coatings.....	169
7.3.2.1 Coating Chemical Composition.....	169
7.3.2.2 Early Stages of Coating Growth.....	172
7.3.2.3 Thicker Coating Formation.....	177
7.4 Concluding Remarks.....	181
7.4.1 Chromate and Permanganate Conversion Coatings.....	181
7.4.2 Comparison with Zinc Phosphate Coatings.....	183
Chapter 8 Concluding Remarks.....	184
8.1 New Results.....	184
8.2 Future Directions.....	188
References.....	190

List of Tables

Table 3.1	Elemental atomic percentages from XPS for 2024-Al samples after coating in ZPO solutions which differ just in the Ni ²⁺ concentration which varies from 500 to 2500 ppm.....	52
Table 3.2	Elemental weight percentages from EDX for different regions of the 2024-Al microstructure shown in Figure 3.4.....	55
Table 3.3	Elemental atomic percentages from SAM for the different microstructural regions of ZPO-coated 2024-Al samples shown in Figure 3.5.....	61
Table 4.1	Elemental atomic percentages from XPS for 2024-Al samples after coating in ZPO solutions, containing 2,000 ppm Ni ²⁺ , showing variation with coating time and initial solution pH.....	77
Table 4.2	Elemental atomic percentages from XPS for 2024-Al samples after coating in ZPO solutions, containing no Ni ²⁺ , showing variations with starting pH and coating time for pH 4.....	84
Table 4.3	Elemental atomic percentages from SAM for different regions of the Al-Cu-Mg second-phase particles in ZPO-coated 2024-Al samples shown in Figure 4.4 (2 min treatment with Ni ²⁺ -containing solutions at initial pH 3, 4, and 5).....	89
Table 4.4	Elemental atomic percentages from SAM for different regions of the Al-Cu-Fe-Mn second-phase particles in ZPO-coated 2024-Al samples shown in Figure 4.6 (2 min treatment with Ni ²⁺ -containing solutions at initial pH 3, 4, and 5).....	93
Table 4.5	Elemental atomic percentages from SAM for different regions of the matrix in ZPO-coated 2024-Al samples shown in Figure 4.6 (2 min treatment with Ni ²⁺ -containing solutions at initial pH 3, 4, and 5).....	98
Table 5.1	Elemental atomic percentages measured by XPS from 2024-Al alloy after dipping for varying times in the ZPO coating solution which contains Mn ²⁺ (see text).....	110
Table 5.2	Elemental atomic percentages from XPS for 2024-Al samples after coating (3 min dip time) in ZPO solutions which differ in the Mn ²⁺ concentration, varying from 0 to 2500 ppm.....	117
Table 6.1	Elemental atomic percentages from SAM for different microstructural regions (Figures 6.1(a) and 6.2(a)) on the mirror-polished 2024-Al surface.....	135

Table 6.2	Elemental atomic percentages from XPS for the 2024-Al surface after polishing, ZPO coating and immersion in NaCl solution for 48 h.....	136
Table 6.3	Elemental atomic percentages from SAM for different microstructural regions (Figures 6.1(b) and 6.2(b)) on the ZPO-coated 2024-Al surface....	138
Table 6.4	Elemental atomic percentages from SAM for different microstructural regions (Figures 6.1(c), 6.2(c), 6.4(a)) on the coated 2024-Al surface after 3 h immersion in NaCl solution.....	143
Table 6.5	Elemental atomic percentages from SAM for different microstructural regions (Figures 6.1(d), 6.2(d), 6.4(b)) on the coated 2024-Al surface after 48 h immersion in NaCl solution.....	144

List of Figures

Figure 1.1	Alloy phase diagrams: (a) schematic of part of the aluminum-copper phase diagram and (b) part of the aluminum-copper-magnesium phase diagram [5] (reproduced with permission).....	3
Figure 1.2	Scanning electron micrograph of 2024-T3 Al alloy microstructure.....	4
Figure 1.3	Schematic of natural oxide layer on high-purity aluminum.....	7
Figure 1.4	Schematic of corrosion (lower purity aluminum) in an aggressive solution.	7
Figure 1.5	Schematic of phosphating process on aluminum.....	11
Figure 1.6	The SEM micrograph in (a) shows a surface of 2024-Al alloy after a full ZPO coating. The bright areas are large ZPO crystals, and coating is also deposited in the areas between the large crystals. The micrograph in (b) shows a Al-Cu-Mg second-phase particle surrounded by the matrix region on a 2024-Al surface (initial stages of ZPO coating).....	11
Figure 2.1	Schematic diagram for (a) photoelectron emission, (b) Auger electron emission, and (c) X-ray emission (fluorescence).....	15
Figure 2.2	XPS spectra from zinc phosphated 2024-Al alloy: (a) survey spectrum (the (A) identify Auger electron peaks), and (b) Zn 2p region.....	16
Figure 2.3	Dependence of inelastic mean free path on electron kinetic energy (schematic).....	18
Figure 2.4	High resolution XPS spectrum (Al 2p region) from zinc phosphated 2024-Al alloy.....	18
Figure 2.5	Schematic of pumping system for MAX 200 XPS spectrometer.....	20
Figure 2.6	Schematic diagram for the lens system and the concentric hemispherical analyzer (CHA) in the MAX 200.....	23
Figure 2.7	Schematic diagram of relevant energy levels for measurements by spectrometer of binding energy for a conducting sample.....	25
Figure 2.8	Shirley non-linear background correction applied to a Mn 2p _{1/2} spectrum.....	28

Figure 2.9	Auger spectrum from zinc phosphated Al alloy.....	30
Figure 2.10	Auger spectra measured from 2024-Al alloy: (a) Al KLL region for the metallic and oxidized forms and (b) high resolution spectrum for part of the Al KLL region (both metallic and oxidized Al are present).....	30
Figure 2.11	Schematic indication of main components for Microlab 350 including the pumping system. SED and BSD indicate the secondary electron and backscattered electron detectors respectively.....	32
Figure 2.12.	Schematic of electron gun for Microlab 350.....	34
Figure 2.13	EDX spectrum measured from the Al-Cu-Mg region in 2024-Al alloy.....	37
Figure 2.14	Schematic for X-ray detector.....	38
Figure 2.15	Schematic of polarization curve for $O_{(aq)} + e^-_{(m)} \leftrightarrow R_{(aq)}$	41
Figure 2.16	Schematic of the three-electrode cell used for polarization measurements...	43
Figure 3.1	SEM micrographs from zinc phosphate (ZPO) coated 2024-Al surfaces. The coating solutions contain increasing amounts of Ni^{2+} : (a) 0, (b) 500, (c) 1000, (d) 2000 and (e) 2500 ppm.....	48
Figure 3.2	Polarization curves measured for samples of 2024-Al coated with ZPO solutions containing different amounts of Ni^{2+} : (a) 0, (b) 500, (c) 1000, (d) 2000 and (e) 2500 ppm.....	49
Figure 3.3	Corrosion currents determined from polarization curves for samples of 2024-Al and high-purity Al which have been coated with ZPO solutions containing different concentrations of Ni^{2+} . The uncertainties in the i_o values are estimated at $\pm 0.5 \times 10^{-6} \text{ Acm}^{-2}$	50
Figure 3.4	SEM micrograph from the 2024-Al surface after treating in a ZPO coating solution that contained 2000 ppm Ni^{2+} ; P1, P2, and P3 identify Al-Cu-Mg particles, while P4 is an Al-Cu-Fe-Mn particle.....	56
Figure 3.5	SEM micrographs from different microstructural regions of the 2024-Al surface after treating with a ZPO coating solution which contained 2000 ppm Ni^{2+} : (a) Al-Cu-Mg particle (sample normal to electron beam); (b) Al-Cu-Mg particle (sample tilted at 60° to electron beam); (c) Al-Cu-Fe-Mn particle (sample normal to electron beam).....	59

Figure 3.6	Wide-scan Auger spectra measured from different ZPO-coated regions on Al-Cu-Mg particle: crystalline region R1 and amorphous region R2 (as in Figure 3.5(a)).....	60
Figure 3.7	Al KLL spectra from amorphous ZPO coatings: R2 region on Al-Cu-Mg particle, R4 on alloy matrix (as in Figure 3.5(a)).....	60
Figure 3.8	SEM micrographs from the high-purity Al surface after treating in ZPO coating solutions that contain varying amounts of Ni ²⁺ : (a) 500, (b) 1000, (c) 1500 and (d) 2000 ppm.....	64
Figure 4.1	SEM micrographs after coating 1200-grit polished 2024-Al samples with ZPO solutions containing 2,000 ppm Ni ²⁺ for 2 min at different starting pH values: (a) pH 3, (b) pH 4 and (c) pH 5.....	72
Figure 4.2	Al 2p region of XPS spectra for 2024-Al dipped in ZPO solutions containing 2,000 ppm Ni ²⁺ for 30 s at different starting pH values: (a) pH 3, (b) pH 4, (c) pH 5.....	73
Figure 4.3	Graphical representation of elemental compositions from XPS for coatings formed from ZPO solutions containing 2,000 ppm Ni ²⁺ applied for different times and at different starting pH values: (a) $Q_P = (Zn+Ni)/P$ and (b) $Q_{Ni} = Ni/(Ni+Zn)$	76
Figure 4.4	SEM micrographs for Al-Cu-Mg second-phase particles on the 2024-Al surface after dipping for 2 min in Ni ²⁺ -containing coating solutions at different pH values: (a) 3, (b) 4 and (c) 5.....	88
Figure 4.5	Graphical representation of elemental compositions from SAM at different microstructural regions for coatings formed from ZPO solutions containing 2,000 ppm Ni ²⁺ at different starting pH values.....	90
Figure 4.6	SEM micrographs showing Al-Cu-Fe-Mn second-phase particles surrounded by the matrix region on a 2024-Al surface after dipping for 2 min in Ni ²⁺ -containing coating solutions at different pH values: (a) 3, (b) 4, (c) 5, (d) 4 (image of Al-Cu-Fe-Mn surface at higher magnification), and (e) 4 (image of matrix region at higher magnification).....	92
Figure 4.7	Al KLL spectra from dark areas on the matrix region of the 2024-Al surface that has been dipped for 2 min in a Ni ²⁺ -containing solution for different pH values: R3 region for pH 3, S4 region for pH 4, T3 region for pH 5.....	96
Figure 4.8	SEM micrographs for second-phase particles on the 2024-Al surface after 2 min immersion in the ZPO coating solution with no Ni ²⁺ and adjusted to pH 4: (a) Al-Cu-Mg particle; (b) Al-Cu-Fe-Mn particle.....	100

Figure 5.1	Al 2p, Mn 2p and Zn 2p spectra for 2024-Al surfaces dipped for 15 s and 60 s in ZPO solutions containing 2000 ppm Mn ²⁺	109
Figure 5.2	SEM micrographs (incident beam 5 kV) from 2024-Al surfaces dipped for increasing times in ZPO coating solutions at 60 °C containing 2000 ppm Mn ²⁺ : (a) 15 s, (b) 60 s, (c) 120 s, (d) 180 s and (e) 300 s (pits on surface are circled).....	111
Figure 5.3	SEM micrographs from ZPO-coated (3 min dip time) 2024-Al surfaces. The coating solutions contain increasing amounts of Mn ²⁺ : (a) 0, (b) 100, (c) 500, (d) 1000, (e) 2000, (f) 2500 ppm.....	114
Figure 5.4	SEM micrographs (incident beam 20 kV) from 2024-Al surfaces dipped for 2 min in ZPO coating solutions (see text) which contained varying amounts of Ni ²⁺ and Mn ²⁺ : (a) no Ni ²⁺ or Mn ²⁺ , (b) 2000 ppm Ni ²⁺ and (c) 2000 ppm Mn ²⁺	120
Figure 5.5	SEM micrographs (incident beam 10 kV) showing Al-Cu-Mg second-phase particles surrounded by the matrix region on a mirror-polished 2024-Al surface after dipping for 2 min in ZPO coating solutions (see text) which contained varying amounts of Ni ²⁺ and Mn ²⁺ : (a) no Ni ²⁺ or Mn ²⁺ , (b) 2000 ppm Ni ²⁺ and (c) 2000 ppm Mn ²⁺	121
Figure 5.6	SEM micrographs (incident beam 10 kV) showing Al-Cu-Fe-Mn second-phase particles surrounded by the matrix region on a mirror-polished 2024-Al surface after dipping for 2 min in ZPO coating solutions (see text) which contained: (a) 2000 ppm Ni ²⁺ and (b) 2000 ppm Mn ²⁺	123
Figure 5.7	Auger spectra from the matrix and Al-Cu-Fe-Mn microstructural regions on a mirror-polished 2024-Al surface after dipping for 2 min in ZPO coating solutions (see text) which contained: (a) 2000 ppm Ni ²⁺ and (b) 2000 ppm Mn ²⁺ . The regions N1 and N2 are defined in Figure 5.6(a); M1 and M2 in Figure 5.6(b).....	124
Figure 5.8	Auger spectra measured from the matrix region of the 2024-Al surface coated in a ZPO solution containing 2000 ppm Mn ²⁺ before (a) and after (c) the sonic treatment (see text).....	126
Figure 6.1	SEM micrographs showing Al-Cu-Mg second-phase particles surrounded by matrix region on the 2024-Al surface after exposure to different sequential treatments: mirror-polishing (a); dipping for 105 s in a ZPO coating solution at 60°C containing 2000 ppm Ni ²⁺ (b), where the bright areas are large ZPO crystals; immersion of coated surfaces in 0.6 M NaCl solution at 20°C for 3 h (c) or 48 h (d).....	132

Figure 6.2	SEM micrographs showing Al-Cu-Fe-Mn second-phase particles surrounded by matrix region on the 2024-Al surface after exposure to different sequential treatments: mirror-polishing (a); dipping for 105 s in a ZPO coating solution at 60°C containing 2000 ppm Ni ²⁺ (b), where the bright areas are large ZPO crystals; immersion of coated surfaces in 0.6 M NaCl solution at 20°C for 3 h (c) or 48 h (d).....	133
Figure 6.3	Auger survey spectra from regions indicated in Figures 6.1(a) and 6.2(a) namely Al-Cu-Mg particle (P1), matrix region (P2), Al-Cu-Fe-Mn particle (P3).....	134
Figure 6.4	SEM micrographs for ZPO-coated surface after immersion in NaCl solution for: (a) 3 h showing corrosion product (R4); (b) 48 h showing an intact Al-Cu-Mg particle, a partly dissolved Al-Cu-Mg particle (pit), and corrosion product (S4).....	142
Figure 6.5	A larger-area SEM micrograph for the ZPO-coated surface after 48 h immersion in NaCl solution to show extensive matrix cracking.....	146
Figure 7.1	SEM images from different regions of 2024-Al alloy after 5 s CCC treatment: (a) intact Al-Cu-Fe-Mn particle; (b) intact Al-Cu-Mg particle (white dots depict positions for Auger point analysis); (c) Al-Cu-Fe-Mn particle demonstrating a partial halo; (d) higher-magnification image of same particle showing trench (marked by arrow) at interface with Al matrix; (e) Al-Cu-Mg particle demonstrating dealloying with a surrounding halo-like structure; (f) Al matrix showing evidence of acid etching and light nodules (marked by arrows).....	155
Figure 7.2	Point Auger spectra measured for 2024-Al after 5 s CCC treatment from: (1) intact Al-Cu-Fe-Mn particle; (2) intact Al-Cu-Mg particle; (3) Al matrix; (4) and (5) two different locations from a Al-Cu-Mg particle that has undergone dealloying; (6) nodule on matrix (as marked by arrows in Figure 7.1(f)); and (7) halo surrounding severely dealloyed Al-Cu-Mg particle.....	156
Figure 7.3	Cr/Al ratios from Auger point analysis measured across interfaces between Al matrix and intact second-phase particles: (a) Al-Cu-Fe-Mn particle and (b) Al-Cu-Mg particle. The open symbols are for 5 s CCC treatment, closed symbols for 30 s CCC treatment; the dashed lines are given as a guide to the eye only. Each curve has its own vertical scale as indicated by the arrows.....	159

Figure 7.4	Al KLL Auger spectra measured from different regions of 2024-Al alloy after CCC treatment. Those in (a) are after 5 s treatment from: (1) central part of intact Al-Cu-Fe-Mn particle; (2) central part of intact Al-Cu-Mg particle; (3) Al matrix; (6) nodule on matrix; (7) halo surrounding severely dealloyed Al-Cu-Mg particle. Spectra in (b) are after 30 s treatment from: (1) intact Al-Cu- Fe-Mn particle; (2) intact Al-Cu-Mg particle; (3) Al matrix; (4) severely dealloyed Al-Cu-Mg particle; (5) halo in vicinity of particle in (4).....	160
Figure 7.5	SEM images from different regions of 2024-Al alloy surface after 30 s CCC treatment: (a) Al-Cu-Fe-Mn particle; (b) Al-Cu-Mg particle that has undergone dissolution; (c) Al-Cu-Mg particle that has remained intact; and (d) Al matrix.....	163
Figure 7.6	Point Auger spectra measured for 2024-Al after 30 s CCC treatment from: (1) intact Al-Cu-Fe-Mn particle; (2) intact Al-Cu-Mg particle; (3) Al matrix (4) Al-Cu-Mg particle that has undergone severe dealloying; and (5) halo in vicinity of particle in (4).....	164
Figure 7.7	Relative amounts from XPS of major (a) and minor (b) metallic components in the surface layer of growing PCCs as a function of treatment time at 25°C. The dashed lines are given to guide the eye.....	170
Figure 7.8	SEM images from different regions of 2024-Al samples after PCC-treatment at 25°C for different coating times: (a) both types of second-phase particle after 1 min; (b) alloy matrix after 1 min; (c) Al-Cu-Mg particle after 20 min; (d) alloy matrix after 20 min. Each scale bar indicates 2 μm	173
Figure 7.9	Auger point spectra measured from 2024-Al samples after PCC-treatment at 25°C for different coating times. (a) 1 min: (1) Al-Cu-Mg particle, (2) Al-Cu-Fe-Mn particle, (3) alloy matrix; (b) 5 min: (4) Al-Cu-Fe-Mn particle, (5) alloy matrix well removed from intermetallic particles, and (6) alloy matrix close to an Al-Cu-Fe-Mn particle. The arrows identify the most intense peaks in the elemental KLL or LMM series.....	175
Figure 7.10	SEM images from different regions of 2024-Al samples after PCC-treatment at 25°C for different coating times: (a) cluster of Al-Cu-Mg particles with uniform coating after 90 min; (b) Al-Cu-Fe-Mn particle with cracked coating after 90 min; (c) hillock-like structure on alloy matrix after 150 min; (d) Al-Cu-Mg particle with peripheral trench after 150 min. Scale bars indicate 10 μm for (a,b), 3 μm for (c,d).....	178

List of Acronyms

AES	Auger electron spectroscopy
BSD	backscattered electron detector
CCC	chromate conversion coating
CHA	concentric hemispherical analyzer
CRR	constant retarding ratio
EDX	energy dispersive X-ray spectroscopy
FTIR	Fourier transform infrared spectroscopy
PCC	permanganate conversion coating
SAM	scanning Auger microscopy
SCE	saturated calomel electrode
SED	secondary electron detector
SEM	scanning electron microscopy
UHV	ultrahigh vacuum
XPS	X-ray photoelectron spectroscopy
ZPO	zinc phosphate

Acknowledgements

I would like to thank my supervisor, Professor K.A.R. Mitchell, for introducing me to surface science. I am grateful for his guidance, encouragement, and help throughout the period of research as well as for his careful reading of this thesis.

I thank Dr. P.C. Wong and Dr. K.C. Wong for their guidance, particularly regarding SAM and XPS measurements. Discussions on SEM and EDX with Ms. M. Mager (Department of Materials Engineering) were appreciated. I would also like to thank Ms. D. Susac for help in the first stages of research and Dr. S. Kulinich for the collaborative research described in Chapter 7. I have had valuable interactions with other (former) members of the group, including Dr. S. Campbell, Dr. L. Zhu, Mr. J. Kim, and Mr. M. Teo. I also acknowledge the efforts of staff in the Chemistry Department Electronics and Mechanical shops (particularly Mr. Z. Germann) for keeping the equipment in working order for this research. In addition, I am grateful to Professor R.W. Lee for his advice and encouragement. Financial support from NSERC in the form of PGS A and B scholarships was appreciated.

Finally, I would like to thank my parents for their support and scientific discussions over many years.

Chapter 1

Introduction

1.1 Aluminum and its Alloys

In 1886, Charles Hall (USA) and Paul Héroult (France) independently developed a method for extracting aluminum by the electrolytic reduction of aluminum oxide (from bauxite, a natural ore) dissolved in molten cryolite (sodium aluminum fluoride). This triggered growth in the production and use of aluminum. Currently, this metal and its alloys are widely used, with applications that extend from automobile, aircraft, and marine applications to the packaging (food and beverage), electrical, and construction industries. Important properties of aluminum include its low density (approximately 35% that of steel), high strength-to-weight ratio, and resistance to corrosion. It is also non-toxic and an excellent conductor of heat and electricity [1,2].

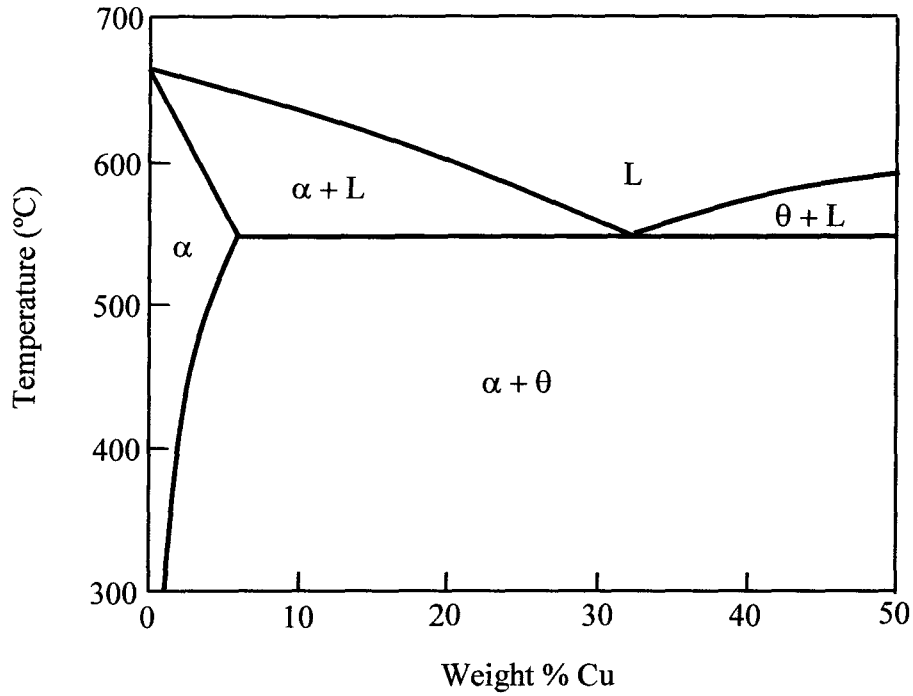
Adding other elements to aluminum, forming alloys, enhances its strength and other properties [1-4]. Alloy nomenclature is based on the alloying elements added to aluminum: Cu, Mn, Si, Mg, and Zn. For example, alloys with the designations 2xxx (e.g. 2024-Al) and 5xxx (e.g. 5754-Al) have Cu and Mg as the main added elements respectively. Unlike cast alloys, wrought alloys can be formed or shaped by mechanical deformation. The designation 2024-T3 identifies a wrought alloy with composition and temper represented as 2024 and T3 respectively. Its composition is (as weight percentages): 3.8-4.9 Cu, 1.2-1.8 Mg, 0.5 Fe, 0.3-0.9 Mn, 0.5 Si, 0.25 Zn, with the balance being Al. In this example, the atomic percentages for the main alloying elements Cu and Mg are similar. The presence of copper in aluminum alloys (especially in combination with magnesium) increases the mechanical strength significantly, but also decreases the alloy corrosion resistance. The 2024-T3 Al alloy is used

for high-strength structural applications (especially aircraft), and is the subject for work described in this thesis. Henceforth 2024-T3 Al will be abbreviated as 2024-Al.

The temper designation (T3) indicates that the alloy has been solution heat treated, cold worked, and naturally aged to a substantially stable condition [3]. Solution heat treatment involves heating the material to an appropriately elevated temperature (e.g. 500 °C for 2024-Al [3]), maintaining that temperature until the alloying elements enter into solid solution, meaning that they become distributed randomly among the Al atoms, and then cooling rapidly [2]. Solution heat treatment in combination with aging (described below) increases alloy strength and hardness [4]. Cold working involves plastic (permanent) deformation of the alloy, using processes such as room temperature rolling, although the alloy itself may heat up to 150°C during the process [2,4]. Cold working also increases alloy strength.

Precipitates of one or more solid phases (up to 10 µm in size for 2024-Al), dispersed within the original alloy phase (the matrix) are developed during aging (also known as precipitation hardening) [2,4]. The process of aging usually involves keeping the alloy at a specific temperature, lower than that used for the solution heat treatment, for a certain time period (e.g. room temperature for four to five days to achieve a T3 temper for 2024-Al [3]). Various solid phases can be formed depending on the temperature of the heat treatment and the concentrations of the alloying elements. This may be illustrated in a simplified manner with reference to a binary phase diagram. Figure 1.1(a) shows part of the phase diagram for the Al-Cu system where the liquid (L) remains as a stable phase at temperatures higher than 550°C and over a wide range of Cu concentrations. Below 550°C there exists a two-phase region with solid phases α (a solid solution of Al with a maximum

(a)



(b)

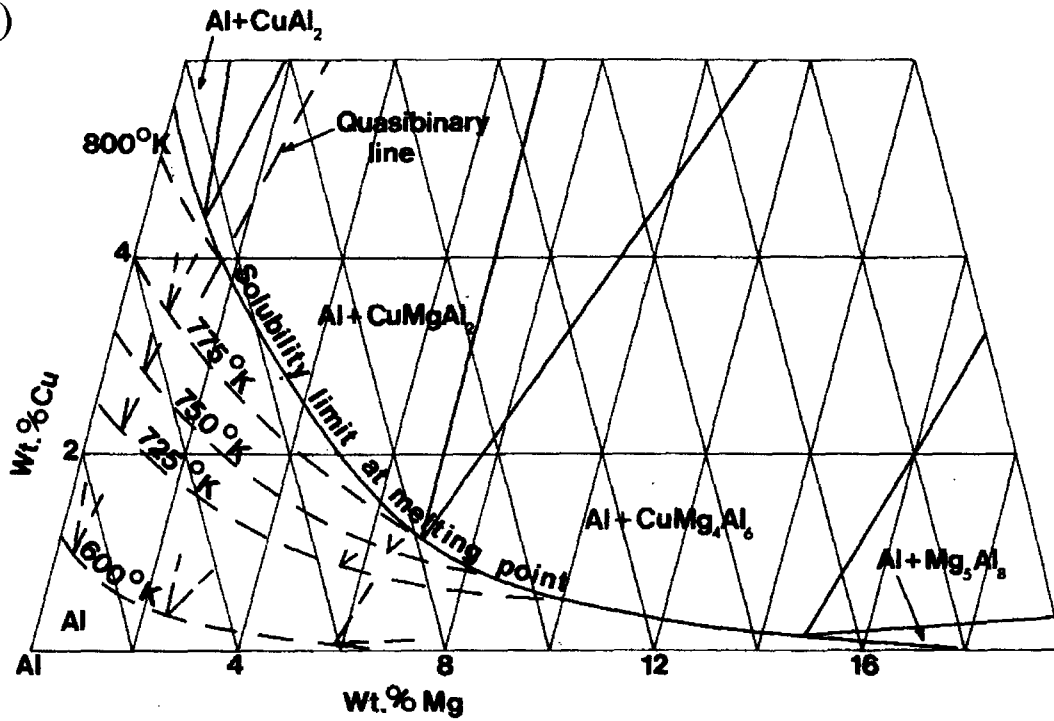


Figure 1.1 Alloy phase diagrams: (a) schematic of part of the aluminum-copper phase diagram and (b) part of the aluminum-copper-magnesium phase diagram [5] (reproduced with permission).

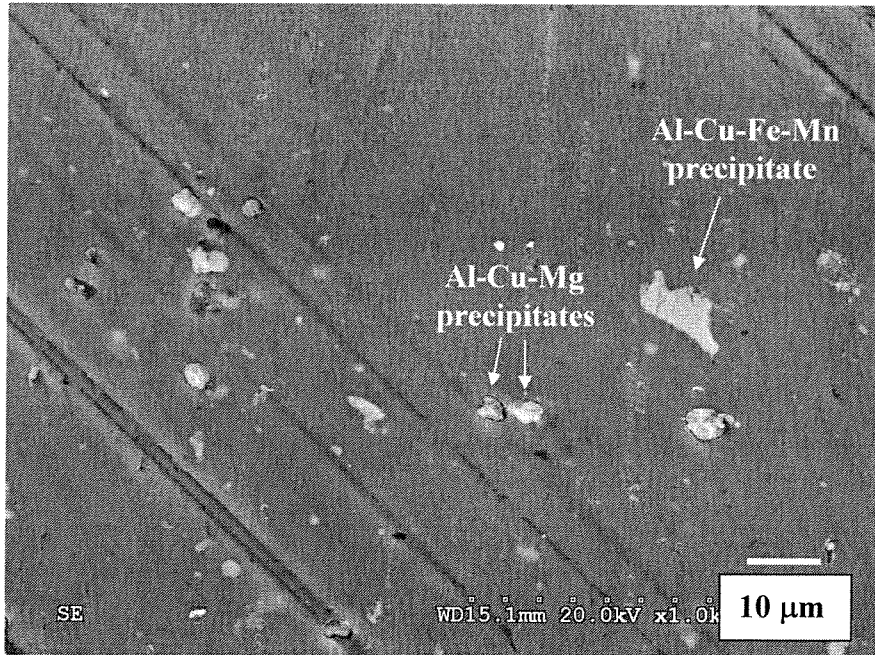


Figure 1.2 Scanning electron micrograph of 2024-T3 Al alloy microstructure.

of around 5 wt % Cu) and θ (the intermetallic compound Al_2Cu). Aging for the Al-Cu system causes the formation of second-phase precipitates (phase θ) dispersed within the solid solution matrix (α). The addition of a third element (Mg) creates more phases. Figure 1.1(b) shows part of the Al-Cu-Mg phase diagram. Al_2CuMg and other intermetallic compounds become stable depending on the amounts of Cu and Mg added to the Al and the temperature at which equilibrium is established.

The microstructure of the alloy reflects the types (compositions) of precipitates present as well as their sizes, shapes, and distributions. For 2024-Al, Al_2CuMg (also known as the S phase), $\text{Al}_6(\text{CuFeMn})$, and Al_2Cu phases have been reported [6,7]. Phases of the type Al_2CuMg (often referred to by the abbreviated notation Al-Cu-Mg) and $\text{Al}_6(\text{CuFeMn})$ (Al-Cu-Fe-Mn) are the focus of the current study. Figure 1.2 shows a scanning electron micrograph of the alloy microstructure. The presence of second-phase particles improves the mechanical properties but also makes the alloy more susceptible to localized corrosion due to galvanic effects [8]. This involves accelerated corrosion of a metal due to its electrical contact with a more noble metal in a conductive environment [1]. Because the matrix region remains in contact with the nobler second-phase particles, accelerated corrosion of the matrix can occur at the particle-matrix interface. The electrochemical characteristics of second-phase particles in aluminum alloys have been surveyed [9]. More generally, the second-phase regions are chemical heterogeneities in the alloys.

1.2 Protection of Aluminum from Corrosion

The formation of a protective oxide layer at its surface slows the corrosion of aluminum under mild oxidizing conditions [1,2]. If damaged in air, the oxide film can reform quickly and continue to protect the metal. In general, the oxide layer on aluminum is

resistant to aqueous solutions in the pH range of about 4 to 8.5 (based on thermodynamic (Pourbaix) considerations [10]); however these limits depend on temperature, the specific form of oxide present, and the presence of other chemical species in solution. Individual ions in solution (e.g. NO_3^-) may have specific effects on the corrosion mechanism [11].

When the pH is kept close to neutral and there is no general attack across the surface, localized corrosion may still occur and is characterized by the formation of pits. For a mildly corrosive environment, the corrosion product (aluminum oxide) may close the pits like a plug to prevent the corrosive solution from reaching the base of the pit, thus stopping the attack. The presence of halide ions (e.g. Cl^-) facilitates pitting corrosion. Pits can be created by dissolution of the matrix region close to noble second-phase particles (due to galvanic effects), or by dissolution of the second-phase particles. Copper in aluminum alloys accelerates corrosion by dissolving and then re-precipitating on the surface (as metallic Cu), creating the conditions for galvanic corrosion [1].

Figure 1.3 schematically shows the oxide film that develops under normal atmospheric conditions. This oxide, of total thickness approximately 10 nm, consists of two layers: a compact inner layer next to the metal (the barrier layer) and an outer layer of hydrated oxide which is thicker and more permeable. At temperatures below 250 °C, $\text{Al}(\text{OH})_3$ is dominant in the oxide [12], however, as indicated in Figure 1.4, the oxide layer can have different chemical compositions above the second-phase particles (heterogeneities), particularly because the oxide film grows into the metal. Consequently, the oxide properties vary across the surface. Aluminum oxide is an insulator, but when it contains iron, for example, it becomes a semiconductor, thereby facilitating the flow of electrons in small local galvanic cells at the iron-containing intermetallic particles [2]. That can facilitate

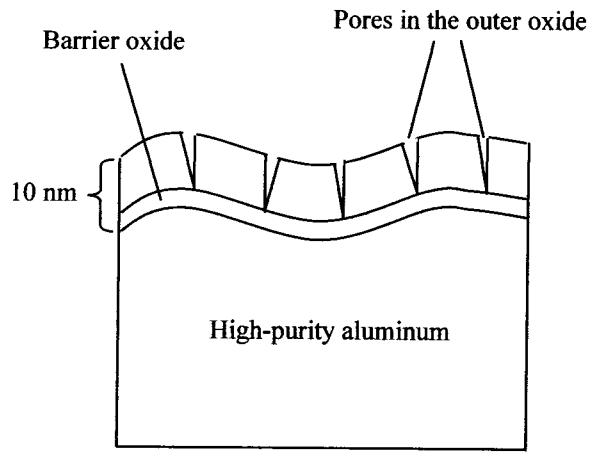


Figure 1.3 Schematic of natural oxide layer on high-purity aluminum.

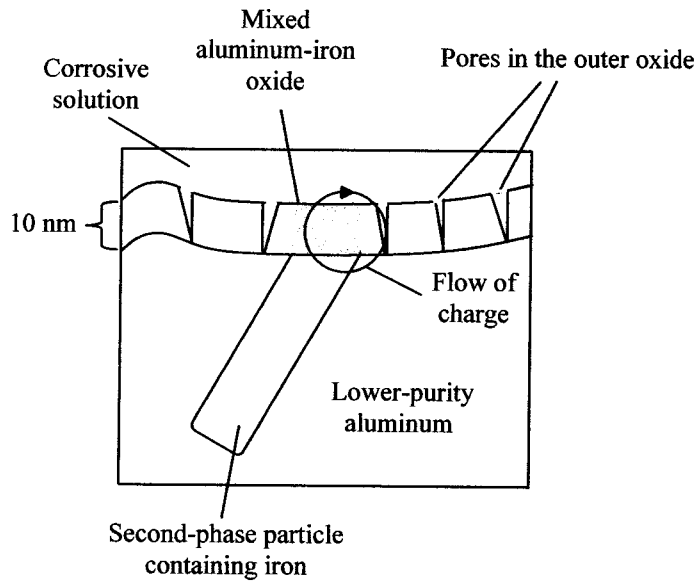


Figure 1.4 Schematic of corrosion (lower purity aluminum) in an aggressive solution.

dissolution of the aluminum substrate.

There are several methods for improving the corrosion resistance of aluminum alloys. Anodizing is one approach and uses an electrolytic process to generate artificial oxide layers [13]. Cladding is another method that is used for 2024-Al. In this approach, the alloy is coated with a thin layer of pure aluminum or aluminum alloy that is anodic to the core material. When the product is in contact with a corrosive solution the cladding dissolves preferentially, thus protecting the core alloy [1,2].

Another approach is to use a conversion coating. Such coatings are thin layers of low-solubility inorganic compounds that form spontaneously when the coating solution contacts the metal surface (either by dipping in the coating solution or by spraying the solution onto the metal). Conversion coatings can provide improved corrosion resistance and also enhance the adhesion for organic finishes [1,14]. Traditionally, the chromate type of conversion coating has provided excellent corrosion resistance due to its self-healing abilities; however, there are indications that the hexavalent chromium compounds involved are carcinogenic [15]. As a result, there are concerns regarding the use and disposal of these materials and alternative coating technologies are being developed [14-16]. The alternative conversion-type coatings include use of cerium oxides [17], as well as permanganates [18] and oxides of zirconium [16,19] and vanadium [20]. The term “conversion coating” originated with phosphating treatments [21-23], which form a main topic of this thesis. A completely different approach to corrosion protection for Al and its alloys involves the use of organosilane compounds as corrosion inhibitors [16]. All these approaches are currently under active development to deal with the challenge of phasing out the use of the chromating process. According to a recent review, combinations of the above-mentioned treatments (e.g. cerium oxide-phosphate [24,25], or a multi-component phosphate bath containing cerium,

zirconium, and vanadium compounds [16]) may prove to be the most effective alternatives to chromate coatings [16].

1.3 Zinc Phosphate Conversion Coatings

That dipping iron into H_3PO_4 can add corrosion protection was recognized more than a century ago [21-23]. Other types of phosphate coatings have been considered including those of zinc, nickel, or manganese, as well as mixed phosphates. Additionally, the coating process has been extended to substrates such as steel and aluminum. Zinc phosphate (ZPO) coatings are used as a pretreatment before paint is applied since they improve paint adhesion and corrosion resistance.

ZPO coatings have low operational costs [26] and provide a good base for organic coatings [2]. Currently the main use of zinc phosphating processes on Al is in situations where mixtures of metals, such as Al, steel, and galvanized steel are being treated in the same process, for example in a car body assembly [16,27,28,29]. The presence of both Zn and Fe in the coating bath makes the process easier to control; however, the amount of Al should not exceed a specific percentage of the total surface area being treated [16]. ZPO coatings on steel have been studied extensively [22] but there are fewer reports on the mechanism of ZPO coating formation on Al alloys. The many inorganic/organic accelerators and additives used in phosphating baths have been summarized and some of the common accelerators are NO_3^- , NO_2^- , and hydroxylamine [22]. Industrial phosphating baths contain Zn^{2+} , Ni^{2+} , and Mn^{2+} and the presence of these three ions increases the coating corrosion resistance and paint adhesion [23].

Figure 1.5 indicates the current understanding for the mechanism for ZPO coating [23,27]. The process starts with the acidic solution etching the overlying oxide (not shown in

diagram) to allow the metal to come in contact with the solution. Dissolution of Al (oxidation) at local anodic sites is coupled with reduction at local cathodic sites involving a solution species, specifically H^+ or a coating bath additive such as NO_3^- . This increases the local pH and in turn drives the precipitation of ZPO. Fluoride ion is added to the coating bath to accelerate etching and to limit free Al^{3+} in solution which can otherwise inhibit formation of a ZPO layer [30]. Other ions (e.g. Mn^{2+} , Ni^{2+}) are often added to the coating bath with a purpose of improving the quality of the resulting coatings [22]. Growth of the phosphate layer is discontinued when a sufficiently large area on the surface has been covered by phosphate, blocking the metal dissolution and reduction reactions required for precipitation. Figure 1.6(a) shows a SEM image of a surface of 2024-Al alloy after a ZPO coating. The areas between the bigger crystals represent pores in the coating which can facilitate anchorage of a paint layer. In general, the coatings consist of a mix of amorphous and crystalline phases. X-ray diffraction has identified crystals of $Zn_3(PO_4)_2 \cdot 4H_2O$ (hopeite) and $Zn_2Fe(PO_4)_2 \cdot 4H_2O$ (phosphophyllite) in specific phosphate coatings [31,32]. For coating baths where manganese and nickel are present the $Zn_{3-x}Mn_x(PO_4)_2 \cdot 4H_2O$ and $Zn_{3-y}Ni_y(PO_4)_2 \cdot 4H_2O$ structures (respectively) have been indicated using several analytical techniques including electron spin resonance [33]. The crystal $Zn_2Ni(PO_4)_2 \cdot 4H_2O$ is isostructural with hopeite, with nickel substituting for zinc at the octahedral sites [34].

There are additional steps which take place before and after the metal is exposed to the phosphating solution: surface polishing and conditioning (also known as activation [35,36]) are two examples of pre-treatments. Post-treatment involves rinsing the coated sample in a corrosion-inhibiting solution in order to seal the porous phosphate coatings [22]. Different pre- and post-treatments and variations in the phosphate coating solution composition have significant effects on the coatings formed [37-40].

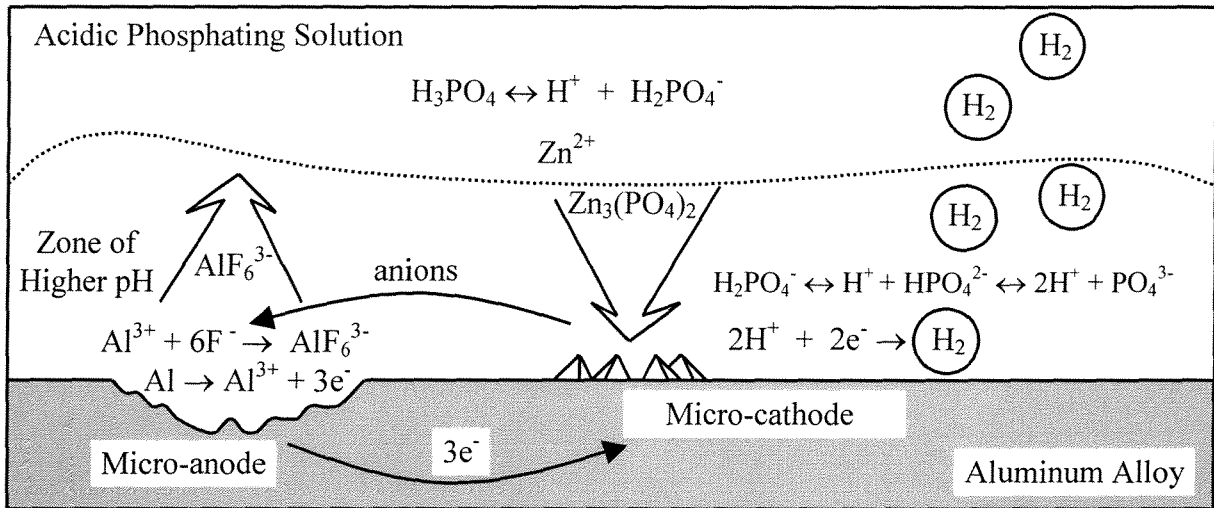


Figure 1.5 Schematic of phosphating process on aluminum.

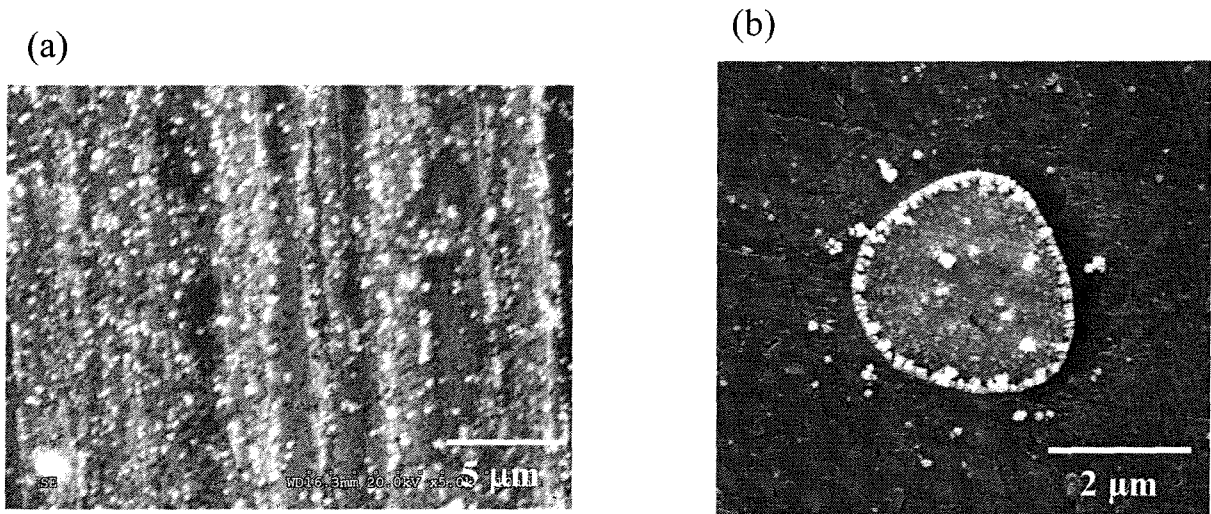


Figure 1.6 The SEM micrograph in (a) shows a surface of 2024-Al alloy after a full ZPO coating. The bright areas are large ZPO crystals, and coating is also deposited in the areas between the large crystals. The micrograph in (b) shows a Al-Cu-Mg second-phase particle surrounded by the matrix region on a 2024-Al surface (initial stages of ZPO coating).

Segregation of Cu from the bulk to the alloy-oxide interface occurs as a result of acid etching for 2024-Al alloy, and an appropriate amount of Cu at the interface improves the properties of the ZPO coating formed after the acid etch pre-treatment [41]. Adding Cu^{2+} to the ZPO coating bath at concentrations up to 10 ppm causes significant changes in coating morphology, adhesion, and corrosion protection [42].

Alloy microstructure influences the formation of ZPO coatings. As Figure 1.6(b) indicates, the initial nucleation of ZPO crystals can occur at interfaces between Al-Cu-Mg second-phase particles and the matrix (2024-Al alloy) [43].

1.4 Objectives of Research

Commercial zinc phosphate baths normally contain Ni^{2+} and Mn^{2+} , and other additives in addition to the main phosphating components of Zn^{2+} , H_3PO_4 , and F^- . These baths have been formulated by empirical testing, in general without a clear appeal to scientific principles. One major objective of the work presented in this thesis is to make a more fundamental exploration of the roles of the additive ions Ni^{2+} and Mn^{2+} in the chemical reactions for the phosphating process on Al. Investigations involved determining how the nature of the coating bath affects properties of the resulting coatings such as thickness, crystal size, chemical composition, and corrosion resistance. These studies are extended to analyze the coatings at different microstructural regions on the 2024-Al alloy surface.

Work in this thesis also aims to explore in detail the influences of surface oxides and the metal near the alloy-oxide interface on zinc phosphate coating formation at different microstructural areas. Additionally, to our knowledge little research has been published with regard to degradation at different micro-regions on a 2024-Al surface which has been coated with zinc phosphate and then exposed to a corrosive solution. Throughout, this work aims to

build a further mechanistic understanding for the formation of zinc phosphate coatings and their properties on the 2024-Al alloy. Additionally, further work is reported for the formation of chromate and permanganate conversion coatings at different micro-regions of the 2024-Al alloy, and comparisons are made with the situation for the zinc phosphate coatings.

1.5 Outline of Thesis

This thesis is organized as follows. Chapter 2 describes the key techniques used in the research including: X-ray photoelectron spectroscopy (XPS), scanning Auger microscopy (SAM), scanning electron microscopy (SEM), energy dispersive X-ray spectroscopy (EDX), and electrochemical polarization. Chapter 3 reports studies for the effect of Ni^{2+} on the zinc phosphating of 2024-Al alloy, while Chapter 4 describes mechanistic aspects of the role of Ni^{2+} in the zinc phosphating process, including the effect of the pH of the coating solution. Chapter 5 describes studies of the use of Mn^{2+} as an additive in ZPO coatings, and compares the effects of Ni^{2+} and Mn^{2+} . Chapter 6 reports on the formation and degradation of ZPO coatings on the 2024-Al alloy with an emphasis on effects at the microstructural level. Chapter 7 describes work done with chromate and permanganate conversion coatings, and compares with the formation of ZPO coatings. Chapter 8 concludes with a thesis summary and suggestions for follow-up research.

Chapter 2

Experimental Methods

2.1 X-ray Photoelectron Spectroscopy

2.1.1 Theory of Technique

X-ray photoelectron spectroscopy (XPS) is a photoemission technique used extensively to examine the composition and chemical states of species at solid surfaces. It was originally named electron spectroscopy for chemical analysis (ESCA). In this method, the surface is irradiated with soft X-rays, causing photoemission of electrons (Figure 2.1(a)), as explained by Einstein. An X-ray photon of energy $h\nu$ interacts with an electron of binding energy E_B , transferring the photon energy to the electron and resulting in its ejection with kinetic energy [44-47]:

$$E_{\text{Kin}} = h\nu - E_B. \quad (2.1)$$

The kinetic energy distribution of the emitted electrons provides detailed information about the solid. In 1954 Siegbahn and co-workers measured the kinetic energy distribution using a high-energy-resolution electron spectrometer and observed well-defined peaks arising from the atomic orbital structure. Further study indicated that shifts in the kinetic energies of the peaks provided chemical state information. In 1966 the same group demonstrated that the electrons detected are from the surface regions of a solid. Siegbahn was awarded the Nobel Prize for Physics in 1981 for his work in developing XPS as a surface analytical technique.

A typical XPS survey spectrum recorded from a zinc phosphated Al alloy is shown in Figure 2.2(a) and consists of peaks on a large background. Electrons comprising the spectral peaks provide most of the useful information although they represent only a small fraction (<1%) of the total emitted electrons. The primary peaks arise from shallow levels (binding

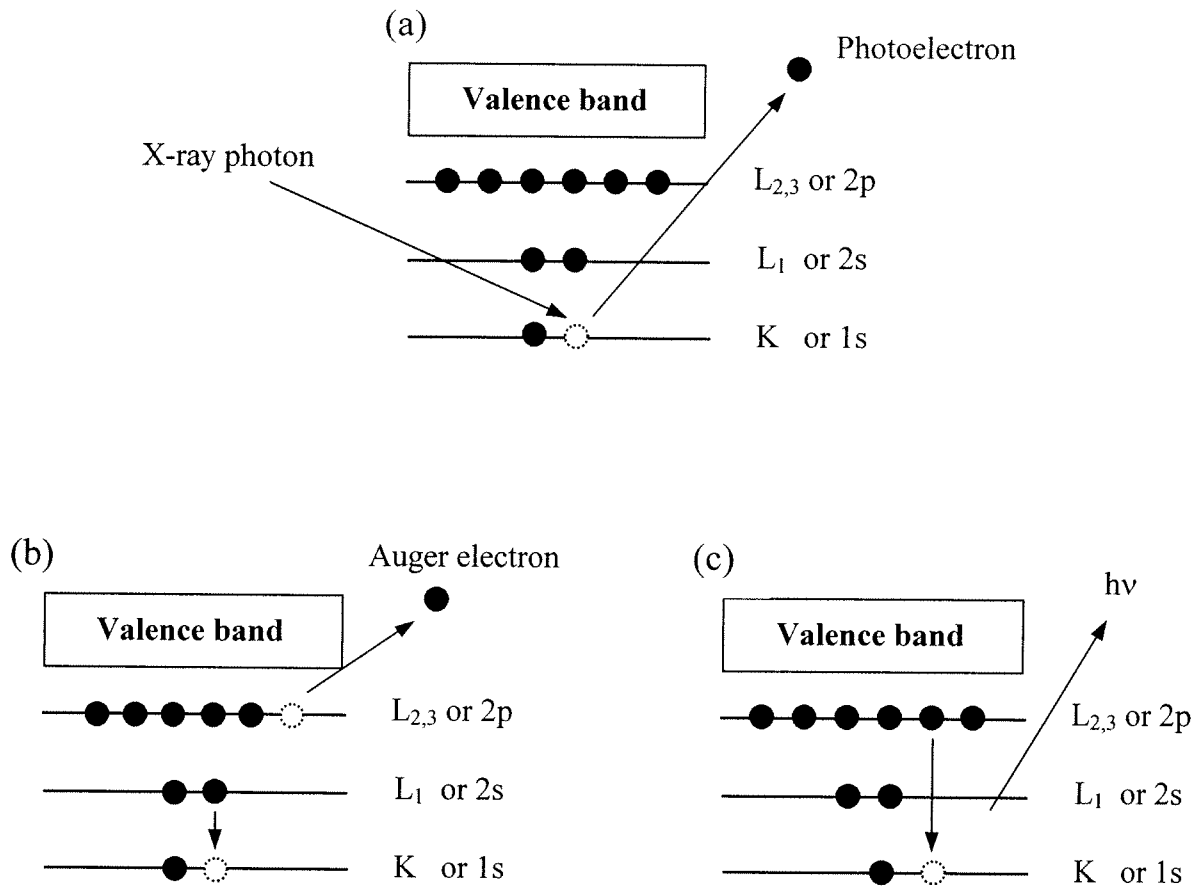


Figure 2.1 Schematic diagram for (a) photoelectron emission, (b) Auger electron emission, and (c) X-ray emission (fluorescence).

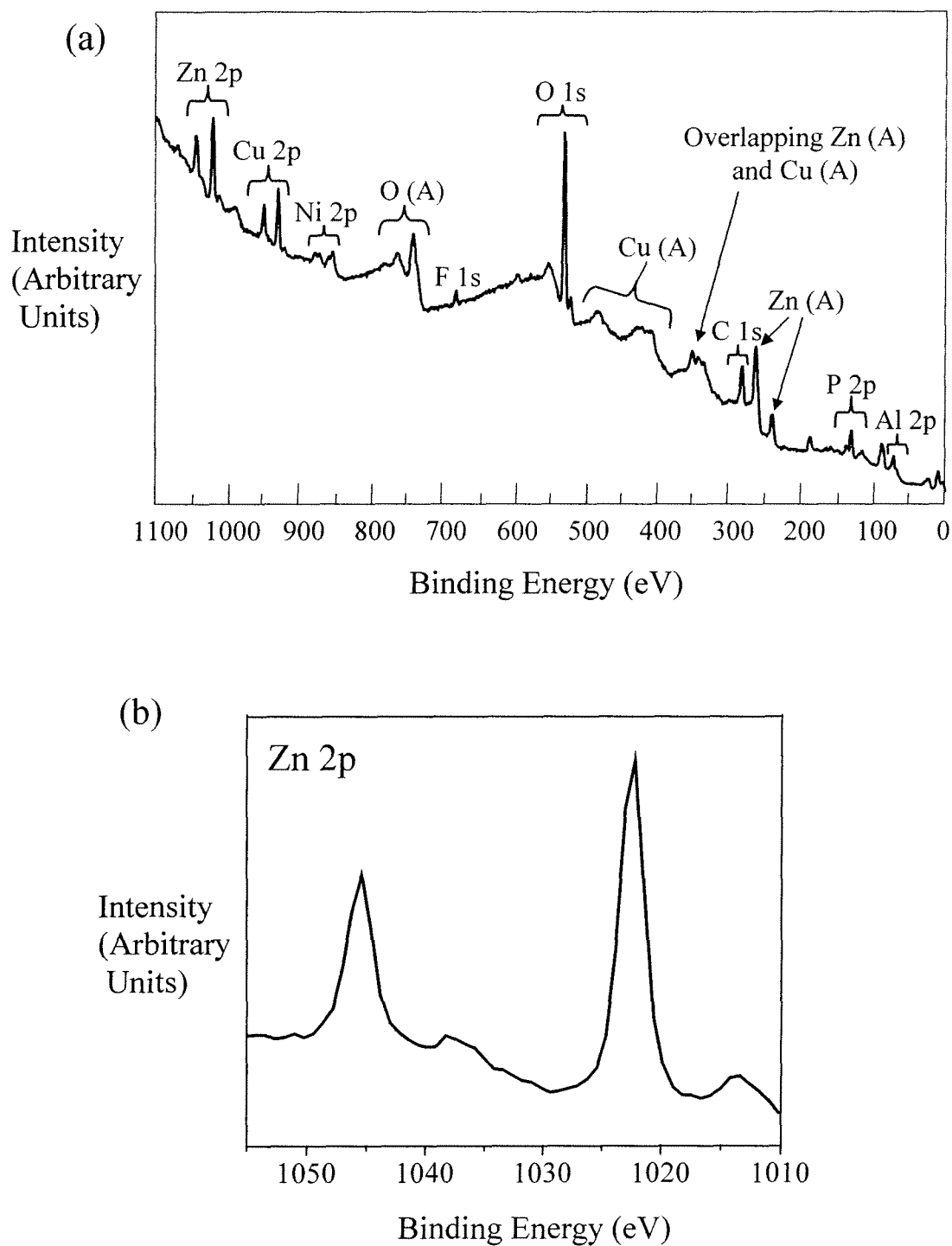


Figure 2.2 XPS spectra from zinc phosphated 2024-Al alloy: (a) survey spectrum (the (A) identify Auger electron peaks), and (b) Zn 2p region.

energies less than 50 eV) and deeper core levels, and also from Auger processes (Section 2.2.1), for each of the elements present in the surface region. Every element except H and He produces core-level and Auger peaks at specific energies, which provide compositional information about the sample.

The Zn 2p photoelectron peak (Figure 2.2(b)) has a doublet structure. This type of splitting is observed for electrons originating in orbitals with angular momentum quantum number l larger than zero (i.e. p,d,f...orbitals). The magnetic interaction between the spin of the electron ($s=1/2$) and its orbital angular momentum (l) is called spin-orbit (or l - s) coupling (governed by quantum number $j = l + s$). Possible values of j are: 1/2 and 3/2 for p orbitals, 3/2 and 5/2 for d orbitals, and 5/2 and 7/2 for f orbitals. Different values of j correspond to states of different energy, resulting in multiple peaks in the XPS spectrum. The intensities of these components are proportional to their respective degeneracies, $2j + 1$, after correcting for the contribution of inelastically scattered electrons to the spectral background.

The surface specificity of XPS depends on the kinetic energies of the electrons involved. X-rays have a low absorption cross-section in solids resulting in penetration depths of 1 μm or more for X-rays of 1000 eV (typical order of magnitude for X-rays used in XPS). However, most of the photoelectrons travel only a few nm before losing energy through inelastic collisions with the electrons in the solid, thus becoming part of the broad background rather than the elemental peaks. The average distance travelled in a solid by an electron before being inelastically scattered (inelastic mean free path, λ) is dependent on the electron kinetic energy and the type of material (Figure 2.3). In XPS the photoelectron kinetic energies are normally in the range 100 – 1500 eV, implying that for normal (90°) emission the photoelectrons have on average originated from the top 10 nm or less of the

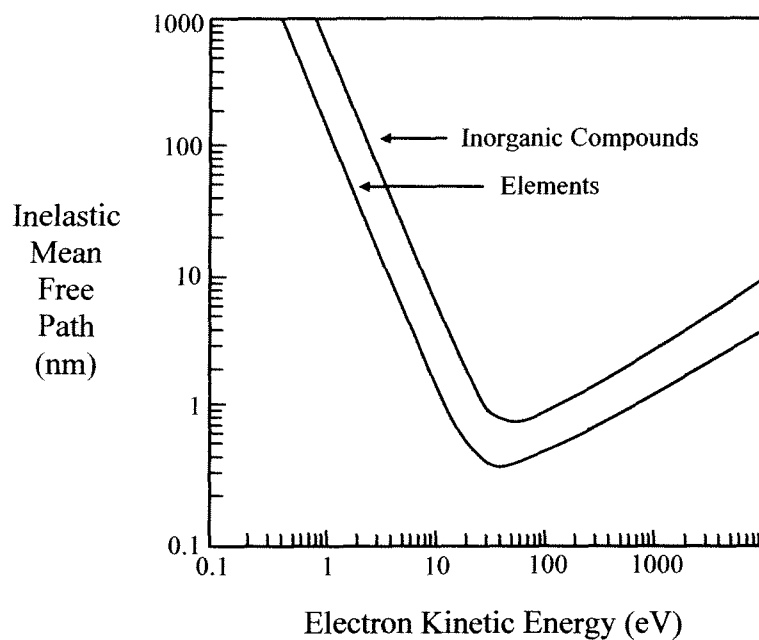


Figure 2.3 Dependence of inelastic mean free path on electron kinetic energy (schematic).

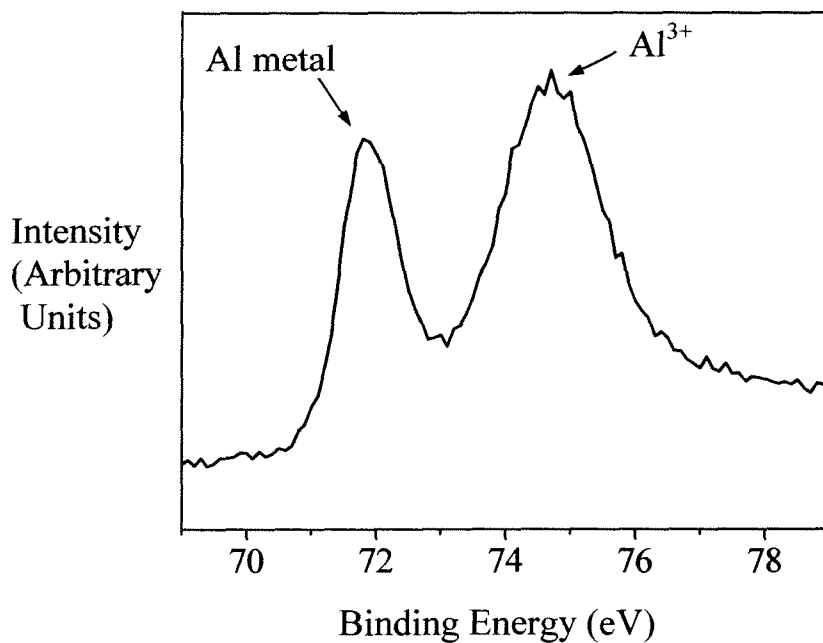


Figure 2.4 High resolution XPS spectrum (Al 2p region) from zinc phosphated 2024-Al alloy.

material. 95% of the signal comes from a depth of 3λ [45].

For a given atom and core level, changes in chemical bonding can modify the binding energy, resulting in shifts in peak position. Figure 2.4 shows an example of two photoelectron peaks in the high resolution Al 2p spectrum obtained from a zinc phosphated Al alloy. The peak at lower binding energy corresponds to metallic Al while the higher binding energy peak represents Al^{3+} . The energy resolution of XPS is limited, and therefore similar chemical states will not necessarily be distinguished by direct observation. Analysis of reference materials can be helpful to identify chemical states, but sometimes there can be challenges in preparing well-defined surfaces due to the presence of persistent surface contamination, multiple chemical states, and the fact that the surface composition may be different from the bulk composition. Useful reference surfaces must be clean, but there may be challenges if the cleaning procedures themselves change the surface, so introducing ambiguities into the spectra.

2.1.2 Instrumentation

Figure 2.5 illustrates a schematic of the XPS spectrometer used in this work. It consists of four interlinked ultrahigh vacuum (UHV) chambers: the transfer chamber (for introducing the sample from the atmosphere into the instrument), the analysis chamber (where the analytical measurements are made), and two preparation chambers (for sample treatments). The analysis chamber is equipped with an X-ray source, energy analyzer with lens system and detector, and an ion gun for sample cleaning. A manual transfer rod moves the sample from the transfer chamber to the analysis chamber, while two additional rods are available for sample transfer from the preparation chambers to the analysis chamber.

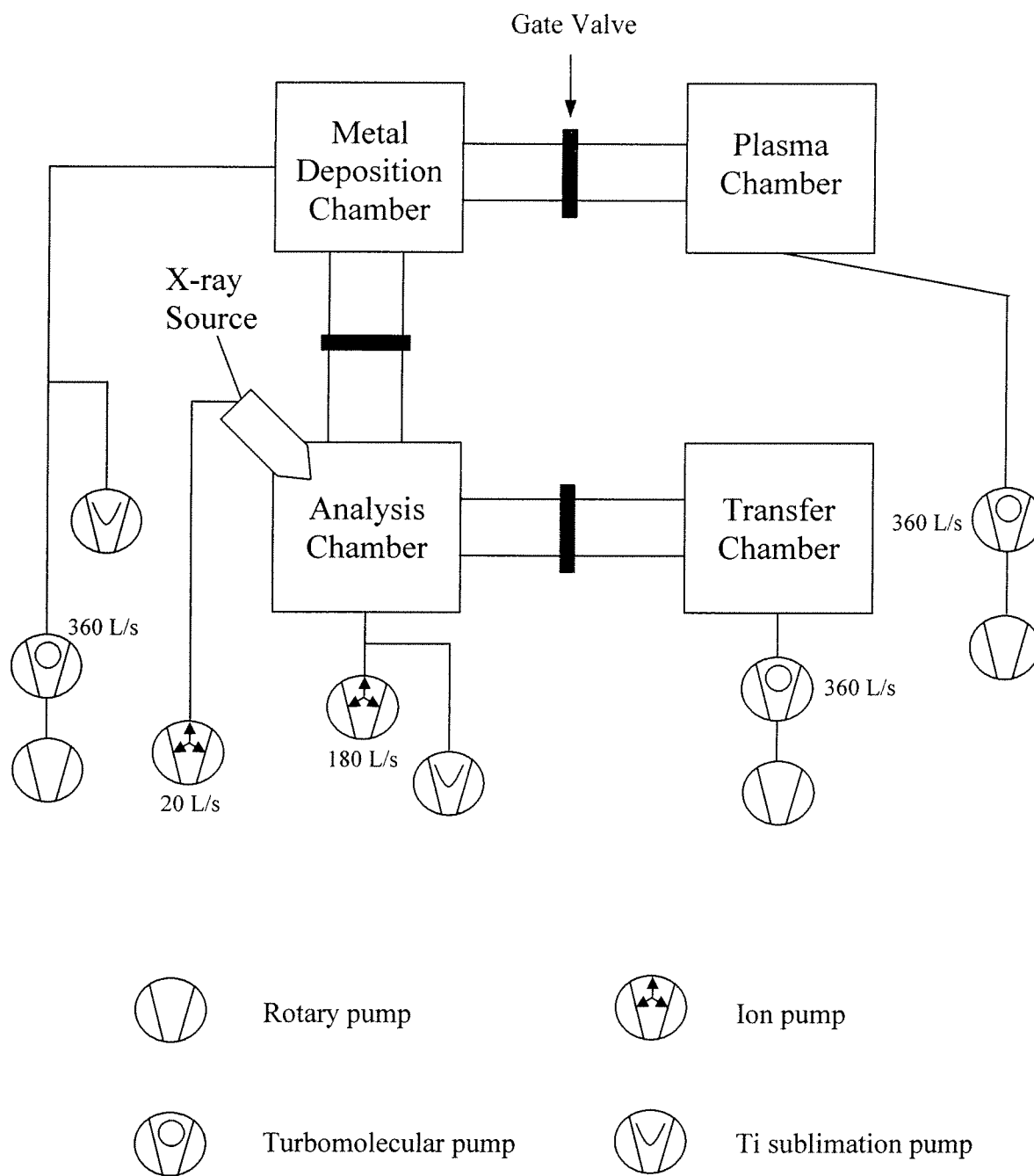


Figure 2.5 Schematic of pumping system for MAX 200 XPS spectrometer.

The XPS experiment should be conducted under vacuum for three reasons: first, emitted photoelectrons must be able to travel from the sample through the analyzer to the detector without colliding with gas molecules [45]. Also, the X-ray source requires vacuum conditions to operate. A third requirement is that the surface composition of the sample under investigation must remain basically constant during the XPS experiment. More stringent vacuum conditions are required to fulfill this requirement and measurements are made when the system pressure is approximately 10^{-9} Torr (UHV conditions [48]).

The UHV conditions required are achieved using a combination of turbomolecular and ion pumps, where each turbomolecular pump is backed by a rotary pump. In addition an auxiliary Ti sublimation pump is used for supplementary pumping of the analysis chamber.

The X-ray source used here is operated by bombarding a water cooled metal anode with high energy electrons (10 to 15 keV) [45]. Core holes are created in the anode atoms, which in turn emit X-rays by fluorescence or electrons. The fluorescent X-rays are used in the XPS experiment (Figure 2.1(a)). Mg and Al are the most commonly-used anode materials, with $K\alpha$ emission lines at 1253.6 eV and 1486.6 eV respectively. An Al window (thickness $\sim 2 \mu\text{m}$) is placed between the X-ray source and sample in order to protect the sample from contamination and stray electrons.

The analyzer system has three main components: collection lens system, energy analyzer, and detector. In order to improve resolution, it is standard practice to retard the electron kinetic energies to a chosen analyzer energy (pass energy). The lens system controls the analysis area on the sample, collects electrons from the sample, and controls the retarding potential used [45]. An area of 7 mm x 4 mm on the sample surface was analyzed for the measurements described in this thesis.

Figure 2.6 shows a schematic diagram of a concentric hemispherical analyzer (CHA); this is a dispersive energy analyzer with the photoelectrons deflected by an electrostatic field [46]. The CHA consists of two concentric hemispheres (radii R_1 and R_2) with a potential difference ΔV between them (the outer hemisphere is at a negative potential with respect to the inner hemisphere). The entrance and exit slits are centred on the central circular orbit of radius $R_0 = (R_1 + R_2)/2$, and electrons within a narrow range of energy can travel from the entrance to the exit of the analyzer without colliding with one of the hemispheres. An electron with pass energy E_P can travel the orbit of radius R_0 when

$$e\Delta V = E_P(R_2/R_1 - R_1/R_2), \quad (2.2)$$

indicating the magnitude of deflecting potential required. The analyzer contribution to resolution ($\Delta E_{\text{analyzer}}$) depends only on the pass energy for fixed slit widths. The relative resolution of the CHA is given by the approximate expression:

$$\Delta E_{\text{analyzer}}/E_P = w/2R_0 + \alpha^2/4, \quad (2.3)$$

where w is the slit width and α is the entrance angle (Figure 2.6). Since the dimensions (R_0) of the analyzer are fixed there is an inverse relationship between the pass energy (E_P) and the slit width.

After passing through the exit slit, electrons are counted using a detector constructed from two channel plates in a chevron array to give 18 separate micro-channels, which act as individual electron multipliers. The retardation potential is scanned and each kinetic energy before retardation is converted to binding energy using Equation 2.1. An XPS spectrum conventionally plots the number of electrons detected against binding energy.

The smaller the pass energy (from Equation 2.3) the higher the energy resolution, but that comes at the expense of reduced signal intensity. In XPS, the pass energy is kept fixed during the acquisition of an entire spectrum, resulting in the same analyzer contribution to

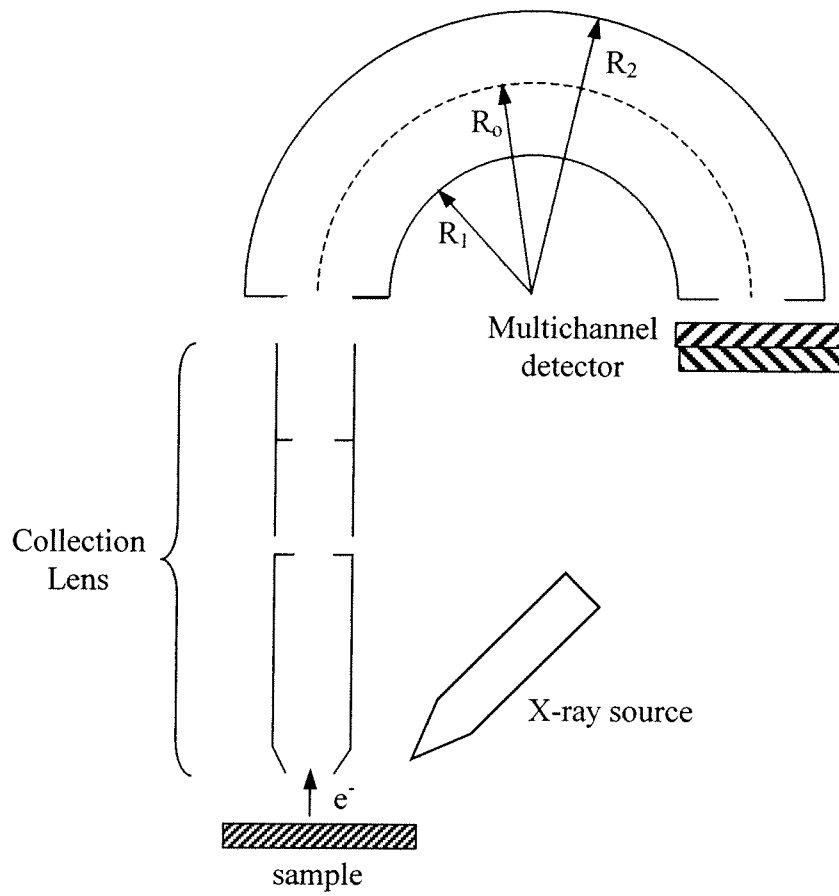


Figure 2.6 Schematic diagram for the lens system and the concentric hemispherical analyzer (CHA) in the MAX 200.

resolution for all peaks (useful for chemical state identification). For wide-scan spectra a pass energy of 192 eV was used, while the narrow-scan spectra (over a restricted energy range) were acquired using a 48 eV pass energy.

Strictly the overall experimental energy resolution (ΔE_{peak}) depends on the line widths of the X-ray source and the core orbital from which the photoelectron originates, as well as on the analyzer. For Gaussian lineshapes the relation is:

$$\Delta E_{\text{peak}} = (\Delta E_{\text{analyzer}}^2 + \Delta E_{\text{source}}^2 + \Delta E_{\text{line}}^2)^{1/2}, \quad (2.4)$$

where $\Delta E_{\text{analyzer}}$ is the analyzer resolution, ΔE_{source} is the full width at half maximum for the X-ray source, and ΔE_{line} is due to the core hole lifetime [44,45].

For a conducting sample, such as a metal, measurements are made with a sample in electrical contact with the spectrometer, and their Fermi levels are equal as shown in Figure 2.7 [45]. The measured photoelectron kinetic energy is E_k , and the relevant equation for calculating E_B is:

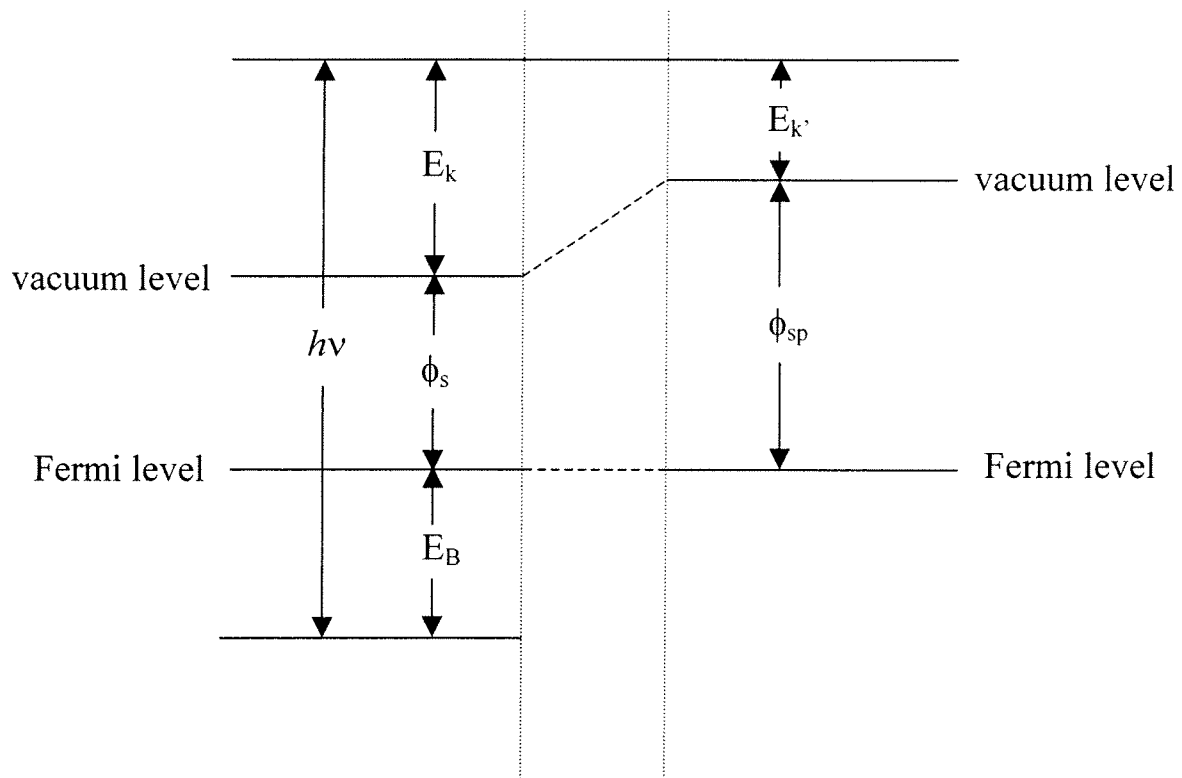
$$E_B = h\nu - E_k - \phi_{\text{sp}}. \quad (2.5)$$

ϕ_{sp} is determined by calibrating with a clean Au standard and adjusting the settings in order that the established E_B values for Au are obtained (i.e. $4f_{7/2}$ signal occurs at 84.0 eV).

Another reference is required for insulating samples when the Fermi energies of sample and spectrometer are no longer equal. Then the binding energy of the C 1s peak due to adventitious hydrocarbon contamination on the sample is assigned to 285.0 eV.

2.1.3 Quantitative Analysis

The area under a photoelectron peak is dependent on the amount of the element present in the region probed. Given sufficient information about the instrument and process,



$h\nu$ = energy of photon

E_k = kinetic energy of photoelectron with respect to vacuum level of sample

ϕ_s = work function of sample (energy difference between Fermi and vacuum levels)

E_B = binding energy of electron in sample with respect to Fermi level

$E_{k'}$ = kinetic energy of photoelectron as measured by spectrometer

ϕ_{sp} = work function of spectrometer

Figure 2.7 Schematic diagram of relevant energy levels for measurements by spectrometer of binding energy for a conducting sample.

in principle the number of photoelectrons can be calculated from first principles. For a particular photoelectron peak, the intensity contribution (dI) for electrons exiting the sample from an infinitesimal thickness dx at depth x is [46]:

$$dI = f \sigma n A T \exp(-x/\lambda) dx. \quad (2.6)$$

In Equation 2.6, f is the X-ray flux, σ is the photoemission cross-section, n is the number of atoms per unit volume of the sample, A is the area on the sample from which measurements are made, T is the transmission function of the instrument, and λ is the inelastic mean free path.

For a sample whose composition is homogeneous within the XPS sampling depth [45], then Equation 2.6 can be integrated to obtain

$$I = f \sigma n A T \lambda. \quad (2.7)$$

For fixed instrumental settings, the X-ray flux and area of sample irradiated do not vary from one sample to another. The transmission function T includes the efficiency of the energy analyzer and is also assumed to remain constant. For each photoelectron peak, the fixed experimental parameters can be combined in a sensitivity factor (S):

$$S = f \sigma A T, \quad (2.8)$$

and rearranging,

$$n = I / S \lambda. \quad (2.9)$$

The value of S is specific to each photoelectron peak and setting for the particular instrument. The composition ratio for two elements in a sample is given by:

$$n_1/n_2 = [(I_1/S_1)/(I_2/S_2)][\lambda_2/\lambda_1]. \quad (2.10)$$

For heterogeneous samples this analysis yields semi-quantitative information and in this situation the ratio λ_2/λ_1 is often taken as constant and close to unity. Then the composition ratio of two elements in the surface region can be calculated with knowledge of the peak

intensities and the appropriate sensitivity factors. The analysis can be generalized to give relative atomic percentages as indicated by

$$N_i = \{ (I_i/S_i) / \sum_x (I_x/S_x) \} \times 100 \quad (2.11)$$

where N_i is the atomic percent of element i and x is summed over the various elements in the sample.

The first step in quantitation involves subtracting the contribution of inelastically-scattered photoelectrons from the peak intensity. The method introduced by Shirley is illustrated in Figure 2.8 and assumes that the background intensity (inelastically scattered electrons) at any energy is proportional to the number of elastically scattered electrons at higher kinetic energy [50]. Then the corrected intensity (over an energy range of E_1 to E_2 , chosen by the operator) is given by the iterative algorithm:

$$N'_{K+1}(E) = N(E) - N(E_2) - C \int_E^{E_2} N'_K(E) dE, \quad (2.12)$$

where $N(E)$ is the observed intensity at E (including the background), $N'_K(E)$ is the count rate after subtraction of the background contribution for the K -th iteration, C is a constant, and $N(E_2)$ is the reference background level (point on the higher kinetic energy (lower binding energy) side of the peak where the background is flat). The process begins with $N'_1(E) = 0$ and continues until $N'_{K+1}(E) \sim N'_K(E)$ which normally requires three or four iterations.

In the most ideal situation where the material analyzed is homogeneous, and sufficient standards specific to the context are available, quantitative analysis of XPS spectra can yield values of elemental composition with uncertainties of less than about 2% [52]. The situation for work presented in this thesis is much more complex since the samples are heterogeneous, and one can only estimate average compositions within the depth probed by the detected photoelectrons. Moreover those depths can differ depending on the specific

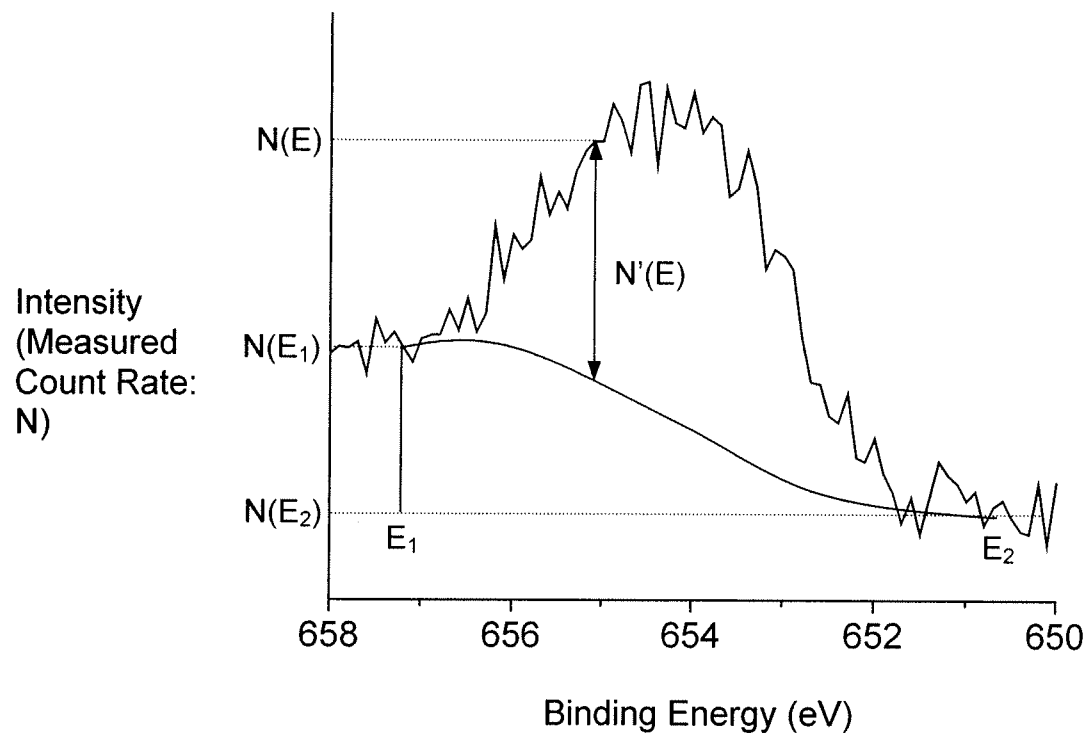


Figure 2.8 Shirley non-linear background correction applied to a Mn $2p_{1/2}$ spectrum.

peak and element. Accordingly the quantitative percentage compositions quoted in the thesis are believed to be accurate to within $\pm 10\%$, as discussed by Briggs and Seah [46].

2.2 Scanning Auger Microscopy

2.2.1 Theory of Techniques

Scanning Auger Microscopy (SAM) is Auger electron spectroscopy (AES) applied to a local region of a surface. AES is based on the Auger effect and is used to determine surface region compositions and chemical states [44,45]. Emission of electrons is stimulated by interaction of incident X-rays or electrons with the surface. SAM has the advantage of local analysis capabilities due to the possibility of focusing and scanning the primary electron beam in the nanometer range. The spatial resolution depends on the focusing capability of the electron gun (~ 10 nm for the Thermo Electron Microlab 350 instrument) and the nature of the surface.

The process that became known as the Auger effect was predicted on theoretical grounds by Rosseland in 1923 and discovered experimentally by Auger in 1926 [51]. It is shown schematically in Figure 2.1(b). Commonly transitions in an Auger process are labelled with symbols K,L,M... for principal quantum number n equal to 1,2,3... respectively for the energy levels involved. The notation is often extended with subscripts (e.g. L_1 for $2s_{1/2}$, L_2 for $2p_{1/2}$, L_3 for $2p_{3/2}$). The primary beam must have sufficient energy to ionize a core level (e.g. K orbital) with binding energy E_K . The system can respond by a two-electron process: the partly empty core electron shell is filled by an electron from a higher level (e.g. E_{L_1}) and another electron (e.g. $E_{L_{2,3}}$) is released from the atom. To a first approximation, the kinetic energy of the released electron (called the Auger electron) relates

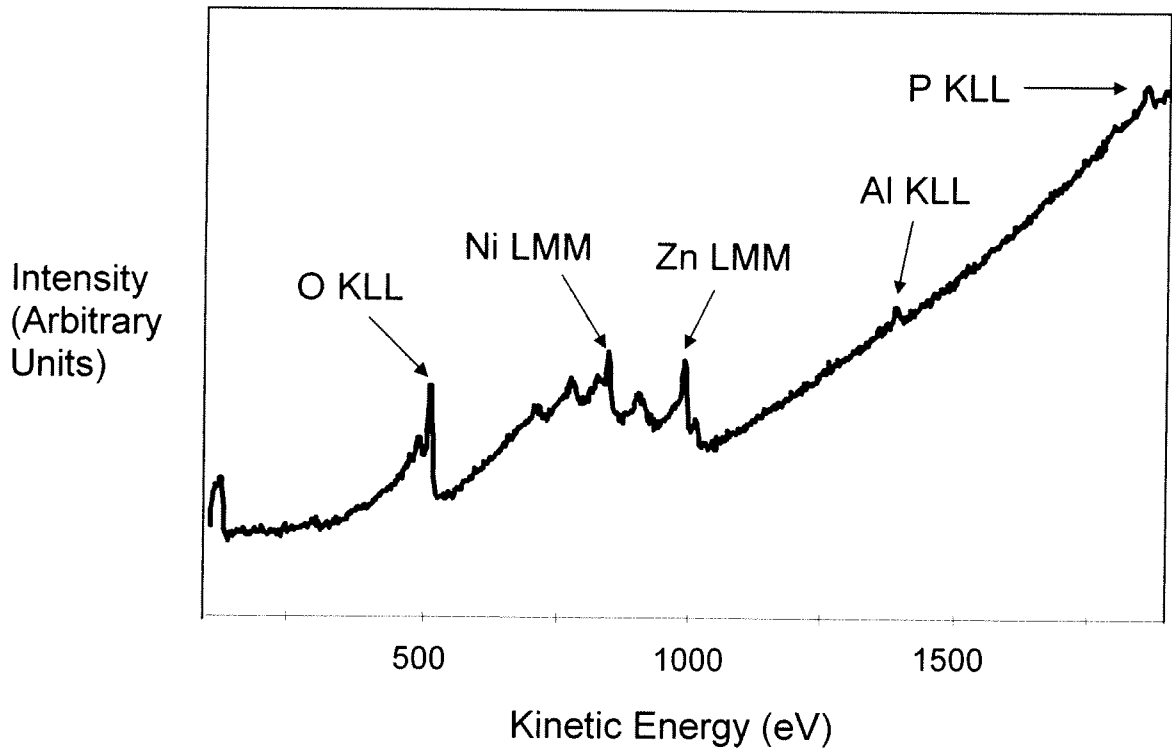


Figure 2.9 Auger spectrum from zinc phosphated Al alloy.

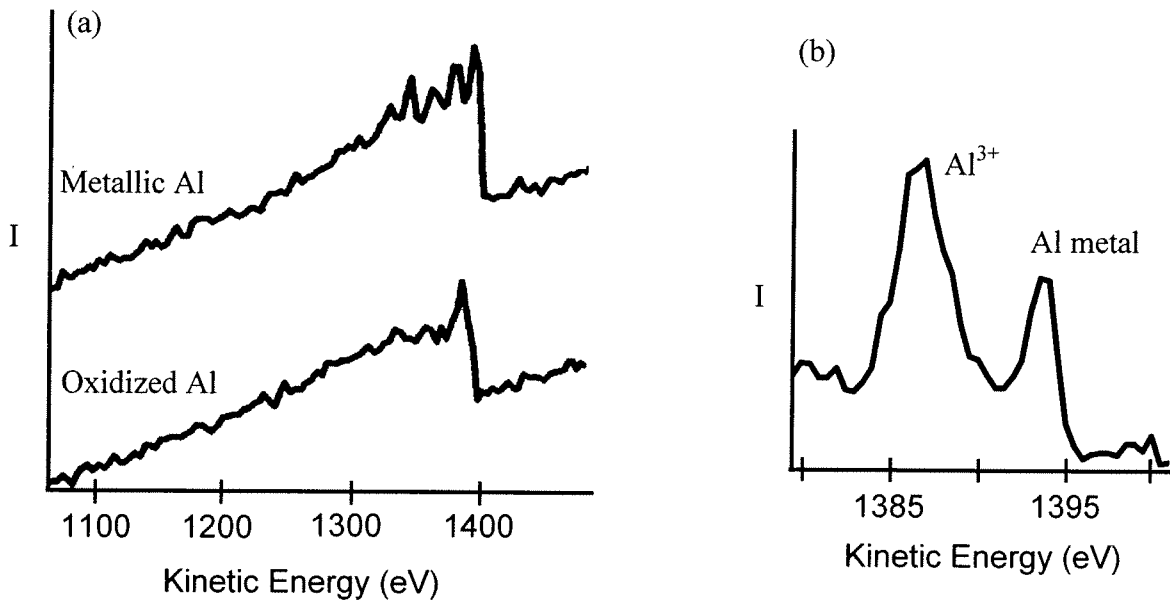


Figure 2.10 Auger spectra measured from 2024-Al alloy: (a) Al KLL region for the metallic and oxidized forms and (b) high resolution spectrum for part of the Al KLL region (both metallic and oxidized Al are present).

to the binding energies of the three electronic levels by:

$$E_{KL1L2,3} = E_K - E_{L1} - E_{L2,3}. \quad (2.15)$$

Strictly this expression needs a correction for the variation of charged species during the Auger process. Auger emission and X-ray emission (Figure 2.1(c)) are competing processes, but Auger emission dominates if the binding energy of the initial core vacancy is less than about 2 keV.

All elements except H and He produce Auger signals at characteristic kinetic energies, which have been tabulated in standard references [46,54]. A sample spectrum is shown in Figure 2.9 from the present work. Auger electrons occur within the same broad range of kinetic energies as photoelectrons in XPS; therefore, their inelastic mean free paths are comparable and so SAM also gives information from about the top 10 nm of the material. Figure 2.10 illustrates an example where chemical state influences the Auger spectrum, especially by strong plasmon loss features in the metallic spectrum that are not present in the oxide spectrum (Figure 2.10(a)). For the Al oxide the most intense peak occurs 6 eV lower than for Al metal (Figure 2.10(b)). Quantitative analysis involves peak integration followed by correction with sensitivity factors, similar to the procedure for XPS (Section 2.1.3). Uncertainties from SAM may be greater than those from XPS due in part to broader peaks, but the approach to measurements with SAM in this work is discussed in Section 3.3.5.

2.2.2 Instrumentation

Figure 2.11 shows the Thermo Electron Microlab 350 system used in this work to measure Auger spectra and some of the SEM images. More detailed information about this system can be found in the Microlab 350 Operating Manual [55]. The Microlab 350 system has a transfer chamber for sample introduction, a preparation chamber for sample

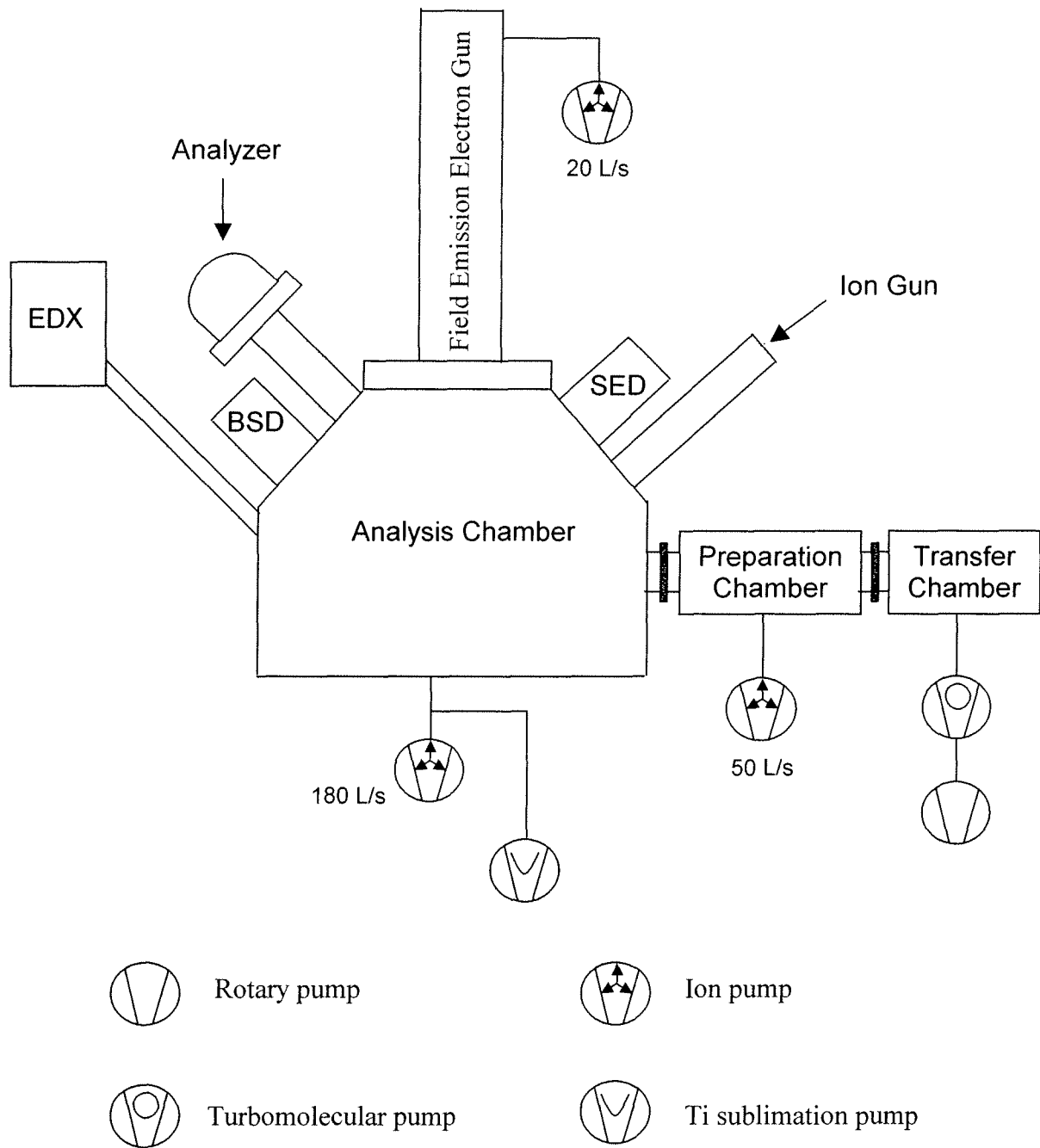


Figure 2.11 Schematic indication of main components for Microlab 350 including the pumping system. SED and BSD indicate the secondary electron and backscattered electron detectors respectively.

treatment, and an analysis chamber for the analytical measurements. Samples are transferred between the chambers using wobble sticks and a rack-pinion transfer rod. The analysis chamber operates under UHV conditions with a base pressure of 10^{-9} Torr, and the arrangement of pumps for the system is indicated in Figure 2.11.

The Microlab 350 is equipped with a Schottky field emission electron source. The field emission tip is made of a single crystal tungsten wire (radius $< 1 \mu\text{m}$) which is coated with zirconium and welded on to the tungsten filament used to heat the tip resistively (~ 1800 K). Application of an electric field (10^7 Vcm^{-1}) to the tip allows electrons to penetrate the potential barrier by tunnelling [56]. The source is fragile and is differentially pumped by an ion pump for stable operation; however, it provides high brightness ($5 \times 10^8 \text{ A/cm}^2\text{steradian}$) and long operating lifetime (~ 5000 h). After extraction from the field emission tip the electrons are focused to $\leq 10 \text{ nm}$ with the system of electromagnetic lenses and apertures shown schematically in Figure 2.12.

The hemispherical energy analyzer on the Microlab 350 is similar to that described in Section 2.1.2. For Auger analysis it is operated in the constant retarding ratio (CRR) mode where the pass energy is varied while the ratio of kinetic energy to pass energy remains constant [46]. This is in contrast to the constant pass energy mode used for XPS. The advantage of the CRR mode is that it provides good resolution at low kinetic energy, where many Auger peaks of interest occur. The reduction in resolution as energy increases is not a serious issue because Auger peaks tend to be broader than photoelectron peaks. Also, for Auger peaks at high kinetic energy it is often necessary to reduce the energy resolution in order to maintain an adequate signal-to-noise ratio. The electron detection system in the Microlab 350 consists of six parallel-connected channeltrons; the analyzer can be set to detect either a specific element or programmed for sequential detection of several signals.

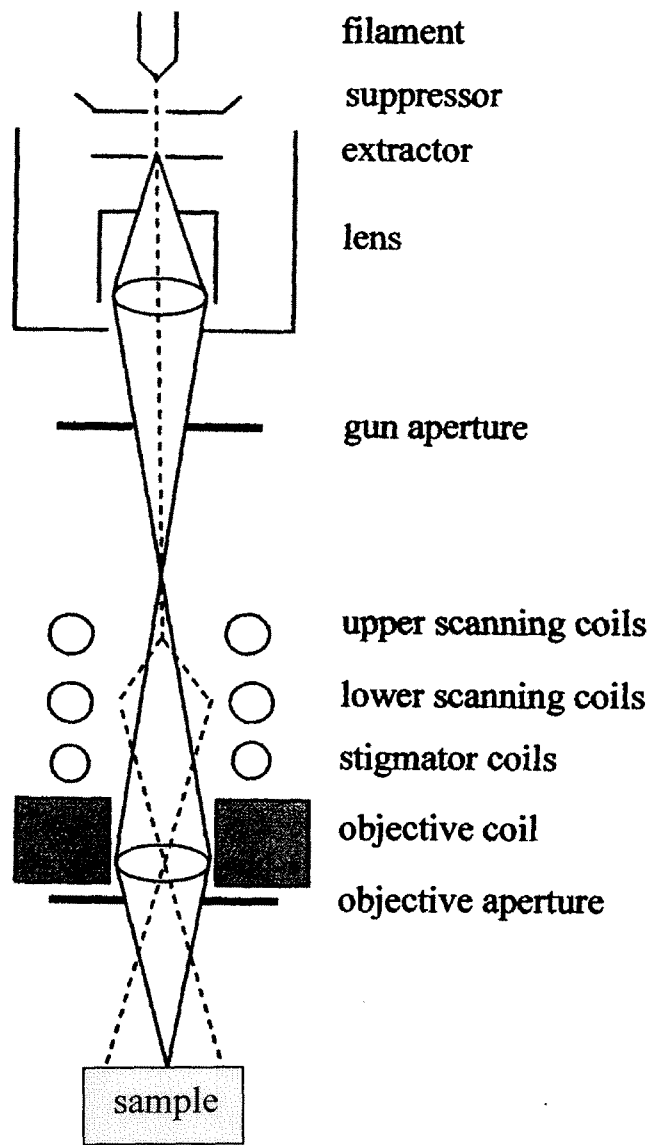


Figure 2.12. Schematic of electron gun for Microlab 350.

There are also detectors for measuring secondary and backscattered electrons, and X-rays (for energy dispersive X-ray analysis). The Avantage software is used for SAM data analysis.

The process of Auger analysis consists of first using the focused electron gun to generate a SEM image for the area of interest. In this process the incident electron beam is rastered across the sample surface and the emitted secondary electrons (up to 50 eV) are collected by the photomultiplier detector to form an image. SEM images (examples are shown in Figure 1.6) give topographical information for the surface and have a three-dimensional appearance that arises from the differences in contrast between various structural features on the sample surface. In the absence of surface charging, small protuberances above the surface often appear brighter than flat regions; also higher atomic numbered elements have a greater yield of secondary electrons than those of low atomic number [57].

Once the SEM image is obtained, the incident electron beam is focused on the particular micro-region of interest and Auger measurements are obtained using the hemispherical analyzer. The electron beam can be focused to one spot for point analysis, moved along a line to create a line profile, or rastered across the surface to create two-dimensional Auger maps for the various elements detected. In general care is needed that measurements are not affected by electron beam damage (as shown for example by a spectrum changing with time).

2.2.3 Other Instruments for SEM

In this work, some SEM images were obtained when the Microlab 350 was unavailable, and these micrographs were generated by the Hitachi S3000N (in the

Department of Materials Engineering). Other micrographs were measured using the Hitachi S4700 (in the Biosciences Department) because this instrument provides images with higher spatial resolution. The Hitachi S3000N instrument is equipped with a tungsten hairpin filament source that produces electrons by thermionic emission with the filament operated at around 2700 K. This type of source can be operated at higher pressure (10^{-3} Torr) compared to the field emission source, but lower brightness (10^5 A/cm²steradian), shorter lifetime (~ 200 h), and higher energy spread are disadvantages [56,60]. In addition, the Hitachi 3000N is equipped with an X-ray detector used for EDX analysis. The Hitachi S4700 has a field emission source operated at 30 kV which facilitates acquisition of higher resolution SEM images, while the Microlab 350 field emission source is operated at lower voltages (e.g. 10 kV) which is more optimal for Auger measurements.

2.3 Energy Dispersive X-ray Spectroscopy

2.3.1 Theory of Technique

In energy dispersive X-ray spectroscopy (EDX), electron beam irradiation of a sample causes emission of X-rays (process in Figure 2.1(c)), which are measured. EDX provides information on elemental composition from depths of several μm (due to the long mean free paths of the photons) [58,60], and therefore contrasts with XPS and SAM. The incident electron beam can be focused sufficiently to analyze regions of μm lateral dimension. For work described in this thesis, EDX was used to assess the chemical composition at different micro-areas of ZPO-coated and corroded samples.

The emitted photon energies are characteristic of the chemical elements present. An example of an EDX spectrum is shown in Figure 2.13 where signal intensity is plotted

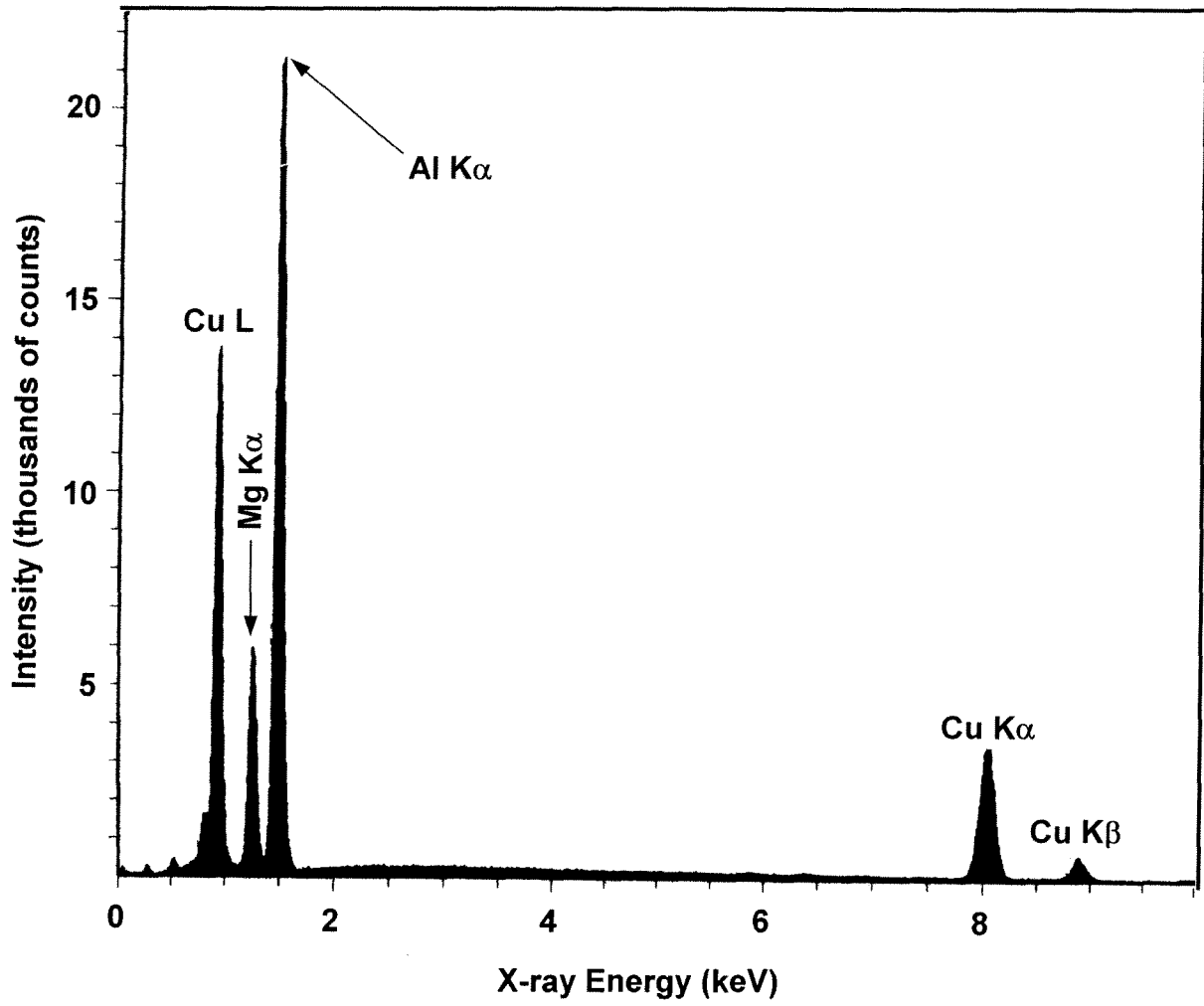


Figure 2.13 EDX spectrum measured from the Al-Cu-Mg region in 2024-Al alloy.

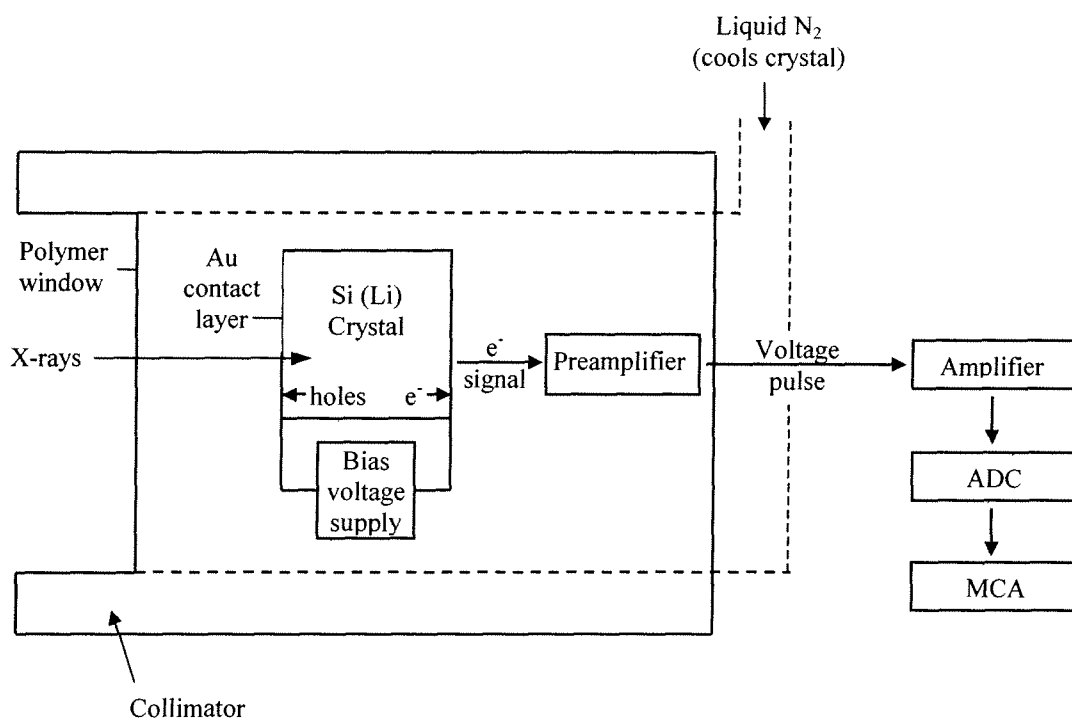


Figure 2.14 Schematic for X-ray detector.

against energy (keV). The Al $K\alpha$, Mg $K\alpha$, and Cu $K\alpha$ peaks are labelled (the notation “ $K\alpha$ ” indicates that in the process of X-ray emission a core vacancy was created in the K shell and filled with an electron from the L shell). Quantitative analysis involves measuring peak areas after application of a background correction. The basic expression for the amount of element Z present in a sample (C_Z) is

$$C_Z = k_Z I_Z / I_{(Z)}; \quad (2.16)$$

where $I_{(Z)}$ is the corrected peak area from a standard composed only of element Z, I_Z is the peak area measured from the specimen being analyzed, and the correction factor k_Z involves three separate corrections for atomic number, self-absorption, and fluorescence (the ZAF correction factor [57]). Quantitative measurements are believed to be accurate to within $\pm 5\%$ [60].

2.3.2 EDX Instrumentation

Some information on the electron source for the Hitachi S3000N instrument was outlined in Section 2.2.3. A schematic diagram of the X-ray detector is indicated in Figure 2.14. The Hitachi S3000N instrument is equipped with a polymer window for transmitting low energy X-rays from light elements (atomic number less than 10), unlike the Be window commonly used in other instruments. After passing through the window, X-rays strike a lithium-doped silicon wafer which is biased (1000 V) to maintain an electron-hole depletion region. The number of electron-hole pairs generated by a given photon is proportional to the X-ray energy and results in a voltage pulse which is measured. The magnitude of the voltage pulse identifies the X-ray energy and the number of voltage pulses measured indicates the signal intensity. The signal is amplified, converted to digital form by the analog-to-digital

converter, and then sorted by the multichannel analyzer [57]. The Quartz XOne software is used for EDX data analysis.

2.4 Electrochemical Polarization

2.4.1 Theory of Technique

Metallic corrosion in aqueous solution is an electrochemical process involving electron transfer at the metal/solution interface. In the general reaction



the two species O and R are in solution and are interconverted by a single electron transfer at the metal electrode, which can provide or take electrons depending on the applied potential. The cathodic current density (i_c) for the forward reaction, and the anodic current density (i_a) for the reverse reaction are given by:

$$i_c = Fk_{red}[O]_o \quad (2.18)$$

$$i_a = Fk_{ox}[R]_o \quad (2.19)$$

where F is the Faraday constant, k_{red} and k_{ox} are the rate constants for the forward (reductive) and reverse (oxidative) reactions, and $[R]_o$ and $[O]_o$ are the concentrations of R and O at the electrode surface [61]. The net current density (i) is

$$i = (i_c - i_a) = F(k_{red}[O]_o - k_{ox}[R]_o). \quad (2.20)$$

The net current is zero for equilibrium, when the anodic and cathodic currents are exactly balanced. The electron transfer reaction (involving electron tunneling from an electrode state to the reactant) can be described using transition state theory, which assumes that reactions proceed through an activated complex elevated in energy above both products and reactants [61,62]. The energy of the activated complex (and hence the energy barriers to be overcome for the forward and backward reactions to proceed) depends on the applied

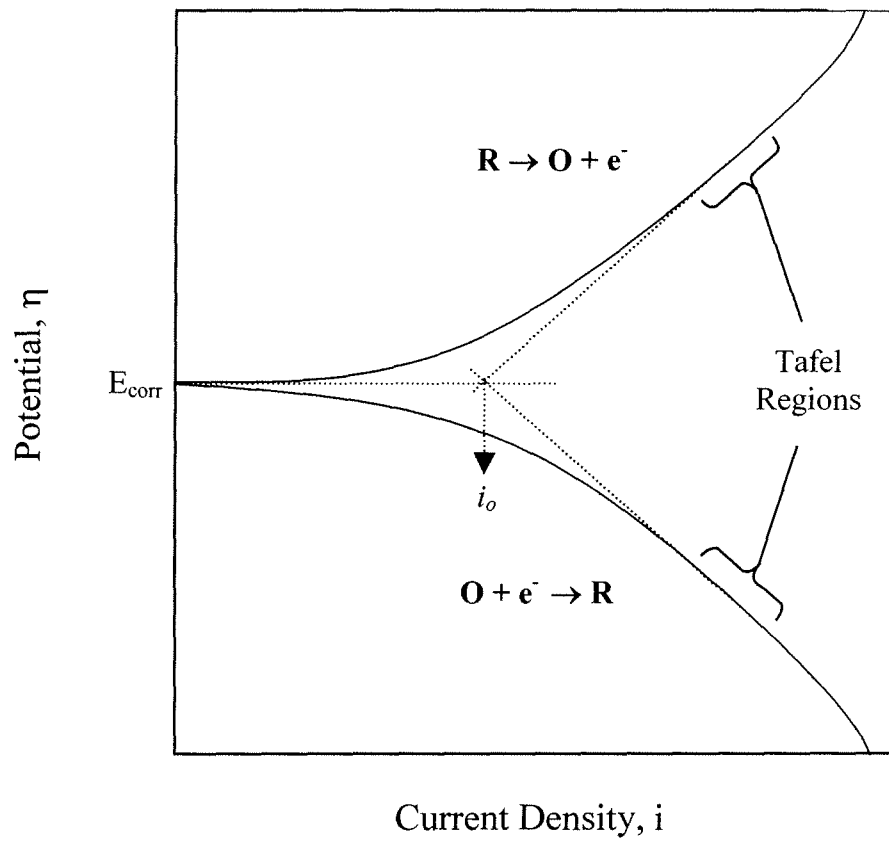


Figure 2.15 Schematic of polarization curve for $O_{(\text{aq})} + e^-_{(\text{m})} \leftrightarrow R_{(\text{aq})}$.

electrode potential. An extension of Equation 2.20 is the Butler-Volmer equation:

$$i = i_0 \left\{ \left(\frac{[R]_o}{[R]_{\text{bulk}}} \right) \exp((1-\alpha)F\eta/RT) - \left(\frac{[O]_o}{[O]_{\text{bulk}}} \right) \exp(-\alpha F\eta/RT) \right\}, \quad (2.21)$$

where i_0 is the exchange current density (equal to the equilibrium anodic or cathodic current density), α is the transfer coefficient (reflects the sensitivity of the transition state to the applied potential), and η is the overpotential (difference between the electrode potential and the equilibrium potential). If the solution is well stirred, the surface and bulk concentrations of the reactants will be equal (i.e. $[R]_o = [R]_{\text{bulk}}$ and $[O]_o = [O]_{\text{bulk}}$), and Equation 2.21 simplifies to:

$$i = i_0 \{ \exp((1-\alpha)F\eta/RT) - \exp(-\alpha F\eta/RT) \}. \quad (2.22)$$

For applied potentials sufficiently large and positive to drive only the oxidative process, the corresponding reductive component is negligible and Equation 2.22 becomes:

$$\ln i = \ln i_0 + (1-\alpha)F\eta/RT. \quad (2.23)$$

Equally for applied negative potentials, where the reductive process is dominant, Equation 2.22 becomes:

$$\ln (-i) = \ln i_0 - \alpha F\eta/RT. \quad (2.24)$$

Tafel analysis involves plotting applied potential E (or η) against $\ln(i)$ as illustrated in Figure 2.15. Equations 2.23 and 2.24 correspond to the linear regions of the curves in the figure.

The exchange current density i_0 can be estimated from the intersection of the two extrapolated Tafel lines (Figure 2.15) [61,63].

Electrochemical polarization measurements provide a direct way for comparing trends in corrosion behaviour. In Chapter 3, polarization curves are used to follow trends in measured i_0 and E_{corr} for different coating treatments applied to 2024-Al alloy surfaces. This is based on the principle that current density (i_0) is an indicator of corrosion rate insofar as a

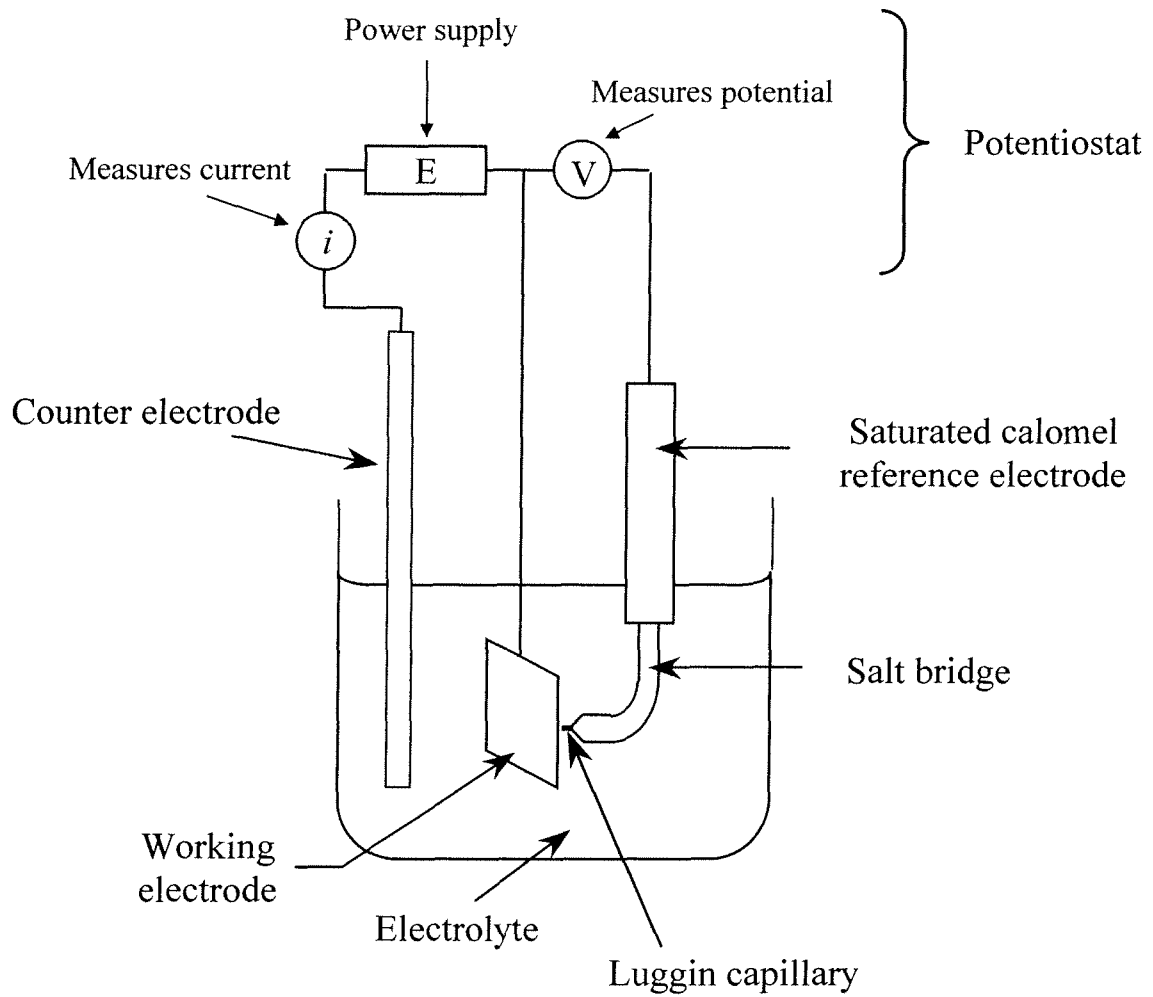


Figure 2.16 Schematic of the three-electrode cell used for polarization measurements.

lower value of i_0 indicates a higher level of protection provided by the coating. These comparisons are made without regard to the specific chemical processes involved [63].

2.4.2 Instrumentation

A schematic for the three-electrode cell used for polarization measurements is shown in Figure 2.16. The electrolyte is 3.5% NaCl solution that is purged with N_2 to remove oxygen and stirred to ensure fast transport of reacting species. The potential is measured between the working electrode, which is the coated metal sample being characterized, and the reference saturated calomel electrode (SCE), while the current flowing between the working electrode and the counter Pt electrode is measured. The reference electrode is connected to the solution close to the working electrode by a Haber-Luggin capillary in order to reduce any potential drop resulting from solution resistance [63]. The potentiostat linearly varies the potential between the working electrode and the reference electrode, and the associated current is recorded. The polarization measurements are made using a Solartron 1286 Electrochemical Interface (Schlumberger Technologies), with Solartron Corrware and Corrview software for data acquisition and plotting. In this work, the corrosion current density i_0 is estimated from the intercept of the extrapolated Tafel cathodic line with the E_{corr} , which is the potential of the system measured before an external voltage is applied. This method is preferred due to difficulties in extrapolating the Tafel line from the anodic region.

Chapter 3

The Effect of Ni^{2+} on Zinc Phosphating of 2024-T3 Al Alloy

3.1 Introduction

Chemical conversion coatings formed on aluminum and its alloys are frequently used to enhance paint adhesion and improve corrosion resistance as discussed in Chapter 1. Zinc phosphating is one type of conversion coating. Extensive work has been applied to zinc phosphate (ZPO) treatments for steel, and this has included the effect of additives, such as Ni^{2+} , Mn^{2+} , NO_3^- and fluoride, on the properties of the resulting coatings [64-73]. For applications to steel, Ni^{2+} is commonly added to ZPO baths in order to produce coatings with more homogeneous structures (finer grain size), and that in turn leads to better paint adhesion [72], lower porosity and improved corrosion protection [64]. The coating process is electrochemical in nature (described in Chapter 1) and results in the precipitation of chemical components other than zinc phosphate. In this thesis ZPO is used generally to refer to the coating.

Preliminary studies in this laboratory indicated that Ni^{2+} is the additive primarily responsible for yielding smaller ZPO grain size on Al alloys. That observation helped define the starting point for the current study, whose main objective is to determine the effect of Ni^{2+} in a ZPO coating bath on the microscopic and macroscopic properties of coatings on 2024-Al alloy. Additionally, parallel studies are made on high-purity Al in order to provide a reference point to help assess how the coating process is affected by the differing chemical composition and microstructure present at the alloy surface. The coatings formed on these

surfaces are examined by a range of characterization techniques including: scanning electron microscopy (SEM), to assess surface topography; X-ray photoelectron spectroscopy (XPS), scanning Auger microscopy (SAM) and energy-dispersive X-ray (EDX) spectroscopy, for chemical analysis; and electrochemical polarization measurements for comparing the corrosion resistance exhibited by differently coated samples.

3.2 Experimental

Square samples ($1 \times 1 \text{ cm}^2$) of commercial 2024-Al alloy and unalloyed Al (99.9% purity) were mechanically polished with SiC sandpaper (up to 1200 grit), but other 2024-Al samples were additionally polished by diamond paste to give a mirror finish ($\sim 1 \text{ }\mu\text{m}$ roughness). After polishing, all samples were ultrasonically cleaned in acetone and methanol. One L of the water-based ZPO solutions (designed specifically for coating of Al) contained: 10.8 mL of 85% H_3PO_4 ; 1.24 g ZnO; 1.11 g NaF; plus varying amounts of Ni^{2+} (as $\text{Ni}(\text{NO}_3)_2$) in the 0 to 2500 ppm range (where ppm = mg/L). Coatings were formed by immersing the Al or alloy samples in such solutions (adjusted to pH 4 using NaOH) at 60°C for 2 min; these conditions are similar to those recommended for use with the Gardobond R2600 commercial phosphating solution (2-4 min at $45\text{-}55^\circ\text{C}$). Each coating treatment was followed by washing the sample in deionized water and drying in air. Additionally, some comparative studies were done on mirror-polished 2024-Al samples after immersing (at 60°C for 2 or 3 min) in solutions containing 1.11 g NaF per L and Ni^{2+} (as $\text{Ni}(\text{NO}_3)_2$) at either 1000 or 2000 ppm, with the pH adjusted to 4 using HCl. After this treatment, these samples were subsequently washed in deionized water and dried in air.

XPS spectra were measured with a Leybold MAX200 spectrometer using the $\text{MgK}\alpha$ source (1253.6 eV) operated at 15 kV, 20 mA. SAM point analysis was carried out using the

primary electron beam set at 10 keV and 3 nA. For the SEM and EDX characterizations, the incident beam was accelerated through 20 kV. The electrochemical polarization measurements were conducted using a potential range of -1.50 to -0.25 V (saturated calomel electrode reference) with a scan rate of 1 mV s^{-1} .

3.3 Results and Discussion

3.3.1 Coating Topography on 2024-Al

Figure 3.1 shows SEM micrographs of the coatings formed on 2024-Al from solutions containing different amounts of Ni^{2+} (0-2500 ppm), and these images especially accentuate the larger coating crystals. As the amount of Ni^{2+} is increased from 0 to 500 ppm, there is a decrease in grain size and the degree of crystalline coverage also appears to decrease. The SEM micrographs show that, as the Ni^{2+} content increases from 500 to 2000 ppm, the grain size remains approximately constant, while the degree of crystalline coverage increases. It seems that the presence of Ni^{2+} causes an increase in the number of nucleation sites. The exact mechanism by which Ni^{2+} causes an increase in the number of nucleation sites is not known and is the subject of continuing investigations.

3.3.2 Electrochemical Characterization

Figure 3.2 shows measurements of electrochemical polarization for ZPO-coated 2024-Al samples in deaerated 0.6 M NaCl solution. The current density, i_o (which increases with corrosion rate and is also known as i_{corr}), was estimated by extrapolating the cathodic branch according to a Tafel analysis. Figure 3.3 presents a plot of i_o vs. Ni^{2+} concentration in the ZPO coating solution for 2024-Al. The presence of Ni^{2+} in the coating solution clearly causes the

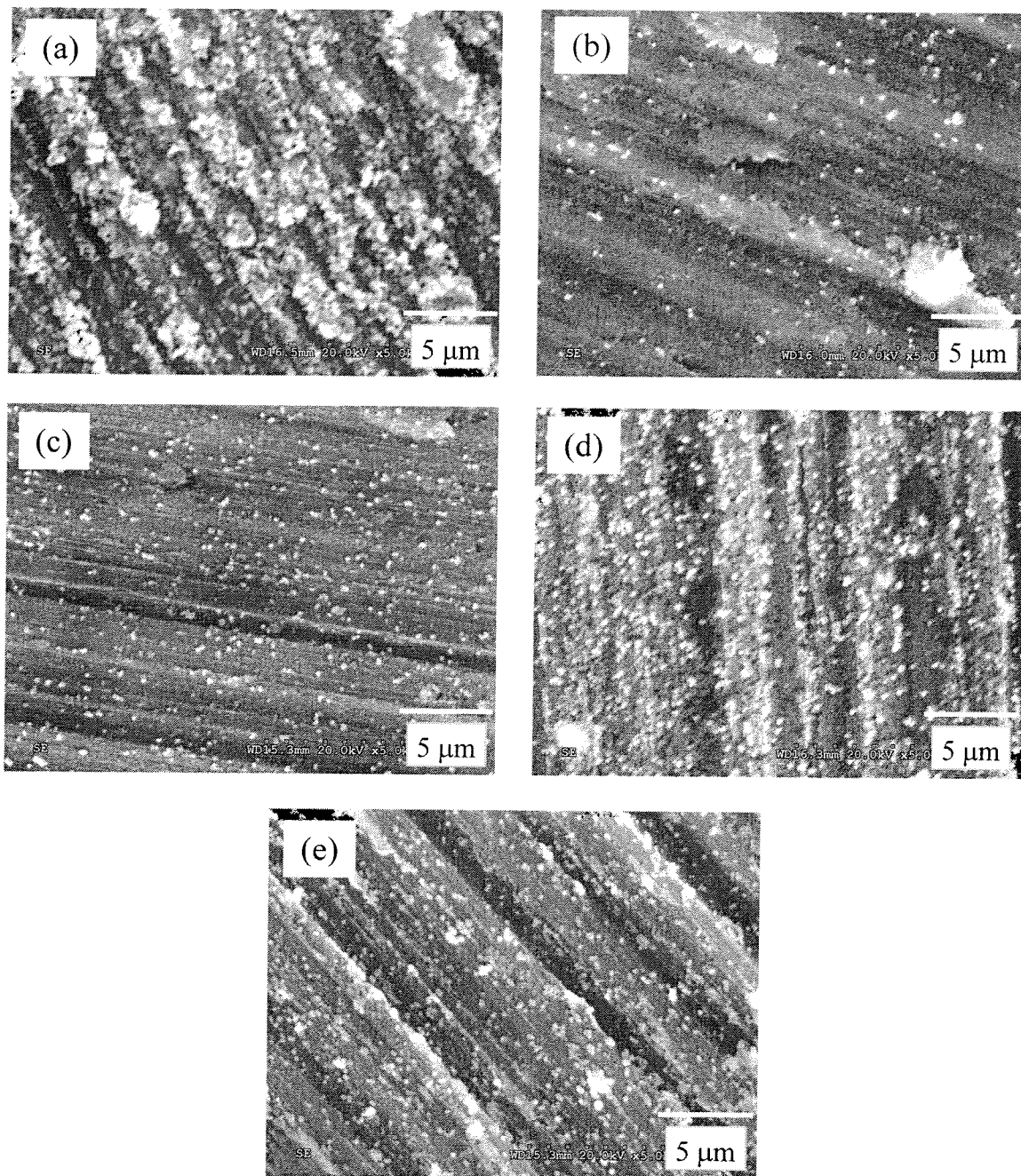


Figure 3.1 SEM micrographs from zinc phosphate (ZPO) coated 2024-Al surfaces. The coating solutions contain increasing amounts of Ni^{2+} : (a) 0, (b) 500, (c) 1000, (d) 2000 and (e) 2500 ppm.

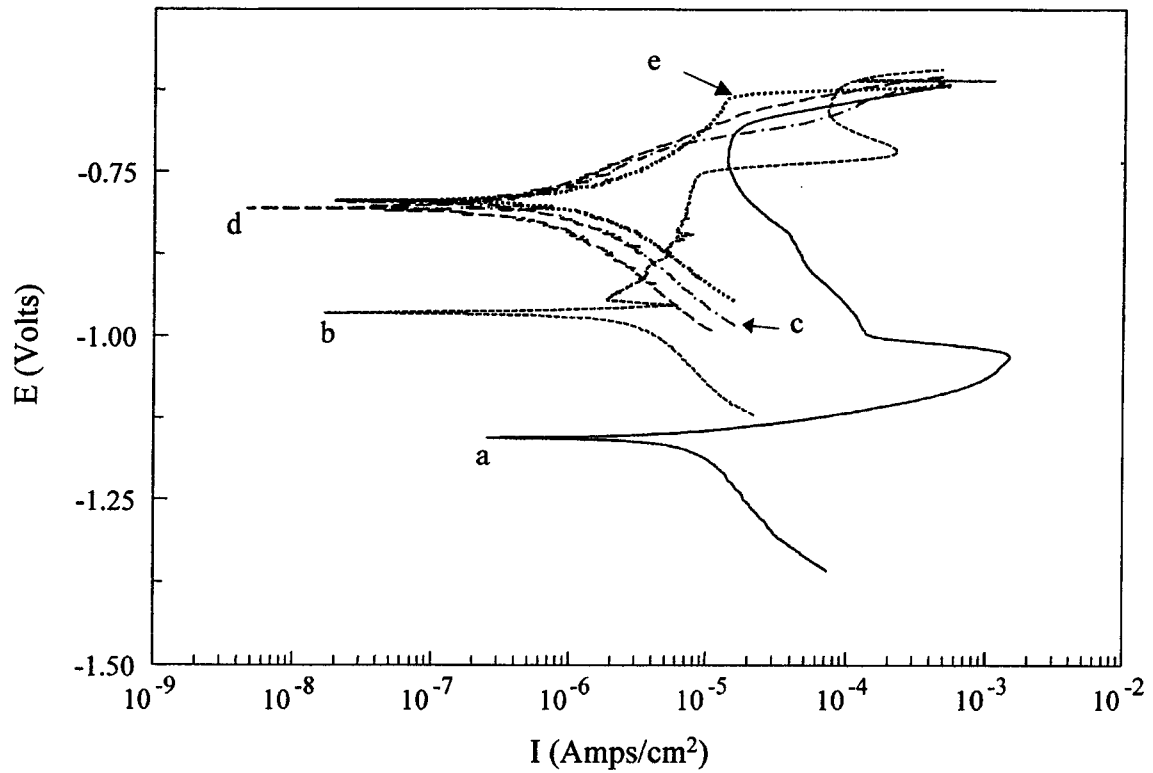


Figure 3.2 Polarization curves measured for samples of 2024-Al coated with ZPO solutions containing different amounts of Ni^{2+} : (a) 0, (b) 500, (c) 1000, (d) 2000 and (e) 2500 ppm.

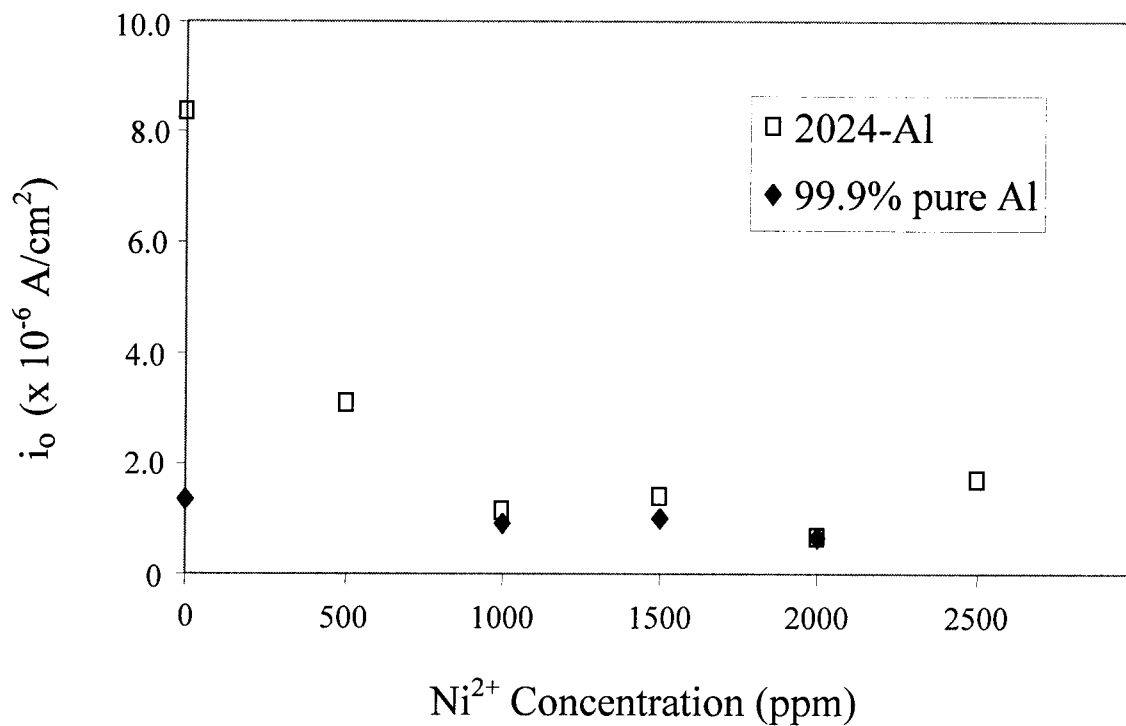


Figure 3.3 Corrosion currents determined from polarization curves for samples of 2024-Al and high-purity Al which have been coated with ZPO solutions containing different concentrations of Ni²⁺. The uncertainties in the i_o values are estimated at $\pm 0.5 \times 10^{-6}$ Acm⁻².

corrosion rate to reduce substantially; thus i_o drops by an order of magnitude as the Ni^{2+} concentration changes from 0 to 2000 ppm. Correspondingly, the corrosion potential (E_{corr}) from the Tafel analysis increases as the Ni^{2+} concentration changes from 0 to 2000 ppm (Figure 3.2), an observation that is consistent with the coatings showing increasingly effective barrier properties [74]. Throughout this work, the quantitative measurements reported are just used to follow trends in behavior. Consistently with the observations here, studies on steel indicate that Ni^{2+} added to ZPO baths increases the corrosion resistance of the resulting coatings [64,72].

3.3.3 Chemical Analysis - Spectroscopic Measurements

Table 3.1 reports elemental composition information measured by XPS from 2024-Al samples coated in ZPO solutions with different Ni^{2+} concentrations, and Figure 2.2(a) shows the survey spectrum from the sample coated with the solution containing 2000 ppm of Ni^{2+} . The quantitative analysis used the component peaks: Zn $2p_{3/2}$ (binding energy 1022.5 eV), Cu $2p_{3/2}$ (932.8 eV), Ni $2p_{3/2}$ (856.4 eV), O 1s (531.6 eV), C 1s (285.0 eV), P 2s (190.9 eV), F 1s (684.8 eV) and Al 2p (Al^{3+} component 74.9 eV, metallic component 2 eV less). The basic coating elements of Zn, P and O are supplemented by the presence of F and Ni, which come from the additions of NaF and $\text{Ni}(\text{NO}_3)_2$ to the coating solution, while Al and Cu are detected from the underlying substrate. The raw data show the presence of C that arises from atmospheric contamination and sample handling, but this is excluded from the comparisons in Table 3.1. There will also be some contribution from contamination in the signals from O, an element that must be present at appreciable levels in the uncontaminated surfaces. The discussion here just uses trends in elemental ratios that do not involve O, and that encourages

the belief that any contamination from this element should have only a small effect on the data analysis reported.

Table 3.1 Elemental atomic percentages from XPS for 2024-Al samples after coating in ZPO solutions which differ just in the Ni²⁺ concentration which varies from 500 to 2500 ppm.[§]

[Ni ²⁺]	500	1000	2000	2500
Zn	8.6	6.2	7.0	7.3
Cu	0.9	0.6	4.7	2.2
Ni	1.2	1.6	3.4	3.3
O	57.8	61.8	58.4	62.2
P	8.5	9.3	9.9	10.3
Al	16.5	12.6	12.9	11.0
F	6.3	7.9	3.8	3.9

[§] Values are believed to be accurate to within ±10% as discussed on page 29

For the samples coated in ZPO solutions containing 500, 1000 or 2000 ppm Ni²⁺, the Al 2p spectra show small structures near 72.5 eV on the Al³⁺ peaks. This indicates that metallic Al is detected, and therefore that these coatings are thinner than the XPS probing depth (<10 nm). As the Ni²⁺ concentration in the coating solution increases from 500 to 2500 ppm, there is a decrease both in the amount of metallic Al detected and in the total Al detected (Table 3.1). These observations are consistent with an increase in coating thickness, and correspondingly with the increase in crystalline coating coverage observed by SEM. Interestingly, the Ni/Zn ratio measured for the coating steadily increases, as the Ni²⁺ concentration in the solution varies from 0 to 2000 ppm (values for the ratio equal 0.14, 0.26 and 0.49 for Ni²⁺ concentrations of 500, 1000 and 2000 ppm respectively). A study of zinc phosphating on steel also indicates that the percentage of nickel in the ZPO film increases with the Ni²⁺ concentration in the coating solution [64].

The Ni 2p spectrum measured from a 2024-Al sample coated with the ZPO solution containing 2000 ppm nickel indicates that the Ni 2p_{3/2} signal occurs at a binding energy of 856.4 eV. At present it is not possible to be specific about the exact form of the Ni in the coating. For example, species such as Ni(OH)₂ [75,76], Ni₂O₃ [77], and NiAl₂O₄ [78] all have Ni 2p_{3/2} binding energies within 0.3 eV of our observed value. Incidentally, a nickel phosphate-type compound [79] has been reported to have a Ni 2p_{3/2} binding energy some 0.8 eV greater than our measured value, although there remains some uncertainty as to whether the calibration procedure used matches that in the present work. Therefore, XPS may not necessarily exclude the presence of nickel phosphate in our coatings.

Data in Table 3.1 show the presence of Cu at the coated alloy surface (Cu is one of the major alloying elements in 2024-Al, as discussed in Chapter 1); the amount of Cu detected is larger in samples treated in solutions with the higher Ni²⁺ concentrations (i.e. 2000 ppm and 2500 ppm) than in those samples that had been treated in solutions containing less Ni²⁺. This is not likely to be due to a larger amount of substrate being exposed since, for coatings formed from solutions with the higher Ni²⁺ concentrations, the Al signal detected within the XPS probe depth is less than for those coatings formed from solutions with the lower Ni²⁺ concentrations. A plausible interpretation is that Cu dissolves from the substrate during the etching stage of the process and then re-precipitates as the coating dominates. Further, it appears that the effectiveness of the etching increases with increasing amounts of Ni(NO₃)₂ in the coating solution. It is also possible that Cu enrichment occurs at the coating-to-alloy interface, particularly since Cu segregation accompanies various chemical treatments such as acid etching [80]. The increase in surface Cu may be responsible (in part) for the increase in coating coverage, since it provides additional cathodic sites at which the coating nucleation can occur. Also, given its higher standard reduction potential compared to Zn or

Al, it may contribute to increased E_{corr} values measured for coatings formed from solutions with higher Ni^{2+} (Figure 3.2) [74].

3.3.4 Effect of Microstructure – EDX Analysis

A 2024-Al sample that was polished to 1 μm roughness, and coated in a ZPO solution containing 2000 ppm of Ni^{2+} , was assessed by SEM and EDX in order to examine the coating distribution with respect to the alloy microstructure. It is known that 2024-Al contains precipitated intermetallic compounds, also known as second-phase particles, of the Al-Cu-Mg and Al-Cu-Fe-Mn types (introduced in Chapter 1). Figure 3.4 shows a SEM image of the ZPO coating (2000 ppm Ni^{2+} in the coating solution) across a local region where the small round Al-Cu-Mg particles (P1, P2, P3) and the larger irregular Al-Cu-Fe-Mn particles (e.g. P4) are present. Crystalline ZPO particles appear to be uniformly distributed across the alloy matrix; however there is a higher concentration of crystals on the Al-Cu-Mg particles, and the Al-Cu-Fe-Mn particles seem not to be coated. Table 3.2 indicates that EDX spectra taken from local regions support the SEM observations. The greater percentages of Zn and P at P1, compared to the matrix and P4, indicate that there is more coating on the Al-Cu-Mg particle than on the matrix or the Al-Cu-Fe-Mn particle. The detection of Zn and P signals in the spectrum taken from the Al-Cu-Fe-Mn particle shows that a ZPO coating is present. In combination with the observation from SEM, this suggests that the local coating has an amorphous, rather than crystalline, form. A further point of interest is that EDX detects Ni from the Al-Cu-Mg particles, but not from the alloy matrix or from the Al-Cu-Fe-Mn particles.

A parallel study involved 2024-Al alloy (1 μm roughness) which was treated in a solution containing 1.11 g/L of NaF and 2000 ppm $\text{Ni}(\text{NO}_3)_2$ (pH \sim 4, adjusted by HCl).

Table 3.2 Elemental weight percentages from EDX for different regions of the 2024-Al microstructure shown in Figure 3.4[§]

Region	matrix	P1 particle*	P4 particle*
Zn	1.5	8.4	1.0
Ni	- [◊]	0.6	-
Al	87.8	55.1	53.3
Cu	4.6	22.5	19.3
Mg	2.0	6.8	-
Fe	-	-	10.1
Mn	0.6	-	11.6
P	†	0.8	†
O	3.4	5.9	4.0

[§] Values are believed to be accurate to within $\pm 5\%$ as discussed on page 39

* P1 = Al-Cu-Mg particle; P4 = Al-Cu-Fe-Mn particle

[◊] The hyphen indicates that the element is not detected

† Amount detected is less than 0.5% and too small to be measured accurately

XPS analysis from the resulting surface (after 3 min in coating solution) indicates the presence of Ni, O, F and Al. The coating is now too thick to allow the detection of significant Cu. Further, the high-resolution spectra show a Ni 2p_{3/2} peak at 855.8 eV binding energy, and an Al 2p peak at 73.4 eV. The latter is probably Al³⁺; comparisons with other observations for the Ni 2p_{3/2} binding energy indicate that the Ni may be incorporated in the form of Ni(OH)₂ [78] and/or Ni₂O₃ [81,82] consistently with another report [83]. EDX data from a similar sample (differing in that the coating time was 2 min) have shown that a higher amount of Ni is detected on the second-phase particles (i.e. Ni in range 2 – 5 wt%) compared with that observed on the matrix (Ni ~0.7 wt%). This indicates that the oxide layer on top of the second-phase particles contains more Ni than the oxide layer on top of the alloy matrix. This is in agreement with Arnott's findings (in the context of AA 7075-T6 exposed to 0.1 M NaCl containing 1000 ppm NiCl₂) which show that film formation is affected by differences in the potential at different regions on the alloy surface [84].

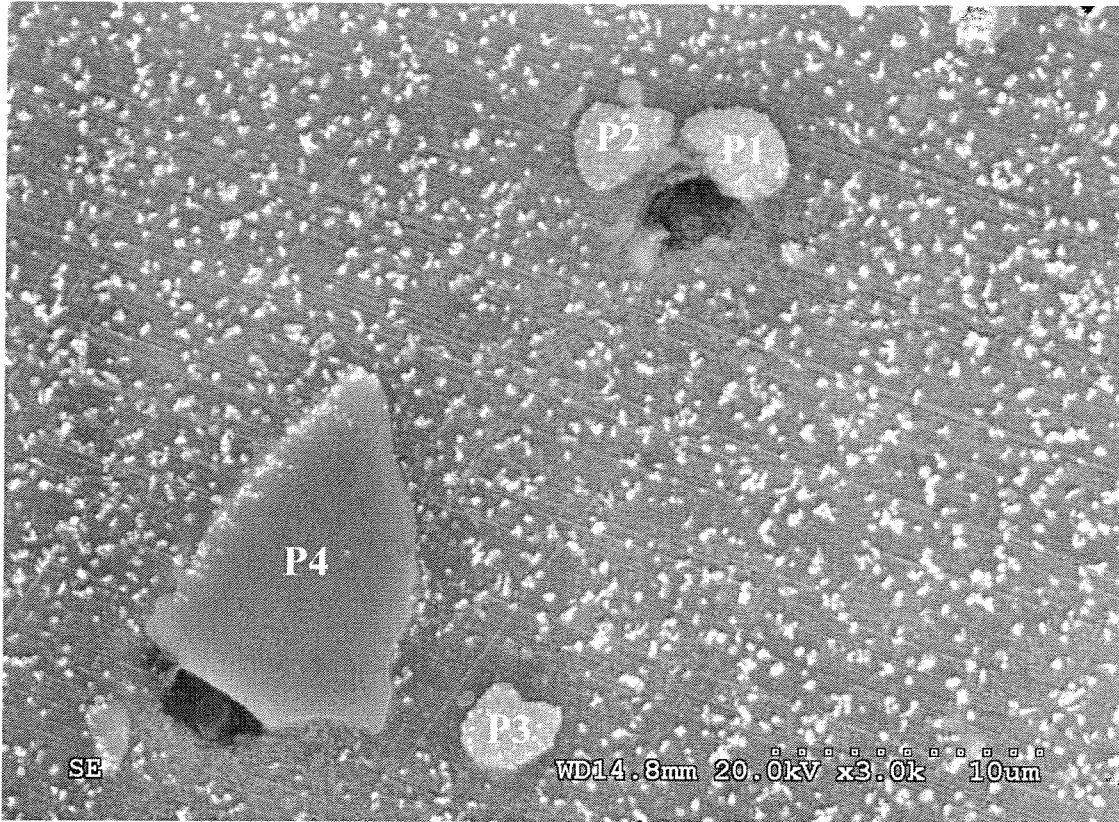


Figure 3.4 SEM micrograph from the 2024-Al surface after treating in a ZPO coating solution that contained 2000 ppm Ni^{2+} ; P1, P2, and P3 identify Al-Cu-Mg particles, while P4 is an Al-Cu-Fe-Mn particle.

As far as the Ni-containing ZPO coating is concerned, the SEM and EDX observations indicate that a higher amount of crystalline coating, as well as a higher Ni content, are associated with the Al-Cu-Mg particle. The presence of nickel may result in part from Ni incorporation into the zinc phosphate [68].

3.3.5 Approach to Measurements on Microstructure

Studies of chemical composition at local microstructural regions of a 2024-Al alloy surface before and after coating are needed to gain a better understanding of the local processes occurring on these heterogeneous surfaces. The challenge is to identify representative regions, particularly since the cost of measurements with SAM indicates that only a limited number of replicates can be measured for the different regions of matrix and second phase particles. Care was therefore taken to choose representative regions for analysis. The regions were selected as described in the following. The study started by using SEM to assess coating topography across the surface. Areas of representative topography could be identified, and they were chosen for analysis of the different regions. Trends for measurement from different apparently representative regions were fully consistent and the apparent relative errors were around 5%. Experience showed that it was important to analyze second phase particles and matrix regions close to each other in order to have similar coating conditions. This approach has been developed previously [53].

Similar to the situation for XPS (Section 2.1.3), in the most ideal case quantitative analysis of SAM spectra for homogeneous samples can yield values of elemental composition with uncertainties of less than about 2% [52]. But as discussed on page 27, the situation for work presented in this thesis is more complex, because of the heterogeneous nature of the surfaces and the regions immediately underneath. More generally, uncertainties

from SAM can be greater than those from XPS due to more overlapping of spectral peaks, and for the types of sample considered here, a 15% error appears appropriate. So, with the uncertainty quoted above for dealing with representative regions for SAM analysis, the reported elemental compositions from SAM are believed, on a conservative basis, to be accurate to within $\pm 20\%$. Accordingly variations are only considered significant when outside these bounds.

3.3.6 Effect of Microstructure – SAM Analysis

SAM measurements provide chemical composition information from the top 5-10 nm of the surface (i.e. the probing depth is much less than that for EDX, as discussed in Chapter 2). Also the lateral spatial resolution is better for SAM than for EDX and that made it possible to measure Auger spectra from the individual crystalline and dark areas on the Al-Cu-Mg particle, whereas the EDX measurements tended to encompass both regions. Figure 3.5 shows SEM images from the ZPO-coated 2024-Al sample at and around the second-phase particles. The image in Figure 3.5(b) was taken after the sample was tilted in order to help reveal the relative heights of surface features; this supports the view that the coating crystals provide the highest features on the surface. Table 3.3 summarizes elemental compositions for different local regions identified in Figure 3.5, where the Auger spectra were measured with the sample normal to the electron beam. Region R1 corresponds to a crystalline coating, while regions R2, R3 and R4 correspond to areas that appear darker in the SEM images.

The Auger measurements indicate that all the microstructural regions are phosphated, although to varying degrees. For example, the darker regions have thinner coatings, as indicated by the presence of a larger Al signal. From comparison with SEM observations, it

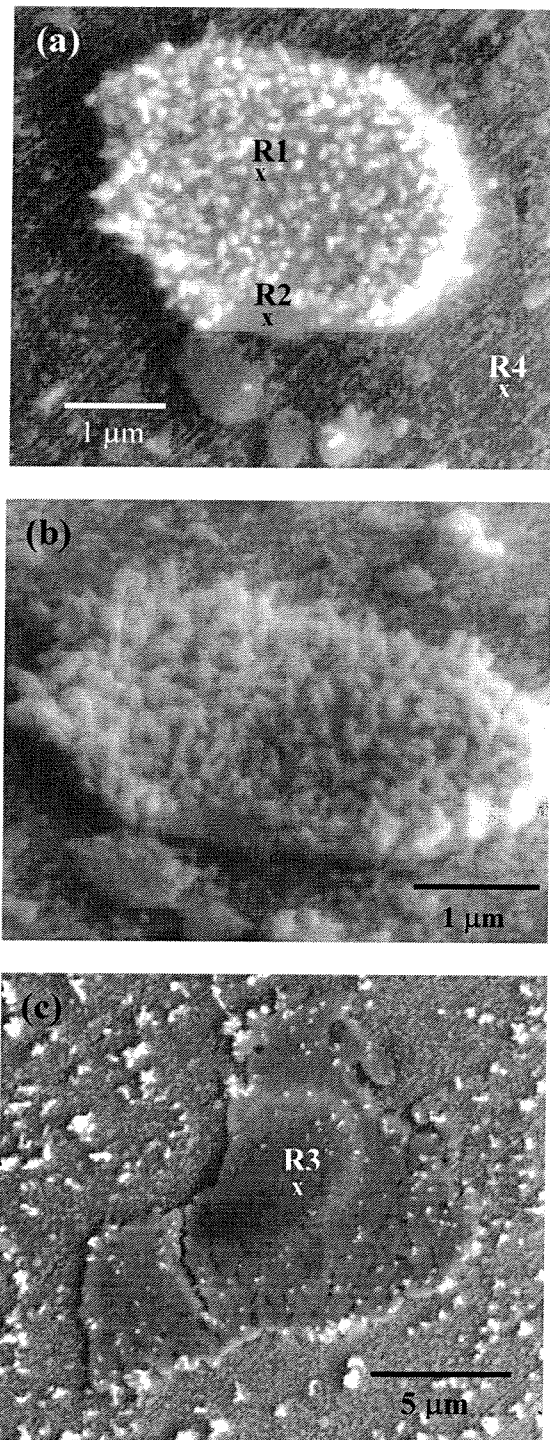


Figure 3.5 SEM micrographs from different microstructural regions of the 2024-Al surface after treating with a ZPO coating solution which contained 2000 ppm Ni^{2+} : (a) Al-Cu-Mg particle (sample normal to electron beam); (b) Al-Cu-Mg particle (sample tilted at 60° to electron beam); (c) Al-Cu-Fe-Mn particle (sample normal to electron beam).

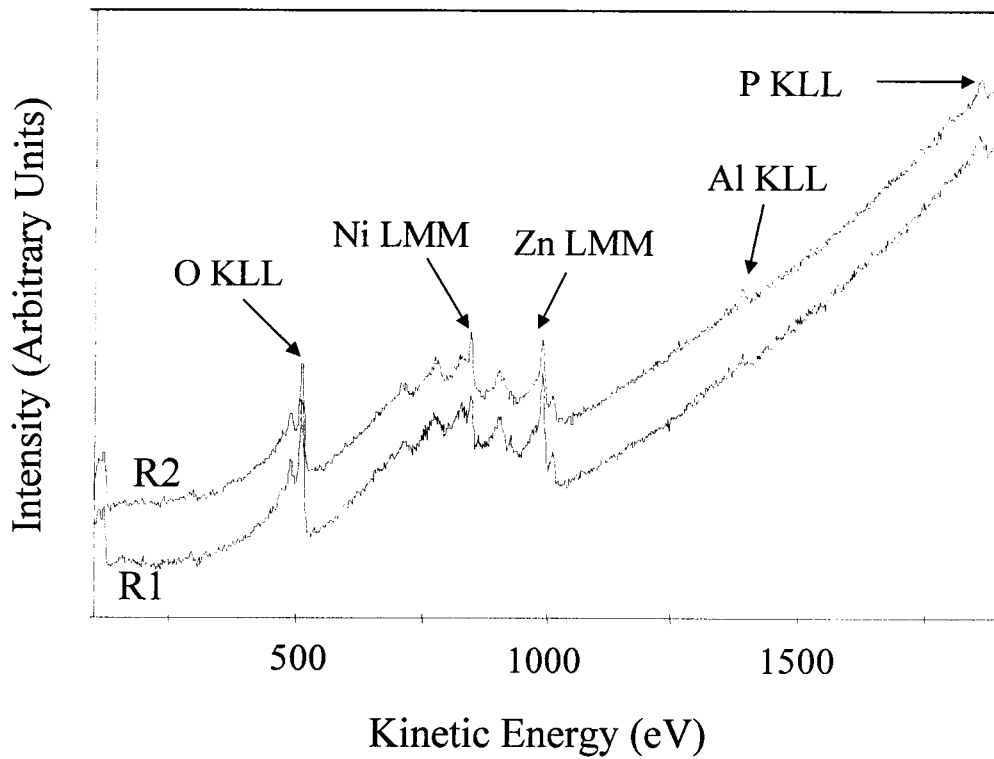


Figure 3.6 Wide-scan Auger spectra measured from different ZPO-coated regions on Al-Cu-Mg particle: crystalline region R1 and amorphous region R2 (as in Figure 3.5(a)).

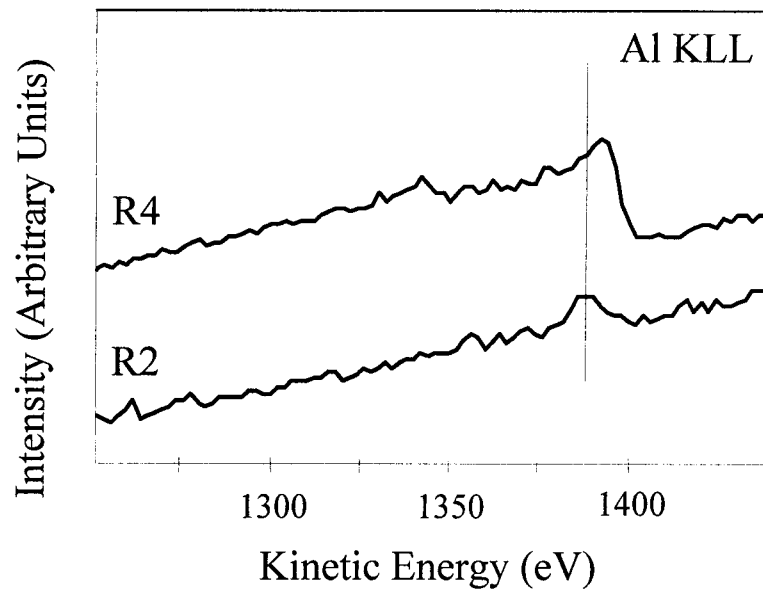


Figure 3.7 Al KLL spectra from amorphous ZPO coatings: R2 region on Al-Cu-Mg particle, R4 on alloy matrix (as in Figure 3.5(a)).

Table 3.3 Elemental atomic percentages from SAM for the different microstructural regions of ZPO-coated 2024–Al samples shown in Figure 3.5.[§]

Region	R1	R2	R3	R4
Zn	17.0	15.1	23.3	10.3
Ni	6.7	10.9	9.6	3.6
Al	†	8.7	12.4	32.9
Cu	†	†	3.9	4.7
O	48.4	42.4	41.7	43.0
P	27.9	22.9	9.2	5.5

[§] Values are believed to be accurate to within $\pm 20\%$ as discussed on page 58

[†] Amount detected is less than 0.5% and too small to be measured accurately

may be concluded that these regions correspond to coatings of amorphous form, although we cannot rule out that these coatings are composed of microcrystallites (dimension $< 0.01 \mu\text{m}$). For simplicity below, we refer to these coatings as having the amorphous form, but the caveat just mentioned should still be recognized.

Figure 3.6 shows spectra measured from two different regions on the coated Al-Cu-Mg particle: crystalline (R1) and amorphous (R2). Labeling of the spectra is limited to the most intense peaks in the KLL and LMM series. (In other measured regions (Table 3.3) some Cu is present (Cu LMM at 918 eV).) Regions R1 and R2 show qualitatively similar elemental compositions. The signal for Zn LMM appears at 990.0 eV and is consistent with expectation for Zn^{2+} [85]. In R1 (where the signals from coating elements are more intense) Ni LMM occurs at 845.8 eV, O KLL at 508.8 eV, and P KLL at 1856.0 eV. In R2 the Al KLL is at 1388.1 eV, which is consistent with Al in the +3 oxidation state [85]. The latter may be due to the presence of some aluminum phosphate or aluminum oxide/hydroxide at the coating-alloy interface, as suggested in a study by Handke *et al.* [86] of the mechanism of ZPO formation on high-purity Al.

The data in Table 3.3 indicate that, at the Al-Cu-Mg particle, the amorphous ZPO coating is thinner than the crystalline coating on the same particle. Variations are also present when the amorphous ZPO coatings are compared at different microstructural regions. For example, their thickness increases in the order: R4 (matrix) < R3 (Al-Cu-Fe-Mn particle) < R2 (Al-Cu-Mg particle). This conclusion is also supported by the difference in Al KLL kinetic energies measured from regions R2 and R4 (Figure 3.7). The signal from R4 is 4.5 eV higher than that from R2, which may indicate that some Al detected from R4 has the metallic form. The presence of more coating on the Al-Cu-Mg particle, compared to the Al-Cu-Fe-Mn particle, is consistent with the observation in Section 3.3.4, and may result from differences in the natures and etching rates of the oxide layers initially present [43].

It is generally thought that nickel deposits by “immersion plating” during the formation of ZPO coatings on steel, thereby creating a nickel-iron galvanic couple (which increases substrate dissolution) [66]. The mechanism of action for Ni^{2+} in ZPO coatings on aluminum may be similar to the galvanic couple suggested above for steel, since the reduction of Ni^{2+} coupled with the oxidation of Al is a spontaneous process ($E^\circ = 1.43 \text{ V}$). The presence of plating presumably contributes to increased coating coverage due to the presence of more cathodic sites. In addition, it can speed up the etching stage of the coating process, thereby affecting the rate of ZPO precipitation.

The Auger spectra show that the Ni/Zn ratio is higher at region R2 (ratio value 0.72) than at region R3 (ratio 0.41) or region R4 (ratio 0.35). This may be a consequence of more Ni plating at the Al-Cu-Mg particle because the oxide layer above that particle dissolves faster than those oxides covering either the matrix or the Al-Cu-Fe-Mn particle [43]. Also, under acidic conditions there may be preferential dissolution of metallic Mg from the Al-Cu-Mg particle. The latter oxidation reaction may form a redox couple with the reduction of

Ni^{2+} ($E^\circ = 2.12 \text{ V}$), thus facilitating Ni plating. The Ni/Zn ratio is also higher at the amorphous region on the Al-Cu-Mg particle (region R2, ratio 0.72) compared to the crystalline coating on the same type of particle (R1, ratio 0.39). The thinner coating at R2 compared to R1 most likely indicates an earlier stage of growth. This is consistent with Ni plating occurring at the initiation of the coating (i.e. at the bottom of the coated layer), but precipitated $\text{Ni}_3(\text{PO}_4)_2$ or mixed zinc-nickel phosphates may also contribute to the total amount of Ni in the coating.

3.3.7 Measurements on High-Purity Al

Figure 3.8 shows SEM images of coatings formed on high-purity Al from ZPO solutions containing different amounts of Ni^{2+} (500-2000 ppm). The micrographs for the Ni^{2+} concentrations of 500, 1000 and 1500 ppm show patches of large coating crystals, but without covering most of the surface. At least 2000 ppm of Ni^{2+} appears required before an appreciable reduction in the coating grain size is observed, but the crystalline coating coverage still generally appears to be poor. This minimum concentration of Ni^{2+} , to reduce the grain size on high-purity Al, is much larger than is the situation for the 2024-Al alloy. For the high-purity case, the nucleation sites for coating are restricted to cathodic impurities and topographical irregularities in the substrate; by contrast, for 2024-Al, the presence of the major alloying element (i.e. Cu) directly provides more cathodic sites, since Cu is a nobler metal than Al. This appears to enable more coating crystals to grow, but to a smaller size, rather than having larger crystals growing on a smaller number of sites.

Polarization measurements were carried out for samples of high-purity Al that had been treated in the ZPO coating solution. In this case, there is no appreciable change in i_0 as the Ni^{2+} concentration increases from 0 to 2000 ppm (Figure 3.3). The degree of reduction in

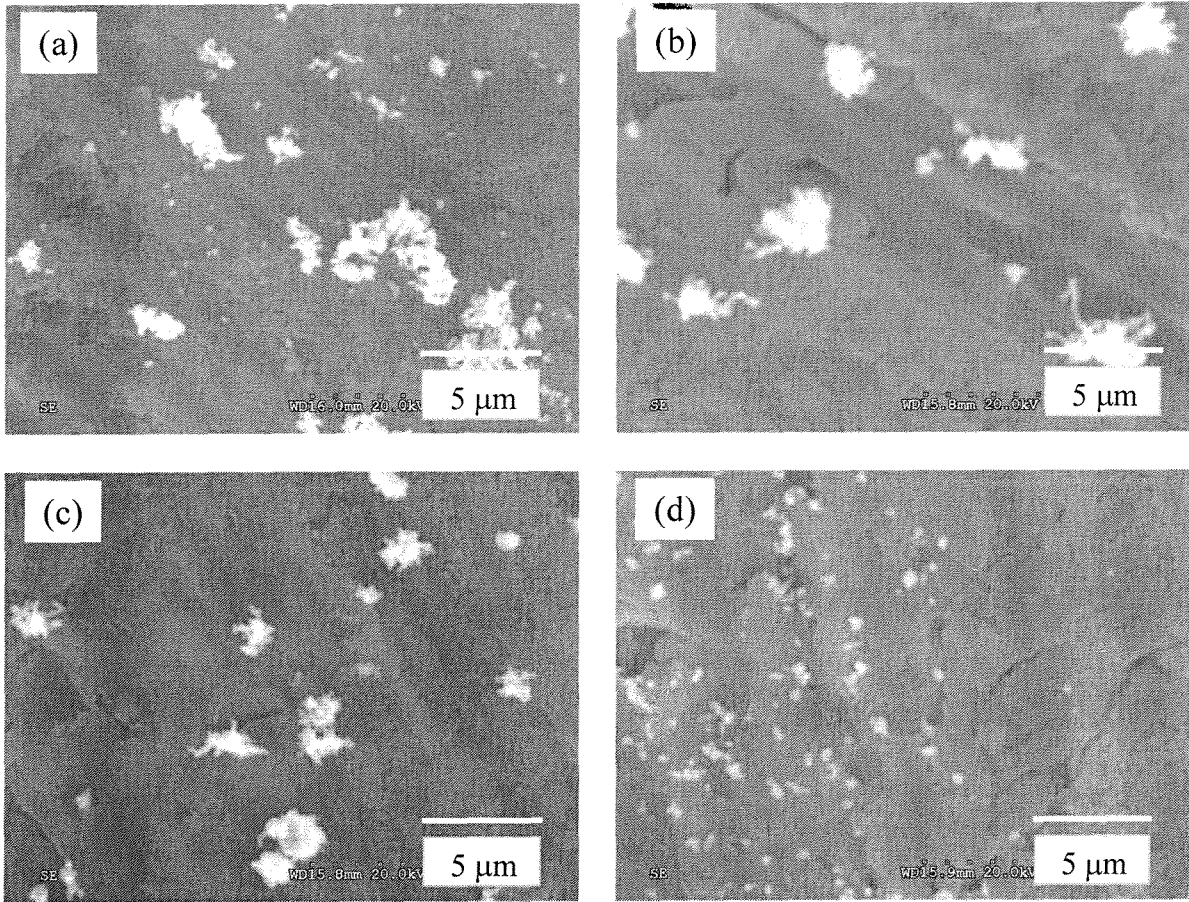


Figure 3.8 SEM micrographs from the high-purity Al surface after treating in ZPO coating solutions that contain varying amounts of Ni^{2+} : (a) 500, (b) 1000, (c) 1500 and (d) 2000 ppm.

corrosion rate is much smaller compared to the situation for 2024-Al; values of E_{corr} for high-purity Al increase from -1.19 to -0.93 V as the Ni^{2+} concentration changes from 0 to 2000 ppm, and that is consistent with the observations reported in Section 3.3.2. The low level of impurities in 99.9% Al, compared with 2024-Al, is responsible for its better corrosion resistance properties, but the reduction in the number of cathodic sites also makes it harder to phosphate.

3.4 Concluding Remarks

This work initiates study of the effects of additives in ZPO solutions for coating Al surfaces. The particular emphasis has been on Ni^{2+} , which has been shown to have a significant effect on macroscopic coating properties: it reduces the grain size for coatings on both 2024-Al alloy and high-purity Al, and improves the corrosion resistance for coatings on the 2024-Al alloy. From observations of the particular Ni^{2+} concentrations studied in this work, it seems that an optimal coating (with high corrosion resistance and high crystalline coverage) on 2024-Al is produced when the Ni^{2+} concentration is at the higher end of the range considered, namely 2000-2500 ppm. The amount of Ni incorporated into the coating layer (indicated by the Ni/Zn ratio) is also highest at these concentrations, an observation that may be taken to suggest that the presence of Ni results in an improved coating.

The ZPO coatings on 2024-Al and on high-purity Al have different characteristics, and that is especially because of the presence of the alloying elements in the former type of metal sample. The presence of Cu in the alloy results in more cathodic sites for nucleation of the coating, but the compositional non-homogeneity, because of the presence of second-phase particles, results in differences in degree of coverage at local regions. The amount of

Ni in the coating, and the coating thickness, also vary at different local regions within the Al-Cu-Mg particle.

Chapter 4

The Effect of pH and Role of Ni²⁺ in Zinc Phosphating of 2024-Al alloy

4.1 Introduction

The equilibria existing in the zinc phosphate coating solution are complex and involve the PO₄³⁻, HPO₄²⁻, H₂PO₄⁻ anions from the phosphoric acid, additives like F⁻ and Ni²⁺, and various hydrolysis reactions. The reactions involved are pH dependent, and the predominant equilibria can change during the coating process, as the pH increases. Further for alloys, which are heterogeneous at the microstructural level (as discussed in Chapter 1), the equilibria at a given instant in a coating process can be different across the different parts of the surface. These various factors can make the development of a full mechanistic description of the coating process quite challenging in this context.

For ZPO coating on the 2024-Al alloy, it has been determined that adding Ni²⁺ to the coating bath reduces the grain size of the deposited film and improves the corrosion resistance (Chapter 3); however, it is not yet clear how Ni²⁺ causes these effects. During the phosphating of steel, it has been suggested that Ni²⁺ reduction, occurring with Fe oxidation, results in the deposition of metallic nickel on the surface [64,66]. For the zinc phosphating of electrogalvanized (zinc coated) steel there are reports that Ni²⁺ incorporates into the coating crystals [68], while in addition Ni²⁺ reduction, driven in this case by Zn oxidation, leads to the formation of a surface Ni-Zn alloy [87]. In that context, studies have also been carried out to investigate the role of nickel in ZPO coating dissolution under alkaline

conditions, where it also has a favorable role [88,89].

The present work involves varying the pH of coating solutions, within the acidic range, and the coating time in order to learn more about the mechanistic role of Ni^{2+} in the ZPO coating formation process on this alloy. The coatings were applied at pH values 3, 4, and 5; the middle value is often considered optimal for this phosphating process, but coatings made at the other values allowed comparisons of behavior for coating solutions that are more and less acidic. Specifically, the experiments aimed to determine whether Ni^{2+} reduction and deposition of metallic Ni occurs during the zinc phosphating of 2024-Al alloy, particularly since Ni^{2+} reduction (with Al oxidation) and Ni metal deposition on Al is believed to be enhanced in more acidic solutions [3]. Samples were dipped in the coating solutions for different times in order to assess the role of Ni during various stages of the coating process. ZPO solutions containing no Ni^{2+} were also used to further the comparisons.

In the first part of this chapter, coatings formed by the different exposures to the ZPO coating solutions were analyzed by X-ray photoelectron spectroscopy (XPS) and scanning electron microscopy (SEM) in order to see the effects of the variables considered on the macroscopic chemical composition of the coatings formed and the effect of varying pH on the morphology. In the second part of this chapter scanning Auger microscopy (SAM) and scanning electron microscopy (SEM) are used to investigate the influence of alloy microstructure on the coatings for the various conditions of application, and also the chemical composition of the differently-sized coating crystals formed. The prime objective of the second part is to assess how the conclusions reached with XPS need extension given that the coating occurs on an intrinsically heterogeneous surface. Together, the first and second parts of this chapter aim to add mechanistic knowledge for the role of Ni^{2+} in the zinc phosphating of 2024-Al alloy.

4.2 Experimental

2024-Al samples were polished in the manner described in Section 3.2. One L of the water-based ZPO solutions (designed specifically for coating of Al) contained: 10.8 mL of 85% H₃PO₄, 1.24 g ZnO, and 1.11 g NaF; 9.91 g of Ni(NO₃)₂ was also added to some of the solutions. The last solution corresponds to 2000 ppm (where ppm equals number of mg Ni²⁺ per kg of solution). Coatings were formed by immersing the alloy samples in such solutions at 60°C for a range of dipping times; each coating treatment was followed by a wash in deionized water and sample drying in air. Throughout, the pH adjustment was done by adding NaOH solution. That reagent was from Fisher for samples prepared by dipping in the “with-Ni” solution for 2 min; for all other coatings, the pH adjustment was done with Analar NaOH (EM Science).

XPS spectra were measured with a Leybold MAX200 spectrometer using the MgK α source (1253.6 eV) operated at 15 kV, 20 mA. The C detected in coatings arises from polishing, as well from the atmospheric exposure. The Si detected comes mainly from polishing. Accordingly these contributions are excluded from the comparisons reported in this paper. Inevitably, there will also be some contribution from contamination in the O signals, an element that must be present at appreciable levels in the uncontaminated surfaces. It is hoped that by emphasizing trends in elemental ratios which do not involve O, the effects of any contamination from this element are minimized for the analyses reported here.

The SAM point analyses and the associated SEM images reported here were carried out using the primary electron beam set at 10 keV and 3 nA. Other SEM characterizations were made with a Hitachi S3000-N instrument (incident beam accelerated through 20 kV) or a Hitachi S4700 instrument (field emission source operated at 30 kV). The EDX

characterizations, made for compositional identification of the second-phase particles, used a Hitachi S3000-N instrument with the incident beam accelerated through 20 kV.

4.3 Results and Discussion

4.3.1 Setting the Scene

The electrochemical process that leads to phosphating starts by the acidic solution etching the oxide layer to allow electronic access with the underlying metal. The conventional view of phosphating is indicated in Figure 1.5. The acid dissociation constants of phosphoric acid (H_3PO_4) are $\text{pK}_1 = 2.15$, $\text{pK}_2 = 7.20$ and $\text{pK}_3 = 12.15$ [90]. The coating solution starts in a definitely acidic state, but the precipitation of tertiary phosphate requires the pH to be increased well into the basic range. This is driven by local reactions at the micro-cathodes, such as H_2 evolution [27], although the reduction of other species present may occur (e.g. reduction of NO_3^- under acidic conditions, for which the standard reduction potentials range from 0.81 to 0.96 V, according to the product formed [91,92]). These processes are in general pH dependent. Therefore it is to be expected that the nature of a coating will change as it forms, and that it may vary accordingly to the starting pH and any additives that are present.

The additive of particular interest here is Ni^{2+} , and previous work (Chapter 3) optimized the nature of the ZPO coating on 2024-Al alloy, and its resulting corrosion resistance, as a function of Ni^{2+} concentration for coating solutions that had an initial pH of 4. The present work now considers a wider range of starting pH, although since previous observations showed that pH 2 does not yield much coating [38], the initial pH values considered here are restricted to 3, 4 and 5. However, the Ni^{2+} concentration is kept fixed at 2,000 ppm, the optimal value for pH 4 (Section 3.4). Another additive of interest is F^- . This

is added to a coating solution with the purpose of accelerating etching and limiting free Al^{3+} in solution, since this species is believed to have a deleterious effect on coating growth [93]. It is generally assumed that F^- complexes to form AlF_6^{3-} , but in principle there is still a possibility of AlF_3 precipitation.

Questions of interest for this work relate to how the starting pH affects the relative proportions of $\text{M}_3(\text{PO}_4)_2$ and MHPO_4 ($\text{M}=\text{Zn}^{2+}$ and/or Ni^{2+}) in the coatings formed, as well as the amounts of Zn and Ni. It is thought that aluminum phosphate will only be present in small amounts due to the presence of F^- , which either complexes or precipitates with Al^{3+} . Finally it should be noted that while primary phosphates are water-soluble and tertiary phosphates insoluble, the secondary phosphates have a more intermediate character. In general various other species can be expected to deposit, including ZnO as has been reported previously [94] and $\text{Zn}(\text{OH})_2$ once the solution at the solid interface is sufficiently basic. ZnAl_2O_4 may also form, but the methods used here are not able to convincingly distinguish between ZnO, $\text{Zn}(\text{OH})_2$, and ZnAl_2O_4 . Accordingly, through this work, when ZnO is referred to as being present in a coating, the statement should be interpreted to include the possibility that $\text{Zn}(\text{OH})_2$ and/or ZnAl_2O_4 may also be present.

At higher pH values when significant PO_4^{3-} is present in solution, ZPO precipitation is expected to dominate due to its appreciably lower solubility [91]. Throughout there are parallel (and opposing) tendencies to change the local pH, and in turn those changes must affect the subsequent precipitation. This work aims to assess how different starting conditions affect the natures of the coatings. That they are affected is immediately seen in Figure 4.1, which shows SEM micrographs of 1200-grit polished 2024-Al surfaces after dipping in ZPO coating baths which contained Ni^{2+} and had been adjusted to the different pH values. It is clear that the starting pH has a marked effect on the density and size of crystals

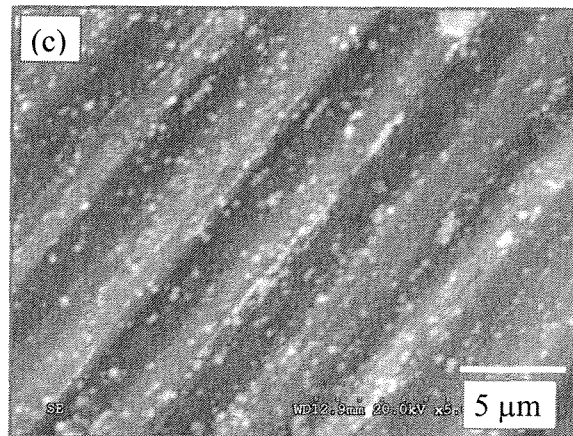
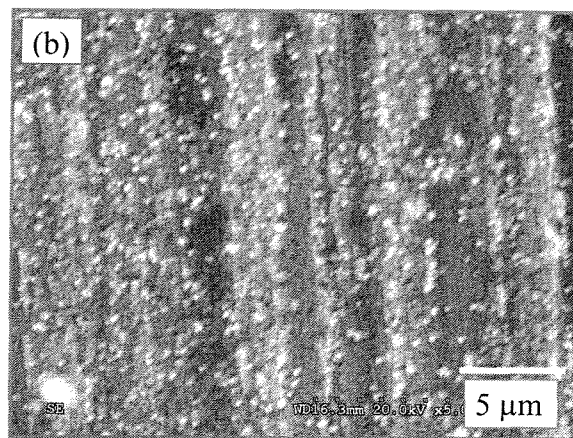
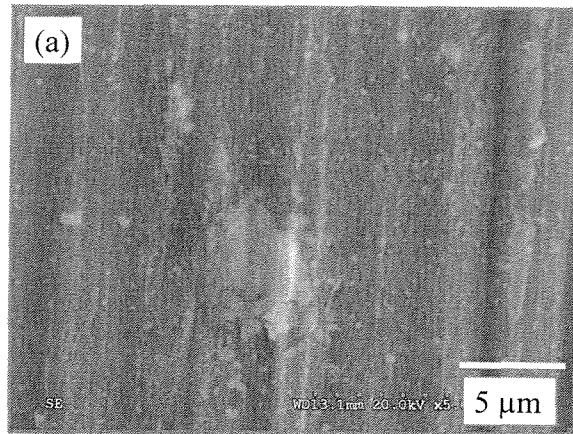


Figure 4.1 SEM micrographs after coating 1200-grit polished 2024-Al samples with ZPO solutions containing 2,000 ppm Ni^{2+} for 2 min at different starting pH values: (a) pH 3, (b) pH 4 and (c) pH 5.

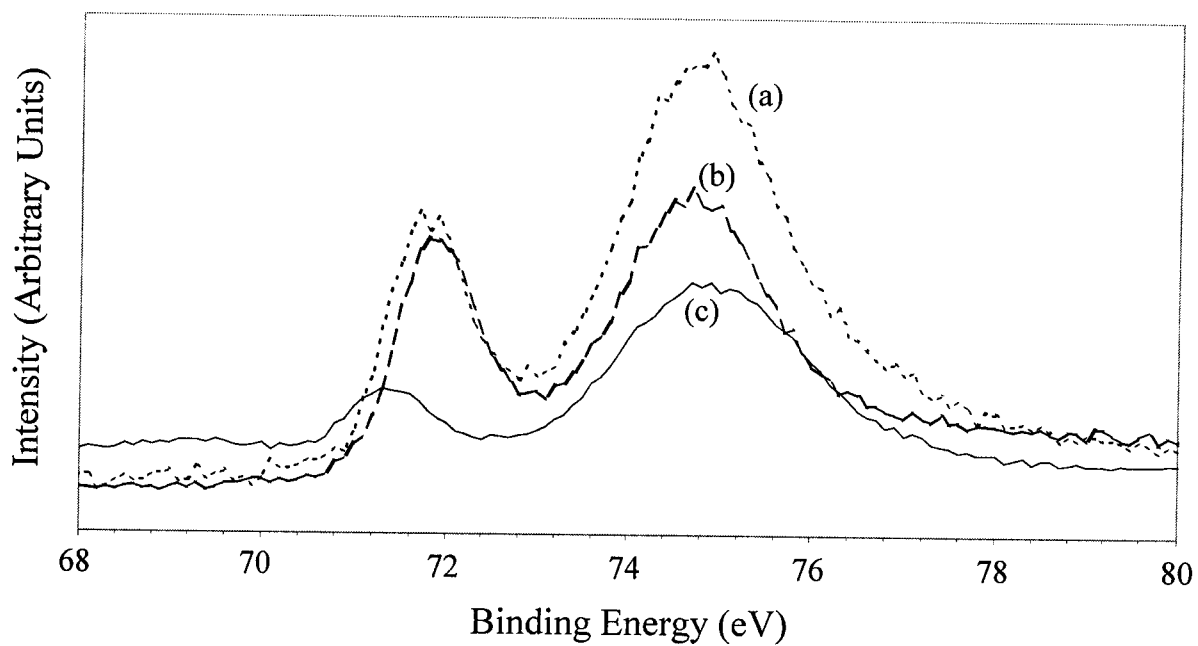


Figure 4.2 Al 2p region of XPS spectra for 2024-Al dipped in ZPO solutions containing 2,000 ppm Ni^{2+} for 30 s at different starting pH values: (a) pH 3, (b) pH 4, (c) pH 5.

in the coatings. These features are discussed further after considering observations by XPS for the corresponding chemical compositions. The specific coating times used (3 s, 7 s, 30 s, 2 min) were selected to assess the coating process during the different stages of ZPO coating formation. 2 min is the optimal coating time when Ni^{2+} is added to the coating solution. 30 s was chosen because it reflects an intermediate stage where the composition of the deposited compounds differs from the situation for the 2 min coating time (as indicated by initial measurements). Analysis of this coating time is therefore likely to give new information about the ZPO coating mechanism. Coatings formed using dipping times of 3 s and 7 s reflect the early stages of the coating process.

4.3.2 Macroscopic Characterization

Chemical compositions from XPS give an overall characterization of the surface regions of the coatings formed, but without regard to variations at the microstructural level. The properties of coatings formed from ZPO solutions containing Ni^{2+} are discussed in Section 4.3.2.1, while the mechanistic role of Ni^{2+} is covered in Section 4.3.2.2; comparisons with ZPO solutions having no Ni^{2+} are discussed in Section 4.3.2.3.

4.3.2.1 Coatings from ZPO Solutions Containing Ni^{2+}

Table 4.1 reports elemental composition information measured by XPS from mirror-polished 2024-Al samples dipped for 30 s (partial coatings) or 2 min (full coatings) in Ni-containing ZPO solutions adjusted to the different starting pH values. In this work the term “coating” refers to both the ZPO coating and the oxide (mainly Al oxide) that forms spontaneously on the alloy surface. The metallic Al signal decreases with increasing time of coating for pH 3 and 4, and that is fully consistent with the coatings being appreciably

thinner after a 30 s exposure to a coating bath compared with a 2 min exposure. Also it is apparent that the coating thickness increases with increasing pH. Figure 4.2 shows Al 2p spectra where the higher binding energy peaks correspond to Al^{3+} while those at lower binding energy are from metallic Al. It is clear that the intensity of the Al 2p metallic component is smaller for the alloy sample coated for 30 s in the pH 5 bath compared to those placed in the baths at pH 3 or 4 for the same time. It is assumed at present that the varying position of the metallic peak results from some differential charging.

It is difficult with XPS to compare the thickness of the 2 min coating prepared starting at pH 5 with those prepared starting at pH 3 and 4 because of overlap between the Ni 3p and Al 2p spectra. However, Auger electron spectra (Section 4.3.3.1.3) do indicate that the coating prepared with pH 5 is thicker than that starting with pH 4. As the coating formation advances, the etching rate and rate of H_2 evolution (H^+ consumption) slows, and this can lead to a decrease in the local pH at the surface because of diffusion from the bulk of the coating solution. This will not only cause a decrease in the $\text{Zn}_3(\text{PO}_4)_2$ precipitation but it may also give some dissolution of phosphate that has already deposited on the surface [95]. For this reason, the coating situation is dynamic, with the possibility of dissolution from a fully coated sample, thereby leaving some uncoated areas. The drop in the local pH should be less for the coating formed at the starting pH of 5, compared to pH 3 or 4, due to the higher pH in the bulk of the coating solution, and this contributes to the thicker coating formed at pH 5.

The data in Table 4.1 show that various trends are operating, and that the nature of the coating is neither constant nor particularly simple. An initial guide to changes in the coating composition is provided by the measured ratio $Q_P (= (\text{Zn}+\text{Ni})/\text{P})$ (Figure 4.3(a)). A coating composed of tertiary phosphate ($\text{M}_3(\text{PO}_4)_2$, where M is a divalent cation) would have a predicted M/P ratio of 1.5 ($Q_P = \text{M}/\text{P}$). The higher Q_P values at the beginning of the

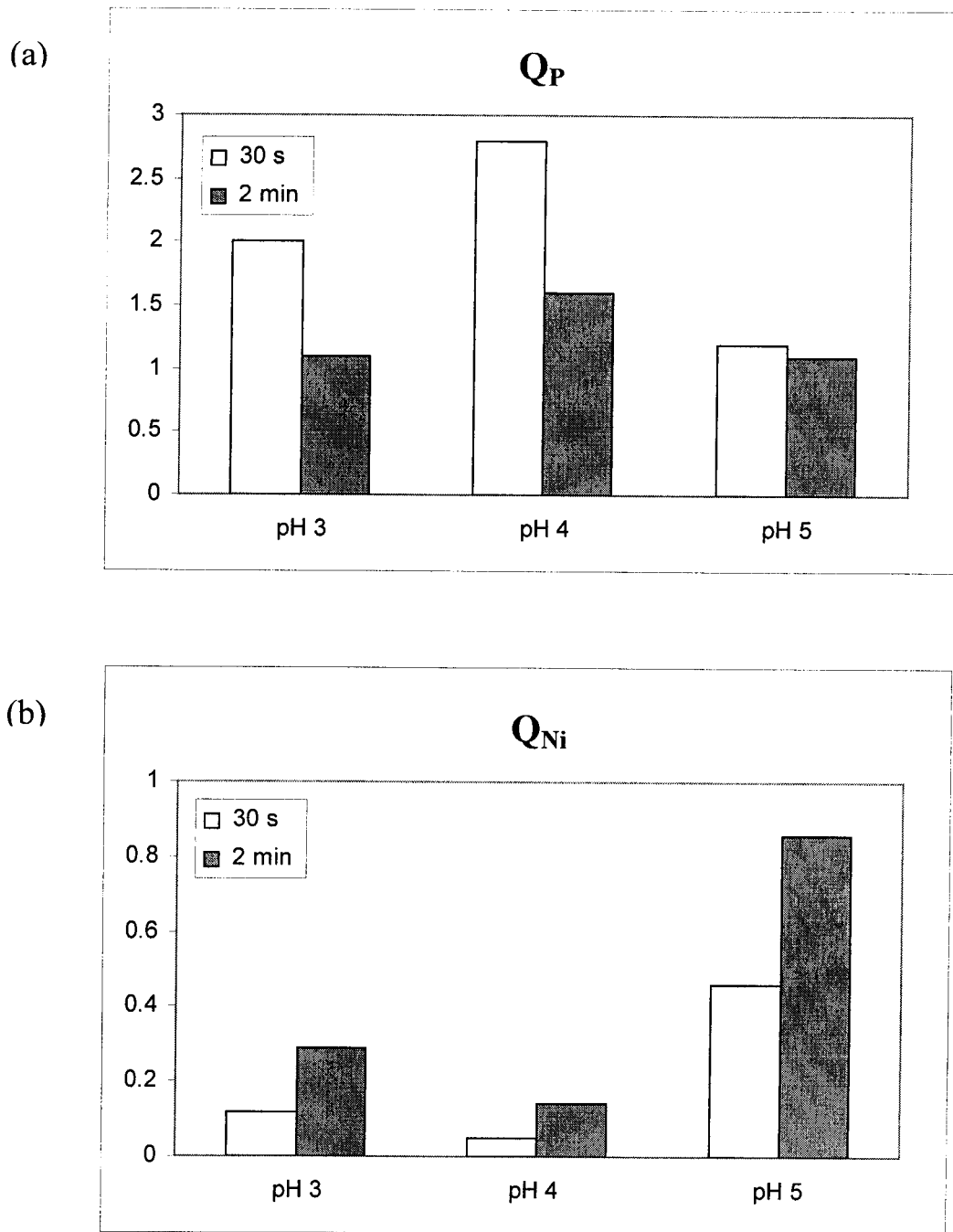


Figure 4.3 Graphical representation of elemental compositions from XPS for coatings formed from ZPO solutions containing 2,000 ppm Ni^{2+} applied for different times and at different starting pH values: (a) $Q_P = (Zn+Ni)/P$ and (b) $Q_{Ni} = Ni/(Ni+Zn)$.

Table 4.1 Elemental atomic percentages from XPS for 2024-Al samples after coating in ZPO solutions, containing 2000 ppm Ni²⁺, showing variation with coating time and initial solution pH.[§]

	pH 3 30 s	pH 3 2 min	pH 4 3s	pH 4 7s	pH 4 30 s	pH 4 2 min	pH 5 30 s	pH 5 2 min
Zn	5.1	3.9	†	0.8	13.2	11.4	4.7	2.1
Cu	0.6	1.6	†	†	0.5	0.8	0.9	-
Ni	0.7	1.6	- [◇]	-	†	1.8	4.0	13.1
Na	-	1.1	-	-	-	†	2.0	-
Ca	-	-	-	-	-	-	2.7	1.5
O	51.4	64.5	52.0	54.2	52.2	62.3	53.1	69.0
P	3.0	5.0	†	2.6	4.8	8.1	7.4	14.2
Al	33.9	19.6	43.1	37.7	25.2	13.0	14.2	*
F	5.1	2.8	3.3	4.5	4.1	2.7	11.1	-

[§] Values are believed to be accurate to within ±10% as discussed on page 29

† Amount detected is less than 0.5% and too small to be measured accurately

[◇] The hyphen indicates that the element is not detected

* Present but not quantifiable due to overlap with Ni peaks (Al 2p signal overlaps with Ni 3p, Al 2s overlaps with Ni 3s)

coating process for pH 3 and 4 strongly suggest the presence of a Zn compound other than zinc phosphate (particularly since the amounts of Ni are comparatively low). The elemental compositions reported in Table 4.1 indicate that a significant portion of the Zn is bonded to O, since no other anionic species can be present in sufficient quantities. A similar conclusion was reported in a study for the zinc phosphating of high-purity Al [94], and is consistent with ZnO (and Zn(OH)₂) being more soluble in acidic than in neutral conditions [91]. Hence, it may be concluded that in the earlier stages of these coating processes the local pH at the alloy surface has not increased sufficiently for the precipitation of tertiary phosphate, but that balances occur between the precipitation of ZnO and that of the secondary phosphate MHPO₄. The presence of the latter in the coating inevitably leads to a decrease in the Q_p ratio, and it follows, for a heterogeneous coating, that a value of Q_p close to 1.5 may not

necessarily indicate tertiary phosphate, since in principle both ZnO and ZnHPO_4 could be present. During the early stages of coating in the pH 5 bath, the local acidity apparently remains low enough that secondary phosphate can precipitate and dominate the coating, as indicated by the Q_P ratio measured after 30 s (Figure 4.3(a)). This implies that the local pH is higher in the pH 5 bath compared to pH 3 and 4, causing more precipitation, and this is consistent with the observation noted above that, after 30 s, there is a thicker coating starting at pH 5 than for pH 3 or 4.

The measured values of the Q_P ratio, close to 1, for the full coatings at pH values of 3 and 5 are strongly suggestive of an appreciable involvement by the secondary phosphate. The observed behavior for the full coatings depends on subtle balances. More etching is expected when the coating process starts at a higher acidity (i.e. lower pH), and that in turn can lead to the release of more electrons for the H^+ to H_2 reduction. However, a greater increase in pH is then required in order to further the precipitation of $\text{Zn}_3(\text{PO}_4)_2$. Thus, starting at pH 3, the increase in the local H^+ concentration required to get precipitation of $\text{Zn}_3(\text{PO}_4)_2$ is one order of magnitude greater than for starting at pH 4. The SEM micrographs (Figure 4.1) indicate that the crystals are smaller for pH 3 than pH 4, and this is also consistent with a lower degree of precipitation when starting at pH 3. On the other hand, the amount of etching will be reduced at pH 5, and the evidence again suggests that the electron transfer is insufficient to raise the pH sufficiently for precipitation of the tertiary phosphate. XPS measurements of the type in Figure 4.2 indicate that the oxide layer on an uncoated sample is as thick as the entire overlayer (coating plus oxide) for a ZPO-coated sample of 2024-Al. The larger Al^{3+}/Al metal ratio at pH 3 and 5 compared to pH 4 (partial coatings), evident in Figure 4.2, is due to a larger portion of the surface which has had no coating precipitation but has a thicker Al oxide layer compared with the coated regions. The overall

indication is that starting with a coating solution at pH 4 provides the best balance between initial etching and the consequent increase in pH to favor the $Zn_3(PO_4)_2$ formation.

The data in Table 4.1 indicate that F is present in the 30 s coatings, with the amount increasing in the order pH 4 < pH 3 < pH 5. The measured Cu 2p_{3/2} binding energies from these coatings (932.3, 932.5, 932.7 eV for pH 3, 4, 5) are too low to be consistent with the presence of CuF₂ (936.1-937.0 eV [47]). The concentrations of Zn²⁺, Ni²⁺ and F⁻ in solution are not high enough for ZnF₂ or NiF₂ precipitation (their solubilities in water are 15.5 and 25.6 g/L respectively [91]). This supports, by elimination, that the precipitated compound is most likely AlF₃ (solubility 5.0 g/L [91]), which is consistent with the observed Al 2p signal (although the major component contributing to the Al³⁺ signal is Al oxide). For solutions adjusted to pH 5, CaF₂ may be present in addition to AlF₃. Al³⁺ will precipitate in the form of AlF₃ rather than remaining in solution as AlF₆³⁻ when the F⁻/Al³⁺ ratio drops below a transition value [90]. At pH 3 there is more etching and greater amounts of Al³⁺ present in solution (compared to pH 4), causing a lower F⁻/Al³⁺ ratio. Therefore more AlF₃ would be expected at pH 3; the greater amount of F in the coating formed at pH 3, compared to 4, confirms this expectation. In a similar way, more AlF₃ precipitation would be expected during the early stages of coating when the etching is maximized and the greatest amount of Al³⁺ is present in solution. The presence of more F in the coating at 30 s compared to 2 min is consistent with this hypothesis and indicates that AlF₃ locates at the bottom of the coating layer (i.e. closest to the metal) for coatings formed from solutions which are not stirred during the coating process. The presence of AlF₃ in the coatings formed by dipping alloy samples into an unstirred coating bath implies that some F⁻ precipitates rather than remaining in the form of the AlF₆³⁻ solution complex [27].

Compounds of Na^+ are generally more soluble than those of the other cations present in the coating solution, and accordingly they precipitate later in the process. This is shown by its detection from coatings formed after 2 min, but not after 30 s, for the pH values of 3 and 4. At pH 5, Na^+ is detected from the coating formed at 30 s, but not 2 min, and it is likely in the form of Na_2HPO_4 with perhaps small amounts of Na_3PO_4 (these are the least soluble of the Na compounds that could reasonably be present). This indicates that Na precipitates quicker in the coating process starting at pH 5, and is consistent with the whole precipitation being faster than when starting at the lower pH values. Ca, a known contaminant in the NaOH used for adjusting the solution pH, is only detected in the coatings formed at pH 5. In that situation, the rates of etching and pH rise are slower, allowing a more complete response of solution species to the change in pH, thereby facilitating more precipitation of different species.

The coating compositions for 2024-Al samples dipped in a pH 4 ZPO bath for 3 s or 7 s are indicated in Table 4.1. For the 3 s coating, aluminum fluoride has deposited on the surface but there is no significant phosphate precipitation. For the 7 s coating, the detection of P implies that phosphate is present. The cations in the precipitated phosphate compounds may be Zn, Cu, or Al from the elemental composition. Zn and Cu are present in small quantities compared to P; therefore, a significant amount of the phosphate must be associated with the Al^{3+} cation. Aluminum phosphate precipitates during the early stages of the coating process because etching of the uncoated alloy by the acidic coating solution creates a large Al^{3+} concentration in the solution near the alloy surface.

4.3.2.2 Mechanistic Issues: Ni²⁺ in Coating Solution

Analysis in Chapter 3 of the Ni 2p_{3/2} signal from the full coating for pH 4 (binding energy 856.4 eV) does not support the presence of nickel metal or NiO (whose binding energies are expected at close to 852.7 and 854.0 eV respectively [47,96]). No metallic Ni or NiO was detected in any of the coatings (at pH 3, 4 or 5) discussed in this work either, and the binding energies observed are only consistent with Ni²⁺. Therefore, there is no direct evidence of Ni²⁺ reduction (driven by Al oxidation) causing Ni deposition on these surfaces. The process of Ni²⁺ reduction may be limited by the presence of competing and more favorable reactions such as the reduction of NO₃⁻ [92]. While nickel metal or NiO are not confirmed, the observed Ni 2p_{3/2} binding energy from the 2 min coating at pH 4 (856.4 eV) is close to values reported for NiAl₂O₄ (856.1-856.3 eV [78,97-99]). The reported binding energies for Ni(OH)₂ (855.5-855.9 eV [78,97,98]) are also sufficiently close so that species cannot be definitively ruled out, but the following discussion recognizes NiAl₂O₄ as being most likely present, and we return to this point in the SAM analysis (Section 4.3.3).

The presence of Ni in the coating, relative to the amount of Zn, is indicated by the Ni/(Zn+Ni) ratio (henceforth referred to as Q_{Ni}) which varies with the pH of the starting solution (Figure 4.3(b)). For all three initial pH values, the amount of Ni in the coating increases as the coating time increases. At pH 3 and 4 (30 s coating), ZnO is present (as described in Section 4.3.2.1) but not much phosphate or NiO. During the early stages of phosphating, solution complexes involving Ni²⁺ may not respond quickly enough to increases in pH (Section 4.3.2.3) for precipitation of NiO to occur. This is consistent with the general trend of ligand substitution reactions being faster for Zn²⁺ than Ni²⁺ [100]. At 2 min, more phosphate has precipitated (Section 4.3.2.1) and therefore it seems likely that the increase in Ni is due in part to precipitation of nickel phosphate perhaps in the form of mixed

zinc-nickel phosphates ($Zn_xNi_{3-x}(PO_4)_2$). Similar findings of mixed zinc-nickel phosphate precipitation are reported for the phosphating of electrogalvanized steel [68]. As mentioned above, the evidence from XPS for coatings formed by a 2 min dip in a Ni^{2+} -containing ZPO solution adjusted to pH 4 is consistent with the presence of $NiAl_2O_4$ and/or $Ni(OH)_2$. Examination of the elemental composition of the coating (Table 4.1) does not suggest the presence of any other Ni^{2+} -containing compounds (particularly since NiF_2 is not present (Section 4.3.2.1)). The absence of NiO is consistent with its lower stability relative to $Ni(OH)_2$ in an aqueous medium [101]. Other observations for 2024-Al have indicated that incorporation of Ni^{2+} into the oxide improves the substrate corrosion resistance [83]. Since we observed earlier that Ni^{2+} in the coating solution improves the corrosion resistance of the alloy substrate (Chapter 3), it may be that a Ni-containing oxide (e.g. like $NiAl_2O_4$) forms during the later stages of the ZPO coating process when some bare metallic or thin oxide regions may be exposed. In principle $ZnAl_2O_4$ could form as well although we have no direct evidence from XPS to indicate its presence. The presence of nickel phosphate may also improve the corrosion resistance although a study of coating dissolution under alkaline conditions (ZPO coatings on zinc-coated steel) indicated that nickel phosphate did not play a significant role in protecting the surface from corrosion [88,89].

The small Q_{Ni} for the coatings formed for a starting pH of 4 (Figure 4.3(b)) may be due to the smaller solubility product of $Zn_3(PO_4)_2$ (5×10^{-36} [102]) compared to $Ni_3(PO_4)_2$ (5×10^{-32} [91]) leading to the preferred precipitation of the former. Similarly, it has been reported that Ni^{2+} replaces Zn^{2+} in tertiary phosphate crystals to only a small extent for coatings on steel and zinc-coated steel [88]. To the best of our knowledge, there is not a lot of information available on Zn-Ni secondary phosphates. The slower reaction rate of complexes involving Ni^{2+} compared to Zn^{2+} may also contribute to the small Q_{Ni} ratio. The

smaller Q_{Ni} ratio at pH 3 and 4, compared to pH 5, for the partially coated surface and the full coatings is due in part to the appreciable precipitation of ZnO. The larger amount of Ni in the coating at pH 5, compared to pH 4, is most likely a result of $NiHPO_4$ and $Ni_3(PO_4)_2$ precipitation. The presence of pure NiO is not consistent with the measured binding energy of the Ni $2p_{3/2}$ signal; in principle $Ni(OH)_2$ has a consistent binding energy, but the large amount of P detected in addition to the small amounts of cationic elements other than Ni implies that nickel phosphate is likely to be present. At pH 5, Ni dominates the full coating (Table 4.1). The rate of alloy dissolution is lower at pH 5 compared to pH 3 and 4. Therefore the increase in pH is slower, allowing more time for the solution complexes involving Ni^{2+} to respond to the increase and precipitation to occur. Further, the rate of alloy dissolution is highest at the beginning of the coating process when more of the alloy is uncoated and exposed to the acidic coating solution. As a result, the rate of H^+ consumption (pH increase) is higher in the early stages (partial coating), resulting in less precipitation of Ni-containing compounds compared to the later stages of the coating process. Also, it is possible that significant amounts of Zn^{2+} have been removed from solution during the early stages of coating, due to the faster response of Zn^{2+} complexes, compared with those of Ni^{2+} , as the pH changes. With the initial molar concentration of Ni^{2+} about twice that of Zn^{2+} , further removal of Zn^{2+} causes a substantial increase in the Ni^{2+} -to- Zn^{2+} ratio in solution, resulting ultimately in the preferential deposition of Ni^{2+} . The observation of a larger value of Q_{Ni} when the formation process starts at pH 3, compared to pH 4, likely results from the lower coating coverage and hence more of the substrate remaining exposed for the formation of the Ni-containing oxide. This may result in improved corrosion protection for the pH 3 coatings, although the coatings formed at pH 4 have better paint adhesion due to the presence of larger coating crystals (Figure 4.1 shows similar density of crystals in both cases, but size

is larger for pH 4). Larger crystals lead to better bonding between the phosphate coating and the paint film as a result of the increase in effective surface area.

4.3.2.3 Coatings from ZPO Solutions with No Ni²⁺

Some 2024-Al samples were coated in phosphating solutions without Ni²⁺ in order to gain further understanding of the role of this additive for the present context. The coatings formed from solutions with no Ni²⁺ at pH 3 and 4 are thicker than those formed from the comparable solutions containing Ni²⁺ (XPS is unable to detect metallic Al from the full coatings in the former cases). XPS data from ZPO coatings on high-purity Al also indicate that thicker coatings form when the coating solution does not contain Ni²⁺ (unpublished observations from this laboratory). Due to the increased coating thickness, F is not detected in coatings formed without Ni²⁺ (Table 4.2) since AlF₃ is located at the bottom of the coating layer (Section 4.3.2.1).

Table 4.2 Elemental atomic percentages from XPS for 2024-Al samples after coating in ZPO solutions, containing no Ni²⁺, showing variations with starting pH and coating time for pH 4.[§]

	pH 3 2 min	pH 4 30 s 2 min		pH 5 2 min
Zn	25.4	21.5	25.4	6.3
Na	- [◇]	-	-	7.7
Ca	-	-	-	4.4
O	67.7	67.4	69.9	43.3
P	6.8	9.6	4.7	6.2
Al*	-	1.4	-	8.9
F	-	-	-	23.1

[§] Values are believed to be accurate to within ±10% as discussed on page 29

[◇] The hyphen indicates that the element is not detected

* Metallic Al is not detected under any of these conditions.

Measurements of classical titration curves can help provide further insight. This involved monitoring the pH as measured volumes of NaOH were added to a fixed volume of each coating solution. The system was allowed to reach equilibrium (indicated by a stable pH) after each addition of NaOH to eliminate the effect of reaction rate on the amount of NaOH required to reach the endpoint. Measurements were carried out for coating solutions with Ni^{2+} and coating solutions without Ni^{2+} . It was observed that the solutions took longer to respond to the addition of NaOH when Ni^{2+} was present in the coating solution compared to the solutions with no added Ni^{2+} . For example, when 1.2×10^{-3} mol of (aqueous) NaOH was added to coating solutions at pH 2.5, the Ni^{2+} -containing solution took about 1.5 times longer to reach a stable pH of 2.9 compared to the solution without Ni^{2+} . This is consistent with observations of relatively slow kinetics for ligand substitution reactions involving Ni^{2+} in solution (compared to Zn^{2+}) [100]. It is considered likely that the slower response observed when Ni^{2+} is present in the coating solution also occurs during the coating process when the local pH at the alloy-solution interface increases. The slow adjustment to increases in pH results in less precipitation since precipitation occurs when the system has adjusted to higher pH conditions. Less precipitation in turn results in a thinner coating. Measurements of pH with added NaOH were similar for the two types of coating solution (in terms of the volume added) for pHs less than 5, but significantly different for pHs above 8. In the latter situation, a larger amount of NaOH must be added to the Ni^{2+} -containing solution, compared to the solution without Ni^{2+} , to reach a particular pH value. This contrast is likely to come from the Ni^{2+} , whose hydrolysis equilibrium can be written as $\text{NiL}_n(\text{H}_2\text{O})^{2+} + \text{H}_2\text{O} \leftrightarrow \text{NiL}_n\text{OH}^+ + \text{H}_3\text{O}^+$, where L represents a coordinating ligand (which could be H_2O). The equilibrium constant is approximately 10^{-10} (when $L = \text{H}_2\text{O}$ [103]) and that has the consequence that a shift to the right-hand side only becomes significant at higher pH values.

This hydrolysis increases the acidity and ensures that a greater amount of NaOH must be added to the “with-Ni” solution, compared to the “no-Ni” solution. This is relevant to the coating process since a greater degree of H^+ consumption will be necessary before solutions containing Ni^{2+} give ZPO deposition than is the case for solutions that do not contain this additive. Consistently, thinner coatings are formed from the Ni^{2+} -containing solution.

The Q_P ratios measured from coatings formed by dipping for 2 min in solutions at pH 3 or 4, which do not contain Ni^{2+} , are considerably larger than the Q_P ratios measured by XPS for coatings formed from the corresponding solutions which contain Ni^{2+} . The larger Q_P ratios appear associated with ZnO deposition during the later stages of precipitation, when the Al etching is reduced. Then there is much less H_2 evolution to combat the effect of acidic solution diffusion from the bulk of the coating bath to the alloy-solution interface, and a reduced drive from the phosphoric acid equilibrium towards PO_4^{3-} . Given that the only elements detected from the coated samples are Zn, O, P and Al (Table 4.2), it seems inevitable that any Zn that is not in the form of a zinc phosphate occurs as oxide or hydroxide, although XPS is not able to distinguish between these two possibilities. The Q_P ratio measured from the coating formed in 30 s from the solution starting at pH 4 is 2.3, while that from the 2 min coating time is 5.4, so suggesting the greater importance of ZnO precipitation during the later stages of the coating process when more of the surface is coated and there is less etching.

The main difference between the coatings formed at pH 5, compared to pH 3 and 4, is that XPS detects more of the trace elements (i.e. Na and Ca), as well as an enhanced percentage of F. Similar to the situation when Ni^{2+} is present in the coating solution, with the pH of the initial coating solution adjusted to 5, the rates of etching and pH rise are less

than for pH 3 and 4, so allowing a more complete response of solution species to the change in pH. This leads to more free F^- in the coating solution and in the resulting coating.

4.3.3 Analysis at Micro-Regions

4.3.3.1 Ni^{2+} -Containing Coatings

The coatings described below were formed by dipping 2024-Al samples in the Ni^{2+} -containing ZPO bath for 2 min (optimal coating time).

4.3.3.1.1 Al-Cu-Mg Second-Phase Particle

Figure 4.4 shows SEM images of Al-Cu-Mg intermetallic particles (round regions, dimension several μm) on surfaces exposed to the Ni^{2+} -containing ZPO coating solution at the different starting pH values 3, 4 and 5. The area surrounding each Al-Cu-Mg particle is the alloy matrix, while the bright areas (dimension 0.5 μm or less) on the intermetallic particles in Figure 4.4(b) and (c) are ZPO coating crystals. Other smaller ZPO particles are apparent only at higher magnification. It is evident that there are more bright areas (larger ZPO crystals) on the pH 4 Al-Cu-Mg particle compared to pH 5, where there are a few ZPO crystals, and pH 3 where no crystals are observed. This trend is similar to that observed for ZPO crystals over the entire alloy surface (Section 4.3.2) when the initial coating pH was varied. Those SEM measurements indicated that the ZPO crystals formed on the surface when the coating solution starts at pH 3 were considerably smaller than at pH 4 since there is less precipitation at pH 3. It is believed that the same phenomenon is responsible for the difference in coating morphology on the Al-Cu-Mg intermetallics in Figure 4.4(a) and (b). Coating crystals are not visible on the intermetallic particle at pH 3 (Figure 4.4(a)) because they are smaller than those formed by coating at pH 4. When the coating bath has an initial

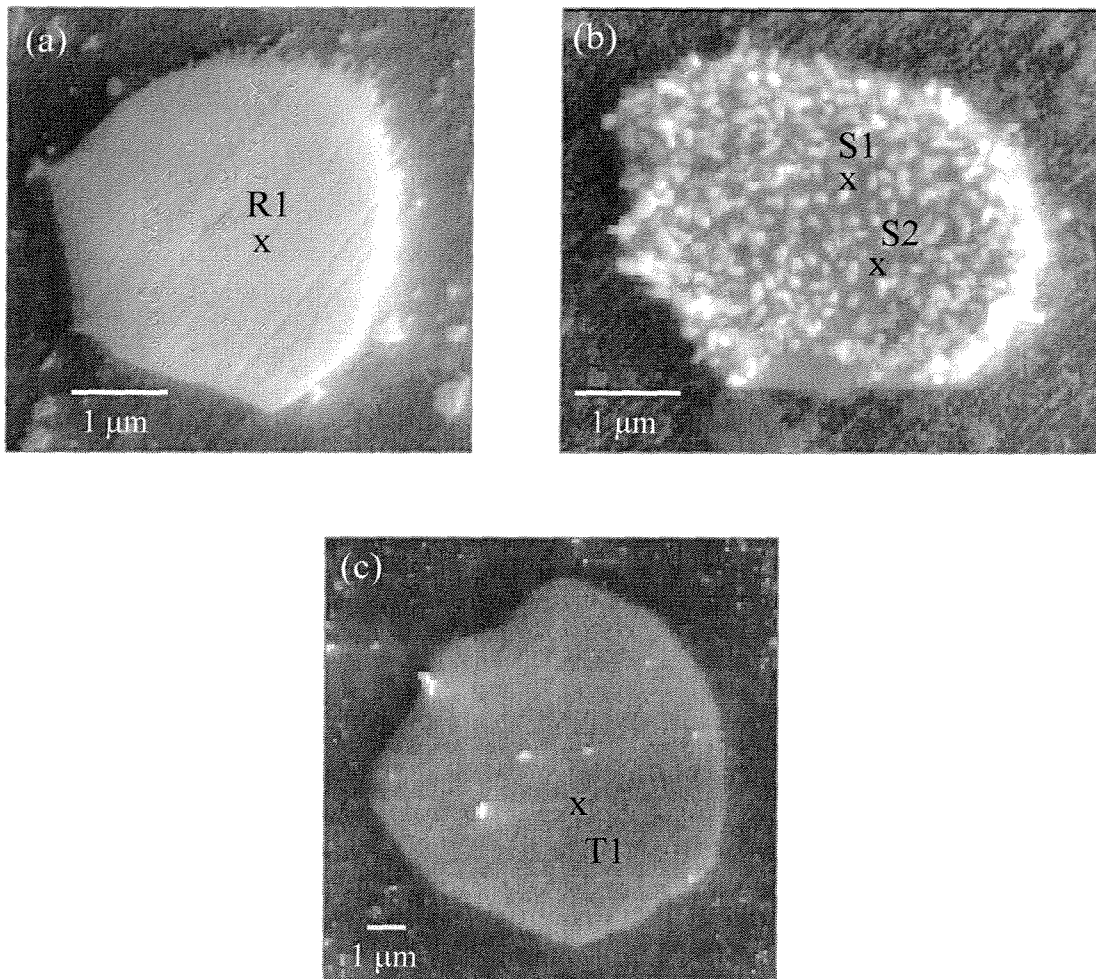


Figure 4.4 SEM micrographs for Al-Cu-Mg second-phase particles on the 2024-Al surface after dipping for 2 min in Ni^{2+} -containing coating solutions at different pH values: (a) 3, (b) 4 and (c) 5.

pH of 5, the alloy is exposed to a less acidic coating solution and there is therefore less dissolution of Mg and Al from the Al-Cu-Mg particle [7], resulting in a lower surface concentration of Cu compared to pH 4. As a result, the Al-Cu-Mg particle is not as cathodic at pH 5 as at pH 4 and there is less coating deposition, resulting in fewer large ZPO crystals. Also, there is less etching at pH 5, resulting in less removal of oxide and hence fewer nucleation sites for coating.

Auger electron spectra were acquired at the regions indicated as R1, S1, S2 and T1 in Figure 4.4, and the coating composition at each region is given in Table 4.3. Metallic Al is not detected from any of the regions, indicating that in each case the coating thickness is greater than the probe depth for the Al KLL signal for all three pH conditions. The Q_{Ni} ratio ($= Ni/(Ni+Zn)$) indicates the amount of Ni in the coating. Figure 4.5 shows values of Q_{Ni} at various microstructural regions for coatings formed from solutions with the different initial pH values. The trend in Q_{Ni} for the Al-Cu-Mg particle (largest Q_{Ni} at pH 5, smallest at pH 4) follows that observed over the macroscopic alloy surface by XPS (Section 4.3.2).

Table 4.3 Elemental atomic percentages from SAM for different regions of the Al-Cu-Mg second-phase particles in ZPO-coated 2024-Al samples shown in Figure 4.4 (2 min treatment with Ni^{2+} -containing solutions at initial pH 3, 4, and 5).[§]

	pH 3	pH 4		pH 5
	R1	S1	S2	T1
Zn	9.5	17.0	14.4	4.5
Cu	- [◇]	†	-	-
Ni	19.4	6.7	12.6	23.0
O	43.8	48.4	41.4	51.4
P	14.2	27.9	21.2	21.2
Al	13.1	†	10.3	-

[§] Values are believed to be accurate to within $\pm 20\%$ as discussed on page 58

[◇] The hyphen indicates that the element is not detected

[†] Amount detected is less than 0.5% and too small to be measured accurately

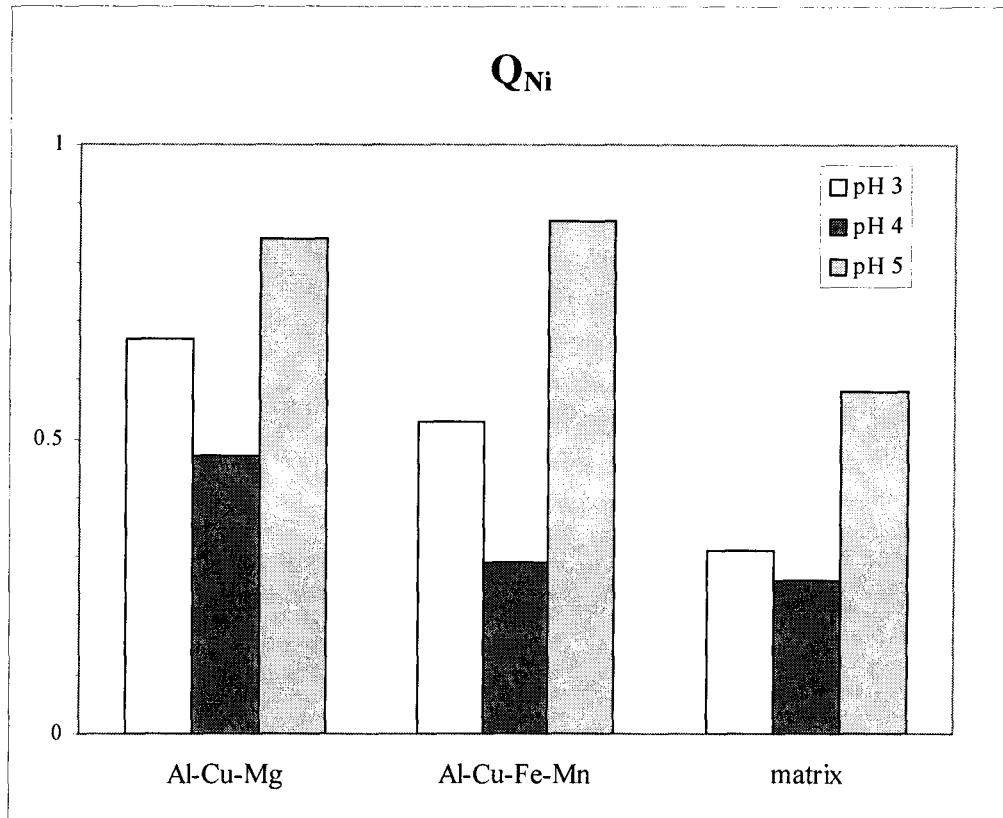


Figure 4.5 Graphical representation of elemental compositions from SAM at different microstructural regions for coatings formed from ZPO solutions containing 2,000 ppm Ni^{2+} at different starting pH values.

For the pH 4 coating (Figure 4.4(b)), the Q_{Ni} ratio is greater at the darker region on the Al-Cu-Mg particle (S2: 0.47) compared to the larger crystal (S1: 0.28), but it is difficult to determine the chemical form of Ni from the Auger spectrum. The most intense Ni LMM peak is at 845.1 eV from the darker region and 845.7 eV from the larger crystal, and the presence of metallic Ni (846.2 eV) cannot be ruled out. A possible explanation for the increased presence of Ni at the darker area, compared to the large crystal, could involve the existence of pores, or uncoated areas, in the coating (e.g. at the nm scale) which remain on the surface after phosphating. In these pores, Al etching may couple with Ni^{2+} reduction, similar to a proposal by Ogle *et al.* for the phosphating of galvanized steel [88]. Alternatively the original oxide layer may dissolve in the acidic solution and then re-form with Ni^{2+} incorporated into the new oxide. Since $NiAl_2O_4$ but not Ni metal is consistent with the XPS observations (Section 4.3.2.2), the second explanation is favored. This may contribute to a “sealing” of the coating, since the Ni-rich oxide has increased resistance to corrosion [83]. More $NiAl_2O_4$ would be expected at the darker region than at the large crystal since the oxide layer will re-form at sites where the alloy substrate is exposed. The increased Ni at the darker area may also be due in part to the presence of nickel phosphate, although there is no definite evidence at this point.

4.3.3.1.2 Al-Cu-Fe-Mn Second-Phase Particle

Figure 4.6(a)-(d) shows SEM images of Al-Cu-Fe-Mn intermetallic particles (irregular regions) on ZPO-coated surfaces, where the initial pH of the coating solution was adjusted to 3, 4 and 5 (2 min coating). The area surrounding the Al-Cu-Fe-Mn intermetallic particle in Figure 4.6(a)-(c) is the alloy matrix. The bright areas on the particles in Figure 4.6(b)-(c) are ZPO coating crystals. It is evident that there are more ZPO crystals on the Al-

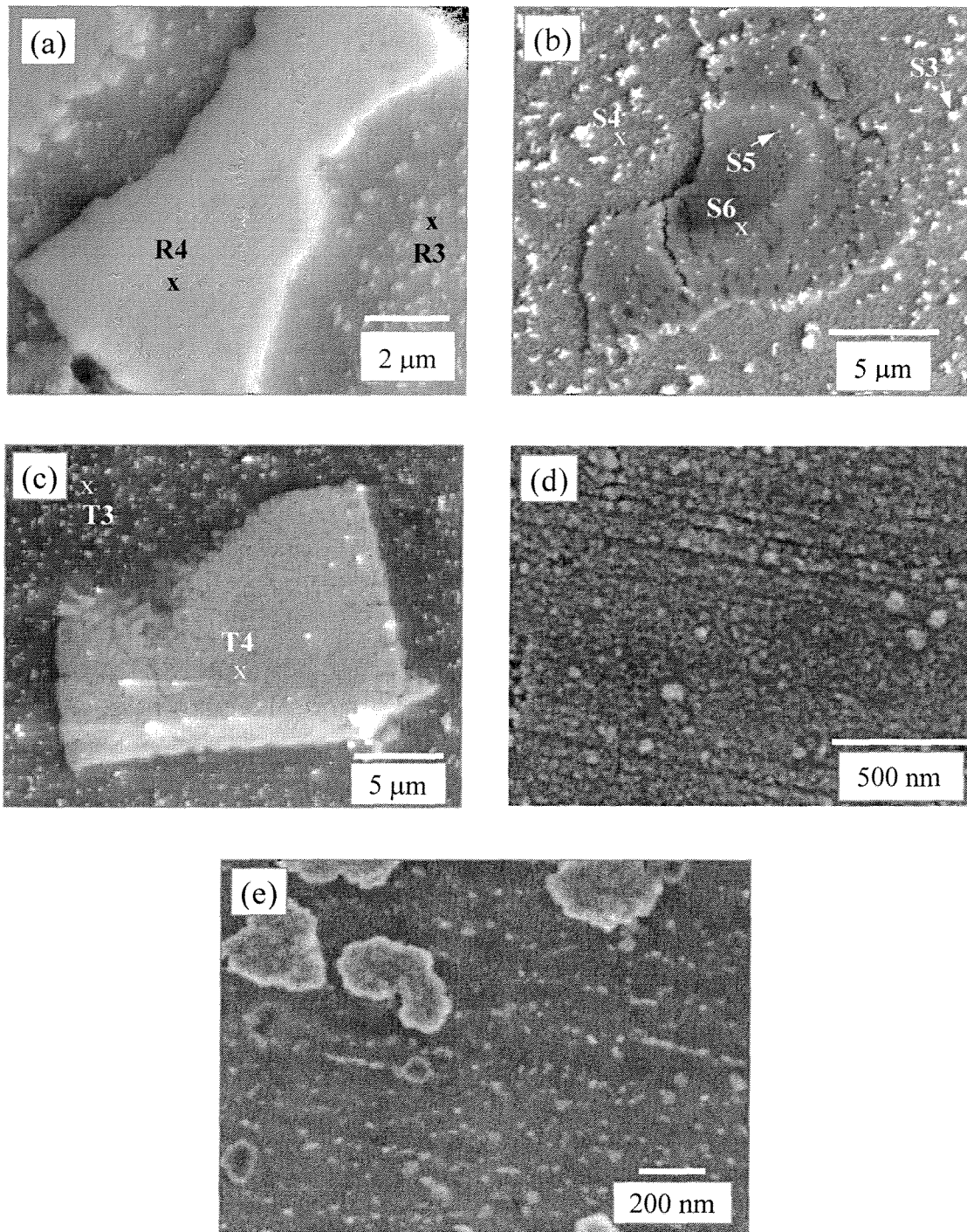


Figure 4.6 SEM micrographs showing Al-Cu-Fe-Mn second-phase particles surrounded by the matrix region on a 2024-Al surface after dipping for 2 min in Ni^{2+} -containing coating solutions at different pH values: (a) 3, (b) 4, (c) 5, (d) 4 (image of Al-Cu-Fe-Mn surface at higher magnification), and (e) 4 (image of matrix region at higher magnification).

Cu-Fe-Mn particle coated at pH 4 compared to coating at pH 5, where there are few large ZPO crystals, or at pH 3 where no crystals are observed. This trend is similar to that observed for the Al-Cu-Mg particle (Section 4.3.3.1.1) and for the overall alloy surface (Section 4.3.2). The surface of the Al-Cu-Fe-Mn particle coated at pH 4 is shown in Figure 4.6(d) at high magnification. Smaller coating particles cover the surface, demonstrating that coating is present on the darker regions of the Al-Cu-Fe-Mn particle (e.g. S6 in Figure 4.6(b)). The SAM analysis also confirms the presence of coating at the darker areas.

Table 4.4 Elemental atomic percentages from SAM for different regions of the Al-Cu-Fe-Mn second-phase particles in ZPO-coated 2024-Al samples shown in Figure 4.6 (2 min treatment with Ni²⁺-containing solutions at initial pH 3, 4, and 5).[§]

	pH 3	pH 4		pH 5
	R4	S5	S6	T4
Zn	13.5	34.2	23.3	4.8
Cu	- [◊]	-	3.9	-
Ni	15.0	8.4	9.6	31.0
O	54.3	50.5	41.7	38.8
P	4.4	6.9	9.2	25.4
Al	12.6	-	12.4	-

[§] Values are believed to be accurate to within ±20% as discussed on page 58

[◊] The hyphen indicates that the element is not detected

Results of SAM analyses at the regions indicated in Figure 4.6 are shown in Table 4.4. Metallic Al is not detected at any of the regions R4, S5, S6 or T4, indicating that the coating is thicker than the probe depth (Al KLL signal) at the Al-Cu-Fe-Mn particle for all three starting pH conditions. The trend in Q_{Ni} (Figure 4.5) for the Al-Cu-Fe-Mn particle (largest Q_{Ni} pH 5, smallest pH 4) is similar to that observed over the macroscopic alloy surface by XPS (Figure 4.3(b)) and to that observed for the Al-Cu-Mg particle (Figure 4.5).

Given that P and O are the only anionic elements detected (Table 4.4), the Q_P ratio ($= (Zn+Ni)/P$) gives information regarding whether Zn and Ni are present in the form of tertiary phosphate (e.g. $Zn_3(PO_4)_2$, $Q_P = 1.5$), secondary phosphate (e.g. $ZnHPO_4$, $Q_P = 1$), or oxide (e.g. ZnO , $Q_P = \infty$). For the optimum pH (4), the Q_P ratio is higher for the ZPO coating on the Al-Cu-Fe-Mn particle (S6: 3.6) compared to the Al-Cu-Mg particle (S2: 1.3), indicating that there is less phosphate present at the Al-Cu-Fe-Mn particle. This may be a consequence of the initial oxide on the Al-Cu-Fe-Mn particle being more resistant to etching compared to oxides on other microstructural areas. Also, there may be a lower etching rate at the Al-Cu-Fe-Mn particle compared to the Al-Cu-Mg particle due to a lower concentration of Mg (dissolves easily) in the Al-Cu-Fe-Mn particle. The etching rate is slower at the Al-Cu-Fe-Mn particle compared to the matrix due to a higher concentration in the Al-Cu-Fe-Mn particle of alloying elements more noble than Al. Either way the resultant pH rise at the local cathodic sites is likely to be slower on the Al-Cu-Fe-Mn particle and, with less PO_4^{3-} present, ZnO precipitation becomes more favored over ZPO.

SAM measurements were also carried out for samples which had been immersed in the coating solution for a shorter time (30 s) than that required to form a full coating (2 min), in order to get information at an earlier stage of coating. SEM images and data from SAM are not reported explicitly for the coatings formed by 30 s immersion, but reference is made to these analyses where relevant. Q_P increases from 2.0 to 3.6 (S6) at the darker area on the Al-Cu-Fe-Mn particle as the coating time increases from 30 s to 2 min, implying that there is less ZnO precipitation in the early stage of coating compared to the later stage. Some phosphate precipitates in the earlier part of the process but, as the surface becomes coated, the rate of etching (slower compared to other microstructural regions) decreases while acidic solution from the bulk of the coating bath diffuses to the solution-metal interface, lowering

the local pH. This results in the precipitation of ZnO as opposed to phosphate during the later stages of coating. Measurements at a larger crystal on the Al-Cu-Fe-Mn particle (e.g. S5) also indicate an increase in ZnO between 30 s and 2 min, and a predominance of ZnO at the Al-Cu-Fe-Mn particle for the full coating.

4.3.3.1.3 Matrix

The alloy matrix (area surrounding second-phase particles in Figures 4.4 and 4.6) is covered by bright areas that are composed of ZPO crystals. Figure 4.6(e) shows a high magnification image of the matrix after the alloy was dipped for 2 min in a Ni²⁺-containing ZPO solution at pH 4. Coating particles on the matrix are less tightly packed than ZPO particles on the Al-Cu-Fe-Mn intermetallic (Figure 4.6(d)). This is most likely due to a larger concentration of cathodic sites (at which coating precipitation occurs) on the intermetallic. Large crystals (dimension ~0.25 μm) are present on the matrix but not on the Al-Cu-Fe-Mn particle, apparently due to the faster rate of etching and the smaller concentration of cathodic sites on the matrix. The faster rate of etching causes more electrons to be available for the reduction reaction, which occurs at the cathodic sites. However, since there are fewer cathodic sites, the reduction reaction (causing an increase in pH) occurs on a limited number of sites instead of less extensively at many sites on the surface. An enhanced pH increase at a few sites on the surface results in more ZPO precipitation at those sites compared to the rest of the surface, so giving the large crystals at these few sites.

Figure 4.7 shows Al KLL spectra, specifically at the points designated R3, S4 and T3, corresponding to darker regions on the alloy matrix for samples coated at pH 3, 4 and 5 (Figure 4.6). The main KLL peak occurs at 1393 eV for metallic Al, while the oxide occurs

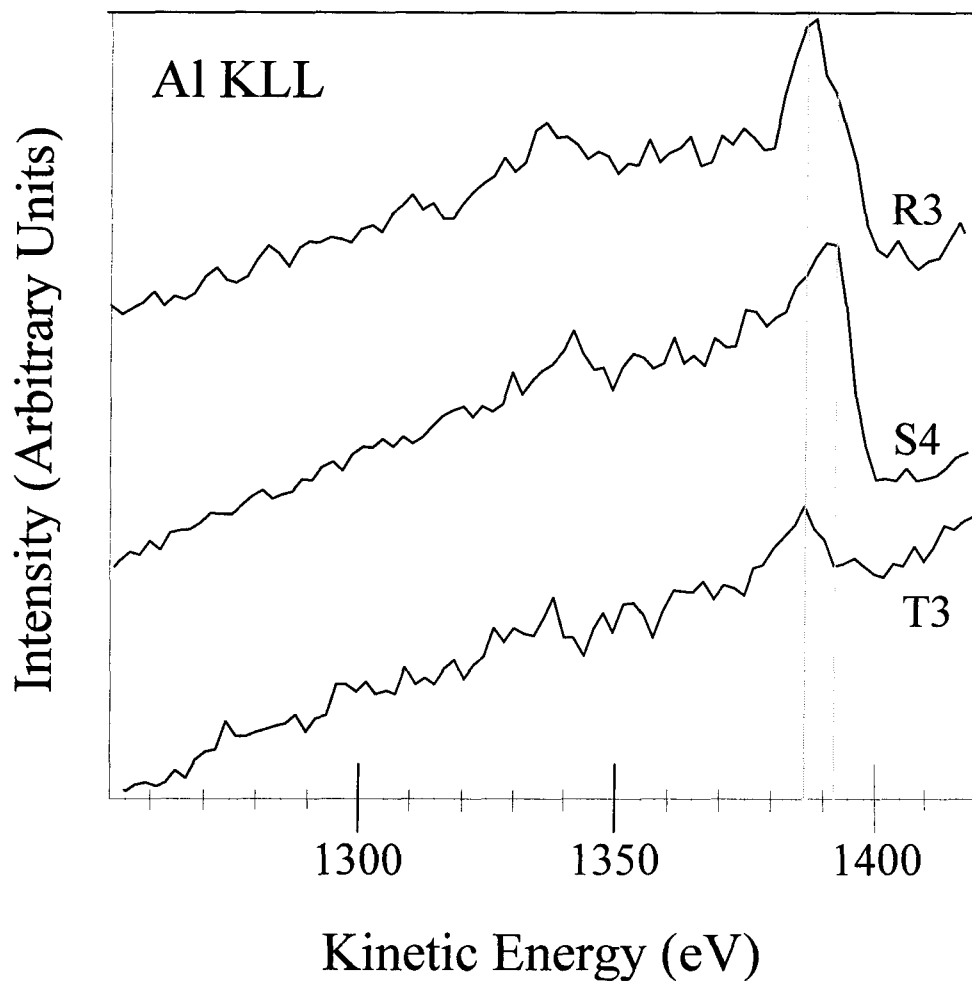


Figure 4.7 Al KLL spectra from dark areas on the matrix region of the 2024-Al surface that has been dipped for 2 min in a Ni^{2+} -containing solution for different pH values: R3 region for pH 3, S4 region for pH 4, T3 region for pH 5.

at 1388 eV [46]. It is evident that metallic Al is detected at pH 4 but not at pH 5, indicating a thicker coating at pH 5, consistent with observations from XPS (Section 4.3.2). For the coating formed at pH 3, the large peak in the Auger spectrum at 1387 eV is likely due to aluminum oxide, apparently with a shoulder associated with metallic Al. This is consistent with the XPS results where the ratio of Al^{3+} /metallic Al is significantly higher for the coating formed from the solution which starts at pH 3 compared to that for pH 4 (Section 4.3.2). There is only a trace amount of P detected at R3 compared to ~6% at S4 (Table 4.5). Therefore, the darker areas on the matrix at pH 3 appear to be coated less compared to the situation starting at pH 4. XPS indicated that the oxide layer on an uncoated 2024-Al sample is as thick as the entire overlayer (coating plus oxide) for a ZPO-coated sample of 2024-Al. Therefore it seems likely that the large amount of aluminum oxide on the darker areas of the matrix at pH 3 comes from uncoated regions on the alloy surface, consistent with observations from XPS for coated samples (Section 4.3.2.1).

The Q_{Ni} for matrix regions is shown in Figure 4.5. Evidently at darker areas on the matrix Q_{Ni} varies with solution pH in a similar manner as at the Al-Cu-Mg and Al-Cu-Fe-Mn particles. SEM analysis has indicated that when Ni^{2+} is present in the coating solution the Al-Cu-Mg particle becomes more cathodic than Al-Cu-Fe-Mn (Section 4.3.3.2.1). The Al-Cu-Fe-Mn particle is itself cathodic to the matrix [104]. As indicated in Figure 4.5, Q_{Ni} for pH 3 increases in the order: matrix < Al-Cu-Fe-Mn < Al-Cu-Mg, in the same order as for pH 4. This indicates that the amount of Ni increases with the degree of cathodicity. XPS indicates that nickel phosphate (perhaps mixed with ZPO e.g. $\text{Zn}_x\text{Ni}_{3-x}(\text{PO}_4)_2$) deposits and/or a mixed Ni-Al oxide (e.g. NiAl_2O_4) forms during the later stages of phosphating (Section 4.3.2). Formation of such an oxide has been reported to occur especially at cathodic sites on 2024-Al in another context [83]. Therefore the larger amount of Ni observed at

Table 4.5 Elemental atomic percentages from SAM for different regions of the matrix in ZPO-coated 2024-Al samples shown in Figure 4.6 (2 min treatment with Ni²⁺-containing solutions at initial pH 3, 4, and 5).[§]

	pH 3	pH 4		pH 5
	R3	S3	S4	T3
Zn	7.9	14.4	10.3	5.7
Cu	2.1	- [◇]	4.7	-
Ni	3.5	7.6	3.6	17.2
Ca	†	-	-	6.8
O	45.1	49.0	43.0	39.9
P	†	17.4	5.5	22.6
Al	41.4	11.7	32.9	7.8

[§] Values are believed to be accurate to within $\pm 20\%$ as discussed on page 58

[◇] The hyphen indicates that the element is not detected

[†] Amount detected is less than 0.5% and too small to be measured accurately

cathodic sites in this situation is consistent with the presence of NiAl₂O₄. The small Q_{Ni} at the Al-Cu-Fe-Mn particle (pH 4) is due to the significant amount of ZnO precipitation (Section 4.3.2.1), which contrasts with the Zn-Ni phosphate which predominates at the other microstructural regions. For pH 5, the values of Q_{Ni} on the Al-Cu-Mg and Al-Cu-Fe-Mn particles are similar, while its value on the matrix is somewhat less (Figure 4.5). For less acidic conditions, there is a smaller change in nature of the Al-Cu-Mg particle (Section 4.3.3.2.1), resulting in greater electrochemical similarity with the Al-Cu-Fe-Mn particle.

The Q_P ratio indicates there is more phosphate present in the larger crystals on the matrix (S3: 1.3) than in the darker region on the matrix (S4: 2.5) due initially to the higher local pH in the solution above the local sites where the larger crystals form. At the darker regions where the local pH is low, ZnO or ZnAl₂O₄ may form (from analysis of the elemental composition at S4). The bigger Q_{Ni} ratio for the larger crystals (S3: 0.35) compared to the darker regions (S4: 0.26) appears due to greater precipitation of nickel

phosphate in the former case. The larger crystals differ in chemical composition from the darker areas on the Al-Cu-Mg and Al-Cu-Fe-Mn particles as well.

4.3.3.2 Coatings Not Containing Ni²⁺

The coatings described in this Section were formed by dipping 2024-Al samples for 2 min in a ZPO bath which contained no Ni²⁺ and was initially adjusted to pH 4. Comparisons will be made with the coatings formed by immersion for 2 min in Ni²⁺-containing ZPO solutions adjusted to pH 4 (Section 4.3.3.1).

4.3.3.2.1 Al-Cu-Mg and Al-Cu-Fe-Mn Second-Phase Particles

A ZPO-coated Al-Cu-Mg second-phase particle, surrounded by alloy matrix, is shown in Figure 4.8(a), while a ZPO-coated Al-Cu-Fe-Mn particle, with its neighboring alloy matrix, is shown in Figure 4.8(b). The SEM micrographs do not show an obvious difference in the amount of coating on the Al-Cu-Mg particle compared to the Al-Cu-Fe-Mn particle. The local coating is thicker than the SAM probe depth at both particles, and consequently metallic Al is not detected. This contrasts with the situation for the Ni²⁺-containing solution (Figures 4.4(b) and 4.6(b)) where more coating occurs on the Al-Cu-Mg particle (greater degree of coating coverage by larger crystals). The slower coating when Ni²⁺ is present results in the second-phase particles receiving a longer exposure to the acidic solution prior to being covered by the protective coating. This can lead to increased leaching of Mg (especially) and of Al from the particle [7], thereby causing a larger increase in pH above the particle, and also a higher concentration of cathodic Cu sites on the remainder of the Al-Cu-Mg particle. Both of these changes are expected to accelerate the coating

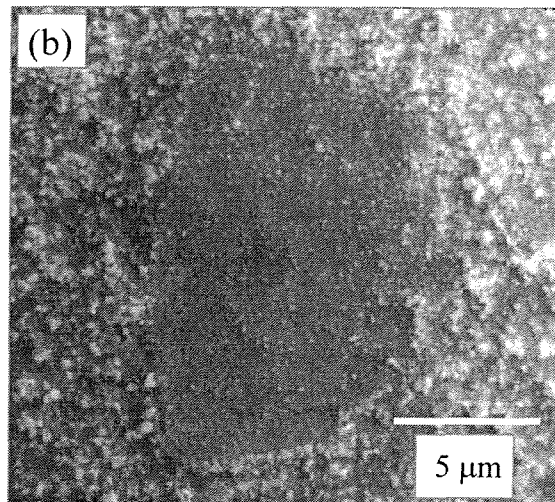
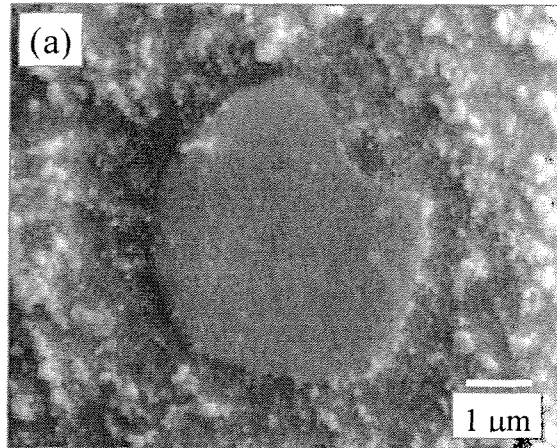


Figure 4.8 SEM micrographs for second-phase particles on the 2024-Al surface after 2 min immersion in the ZPO coating solution with no Ni^{2+} and adjusted to pH 4: (a) Al-Cu-Mg particle; (b) Al-Cu-Fe-Mn particle.

deposition. In the case of the ZPO solution without Ni^{2+} , the coating deposition occurs faster with less Mg dissolution and so less change in the nature of the Al-Cu-Mg particle. This conclusion is consistent with findings from a study of 2024-Al surface intermetallics in NaCl solution. The addition of chromate ions to the solution, causing a Cr-rich coating to form covering the Al-Cu-Mg surface, inhibits Mg dissolution and retards Cu enrichment on the Al-Cu-Mg particles [105] similar to the situation when the ZPO solution does not contain Ni^{2+} .

4.3.3.2.2 Matrix

SAM measurements indicate that after 30 s there is more coating on the second-phase particles than on the matrix. The metallic Al KLL peak (1393 eV) is detected at the matrix but not at the Al-Cu-Mg or Al-Cu-Fe-Mn particles. The SEM micrographs in Figure 4.8 indicate there is more coating on the matrix after 2 min (particularly by larger ZPO crystals) than on the intermetallic particles. In the early stages of coating, the microstructural areas with more cathodic sites become coated the most. In the later stages as the cathodic sites become coated, the relative rates of precipitation are determined by etching at the different sites (this should be faster at the matrix, which contains a higher concentration of anodic sites).

In Section 4.3.2, XPS investigations indicated that ZPO coatings formed at the optimum pH from solutions without Ni^{2+} are thicker than the corresponding coatings formed from solutions containing Ni^{2+} due to faster coating precipitation. SAM confirms this result as indicated by the detection of metallic Al below coatings containing Ni^{2+} but not for coatings where Ni^{2+} is absent. The pattern of coating thickness on different microstructural

areas for solutions containing Ni^{2+} after 2 min (Section 4.3.3.1) is similar to that for solutions not containing Ni^{2+} after 30 s, a direct consequence of faster precipitation in the latter case.

4.3.3.3 Comparison with XPS Observations

The SAM results discussed in this work for coatings formed from solutions containing Ni^{2+} are consistent with the following observations deduced from XPS and described in Section 4.3.2:

- For an initial coating solution pH of 3, 4 and 5, there is more Ni in the coating (Q_{Ni} increases) as the coating time increases from 30 s to 2 min.
- The amount of Ni in the coating, as indicated by Q_{Ni} , is less when the initial solution pH is 3 or 4 compared to pH 5 (both partial and full coatings).
- When the initial solution pH is either 3 or 4, ZnO dominates the partial (30 s) coatings but there is a significant amount of phosphate precipitation between 30 s and 2 min, as indicated by the decrease in Q_{P} .
- When the coating solution starts at pH 5, the partial coatings are dominated by phosphate, as indicated by low values for Q_{P} .
- The measured Q_{P} ratios are consistent with more ZPO deposition during the formation of the full coating from the solution initially at pH 4 compared to starting at either pH 3 or 5.

Unlike the situation with XPS, no conclusions can be drawn by SAM for the presence of F in the coatings, and this is a consequence of the comparatively low sensitivity factor for the F KLL signal. In addition, for the coatings formed from solutions not containing Ni^{2+} , the following trends from SAM are consistent with results from XPS reported in Section 4.3.2:

- Coatings formed from solutions initially at pH 3 and 4 are thicker when Ni^{2+} is not present in the coating solution.
- Alloy samples dipped for 2 min have a thicker coating compared to those dipped for 30 s.
- Significant ZnO deposition occurs between 30 s and 2 min.

4.4 Concluding Remarks

It is clear from this work that the chemical composition of the coating varies significantly depending on the initial pH of the coating solution and whether or not Ni^{2+} has been added. The nature of the coating during any stage of the zinc phosphating process depends on the local pH at the alloy-solution interface. The phosphoric acid, which is a major component of the coating solution, exists in different forms in solution, depending on the pH. At higher pH values, the insoluble tertiary phosphate PO_4^{3-} is favored, and that gives rise to the intended coating. For the conditions considered, a 2 min dip in the unstirred coating bath is sufficient to get a good coverage. At each stage, there are balances. Throughout the aim is to optimize the corrosion protection and paint adhesion by getting the greatest degree of surface coverage by insoluble ZPO crystals.

The results in this chapter show that the Ni^{2+} additive has two main roles in the zinc phosphating process on 2024-Al. First, the rate of increase in local solution pH is limited by the slower kinetics of reactions involving Ni^{2+} compared to Zn^{2+} , leading to thinner ZPO coatings when Ni^{2+} is present in the coating solution. Second, most Ni^{2+} deposition occurs during the later stages of the coating process (i.e. between 30 s and 2 min). This deposition involves the formation of a Ni-rich oxide (referred to as NiAl_2O_4) on the alloy surface and nickel phosphate deposition. XPS and SAM support the presence of NiAl_2O_4 and SAM also indicates that NiAl_2O_4 deposition occurs especially at cathodic sites. Previously it was found

that the addition of Ni^{2+} to the ZPO coating solution caused an improvement in the corrosion resistance of the resulting coatings in spite of an accompanying decrease in coating thickness (Chapter 3). The increased corrosion resistance is most likely due to the presence in coating pores of NiAl_2O_4 , which is more resistant to degradation than aluminum oxide. No evidence has been found for Ni plating, and this behavior therefore appears to contrast with the situation during the phosphating of electrogalvanized steel, for which plating has been postulated [87]. It is expected that Ni^{2+} precipitates in the form of mixed zinc-nickel phosphates ($\text{Zn}_x\text{Ni}_{3-x}(\text{PO}_4)_2$) as this compound has been observed in phosphate coatings on other substrates [68].

Precipitation of coating components is sensitive to the local pH at the alloy-coating interface which varies during the coating process in a different way depending on the starting pH. A thicker coating (more precipitation) results when the starting pH is 5 compared to pH 3 and 4. As far as coating morphology is concerned, the greatest coating coverage in terms of larger crystals (0.2-0.5 μm across) occurs at pH 4.

The XPS observations for the early stages of coating indicate that AlF_3 precipitates first during the coating process. This indicates that F^- incorporates into the coating in addition to its intended role of remaining in solution as AlF_6^{3-} . This is followed by the precipitation of aluminum phosphate. Subsequently a layer of ZnO (perhaps with $\text{Zn}(\text{OH})_2$ and/or ZnAl_2O_4) deposits, followed by precipitation of zinc and nickel phosphates.

SAM gives new information about the composition of ZPO coatings at different microstructural regions. When Ni^{2+} is present in the coating solution, the chemical composition of the coating above the Al-Cu-Fe-Mn particle is different from the coating on the rest of the surface as ZnO rather than ZPO predominates; that is apparently due to the slower etching rate at the Al-Cu-Fe-Mn particle.

The coating pattern (thickness and composition) across the 2024-Al surface differs depending on whether the coating solution contains Ni^{2+} . With Ni^{2+} , the Al-Cu-Mg particles are coated more thickly than the Al-Cu-Fe-Mn particles, while there is no clear difference in the extent of coating when Ni^{2+} is absent. This is a consequence of the slowing of the coating rate caused by 2000 ppm Ni^{2+} , which permits more Mg and Al from the Al-Cu-Mg particle to dissolve, so leaving more local cathodic sites on the surface; in turn this facilitates the coating precipitation. There is some evidence to indicate that when Ni^{2+} is not present in the coating solution, the matrix becomes more thickly coated than the second-phase particles.

Chapter 5

Effect of Mn^{2+} Additive on the Zinc Phosphating of 2024-Al Alloy

5.1 Introduction

Mn^{2+} added to ZPO coating baths improves the corrosion protection provided by the resulting coatings on steel [64] and zinc-coated steel [106]. The adhesion of a primer to the ZPO coating is also improved in the latter context [106,107], where the addition of Mn^{2+} reduces the coating crystal size more than is the case with Ni^{2+} [68]. Studies have also been carried out for zinc-coated steel to investigate ZPO coating dissolution under alkaline conditions, where Mn^{2+} has a favorable role [88].

The present chapter aims to learn about the effect of Mn^{2+} additive in ZPO-coating baths, applied to the 2024-Al alloy. The emphasis here is on the effects of immersion time and Mn^{2+} concentration in the ZPO solution on the resulting coatings with regard to morphology and composition. The investigation uses scanning electron microscopy (SEM) to assess surface topography, and X-ray photoelectron spectroscopy (XPS) and scanning Auger microscopy (SAM) for surface chemical analysis. This chapter also compares the effects of Ni^{2+} and Mn^{2+} on ZPO coatings formed on the 2024-Al alloy, which contains second-phase particles of the Al-Cu-Mg and Al-Cu-Fe-Mn types (described in Chapter 1). The microanodic or microcathodic behaviors exhibited by these particles (relative to the matrix) influence the coating deposition, and this chapter describes how coating patterns at the surface microstructure vary depending on the additive.

5.2 Experimental

Square samples ($1 \times 1 \text{ cm}^2$) of commercial 2024-Al alloy were mechanically polished with aluminum oxide sandpaper (up to 1200 grit); some other samples were additionally polished by diamond paste to give a mirror finish ($\sim 1 \text{ }\mu\text{m}$ roughness), and this was needed to assess coatings at the microstructural level. After polishing, all samples were ultrasonically cleaned in acetone and methanol. One L of the water-based ZPO solutions (designed specifically for coating of Al) contained: 10.8 mL of 85% H_3PO_4 , 1.24 g ZnO, and 1.11 g NaF plus varying amounts of Mn^{2+} (as $\text{Mn}(\text{NO}_3)_2$) in the 0 to 2500 ppm range (where ppm = mg/L). Comparison was made with Ni^{2+} -containing coating baths where the same solution was used except that 2000 ppm Ni^{2+} (9.91 gL^{-1} of $\text{Ni}(\text{NO}_3)_2 \cdot 6\text{H}_2\text{O}$) were added instead of 2000 ppm Mn^{2+} (9.79 gL^{-1} of $\text{Mn}(\text{NO}_3)_2 \cdot 5\text{H}_2\text{O}$). Coatings were formed by immersing the alloy samples in such solutions at 60°C , conditions that are similar to those recommended for use with the Gardobond R2600 commercial phosphating solution. Before immersion the solution pH was adjusted (using NaOH) to the range 3.8-4.0 reducing the amount of free acid to minimal levels. Each coating treatment was completed by washing the sample in deionized water and drying in argon.

XPS spectra were measured with a Leybold MAX200 spectrometer using the $\text{MgK}\alpha$ source (1253.6 eV) operated at 15 kV, 20 mA. Auger point analyses and the associated SEM characterizations were performed with the primary electron beam set at 10 keV and 3 nA. Other SEM micrographs were obtained using a Hitachi S-3000N instrument, with the incident beam accelerated through either 5 or 20 kV depending on the probe depth desired for the particular sample [108].

5.3 Results and Discussion

5.3.1 Growth of Coating

5.3.1.1 Characterizations with XPS

Figure 5.1 shows Al 2p, Mn 2p and Zn 2p spectra measured from 2024-Al samples immersed for different times in ZPO solutions containing Mn^{2+} . For the Al 2p spectra, the peak at higher binding energy is due to the presence of Al^{3+} , while that at lower binding energy corresponds to metallic Al (from the alloy substrate). The decrease in the peak for metallic Al, and the increase in the Zn and Mn peak intensities, as the coating time increases from 15 s to 60 s, implies an increase in coating thickness. The largest XPS signals for Zn, Mn and P, and the smallest metallic Al signal, occur for the sample immersed in the coating bath for 180 s, which helps to identify the optimal coating time.

The Mn $2p_{3/2}$ binding energy is in the range 642.0-642.2 eV, and essentially constant with immersion time. This is consistent with the reported binding energies for manganese phosphate (642.0 eV [109] and 641.8 eV [110]), although strictly on binding energies alone we cannot rule out the presence of MnAl_2O_4 (reported at 641.5 eV [111]), MnO (641.0 eV [112] and 641.5 eV [113]), or MnF_2 (642.7 eV [113]). However, MnF_2 is not expected since the concentrations of Mn^{2+} and F^- in the coating solution are not high enough to exceed its solubility product (5.1×10^{-3} at 25°C [114]).

The chemical compositions of the ZPO coatings, according to XPS, are reported in Table 5.1. The raw data show the presence of C that arises from atmospheric contamination and sample handling, but this is excluded from the comparisons in Table 5.1. Also excluded is Cu, the main alloying element in 2024-Al, which is detected in trace amounts (<0.3%) only from the surface that had been immersed in the coating bath for 15 s. F precipitates in the form of AlF_3 during the early stages of coating and therefore is found in close proximity

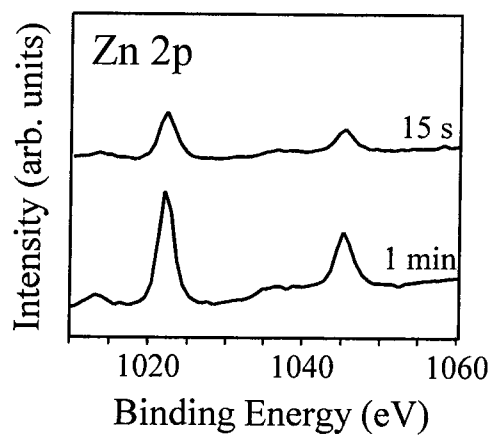
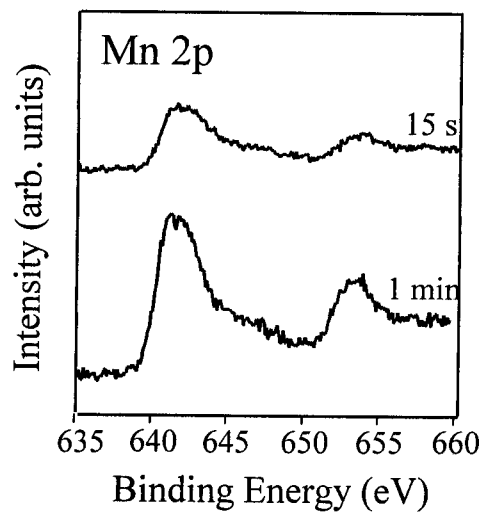
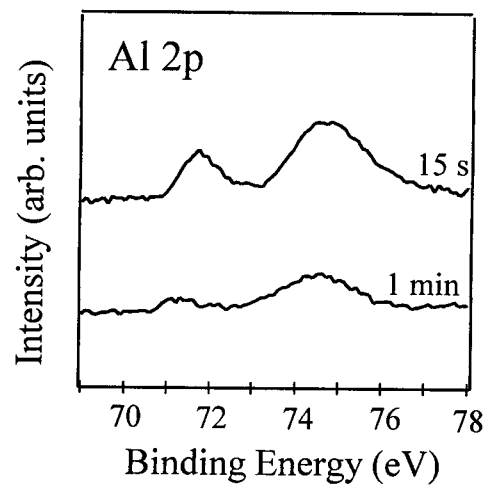


Figure 5.1 Al 2p, Mn 2p and Zn 2p spectra for 2024-Al surfaces dipped for 15 s and 60 s in ZPO solutions containing 2000 ppm Mn^{2+} .

Table 5.1 Elemental atomic percentages measured by XPS from 2024-Al alloy after dipping for varying times in the ZPO coating solution which contains Mn^{2+} (see text).[§]

	15 s	60 s	120 s	180 s	300 s
Zn	4.7	8.7	9.8	9.8	6.4
Mn	2.5	4.5	4.4	5.1	4.0
O	66.4	70.0	68.8	69.0	72.3
P	8.2	13.3	14.3	16.1	13.8
Al	15.6	2.7	2.0	†	2.3
F	2.5	0.8	0.9	†	1.2

[§] Values are believed to be accurate to within $\pm 10\%$ as discussed on page 29

† Amount detected is less than 0.5% and too small to be measured accurately

to the alloy surface (as described in Chapter 4). For the sample immersed for 180 s, the coating is too thick for Al and F to be observed by XPS, but at 300 s both Al and F reappear, and less Zn, Mn, and P are detected (compared with 180 s); these observations indicate a reduction in the coating after 300 s, which reflects the dynamic nature of the coating process. It appears that during its later stages, when most of the alloy surface is covered with ZPO, the etching rate decreases as less metal is exposed to the acidic coating solution. This reduces the supply of electrons for H^+ reduction, and hence lowers the driving force for the pH to increase at the alloy-solution interface. In turn, the pH decreases at the interface, as a result of diffusion from the bulk solution and dissolution occurs for the ZPO coating.

The amount of Mn in the coating, relative to Zn, is indicated by the $Mn/(Zn+Mn)$ ratio, which remains constant at about 0.34 as the coating time increases from 15 s to 180 s. There is less Mn than Zn in the coating even though the concentration of Mn^{2+} in the coating solution is approximately twice that of Zn^{2+} . This is believed to be a consequence of the relatively slow kinetics for ligand substitution reactions involving Mn^{2+} in solution (compared to Zn^{2+}) [100], which has been specifically confirmed by measurements for ZPO

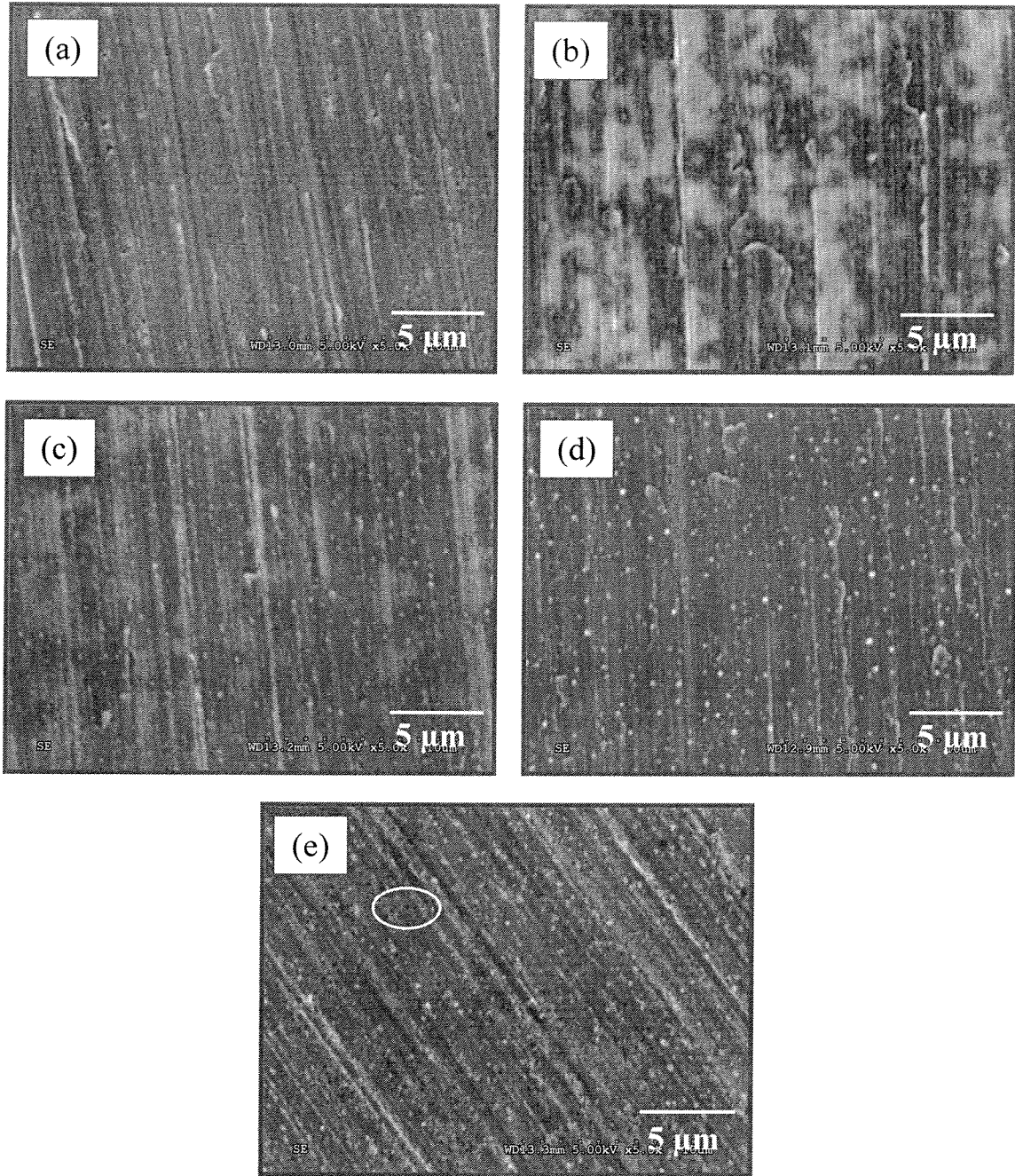


Figure 5.2 SEM micrographs (incident beam 5 kV) from 2024-Al surfaces dipped for increasing times in ZPO coating solutions at 60 °C containing 2000 ppm Mn^{2+} : (a) 15 s, (b) 60 s, (c) 120 s, (d) 180 s and (e) 300 s (pits on surface are circled).

solutions involving the presence of Mn^{2+} (Section 5.3.2). Basically the metal ions in solution form a series of complexes with the H_2PO_4^- , HPO_4^{2-} and PO_4^{3-} ions [110], and as the pH increases the involvement of PO_4^{3-} increases over that of the other phosphate ions. Complexes between PO_4^{3-} and the metal cations are precursors to phosphate precipitation, but the slower kinetics for Mn^{2+} complexes results in the slower precipitation of tertiary phosphate at the alloy-solution interface during the coating process.

5.3.1.2 Coating Morphology

Figure 5.2 shows SEM micrographs from coatings formed by immersing 2024-Al samples for different times in ZPO solutions containing Mn^{2+} . After 15 s coating only a few crystals can be observed on the surface, although XPS analysis (Table 5.1) indicates that an appreciable amount of ZPO has precipitated. The surface of the alloy after dipping in the coating solution for 120 s (Figure 5.2(c)) indicates the presence of fine coating crystals (round white areas). The absence of a metallic component in the XPS Al 2p spectrum indicates that this coating must provide a complete coverage, and therefore it can be concluded that most of the precipitated particles are too small to be seen in the micrograph.

Dark and light patches are observed on the alloy surfaces dipped for 60 and 120 s (Figure 5.2(b),(c)). SEM analysis at higher magnification indicates that coating particles are present on both the dark and light regions (120 s coating), and this is confirmed by SAM which also indicates that more Zn and Mn are present on the dark patches compared to the light patches. This is believed to originate with non-uniform etching when the alloy is immersed in the coating bath. In particular, given that imaging with the 5 kV electron beam is expected to emphasize especially the near-surface regions of the material [108], it is

possible that the light areas correspond to larger amounts of unetched aluminum oxide which act to hinder the cathodic reactions, so resulting in less coating deposition.

The coating crystals are more prominent (brighter in SEM images) for the immersion for 120 s (Figure 5.2(c)) compared to 60 s (Figure 5.2(b)), and there is a further increase at 180 s (Figure 5.2(d)), implying more precipitation with increase in coating time. This is consistent with the enhanced coating thickness determined by XPS; also, the small pits on the surface of the 300 s sample (black spots, dimension $\sim 0.2 \mu\text{m}$, circled in Figure 5.2(e)) indicate dissolution consistent with the chemical data noted in Section 5.3.1.1.

5.3.2 Effect of Mn^{2+} Concentration

5.3.2.1 Coating Topography

SEM micrographs of the coatings formed on 2024-Al from solutions containing different amounts of Mn^{2+} (0-2500 ppm) are shown in Figure 5.3. As the Mn^{2+} concentration in solution increases from 0 to 500 ppm, both the average crystal size and the degree of coating coverage decrease. The parallel lines visible in the images (especially at higher Mn^{2+} concentrations) were created during the polishing process. Their prominence underscores the small coating crystal size in comparison to the size of the polishing grooves. At 2000 ppm some fine crystals are visible but the absence of a metallic Al signal in the X-ray photoelectron spectrum indicates that the surface is completely covered with ZPO coating. Therefore, it seems that many of the crystals present are not prominent in the SEM images. The presence of Mn^{2+} in the coating solution at the alloy surface may provide extra nucleation sites (in addition to Zn^{2+} species present) for phosphate precipitation, reducing the average crystal size.

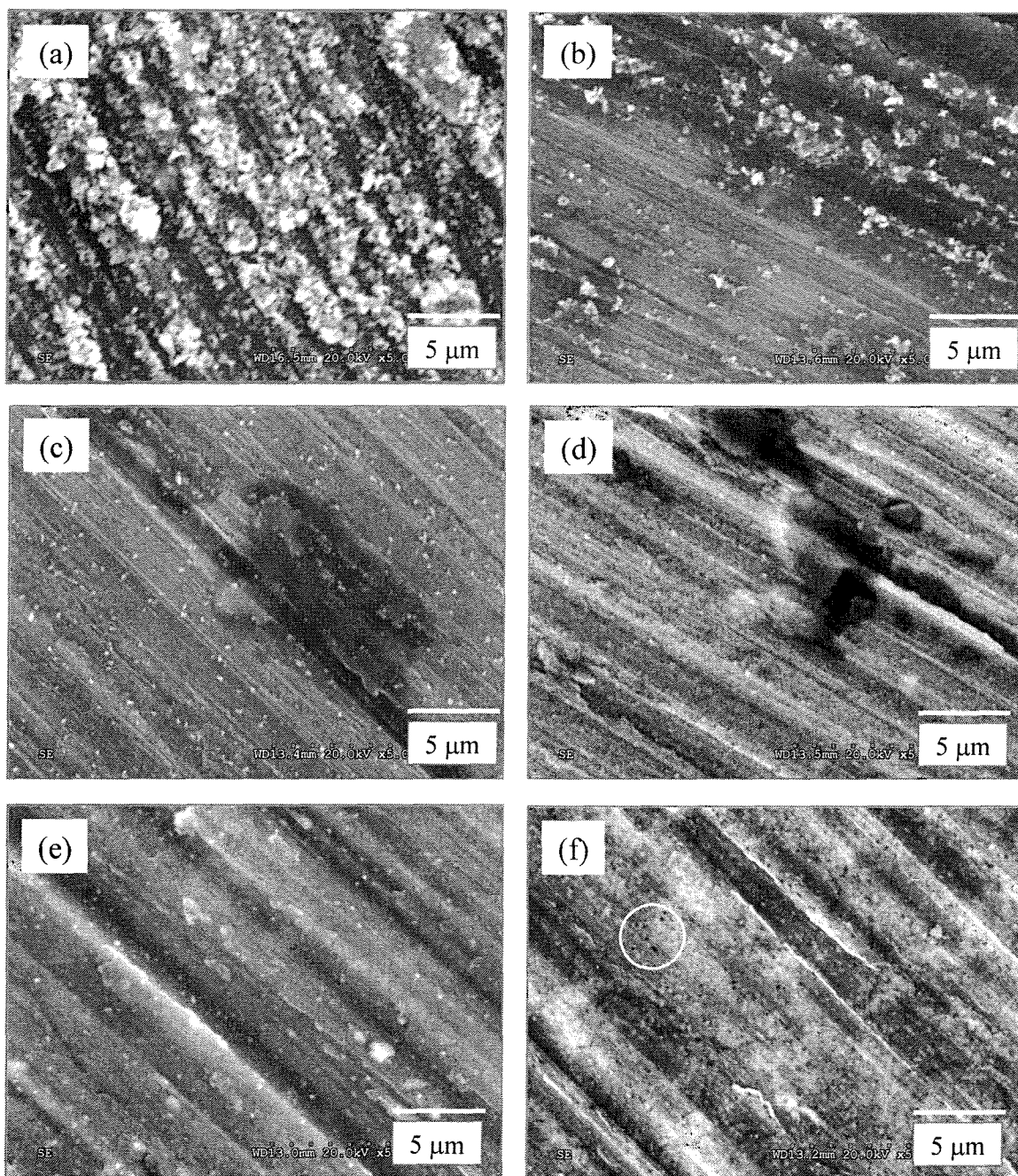


Figure 5.3 SEM micrographs from ZPO-coated (3 min dip time) 2024-Al surfaces. The coating solutions contain increasing amounts of Mn^{2+} : (a) 0, (b) 100, (c) 500, (d) 1000, (e) 2000, (f) 2500 ppm.

Some areas on the surface coated with 100 ppm Mn^{2+} (Figure 5.3(b)) have larger coating crystals, resembling the coating produced when no Mn^{2+} is present in the coating solution (Figure 5.3(a)). Other parts of the 100 ppm Mn^{2+} coating have a smaller degree of coating coverage. The Mn^{2+} hydrolysis equilibrium can be written as $\text{MnL}_n(\text{H}_2\text{O})^{2+} + \text{H}_2\text{O} \leftrightarrow \text{MnL}_n\text{OH}^+ + \text{H}_3\text{O}^+$, where L represents a coordinating ligand. The equilibrium constant is approximately 10^{-10} (when $\text{L} = \text{H}_2\text{O}$ [103]) and that has the consequence that a shift to the right-hand side only becomes significant at higher pH values. This hydrolysis increases the acidity, which is relevant to the coating process because a greater degree of H^+ consumption will be necessary before solutions containing Mn^{2+} give ZPO deposition than is the case for solutions that do not contain this additive. At some surface regions (on the alloy coated in the 100 ppm Mn^{2+} solution), there is only sufficient H^+ consumption to yield a small amount of precipitation, resulting in a lower degree of coating coverage.

There are pits (dark spots) on the surface of the alloy sample coated in a ZPO solution containing 2500 ppm Mn^{2+} (some of the pits are within the circle in Figure 5.3(f)). The rate of coating precipitation is higher at 2500 ppm compared to lower Mn^{2+} concentrations, resulting in the surface becoming coated more quickly. Consequently there is less uncovered metal and less alloy etching, which in turn reduces the rate of local pH increase. Diffusion of H^+ ions from the bulk of solution to the coating-solution interface causes the pH to decrease, and the pH increase caused by etching is not sufficient to counteract the effect of H^+ diffusion. Therefore, dissolution of the coating and pitting in the coating and/or substrate results.

Dark and light patches have been observed on a number of coated samples. The region near the centre of Figure 5.3(c) approximately $10 \mu\text{m} \times 5 \mu\text{m}$ in size is a dark patch. Similar patches of varying size are observed on the coated surfaces in Figure 5.3 parts (b)

and (f). The dark and light patches correspond to smaller and larger amounts of Al oxide respectively (Section 5.3.1). The dark regions in Figure 5.3(d) are pits formed where second-phase particles have dissolved.

5.3.2.2 Chemical Analysis

No detection of metallic Al by X-ray photoelectron spectroscopy (XPS) indicates that the coating is thicker than the probe depth of the technique (~10 nm). Metallic Al is not detected for 0, 100, 2000, or 2500 ppm Mn^{2+} ; however, it is present at 500 and 1000 ppm. The greater Mn^{2+} concentration in the 2000 and 2500 ppm coating solutions compared to 500 and 1000 ppm causes more manganese phosphate precipitation, resulting in thicker coatings. Further experiments were carried out to develop an understanding of why the coatings at 500 and 1000 ppm are thinner compared to those with no Mn^{2+} . Measurements were made for two initial ZPO coating solutions, one with no Mn^{2+} and the other with 2000 ppm Mn^{2+} (a large Mn^{2+} concentration was used to make the two solutions sufficiently different in composition). The pH was monitored as fixed volumes of the coating solutions were titrated with NaOH. Each system was allowed to reach equilibrium (indicated by a stable pH) after each addition of NaOH. It was observed that the solutions took longer to respond to the addition of NaOH when Mn^{2+} was present in the coating solution compared to the solution with no added Mn^{2+} . It is considered likely that the slower response observed when Mn^{2+} is present in the coating solution also occurs during the coating process when the local pH at the alloy-solution interface increases. The slow adjustment to increases in pH results in less precipitation since that occurs when the system has adjusted to higher pH conditions. Less precipitation in turn results in a thinner coating (500 and 1000 ppm coating solutions). Mn^{2+} causes two opposing effects for solutions containing larger amounts of the ion (2000, 2500

ppm): sluggish solution kinetics involving Mn^{2+} slow the rate of precipitation, but the large Mn^{2+} concentration increases the driving force for precipitation.

As discussed previously, SEM images indicate that the coating morphology on parts of the 100 ppm-coated surface is similar to the surface coated with no Mn^{2+} . Additionally, the non-detection of metallic Al from both of these coatings implies that they are generally thicker than the overlayers formed from the 500 and 1000 ppm coating solutions. This is most probably due to the presence of larger coating crystals in the 0 and 100 ppm coatings. The thicker coating at 500 compared to 1000 ppm (reflected in the smaller metallic Al peak at 500 ppm) may be due to slightly larger coating crystals at 500 ppm.

Table 5.2 Elemental atomic percentages from XPS for 2024-Al samples after coating (3 min dip time) in ZPO solutions which differ in the Mn^{2+} concentration, varying from 0 to 2500 ppm.[§]

	0	100	500	1000	2000	2500
Zn	26.5	15.5	13.1	9.4	7.6	6.5
Cu	- [◇]	†	†	†	†	0.7
Mn	-	-	1.2	1.8	4.3	5.0
O	64.1	70.2	63.1	61.8	70.3	71.8
P	9.5	11.8	8.7	8.8	14.5	11.6
Al*	-	1.7	9.9	15.1	2.1	3.6
F	-	†	4.1	3.0	0.9	0.8

[§] Values are believed to be accurate to within $\pm 10\%$ as discussed on page 29

[◇] The hyphen indicates that the element is not detected

[†] Amount detected is less than 0.5% and too small to be measured accurately

* Includes both metallic Al and Al^{3+}

Table 5.2 reports elemental composition information measured by XPS from 2024-Al samples coated in ZPO solutions with different Mn^{2+} concentrations. The $Mn/(Mn+Zn)$ ratio for the coating steadily increases as the Mn^{2+} concentration in the solution varies from 100 to 2500 ppm (values for the ratio equal 0, 0.09, 0.16, 0.29, 0.36, and 0.44 for Mn^{2+} concentrations of 100, 500, 1000, 1500, 2000, and 2500 ppm respectively). The amount of

Mn^{2+} compared to Zn^{2+} in the coating is less than their respective amounts in the coating solution (molar concentrations of Mn^{2+} in the coating solutions are 0.002, 0.009, 0.018, 0.027, 0.036, and 0.046 M for ppm concentrations of 100, 500, 1000, 1500, 2000, and 2500 respectively, while the Zn^{2+} molar concentration is 0.015 M). This is due to the slower Mn^{2+} solution kinetics in response to increases in solution pH, which results in less Mn^{2+} precipitation.

5.3.3 Comparison of Effects of Mn^{2+} and Ni^{2+}

5.3.3.1 Macroscopic Analysis

Chapters 3 and 4 described investigations of the effect of Ni^{2+} on the zinc phosphating of 2024-Al alloy. The ZPO coatings formed from baths with Ni^{2+} additive, and with Mn^{2+} , are both thinner than that formed from an equivalent ZPO coating bath that does not include these additives. The rate of increase in solution pH at the alloy surface is slowed by the sluggish solution kinetics of Ni^{2+} and Mn^{2+} ions compared to Zn^{2+} (verified experimentally (Sections 4.3.2.3 and 5.3.2)), leading to less precipitation and thinner coatings when either Ni^{2+} or Mn^{2+} is present. The intensities of the Al 2p metallic components indicate that the ZPO coating with Mn^{2+} in the coating solution is thicker than that with Ni^{2+} present. The greater precipitation of manganese phosphates compared to nickel phosphates has also been observed for the phosphating of steel, where the ZPO solution contained approximately equal amounts of Ni^{2+} and Mn^{2+} , yet the coating formed had more of the latter [88]. This is believed to relate to the relative solubilities of the zinc and manganese phosphates.

SEM images of coatings formed on 2024-Al from solutions of differing composition are shown in Figure 5.4, where the sizes of the coating crystals can be compared with the situation where neither Ni^{2+} nor Mn^{2+} are added to the coating solution (Figure 5.4(a)). The crystals are clearly smaller when either the Ni^{2+} (Figure 5.4(b)) or Mn^{2+} (Figure 5.4(c)) additive is present in the coating bath. For the concentrations stated, the number of metal cations in the solution without Ni^{2+} or Mn^{2+} is least, apparently resulting in fewer nucleation sites and larger crystals. Additionally, the presence of the Ni^{2+} additive (Figure 5.4(b)) causes larger coating crystals than is the case with Mn^{2+} (Figure 5.4(c)). XPS data indicate that during the early stages of coating from the Mn^{2+} -containing solution (Section 5.3.1.1), there is deposition of both Mn and Zn, but only Zn precipitation occurs from the Ni^{2+} -containing solution (Chapter 4). This suggests that there are more metal cations precipitating in the early stages for the Mn^{2+} -containing coating bath compared to the Ni^{2+} -containing bath. In turn this would imply a greater number of nucleation sites in the Mn^{2+} case, resulting in a larger number of smaller crystals. That more Mn precipitates than Ni follows from the lower solubility of manganese phosphates compared to nickel phosphates (this is suggested by the solubility products at 25°C of MnHPO_4 (3.6×10^{-8}), NiHPO_4 (1.5×10^{-6}), $\text{Mn}_3(\text{PO}_4)_2$ (5.6×10^{-33}) and $\text{Ni}_3(\text{PO}_4)_2$ (4.7×10^{-32}) [114,115,116]), although other influences could be involved since the phosphating process does not necessarily pass through equilibrium states.

5.3.3.2 Microstructural Regions

Figure 5.5 compares SEM images of ZPO-coated Al-Cu-Mg second phase particles and surrounding matrix regions formed from three coating baths which differ only in the presence of Ni^{2+} or Mn^{2+} (one has neither of these additives, one has 2000 ppm of Ni^{2+} , and

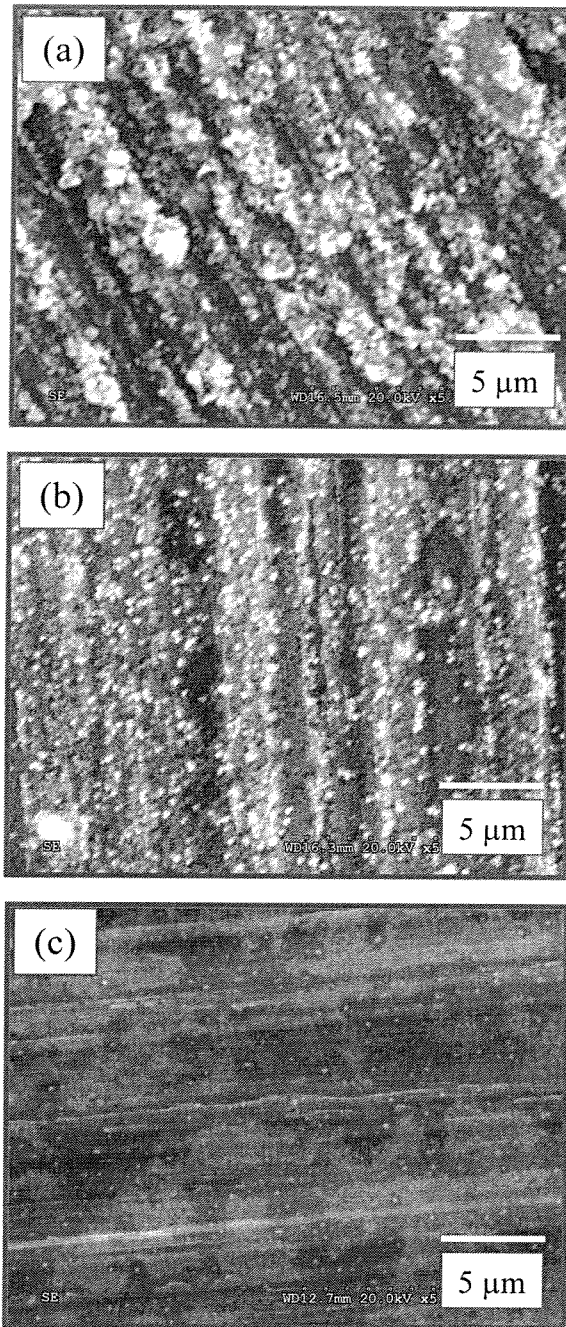


Figure 5.4 SEM micrographs (incident beam 20 kV) from 2024-Al surfaces dipped for 2 min in ZPO coating solutions (see text) which contained varying amounts of Ni^{2+} and Mn^{2+} : (a) no Ni^{2+} or Mn^{2+} , (b) 2000 ppm Ni^{2+} and (c) 2000 ppm Mn^{2+} .

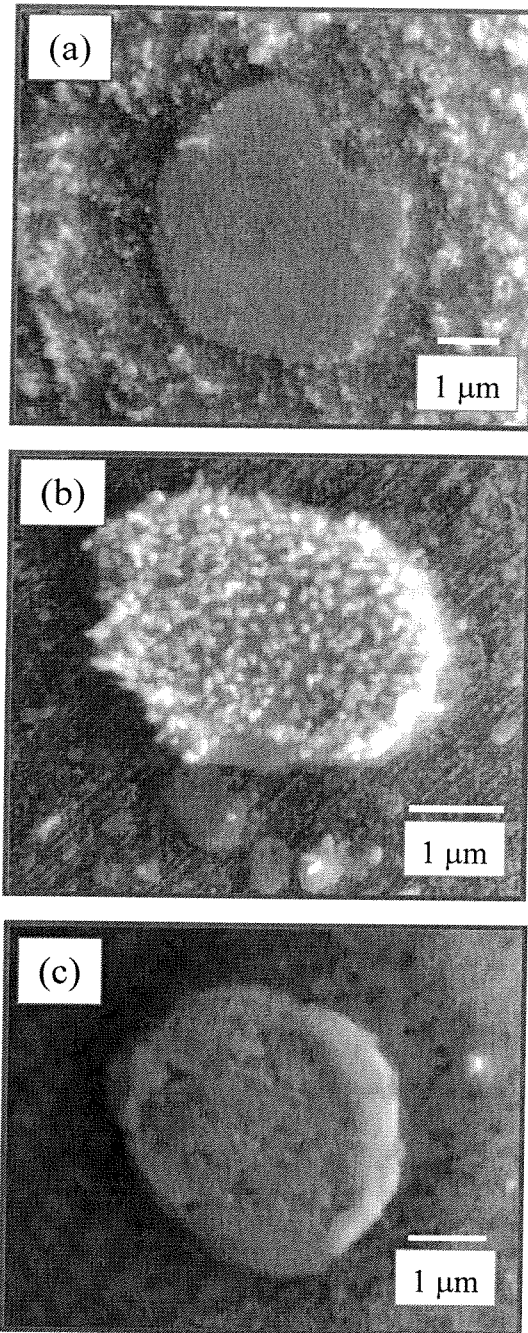


Figure 5.5 SEM micrographs (incident beam 10 kV) showing Al-Cu-Mg second-phase particles surrounded by the matrix region on a mirror-polished 2024-Al surface after dipping for 2 min in ZPO coating solutions (see text) which contained varying amounts of Ni^{2+} and Mn^{2+} : (a) no Ni^{2+} or Mn^{2+} , (b) 2000 ppm Ni^{2+} and (c) 2000 ppm Mn^{2+} .

the other has 2000 ppm of Mn^{2+}). More coating crystals are seen on the matrix compared to the Al-Cu-Mg particle for coating from the bath without Ni^{2+} or Mn^{2+} (Figure 5.5(a)), and the reverse situation is apparent for the Ni^{2+} -containing coating (Figure 5.5(b)). However, the SEM micrograph for the coating from the Mn^{2+} -containing bath (Figure 5.5(c)) does not show such a strong contrast, although SAM confirms that deposition has occurred on both the Al-Cu-Mg and matrix regions. Overall it can be concluded that the amounts of coating on the matrix and the Al-Cu-Mg particle are more similar for the coating with Mn^{2+} compared to use of the other two coating solutions.

Figure 5.6 shows SEM images of Al-Cu-Fe-Mn intermetallic particles surrounded by the matrix region for separate ZPO treatments involving 2000 ppm Ni^{2+} in the coating bath and 2000 ppm Mn^{2+} . Auger electron spectra were acquired at the regions indicated as N1, N2, M1, and M2. For use of the solution with Ni^{2+} additive, metallic Al is detected at N2 but not at N1; additionally, the Zn and Ni signals (Figure 5.7) are more intense on the particle (N1) than on the matrix (N2). These differences indicate that the coating is thicker on the particle than on the matrix. By contrast with the Mn^{2+} additive, the spectra for the Al-Cu-Fe-Mn particle (M1) and the matrix (M2) are similar, implying that the coating is compositionally more uniform. The behavior of the Al-Cu-Fe-Mn particle is similar to that of the Al-Cu-Mg particle (described above).

During the coating process, the second-phase particles are the first microstructural areas to be coated due to their cathodic nature [43]. Subsequently, the relative rates of precipitation are determined by etching at the local anodic sites (faster at the matrix) (Chapter 4). As mentioned above, the total precipitation as observed by XPS increases in the order: ZPO coating with Ni^{2+} < ZPO coating with Mn^{2+} < ZPO coating without Ni^{2+} or Mn^{2+} .

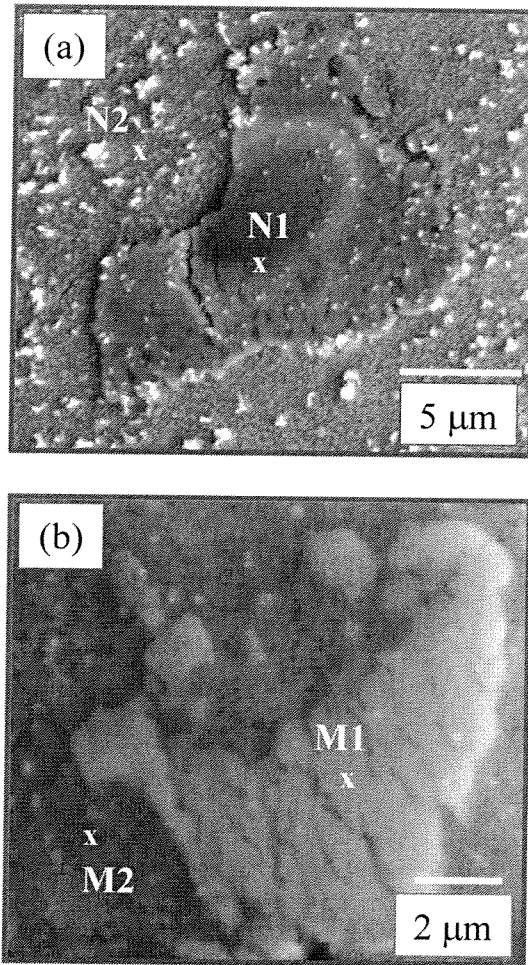


Figure 5.6 SEM micrographs (incident beam 10 kV) showing Al-Cu-Fe-Mn second-phase particles surrounded by the matrix region on a mirror-polished 2024-Al surface after dipping for 2 min in ZPO coating solutions (see text) which contained: (a) 2000 ppm Ni^{2+} and (b) 2000 ppm Mn^{2+} .

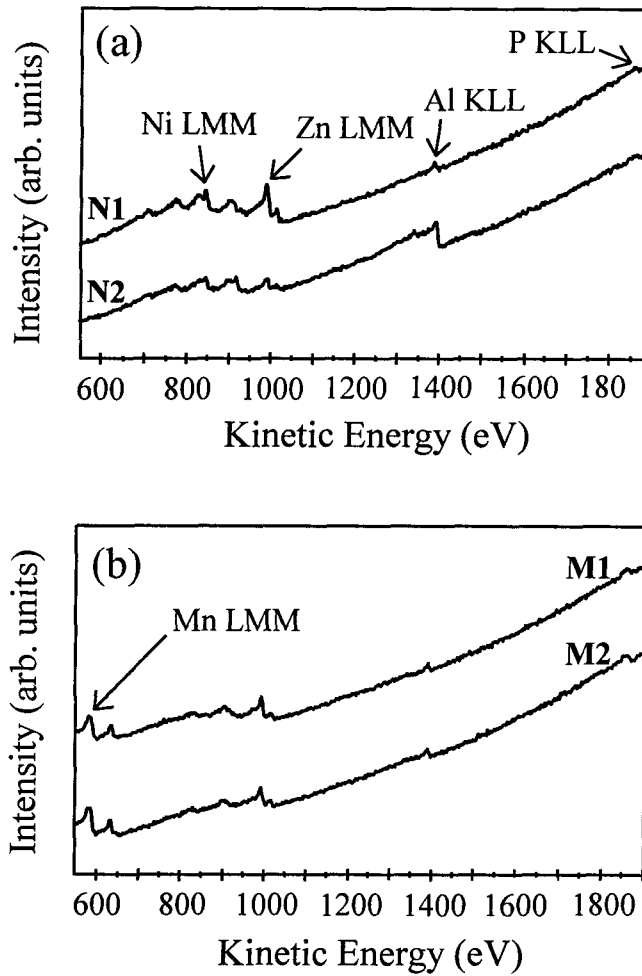


Figure 5.7 Auger spectra from the matrix and Al-Cu-Fe-Mn microstructural regions on a mirror-polished 2024-Al surface after dipping for 2 min in ZPO coating solutions (see text) which contained: (a) 2000 ppm Ni^{2+} and (b) 2000 ppm Mn^{2+} . The regions N1 and N2 are defined in Figure 5.6(a); M1 and M2 in Figure 5.6(b).

As a result, for the Ni^{2+} -containing coating, the second-phase particles are coated and there is a small amount of precipitation on the matrix. There is more coating on the matrix region for the Mn^{2+} -containing bath, and the greatest coating on the matrix occurs from the solution without Ni^{2+} or Mn^{2+} . Overall, the use of Mn^{2+} improves the evenness of coating distribution across the whole surface as it causes the degree of precipitation on the matrix during the later stages of coating to be similar to the amount of precipitation on the second-phase particles in the early stages.

5.3.4 Coating Adhesion

The Mn^{2+} -containing ZPO coating (2 min immersion time) was subjected to a simple de-adhesion test. After an initial immersion in distilled water, the sample was subjected to a water-based sonication for 20 min. Subsequently it was dried in the air and re-analyzed by SAM. After sonication there is less P on the surface in general but P is still detected at all microstructural regions, indicating that the coating has not been completely removed from any region. As one example, Figure 5.8 shows Auger spectra for the matrix region before and after sonication. Greater amounts of Al^{3+} are detected after the sonic treatment; this may come from the aluminum oxide layer between the metal and the ZPO coating. After some of the less tightly bound ZPO coating is removed by the sonic treatment, a larger amount of the underlying oxide layer is detected by SAM. At areas where the ZPO coating is completely removed, the underlying oxide may increase in thickness by the exposure to water. In any event, this preliminary test does not identify any particular weakness at specific microstructural regions of the coating-alloy interface. Hence this reinforces the observation of a more even

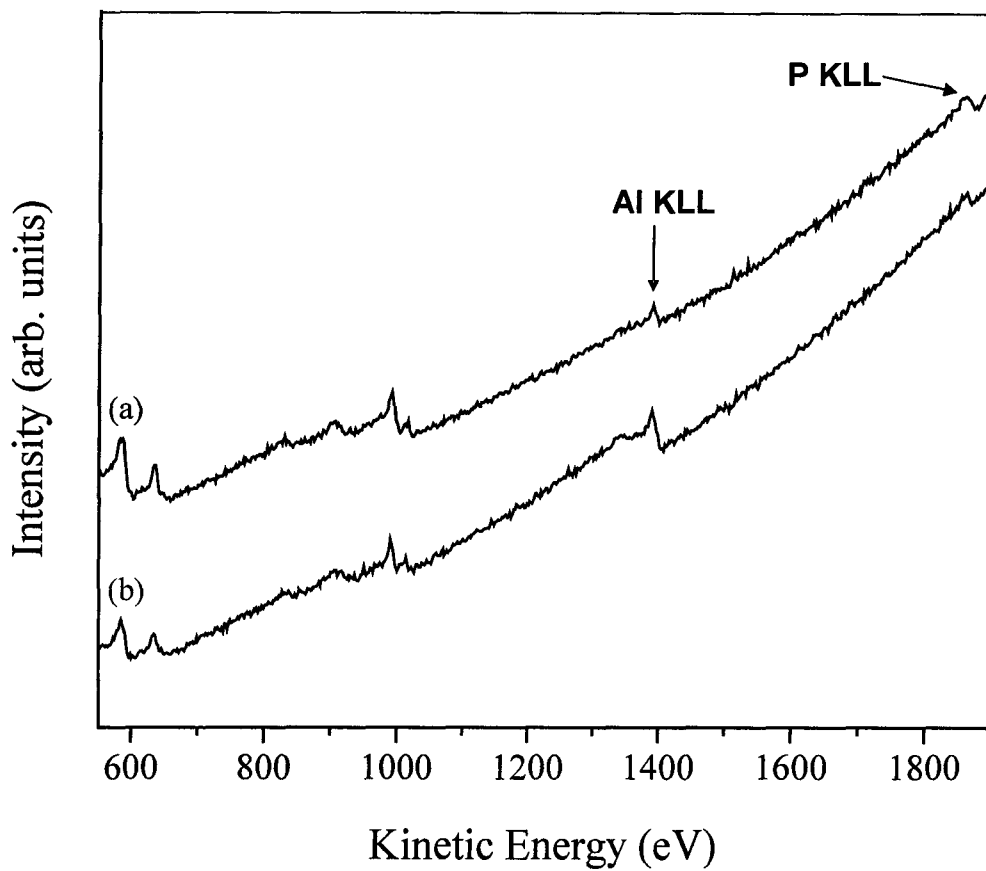


Figure 5.8 Auger spectra measured from the matrix region of the 2024-Al surface coated in a ZPO solution containing 2000 ppm Mn^{2+} before (a) and after (b) the sonic treatment (see text).

distribution of coating over the alloy surface when Mn^{2+} is present in the coating solution, although strictly better interfacial adhesion does not necessarily require an even coating.

5.4 Concluding Remarks

Mn^{2+} added to a ZPO solution for coating 2024-Al alloy has a significant effect on macroscopic coating properties: it causes a decrease in crystal size and coating thickness. From observations in this chapter, it seems an optimal coating (in terms of coating morphology and thickness) is formed when the Mn^{2+} concentration is 2000 ppm. This chapter also adds to our knowledge for the effect of Ni^{2+} and Mn^{2+} additives in a ZPO coating bath. Both additives act to decrease the size of the coating crystals, but Mn^{2+} causes a more significant reduction. The coating formed with the bath containing the Mn^{2+} additive is thicker than that formed with Ni^{2+} in the coating bath, although thinner than the coating formed with neither Ni^{2+} nor Mn^{2+} in the bath. The latter is however less favorable because of the larger crystals that form the coating.

This chapter shows that, for the conditions used, a 3 min immersion in the coating bath is optimal, whereas with longer times the coating starts to dissolve as the etching reduces and the pH decreases at the coating-solution interface. In general, the coating process also varies with position across a heterogeneous Al-alloy surface, but the analysis with SAM shows that the Mn^{2+} additive acts to improve the evenness of coating distribution (compared with the Ni^{2+} additive) across the different microstructural regions of a 2024-Al surface. Throughout, the deposition patterns across a surface are affected significantly by additives in the ZPO coating solution, which also affect composition within the coating. Thus while Mn^{2+} deposits during the earlier stages of the coating process, a significant precipitation of Ni^{2+} does not occur until the later stages (Chapter 4).

Chapter 6

Microstructural Effects on the Formation and Degradation of Zinc Phosphate Coatings on 2024-Al Alloy

6.1 Introduction

The different chemical compositions of the second-phase regions can lead to different surface properties at the microstructural level. It is often generally considered that these differences may originate with their different electrochemical characteristics, such as by exhibiting microanodic or microcathodic behavior relative to the matrix, but in principle the nature of the oxides at the different microstructural regions prior to putting into a coating solution may also have a role.

Metallic Al oxidizes readily, forming an oxide overlayer, and this is protective at least for mildly oxidizing conditions, but differences are expected for the second-phase particles in terms of oxide formation, ZPO coating characteristics and stability in a corrosive environment. During the early stages of the zinc phosphate coating of 2024-Al alloy, ZPO crystals form on the Al-Cu-Mg second-phase particles, rather than on the matrix or on the Al-Cu-Fe-Mn particles, with the initial nucleation occurring at interfaces between Al-Cu-Mg particles and the matrix [43]. Later in the coating process ZPO forms on the Al-Cu-Fe-Mn particle, followed by ZPO deposition at the matrix region (Chapter 4). Other work describes how coating patterns at the surface microstructure vary depending on the additives present in the ZPO coating bath (Chapter 5). Also, the Al-Cu-Mg and Al-Cu-Fe-Mn second phases at a 2024-Al alloy surface are generally initiation sites for corrosion [8]; for example,

characterization of chromate conversion coatings (CCCs) on an aluminum alloy by surface analysis before and after salt fog exposure indicates that coating failure occurs at Cu-containing intermetallic sites [117]. Another study indicates the presence of defects in CCCs at the intermetallic compounds can cause corrosion to occur preferentially at these locations [118]. Recent reports described the use of magnetron sputtering to prepare model second phases in order to study their specific surface chemistries [13,119], although it is also important to do that in the context of actual alloys and to assess how well the ZPO coating protects the different regions.

This chapter extends from earlier studies of the ZPO coating process (e.g. Chapters 4 and 5), and a previous report [43] which reviewed mechanistic aspects of ZPO coating at different microstructural regions of 2024-Al. The present chapter aims to explore further the mechanisms involved, particularly in terms of the influence of surface oxides on ZPO coating formation. A second objective is to investigate the nature of the metal near the alloy-oxide interface after surface polishing and its subsequent effect on the ZPO coating. The present chapter also aims to explore the degradation of a ZPO-coated 2024-Al surface after exposure to corrosive conditions. Throughout there is an emphasis on relating the formation and degradation of ZPO coatings to the nature of the various microstructural regions on the surface of the 2024-Al alloy. The approach uses scanning electron microscopy (SEM) to assess surface topography, and X-ray photoelectron spectroscopy (XPS) and Auger electron spectroscopy (AES), in the scanning Auger microscopy (SAM) mode, for the surface chemical characterizations; XPS over the whole surface and SAM at the local regions.

6.2 Experimental Details

Square samples (1x1 cm²) of commercial 2024-Al alloy were mechanically polished with aluminum oxide sandpaper (up to 1200 grit) and additionally polished by diamond paste to give a mirror finish (~1 μm roughness); this was needed to assess coatings at the microstructural level. Deionized water was used for the initial sandpaper polishing and for sample rinsing in between the different stages of polishing. After polishing, each sample was ultrasonically cleaned in acetone and methanol, and then exposed to air for 15 min before being placed under vacuum (pressure in the 10⁻¹ Pa range) to minimize further sample oxidation before SAM analysis. After the SAM analysis, the alloy sample was rapidly transferred to a ZPO coating solution at 60°C where it was immersed for 105 s. One L of the water-based Ni²⁺-containing ZPO solution (designed specifically for coating of Al alloys) contained: 10.8 mL of 85% H₃PO₄, 1.24 g ZnO, 1.11 g NaF, and 9.91 g of Ni(NO₃)₂·6H₂O; before each immersion the pH of the coating solution was adjusted to the range 3.8-4.0 by adding NaOH. In each case the coating treatment was completed by rinsing the sample in deionized water and drying in argon; the sample was then re-inserted in the vacuum chamber and later analyzed by SAM. Subsequently the samples were immersed in a NaCl solution (0.6 M, pH 6) for times ranging from 1 to 48 h, and rinsed with deionized water prior to some samples being re-characterized with SAM. Duplicate samples were prepared and characterized for each treatment of polishing, coating and subsequent exposure to corrosive conditions.

Auger analyses were performed using the primary electron beam set at 10 keV and 3 nA. Survey and higher energy resolution spectra were measured with the constant retard ratio set at 4 and 40 respectively. XPS spectra were measured with a Leybold MAX200 spectrometer using the Al Kα source (1486.6 eV operated at 15 kV, 20 mA). Contributions

from surface C contamination have not been included in the tables presented in this work. SEM characterizations (secondary electron images) made in conjunction with Auger measurements were performed using a 10 kV accelerating voltage. EDX measurements used a Hitachi S3000-N instrument with an acceleration voltage of 20 kV.

6.3 Results and Discussion

6.3.1 2024-Al Before Dipping in ZPO Coating Bath

SEM images of the Al-Cu-Mg and Al-Cu-Fe-Mn second-phase particles (and the surrounding matrix region) on the polished 2024-Al surface are shown in Figures 6.1(a) and 6.2(a). Auger electron spectra, shown in Figure 6.3, were acquired at the points indicated by P1, P2, and P3 (Figures 6.1(a) and 6.2(a)) for the Al-Cu-Mg, matrix and Al-Cu-Fe-Mn regions respectively. Quantitative measurements are summarized in Table 6.1. The spectrum from P1 has a substantial Cu signal with the surface Cu/Al ratio equal to 2.8, and hence much greater than the value predicted from the formula for the compound Al_2CuMg . At higher magnification for the spectrum from P1, only a very small peak is found at 860 eV, which indicates that most of the Cu detected is in the metallic form [120]. During the polishing process preferential dissolution of Al and Mg occurs, compared to Cu, resulting in a Cu-rich surface. While a previous report indicated that Mg and Al dissolution occurs at the Al-Cu-Mg particle during immersion in the ZPO coating solution [43], the present work indicates that this type of dissolution also occurs during the polishing process. A similar enrichment was observed previously for 2024-Al alloy in a corrosive solution [7], and such observations fit expectation in terms of the correlation with the quantity $\Delta G_f^\circ/n$ [121]. After polishing, the amount of Mg detected at Al-Cu-Mg particles varies, with some particles having more Mg (P1 in Table 6.1) and others less. Given the low reduction potential for Mg,

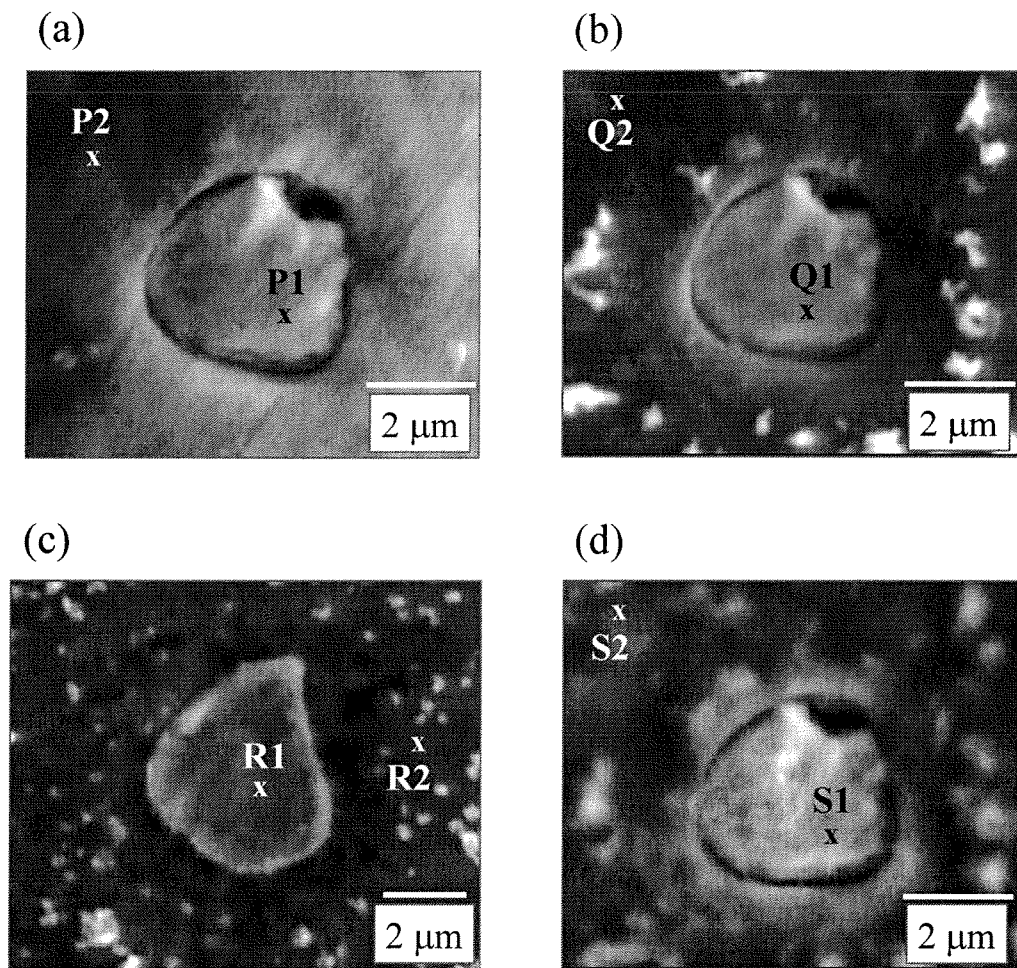


Figure 6.1 SEM micrographs showing Al-Cu-Mg second-phase particles surrounded by matrix region on the 2024-Al surface after exposure to different sequential treatments: mirror-polishing (a); dipping for 105 s in a ZPO coating solution at 60°C containing 2000 ppm Ni^{2+} (b), where the bright areas are large ZPO crystals; immersion of coated surfaces in 0.6 M NaCl solution at 20°C for 3 h (c) or 48 h (d).

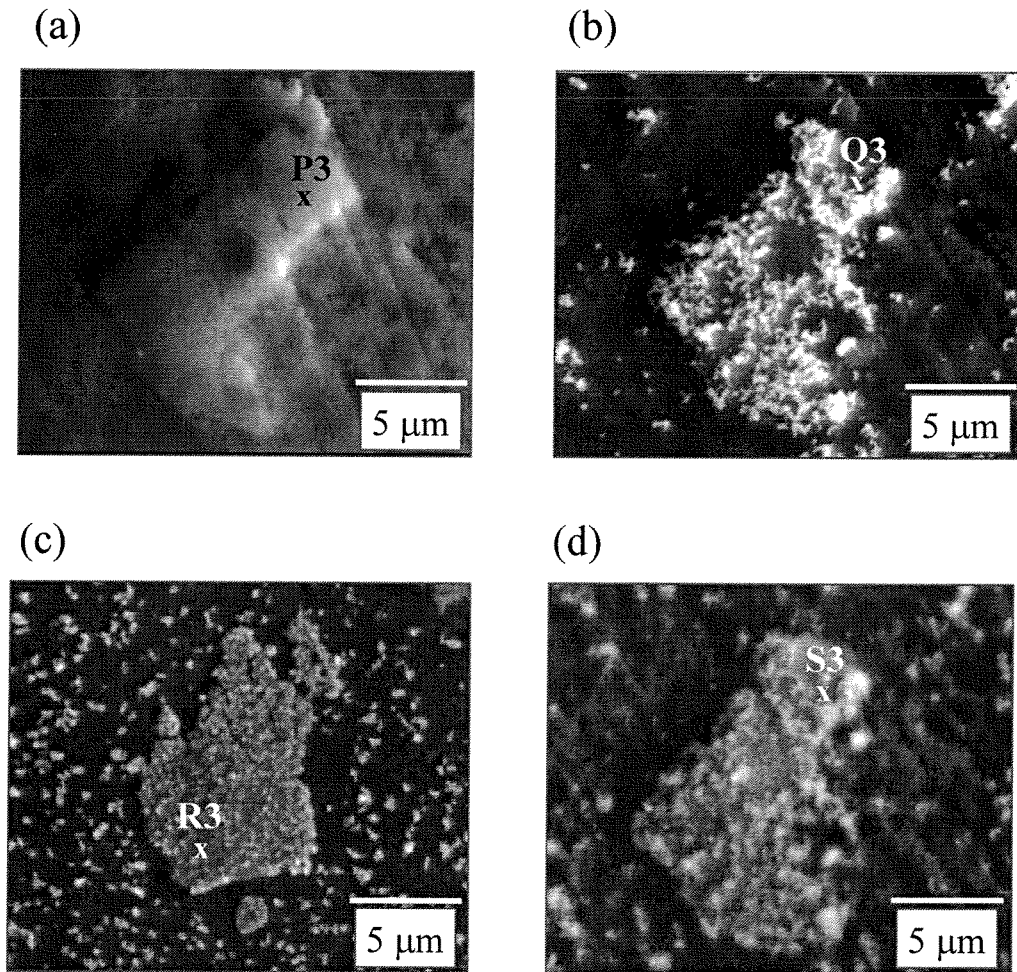


Figure 6.2 SEM micrographs showing Al-Cu-Fe-Mn second-phase particles surrounded by matrix region on the 2024-Al surface after exposure to different sequential treatments: mirror-polishing (a); dipping for 105 s in a ZPO coating solution at 60°C containing 2000 ppm Ni^{2+} (b), where the bright areas are large ZPO crystals; immersion of coated surfaces in 0.6 M NaCl solution at 20°C for 3 h (c) or 48 h (d).

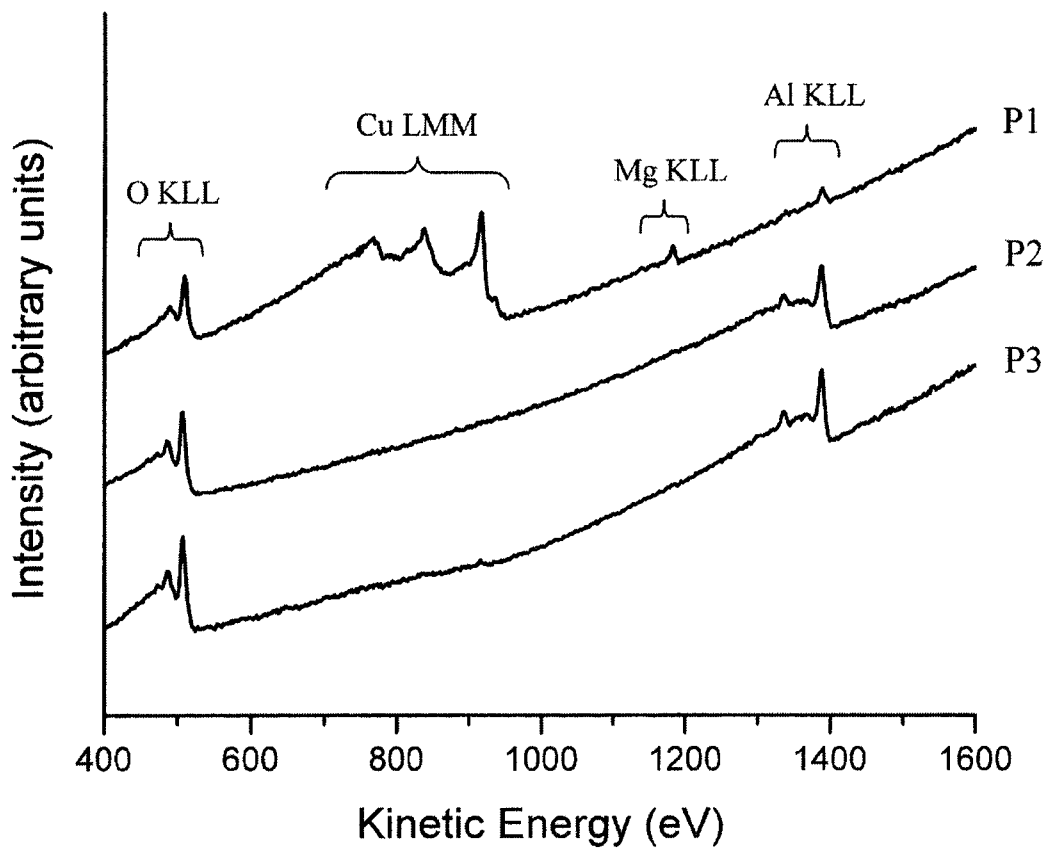


Figure 6.3 Auger survey spectra from regions indicated in Figures 6.1(a) and 6.2(a) namely Al-Cu-Mg particle (P1), matrix region (P2), Al-Cu-Fe-Mn particle (P3).

Table 6.1 Elemental atomic percentages from SAM for different microstructural regions (Figures 6.1(a) and 6.2(a)) on the mirror-polished 2024-Al surface.[§]

	Al-Cu-Mg P1	matrix P2	Al-Cu-Fe-Mn P3
O	46.8	62.7	61.5
Cu	24.6	- [◇]	†
Mg	20.0	-	-
Al	8.8	37.5	38.4

[§] Values are believed to be accurate to within $\pm 20\%$ as discussed on page 58

[◇] The hyphen indicates that the element is not detected

[†] Amount detected is less than 0.5% and too small to be measured accurately

a significant amount of the detected Mg is expected to be in the form of oxide and located over the particle surface. Under the conditions applied, Mg is only detected at the Al-Cu-Mg particles. Mg oxide and Al oxide are present in the surface region of the Al-Cu-Mg particle (although, since the exact form of the MgO is unknown, it is subsequently referred to as Mg-Al oxide).

The Auger electron spectrum measured for position P2 (matrix) is dominated by peaks for Al and O, as summarized in Table 6.1. A higher resolution scan of the Al KLL spectrum from P2 indicates that the dominant chemical state is Al^{3+} , so implying that Al oxide is the main component at that region, since O is the only anionic element detected. Table 6.1 reports that no Cu is detected by AES at the matrix (P2); the larger Cu concentration at the Al-Cu-Fe-Mn particle (P3) is recognized, although neither Fe nor Mn are detected (Figure 6.3). XPS confirms the presence of oxide over the surface, but does not observe Mg, Mn or Fe (Table 6.2). Quantitative AES analysis indicates that the proportions of Al^{3+} at the matrix and at the Al-Cu-Fe-Mn particle are comparable (32% and 36% respectively for the sample in Table 6.1), although that at the Al-Cu-Mg particle is appreciably less (9% or less for all replicate measurements). The larger relative amount of metallic Al detected from the matrix, compared to the Al-Cu-Fe-Mn particle (6% and 2%

respectively), is due in part to less airborne C contamination found at the matrix region, but the detection of the metallic component from both micro-regions indicates that the entire oxide region is probed in both cases. The similarity in the compositions for the Al-Cu-Fe-Mn and matrix surface regions is indicated in Table 6.1.

Table 6.2 Elemental atomic percentages from XPS for the 2024-Al surface after polishing, ZPO coating and immersion in NaCl solution for 48 h.[§]

	Mirror-polished	ZPO-coated	ZPO-coated & immersed
Zn	- [◊]	9.0	1.7
Cu	†	2.0	†
Ni	-	2.4	-
O	65.7	60.1	72.4
F	-	2.6	-
Cl	-	-	-
P	-	9.5	-
Al ³⁺	31.6	12.7	25.8
Al _{met}	2.5	1.7	-

[§] Values are believed to be accurate to within $\pm 10\%$ as discussed on page 29

[◊] The hyphen indicates that the element is not detected

† Amount detected is less than 0.5% and too small to be measured accurately

6.3.1.1 Oxide Thickness

The thickness of the oxide at the matrix region is determined using the following analysis. For a sample consisting of an overlayer (thickness d) on a substrate, a simple model can be used to estimate its thickness provided both the overlayer and substrate are uniform and homogeneous. Equation 2.6 can be integrated for the substrate and overlayer to yield:

$$I_s = f \sigma n_s A T \lambda_s \exp(-d/\lambda_{so}) \quad (6.1)$$

$$I_o = f \sigma n_o A T \lambda_o [1 - \exp(-d/\lambda_o)] \quad (6.2)$$

for intensities of a specific photoelectron peak from the substrate (I_s) and the overlayer (I_o) respectively. Concentrations of the atom being analyzed are given by n_s and n_o ; λ_s and λ_o

represent the inelastic mean free paths for photoelectrons originating in, and travelling in, the substrate and overlayer respectively, while λ_{so} is the inelastic mean free path of photoelectrons from the substrate travelling in the overlayer. A similar analysis can be used for Auger peaks.

Equations 6.1 and 6.2 can be applied to the matrix region where a layer of aluminum oxide (overlayer) covers aluminum metal (substrate). The ratio I_o / I_s becomes

$$I_o/I_s = I_{oxide}/I_{metal} = (n_o/n_s) [\exp(d/\lambda_o) - 1], \quad (6.3)$$

if it can be assumed that λ_o , λ_s , and λ_{so} have similar values, for which there is supporting evidence [122]. The quantities n_o and n_s are calculated from the densities and molecular masses of Al_2O_3 and Al metal:

$$n_o = 2 [(3.97 \text{ g cm}^{-3}) / (101.96 \text{ g mol}^{-1})] = 0.0779 \text{ mol Al cm}^{-3} \quad (6.4)$$

$$n_s = (2.70 \text{ g cm}^{-3}) / (26.98 \text{ g mol}^{-1}) = 0.100 \text{ mol Al cm}^{-3} \quad (6.5)$$

and λ_o is assumed to be 27 Å [122]. The measured ratio I_o/I_s is 10.8/2.0 which yields a calculated value of 56 Å for d (thickness of oxide). In another context, where Al samples were exposed to water vapour or humid air, oxide thicknesses of up to 23 Å were determined [123]. The oxide growth is more extensive in the present situation, apparently because of the sample being in contact with liquid water during the polishing process.

6.3.2 2024-Al After Dipping in ZPO Coating Bath

After polishing and characterization, the 2024-Al sample was treated in the ZPO coating bath for 105 s and then re-analyzed. Auger spectra were acquired at the regions shown in Figures 6.1(b) and 6.2(b). The coating appears in two forms: large bright crystals and the matrix areas which appear darker in the SEM images. Since the matrix is the dominant surface region in area, its coating is most representative of the overall surface

composition, but elements in their metallic form are detected from the underlying substrate only at the matrix (Q2) indicating the region where the coating is thinnest. In turn that may suggest the possibility that the coating will provide less protection for that region in a corrosive environment.

At the second-phase particles, the coating is sufficiently thick to prevent the detection of Auger electrons from the metallic substrate. Mg, Fe and Mn are not detected by the surface analytical methods used here from any region of this surface. For coated samples, there are overlaps between the Cu Auger peaks with the Zn LMM, Ni LMM, and P LMM signals, thereby inhibiting the ability of Auger analysis in this context to indicate the presence or absence of Cu. More P is detected at Q1, compared to Q2 and Q3 (Table 6.3),

Table 6.3 Elemental atomic percentages from SAM for different microstructural regions (Figures 6.1(b) and 6.2(b)) on the ZPO-coated 2024-Al surface.[§]

	Al-Cu-Mg Q1	matrix Q2	Al-Cu-Fe-Mn Q3
O	34.0	42.1	45.1
Ni	13.3	6.1	8.9
Zn	21.9	20.7	21.0
Al	4.6	16.2	8.8
P	26.2	14.8	16.2

[§] Values are believed to be accurate to within $\pm 20\%$ as discussed on page 58

implying that the amount of phosphate deposition is greatest at the Al-Cu-Mg particle; this is consistent with other measurements where more coating forms at the Al-Cu-Mg particles, compared with the other regions, after a short (3 s) dip in this same ZPO coating bath, as well as in an independent commercial bath [43]. For the coating solutions used in this work, the relative amounts of ZPO at the different microstructural areas in the early stages of coating are similar to the amounts at the later stages.

AES analysis confirms that the oxides at the Al-Cu-Fe-Mn and matrix regions are

similar in composition, for the particular polishing conditions and extent of air exposure used (Section 6.3.1). Insofar as the etching rates depend just on the surface composition, these rates are expected to be quite similar; therefore the observed differences in ZPO coating characteristics on the Al-Cu-Fe-Mn and matrix areas (i.e. more and less respectively) must especially arise from another factor. This supports a common view that emphasizes the electrochemical characteristics for the regions concerned, specifically that the Al-Cu-Fe-Mn particles are more cathodic than the matrix [124]. In turn this will lead to accelerated reduction reactions at the Al-Cu-Fe-Mn particles, and an increase in the local solution pH, so causing more phosphate deposition compared with the matrix.

Previously it was hypothesized that an oxide containing Mg and Al covers the Al-Cu-Mg particle [43], and that would etch quicker than Al oxide alone given the experience that Mg-rich oxide films tend to be porous and less protective [125]. Electrochemical data also suggest that the passive films formed on Al-Cu-Mg intermetallic particles are less protective than those formed on the matrix of 2024-Al [119]. The present work confirms the presence of Mg-Al oxide in the surface region of the Al-Cu-Mg particle and so supports the above-mentioned hypothesis. Together these observations are consistent with the fastest removal of surface oxide occurring at the Al-Cu-Mg region. In turn that helps promote the coating deposition at this area, but the presence of more ZPO coating at the Al-Cu-Mg particle, compared with the other microstructural regions, is also influenced by an increase in cathodicity as a result of the Cu-rich metal layer below the surface oxide (Section 6.3.1).

The Ni/Zn ratios from Auger spectra (Table 6.3) increase in the order matrix (0.29), Al-Cu-Fe-Mn particle (0.42) and Al-Cu-Mg particle (0.61). This is also the order of the expected cathodicities since the Al-Cu-Fe-Mn region is believed to be more cathodic than the alloy matrix [124]. In general a surface is more likely to promote cathodic (reduction)

reactions if it contains metals with higher reduction potentials. The Al-Cu-Mg surface is richer in Cu (which has a higher reduction potential than Al) compared to the other micro-regions, and is therefore considered to be the most cathodic area (other alloying elements are not considered in this argument, because although they are present deeper down, they are not detected in the metallic forms by the surface analytical techniques). This trend in cathodicities fully matches the observations in this work for ZPO coating thickness, but the increase in Ni/Zn ratio is also believed to follow an increase in amount for the mixed Ni-Al oxide formed during the coating process, as has been discussed previously for the Al-Cu-Mg region (Chapter 4). The increase in Ni-Al oxide formation with surface cathodicity was suggested in an earlier report involving treatment of 2024-Al alloy in a corrosive solution containing Ni²⁺ [83].

6.3.3 Corroded ZPO Coating on 2024-Al

The ZPO-coated samples, as described above, were exposed to 0.6 M NaCl solution for periods ranging from 1 to 48 h in order to gain more understanding of the corrosion mechanism for these coated surfaces. SAM analysis for the sample treated for the shortest time indicated that the coating did not change appreciably as a result of the 1 h immersion in the NaCl solution, and that influenced the choice of 3 h, as well as the longest treatment time (48 h), for detailed characterization.

6.3.3.1 Initiation of Corrosion (3 h Immersion)

SEM images of ZPO-coated Al-Cu-Mg and Al-Cu-Fe-Mn particles before and after the 3 h immersion in the NaCl solution are shown in Figures 6.1(b),(c) and 6.2(b),(c). There is a trench (~1 μm in width) surrounding part of the Al-Cu-Mg particle in Figure 6.1(c).

More metallic Al is detected from this region, and less Ni and Zn, compared to the matrix region further away (R2). That implies less ZPO coating in the trench. Further, since the trench is not present prior to the NaCl exposure (Figure 6.1(b)), it follows that feature results from preferential attack by the corrosive solution.

SAM analysis (Tables 6.3 and 6.4) indicates that after immersion in the corrosive solution for 3 h, the amounts of Zn, Ni and P decrease at the Al-Cu-Mg and matrix areas, while the amounts of Al increase. At the Al-Cu-Fe-Mn region there is a decrease in Ni and P and an increase in Al, while the amount of Zn remains constant. A general decrease in coating elements, accompanied by an increase in Al, is observed for the large coating crystals (bright areas) on the matrix and Al-Cu-Fe-Mn regions. Across the surface the zinc phosphate in the coating dissolves in the corrosive environment and Zn^{2+} and Ni^{2+} ions re-precipitate on the surface as oxide, consistent with studies of phosphate coatings on steel and their degradation under alkaline conditions [88,89]. There is also oxidation of Al at surface regions not covered by ZPO.

After immersion in the NaCl solution for 3 h, no P (indicative of phosphate) is detected at the matrix or the Al-Cu-Fe-Mn region, but it is still present at the Al-Cu-Mg region, presumably as a consequence of the larger amount of phosphate at that region compared to the other microstructural areas prior to immersion in the corrosive solution (Section 6.3.2). Trace quantities of Cl detected at the matrix region are due to the precipitation of Al, Zn and/or Ni chlorides. Corrosion product forms at a number of locations on the matrix region of the surface (e.g. R4 in Figure 6.4(a)) and is composed mainly of aluminum oxide with trace amounts of zinc oxide (Table 6.4). The first originates

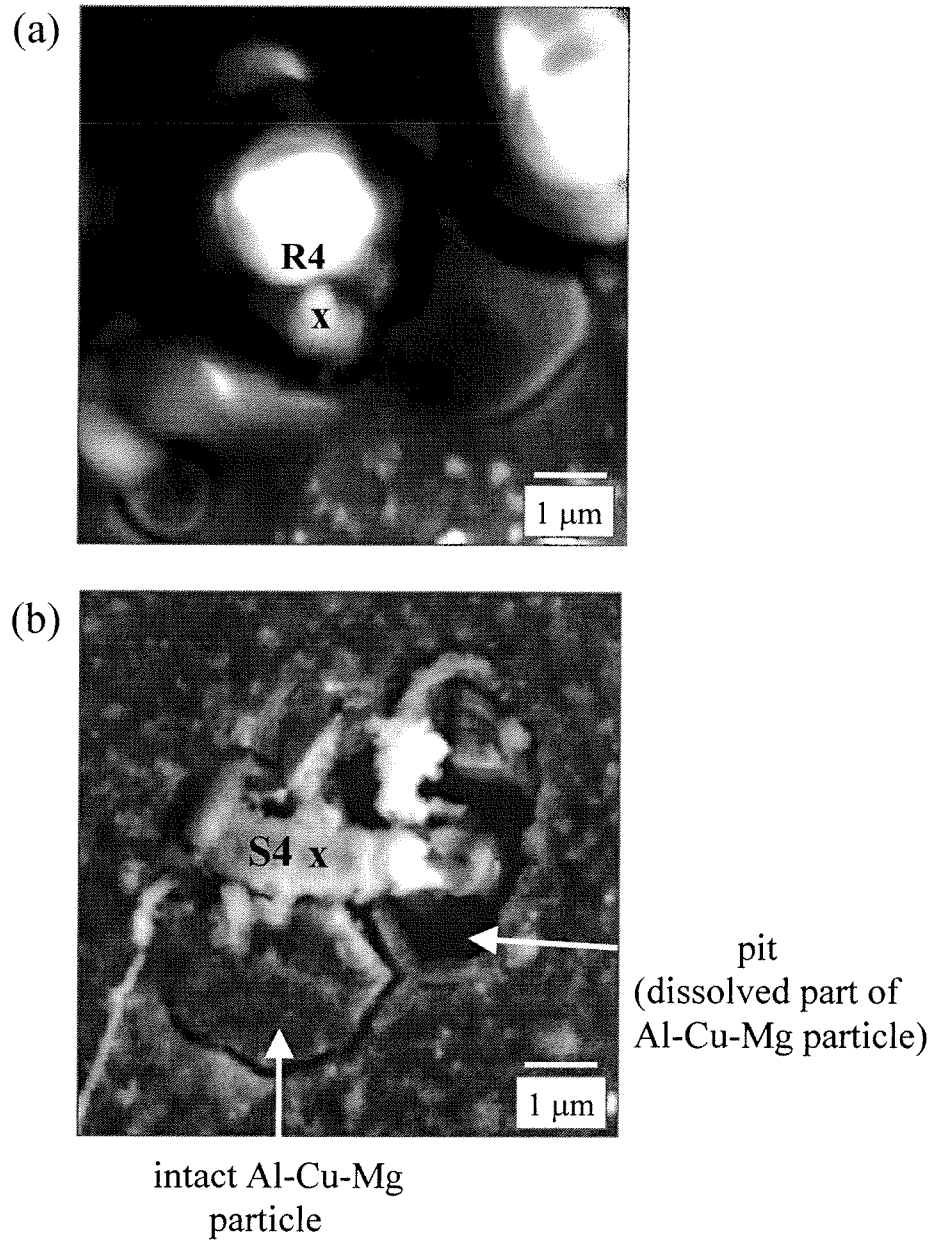


Figure 6.4 SEM micrographs for ZPO-coated surface after immersion in NaCl solution for: (a) 3 h showing corrosion product (R4); (b) 48 h showing an intact Al-Cu-Mg particle, a partly dissolved Al-Cu-Mg particle (pit), and corrosion product (S4).

Table 6.4 Elemental atomic percentages from SAM for different microstructural regions (Figures 6.1(c), 6.2(c), 6.4(a)) on the coated 2024-Al surface after 3 h immersion in NaCl solution.[§]

	Al-Cu-Mg R1	matrix R2	Al-Cu-Fe-Mn R3	Corr prod* R4
O	45.0	48.8	50.5	70.2
Ni	9.4	3.9	5.8	- [◇]
Zn	11.3	17.1	19.8	†
Al	26.1	30.2	23.9	29.8
P	8.3	-	-	-
Cl	-	†	-	-

[§] Values are believed to be accurate to within $\pm 20\%$ as discussed on page 58

* Corrosion product

[◇] The hyphen indicates that the element is not detected

† Amount detected is less than 0.5% and too small to be measured accurately

with corrosion of the alloy matrix, while the zinc oxide comes from degradation of the ZPO coating.

6.3.3.2 More Extensive Degradation (48 h Immersion)

XPS analysis (Table 6.2) indicates that there is a significant decrease in the amounts of Zn, Cu, Ni, F and P for the ZPO-coated surface after immersion in the NaCl solution for 48 h compared to the ZPO-coated surface which had not been dipped in NaCl solution (the mentioned elements are all found in the ZPO coating). There is also an increase in Al^{3+} after the 48 h exposure. This is understood by the partly corroded coating dissolving upon further exposure to the corrosive environment, along with oxidation of the uncovered Al surface; also some Zn^{2+} ions in solution re-precipitate on the surface as oxide. SAM analysis (Table 6.5) indicates that the chemical compositions at all microstructural regions become similar after exposure to the corrosive conditions for 48 h. For the same sample a larger amount of C from airborne contamination is detected by XPS compared to AES. No metallic Al is detected by XPS, and therefore the photoelectrons studied do not originate from as deep as

the oxide-metal interface, but Auger electrons are recognized from the whole oxide layer and part of the underlying metal, in part because of removal of C contamination by the incident electron beam. By similar reasoning, the amounts of Zn and Al detected by XPS, which does

Table 6.5 Elemental atomic percentages from SAM for different microstructural regions (Figures 6.1(d), 6.2(d), 6.4(b)) on the coated 2024-Al surface after 48 h immersion in NaCl solution.[§]

	Al-Cu-Mg S1	matrix S2	Al-Cu-Fe-Mn S3	Corr prod* S4
O	59.0	57.4	62.4	18.6
Zn	3.8	3.7	3.0	†
Al	37.2	38.9	34.6	12.5
Cl	- [◊]	-	-	61.7
Cu	-	-	-	1.0
Mg	-	-	-	6.1

[§] Values are believed to be accurate to within $\pm 20\%$ as discussed on page 58

* Corrosion product

† Amount detected is less than 0.5% and too small to be measured accurately

◊ The hyphen indicates that the element is not detected

not probe the entire oxide layer, are less than those seen by AES. A significant portion of the Cu detected by XPS probably comes from partially dissolved Al_2CuMg particles which decompose into metallic Cu clusters that are redistributed across the whole surface [7].

The oxide is dominated by Al at all microstructural regions. The detection by AES of metallic Al at the Al-Cu-Mg region, and the absence of metallic Cu, indicates that the Cu-rich dealloyed layer formed during the polishing process, and existing after the ZPO coating [43], is no longer present. The SEM image in Figure 6.1(d) for a coated Al-Cu-Mg particle after 48 h immersion in the NaCl solution shows the matrix area surrounding the particle as brighter compared to matrix regions further away due to charging of the insulating oxide [126]. More matrix etching resulting in the formation of Al oxide, is expected near the Al-Cu-Mg particle because of galvanic coupling with the matrix [7].

The corrosion product (bright particles) on the matrix and Al-Cu-Fe-Mn regions (Figures 6.1(d) and 6.2(d)) are at similar locations to the corresponding ZPO coating crystals before the corrosive treatment (Figures 6.1(b) and 6.2(b)), suggesting that during the dissolution of ZPO and precipitation of oxides the large particles are preferred locations for deposition of the precipitates.

A small number (~5-10%) of the Al-Cu-Mg particles partially dissolve after immersion in the corrosive solution. One example is identified in Figure 6.4(b); in addition that figure also shows a corrosion product (S4) and an intact Al-Cu-Mg particle. Region S4 was analyzed by AES and the elemental compositions deduced are included in Table 6.5. The elements Cl, Al, Mg, and a small amount of Cu, are detected at the corrosion product (S4). The large amount of Cl present (also substantiated by EDX analysis) implies that the dominant chemical species are AlCl_3 and MgCl_2 . The presence of Al, Mg, and Cu suggests that metal ions in the corrosion product come from the partly-dissolved Al-Cu-Mg particle, and the relative amounts of Cu and Mg in corrosion products vary across the surface according to the extent of dissolution of the Al-Cu-Mg particle from which they originate. Chloride has been observed only near surface pits, such as for a dissolved Al-Cu-Mg particle. It appears that at these regions, the local metal ion concentrations in solution become sufficiently high to allow precipitation of chloride-containing corrosion product (e.g. AlCl_3 , MgCl_2 and CuCl_2).

6.3.3.3 Corrosion Protection Provided by ZPO Coating

An SEM image taken after the 48 h exposure to the NaCl solution is shown in Figure 6.5. It shows intact second-phase particles (particularly in the top part of the image), cracked areas where substrate dissolution has occurred, and corrosion product (bright particles). The

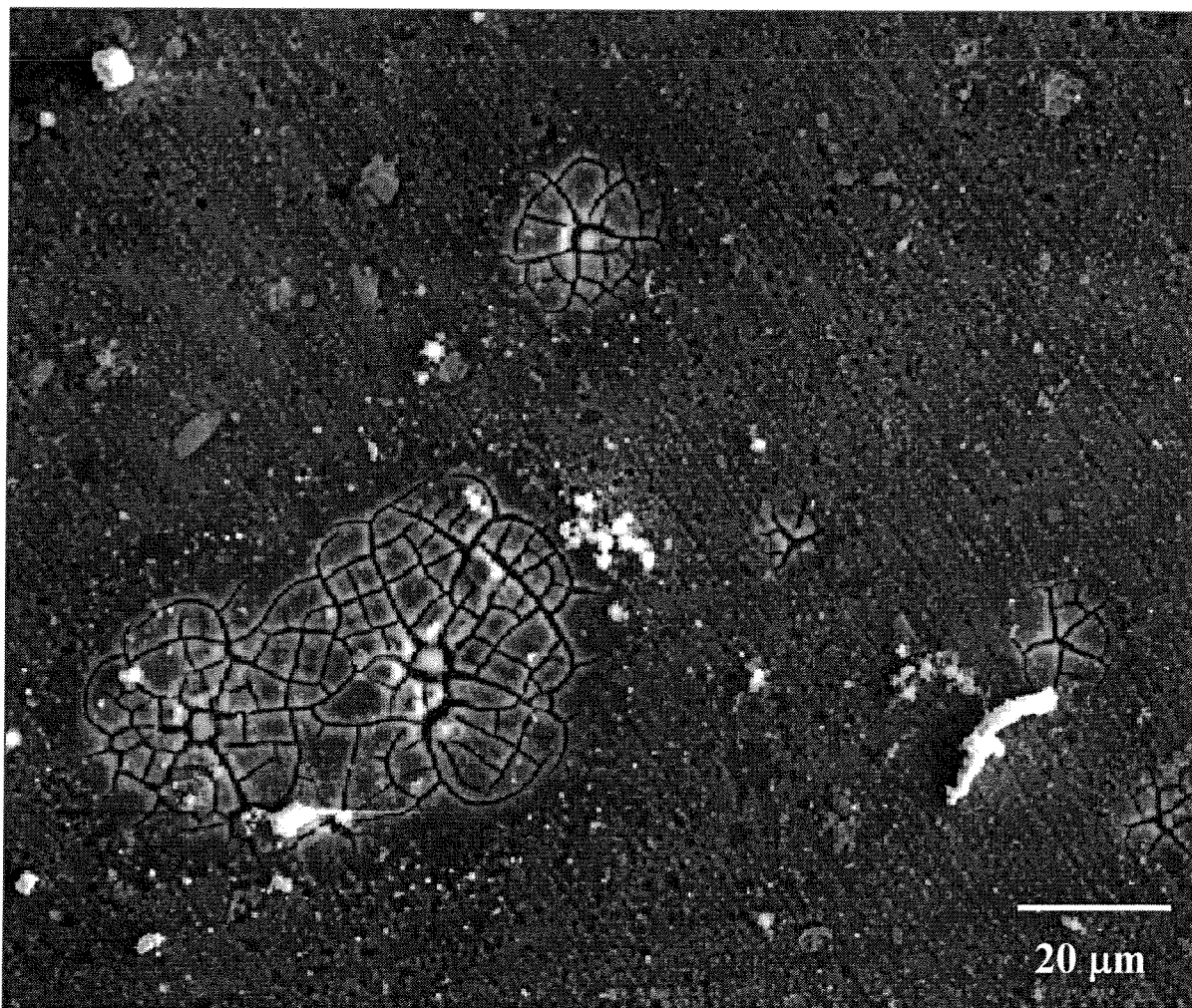


Figure 6.5 A larger-area SEM micrograph for the ZPO-coated surface after 48 h immersion in NaCl solution to show extensive matrix cracking.

cracked areas occur in the matrix region of the alloy surface and they are not associated with the second-phase particles (this confirmed by EDX analysis). For the 3 h exposure, a smaller number of cracks and corrosion product are found at scattered regions on the alloy matrix (and this where the corrosive attack starts). For the 48 h exposure, dissolution of a few Al-Cu-Mg particles results in the formation of pits (Figure 6.4(b)). The appearance of cracks, pits and corrosion product demonstrates a weakness of the ZPO coating for protecting the alloy substrate at these locations (i.e. matrix and a few Al-Cu-Mg regions). The tendency for a small number of Al-Cu-Mg particles to dissolve is consistent with another report [8], perhaps because those particles are located at the confluence of grain boundaries in the alloy (which are known to be chemically reactive regions [4]), rather than as a result of the ZPO coating. In other work, SEM observations at higher magnification indicated that the ZPO coating (formed without a post-treatment rinse) is more porous at the matrix compared to the Al-Cu-Fe-Mn particles (Chapter 4). Also, the extra Ni-Al oxide is believed to help enhance protection for the Al-Cu-Mg particles [83]. These points together suggest that the corrosive solution in the present work comes into contact with metal earlier at the matrix region than at the second-phase particles, and therefore that the ZPO coating provides less protection to the matrix compared with the particles.

A study of uncoated 2024-Al after immersion in NaCl solution indicated that pitting corrosion is favored at the Al-Cu-Mg and Al-Cu-Fe-Mn particles compared to the matrix [8]. SEM investigations of uncoated 2024-Al after immersion in a NaCl solution, similar to that used in the present work, indicate that the first occurrence of pitting happens within 3.5 h, with the matrix adjacent to Al-Cu-Mg particles forming trenches (width $\sim 0.5 \mu\text{m}$) [105,127]. This width of trench is not observed in the present work at Al-Cu-Mg particles

on the ZPO-coated surface after much longer exposures (e.g. 48 h, Figure 6.1(d)). Kolics *et al.* used AES to study a 2024-Al sample dipped in 0.1 M NaCl solution (pH 6.0) for 90 min, and reported that an iron oxide corrosion product formed on the Al-Cu-Fe-Mn particle [105]. The non-detection of iron oxide at this type of particle in the present work, after longer exposures and higher NaCl concentrations, implies that the ZPO coating delays the onset of corrosion. The Al-Cu-Mg and Al-Cu-Fe-Mn regions appear to receive some enhanced protection from dissolution by the ZPO coating and the subsequently-formed oxide layers.

6.4 Concluding Remarks

This chapter contributes new information for the effect on ZPO coating formation of the surface oxides and underlying metal substrate at different microstructural areas on the 2024-Al alloy. AES measurements indicate that mechanical polishing in water causes the Al-Cu-Mg particle surface to become rich in metallic Cu, while the covering oxide subsequently formed predominantly involves Al and Mg. The oxide on the Al-Cu-Mg particle has a composition that is more easily etched, compared with the Al-Cu-Fe-Mn and matrix regions, where Al oxide is the main component. As a result, when dipped in the acidic coating solution, the Al-Cu-Mg particles are the first locations on the whole surface where metal contacts the solution, triggering reactions leading to coating deposition. The Cu-rich metal layer beneath the surface oxide is more cathodic than the other microstructural areas and is another factor causing increased coating deposition at the Al-Cu-Mg particle. It was determined that the oxide compositions at the matrix and Al-Cu-Fe-Mn regions are very similar, although the ZPO coating characteristics at these two micro-regions are quite

different. That gives further direct support to the prevalent idea that electrochemical properties of the underlying metal substrate have a dominant influence on coating formation.

Immersion of a ZPO-coated 2024-Al sample in the corrosive NaCl solution for 3 h results in partial dissolution of the ZPO and precipitation of Zn-Ni oxide, accompanied by oxidation of Al metal. Phosphate at the Al-Cu-Fe-Mn and matrix regions dissolves, but some phosphate coating remains at the Al-Cu-Mg region. However, as a result of the extended exposure for 48 h, phosphate is completely removed from all regions on the surface, and a layer containing Al and Zn oxides forms on the alloy. Corrosion occurs first at the matrix region on the coated surface, as noted in Section 6.3.3.3. The ZPO coating provides more protection to the second-phase particles compared to the matrix, due to the different characteristics (e.g. morphology, composition) of the coating at each microstructural area.

Chapter 7

Growth of Chromate and Permanganate Conversion Coatings on 2024-Al Alloy

7.1 Introduction

Chromate conversion coatings (CCCs) formed by immersion in an acidic solution of chromate and fluoride have long been used for the anticorrosive protection of aluminium alloys [128-138], although health and environmental considerations have more recently led to legislative limitations on their continued use. Accordingly, there are strong pressures to develop alternative coatings (Chapter 1), but to date none of the new processes seems to match the performance and versatility of the CCCs. The present chapter is motivated by the belief that the presence of more fundamental knowledge for how the CCCs form and work may help to spur the development of new environmentally-friendly protective coatings.

While the microstructure of the alloy 2024-Al has been the subject of extensive investigation, studies of the mechanisms of CCC growth on this alloy remain quite limited [135,136]. Some factors associated with the nucleation and development of a CCC on such a heterogeneous alloy surface remain unclear. For instance, Waldrop and Kendig reported a significant difference in coating nucleation behaviour on the alloy matrix and on the two types of second-phase particle [139]. After a short immersion in a chromate bath, the film nucleation was reported to be faster on the Al-Cu-Fe-Mn particles than on the Al matrix, whereas that on the Al-Cu-Mg particles was considerably slower [139]. In other studies the final coating thickness on the second-phase particles was indicated to be less than on the alloy

matrix [140,141]. Hagans and Haas reported that after a CCC treatment for 3 min, the film thickness on the various regions of the 2024-Al surface followed the order: alloy matrix > Al-Cu-Mg > Al-Cu-Fe-Mn [130], and so raised doubts on the preferential CCC formation at the particles. Later Brown and Kobayashi used an ultramicrotomed 2024-Al sample and concluded that the initial stages of CCC growth occurred at the second-phase particles, and randomly over the alloy matrix region, including regions adjacent to the particles [136]. Most recently, Campestrini *et al.* [135] reported that the initial CCC nucleation occurs on the second-phase particles, with the later film growth over the alloy matrix. However, in the work to date, the local coating chemistry has not been determined by using a surface analytical technique.

The research reported in this chapter reinvestigates the early stages of CCC growth over the different microstructural regions of a 2024-Al surface. Scanning Auger microscopy, with its capability of providing high spatial resolution, was used for the first time to investigate the nucleation and growth processes for CCCs on this alloy. Complementary characterizations were made using scanning electron microscopy (SEM). This project aims to refine mechanistic understanding for the CCC process, and to reconcile with earlier observations that have often appeared conflicting.

One alternative approach to CCCs is provided by permanganate conversion coatings (PCCs) which are reported to give comparable protective properties, but without the deleterious environmental effects of the CCCs [142-147]. The PCC system is based on Mn(VII) in solution being reduced to oxide of lower oxidation state which coats and passivates the substrate analogously to the CCC process [142,144], where chromates are reduced to Cr(III) oxide/hydroxide, along with metallic oxidation. Similar to CCCs, the PCC process is reported to be self-limiting, and does not continue beyond the formation of a thin

yellow-gold film [144]. After drying, the PCC-coated metal is usually painted, and there are reports of favorable properties, such as for paint adhesion and filiform corrosion protection [143-147].

However, there are some differences between the CCC and PCC systems. While the CCC process gives a protective inorganic polymer, the PCC system does not, which makes it less affected by heat, and gives fewer restrictions for painting compared with the CCCs [144,148]. For many Al alloys, PCCs and CCCs are reported to provide similar levels of corrosion protection [144-147], but the former work less well for the Cu and Zn-rich alloys (2XXX and 7XXX series), where use of an organic seal is needed after a PCC treatment in order to increase the corrosion resistance sufficiently. In the context of Mg alloys, PCCs have also been reported to give similar corrosion resistance to the CCCs [149-153], and another development is based on a permanganate-phosphate treatment [154,155].

Although PCCs appear to have some promising properties as possible alternatives to CCCs on Al alloys [142-144], information on these coatings is limited and often restricted to patent claims [145-147,156]. While Danilidis *et al.* [142] described PCCs grown by a 'no-rinse' procedure on AA3003 alloy, and Bibber has reported promising anticorrosive performances for PCCs on various Al alloys [143-147], the formation and growth mechanisms of such coatings are still unknown. That issue is investigated in this research which depends on using scanning Auger microscopy, X-ray photoelectron spectroscopy (XPS), scanning electron microscopy (SEM) and energy-dispersive X-ray (EDX) spectroscopy to follow both early and later growth stages of PCCs over 2024-Al. Special attention was paid to early growth over the Al-Cu-Mg and Al-Cu-Fe-Mn second-phase particles, as well as on the alloy matrix.

7.2 Experimental Details

The study used 2024-Al plates ($1 \times 1 \text{ cm}^2$) which had been polished in the manner described in Section 3.2. The polished samples were dipped in the CCC bath at room temperature for periods between 3 s and 2 min; the bath was formed by mixing 4 g CrO_3 , 3.5 g $\text{Na}_2\text{Cr}_2\text{O}_7$ and 0.8 g NaF per 1 L of deionized water, as used previously by Sun *et al.* [80] and Brown and Kobayashi [136]. Other polished samples were coated by immersion in a PCC solution containing 0.1 M KMnO_4 and 0.05 M $\text{Na}_2\text{B}_4\text{O}_7 \cdot 10 \text{ H}_2\text{O}$ (borax) at 25°C for periods ranging from 1 to 210 min. The bath recipe used is among those proposed by Bibber [145-147], and the concentration of KMnO_4 is close to that used by Danilidis *et al.* [142]. During the permanganate treatment, the solution was stirred and the samples were suspended vertically in the bath. Because of previous interest in the effect of temperature on PCC coatings [143-147], two additional samples were prepared by coating for 3 min at 50°C in one case and at 68°C in the other. As a final step (for both chromate and permanganate treatments), each coated sample was rinsed in distilled water and dried in air.

The Auger point analyses and the associated SEM images were conducted using the primary electron beam set at 10 keV and 4 nA. Other SEM micrographs were obtained using a Hitachi S-4700 microscope. XPS measurements were made with a Leybold MAX200 spectrometer using the Mg $\text{K}\alpha$ (1253.6 eV) or Al $\text{K}\alpha$ (1486.6 eV) sources operated at 15 kV and 20 mA. A Hitachi S-3000N microscope with the incident beam accelerated through 5 or 20 kV was used for the EDX and associated SEM analyses. Each EDX spectrum was acquired over a collection time of 100 s.

7.3 Results and Discussion

7.3.1 Chromate Coatings

7.3.1.1 Auger Spectra

7.3.1.1.1 Sample After 5 s Immersion

Figure 7.1 shows examples of major microstructural features on the 2024-Al surface after the chromate treatment for 5 s. While some second-phase particles appear to remain intact without marked change according to the SEM micrographs (Figures 7.1(a),(b)), others show some modification has occurred. The example in Figure 7.1(c) for a Al-Cu-Fe-Mn particle is consistent with the effects of galvanic coupling near the boundary between the particle and matrix, and Figure 7.1(d) shows an enlarged fragment where this type of interaction has led to the formation of a peripheral trench (i.e. at the boundary between the particle and the alloy matrix). In addition, some Al-Cu-Mg particles appear to have selectively dissolved leaving pits and/or porous remnants (e.g. Figure 7.1(e)). Sometimes the pitting and peripheral trench formation leads to porous halo-like structures surrounding either the Al-Cu-Fe-Mn (Figures 7.1(c),(d)) or the Al-Cu-Mg (Figure 7.1(e)) types of particle. A view of the topography of the alloy matrix is presented in Figure 7.1(f). In addition to scratches originating with the polishing, the effects of acid etching are seen, as well as the appearance of nodule-like features (bright round spots in Figure 7.1(f) with dimension 50 nm or less).

In earlier work, both the above-mentioned halos and the nodules have been supposed to originate with CCC precipitates [136], but Auger electron spectra offer the opportunity to assess directly composition at the different regions. Figure 7.2 presents some particular spectra from a visually intact Al-Cu-Mn-Fe particle (spectrum 1), from an intact Al-Cu-Mg particle (2), and from the alloy matrix (3); for comparison (4) and (5) are from two different

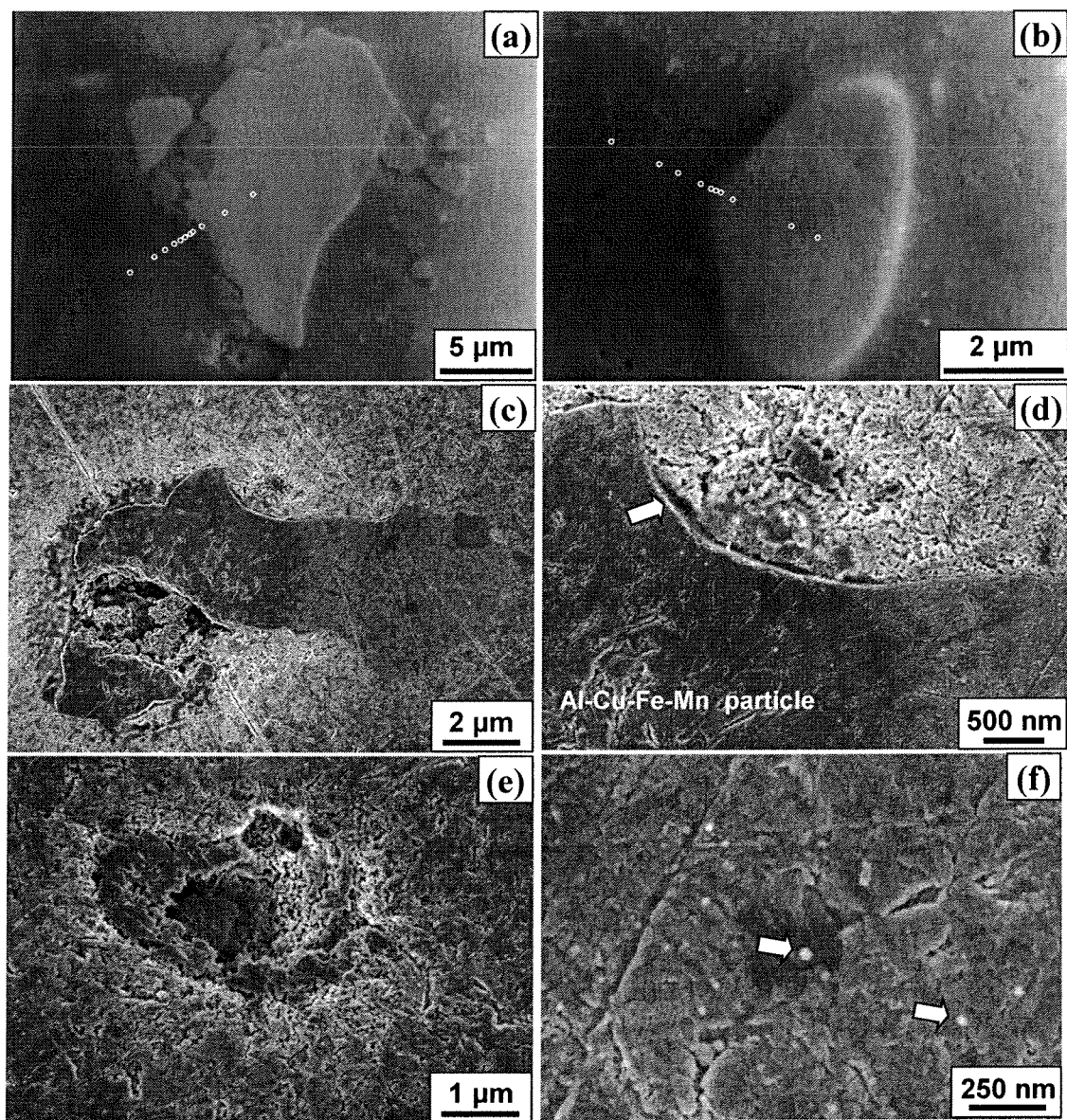


Figure 7.1 SEM images from different regions of 2024-Al alloy after 5 s CCC treatment: (a) intact Al-Cu-Fe-Mn particle; (b) intact Al-Cu-Mg particle (white dots depict positions for Auger point analysis); (c) Al-Cu-Fe-Mn particle demonstrating a partial halo; (d) higher-magnification image of same particle showing trench (marked by arrow) at interface with Al matrix; (e) Al-Cu-Mg particle demonstrating dealloying with a surrounding halo-like structure; (f) Al matrix showing evidence of acid etching and light nodules (marked by arrows).

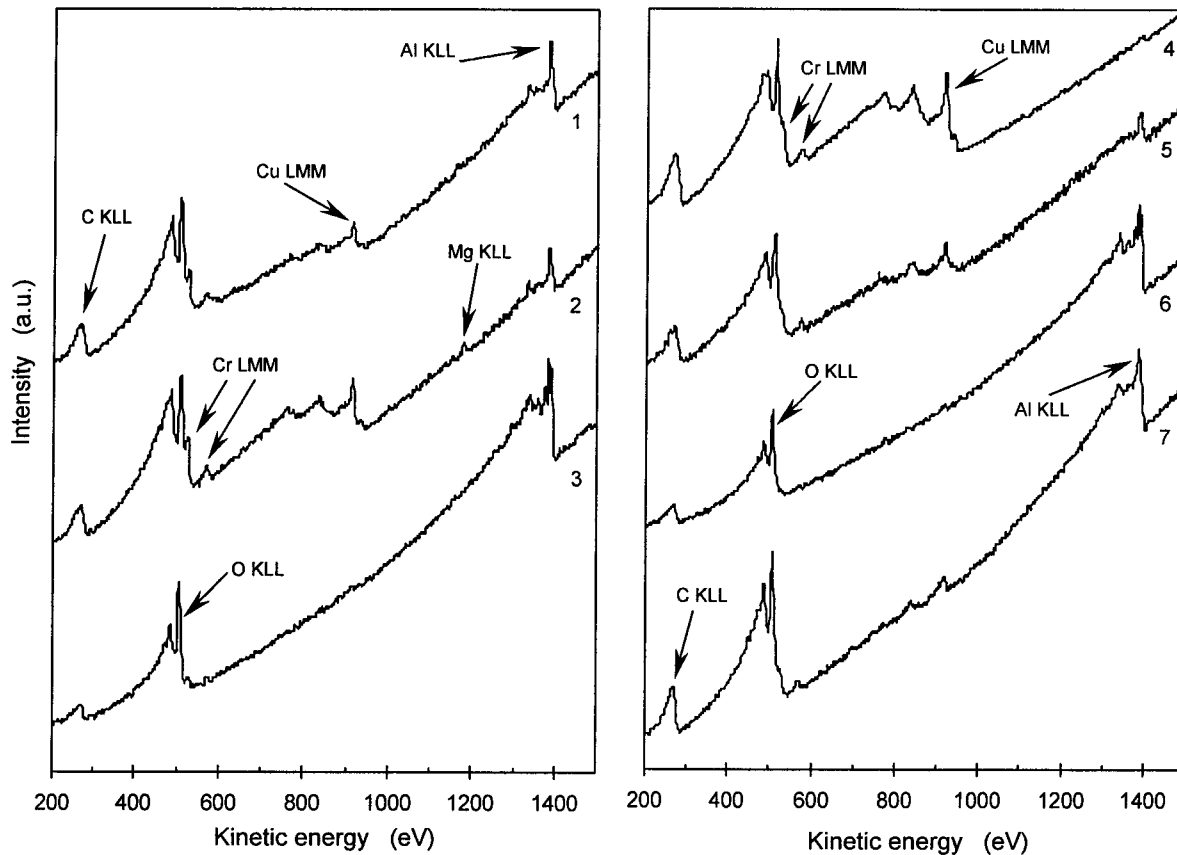


Figure 7.2 Point Auger spectra measured for 2024-Al after 5 s CCC treatment from: (1) intact Al-Cu-Fe-Mn particle; (2) intact Al-Cu-Mg particle; (3) Al matrix; (4) and (5) two different locations from a Al-Cu-Mg particle that has undergone dealloying; (6) nodule on matrix (as marked by arrows in Figure 7.1(f)); and (7) halo surrounding severely dealloyed Al-Cu-Mg particle.

regions of a dealloyed Al-Cu-Mg particle, while (6) is from a nodule on the alloy matrix and (7) is from a halo surrounding a dealloyed Al-Cu-Mg particle. Some characteristic elemental peaks are marked by arrows including Cr LMM transitions (kinetic energies 529 and 571 eV), Cu LMM (918 eV), Mg KLL (1249 eV), Al KLL (1393 eV), O KLL (506 eV) and C KLL (266 eV). The examples represented in Figure 7.2 show considerable variation in composition for these different regions after the 5 s chromate treatment.

In Figure 7.2, the intact Al-Cu-Fe-Mn particle (spectrum (1)) and Al-Cu-Mg particle (2) both show appreciable signals for Al and Cu, as well as Cr from the coating. Spectrum (3) from the alloy matrix shows especially the presence of Al and O, with some adventitious C and just a trace of Cr. Spectra (4) and (5) from two regions of the same dealloyed Al-Cu-Mg particle show contrasting behaviour. Spectrum (4) indicates that strong dissolution of Mg and Al has occurred from that location, with an enhanced Cu signal (metallic and oxidized Cu), while spectrum (5) is more similar to that of the intact Al-Cu-Mg particle (except that the Mg KLL signal is not detected and the Cr signal is weaker in the former case). The dealloying associated with spectra (4) and (5) corresponds to the type of porous structure seen in Figure 7.1(e), and in corrosion tests [7,157]. The surface of this Al-Cu-Mg particle is inhomogeneous, with varying Cu and Al content for the surface region, and apparently no Mg is detected from within the probe depth. At some locations of this particle (see spectrum (4)), Cu, O and Cr are detectable with only a trace signal for Al. In contrast, spectrum (2) in Figure 7.2 was taken over an Al-Cu-Mg particle that seemed not to have dissolved after 5 s; in that case Mg is still detected with a larger presence of Al.

Spectrum (6) from the nodule is very similar to that of the alloy matrix (although no Cr is detected on the nodule), and both appear to be composed mainly of oxidized Al. Hence this observation does not support the view expressed by Brown and Kobayashi that the nodules

represent incipient CCC formation on the alloy matrix [136]. In previous discussions of early CCC growth, much attention has been paid to the halos surrounding the electrochemically active particles at the initial stage of film nucleation [135,136]. Such halos have been thought to result from local CCC deposition, however the Auger spectra in Figure 7.2 do not support that view. For example, comparison of spectra (3) and (7) shows that the amounts of Cr over the Al matrix and the halo-like structure are comparable, while much more Cr is detected over the intact second-phase particles (spectra (1) and (2)).

Measurements of Cr/Al ratios from the Auger analyses at different positions across the matrix-particle interface for both the Al-Cu-Fe-Mn and Al-Cu-Mg types of particle, where there is no evidence for significant dealloying after 5 s, are presented in Figure 7.3. The particles studied are those shown in Figures 7.1(a),(b), where the white dots indicate the locations of the point Auger analyses made for these measurements. The results in Figure 7.3 for the 5 s chromate treatment (open symbols) show that the Cr/Al ratio distribution is relatively constant across these particles. The values are considerably larger than for the adjacent Al matrix, where after 5 s there is only a small amount of Cr and, accordingly, the Al detected is relatively increased compared with the particles. The somewhat lower value of Cr/Al at the matrix-particle interface (open diamonds in Figure 7.3(a)) is believed to result from the strong electrochemical dissolution of matrix by the second-phase particle [135,136], although trench formation is not visible in Figure 7.1(a). The decrease in Cr/Al ratio at the periphery of the Al-Cu-Mg particle (shown in Figure 7.1(b)) is not so prominent in Figure 7.3(b) (open squares), which suggests a lower cathodicity for that particle. While different particles (without direct evidence for dealloying) showed somewhat different individual values for the Cr/Al ratio, the trends from point analyses across the interface regions matched well with the situation reported in Figure 7.3 for after 5 s of coating (open symbols).

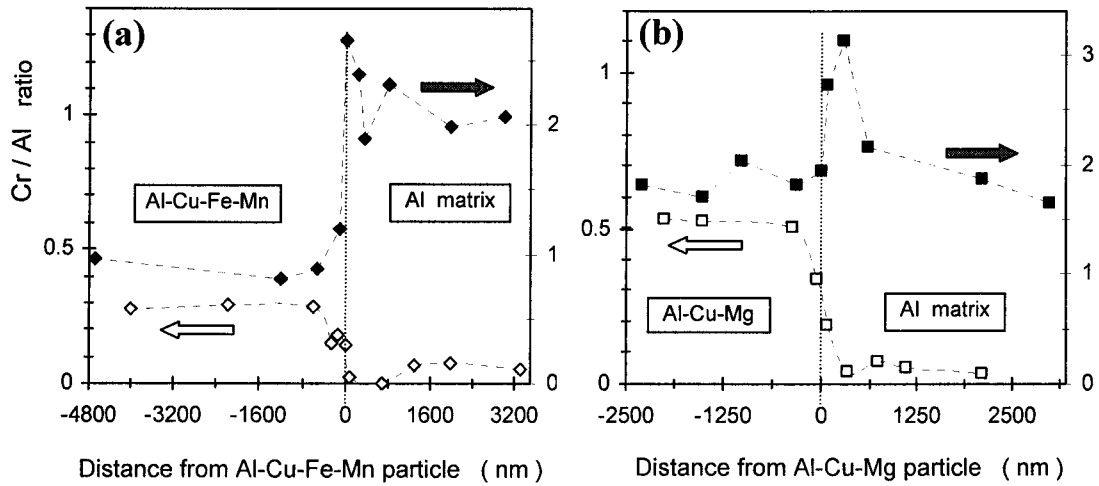


Figure 7.3 Cr/Al ratios from Auger point analysis measured across interfaces between Al matrix and intact second-phase particles: (a) Al-Cu-Fe-Mn particle and (b) Al-Cu-Mg particle. The open symbols are for 5 s CCC treatment, closed symbols for 30 s CCC treatment; the dashed lines are given as a guide to the eye only. Each curve has its own vertical scale as indicated by the arrows.

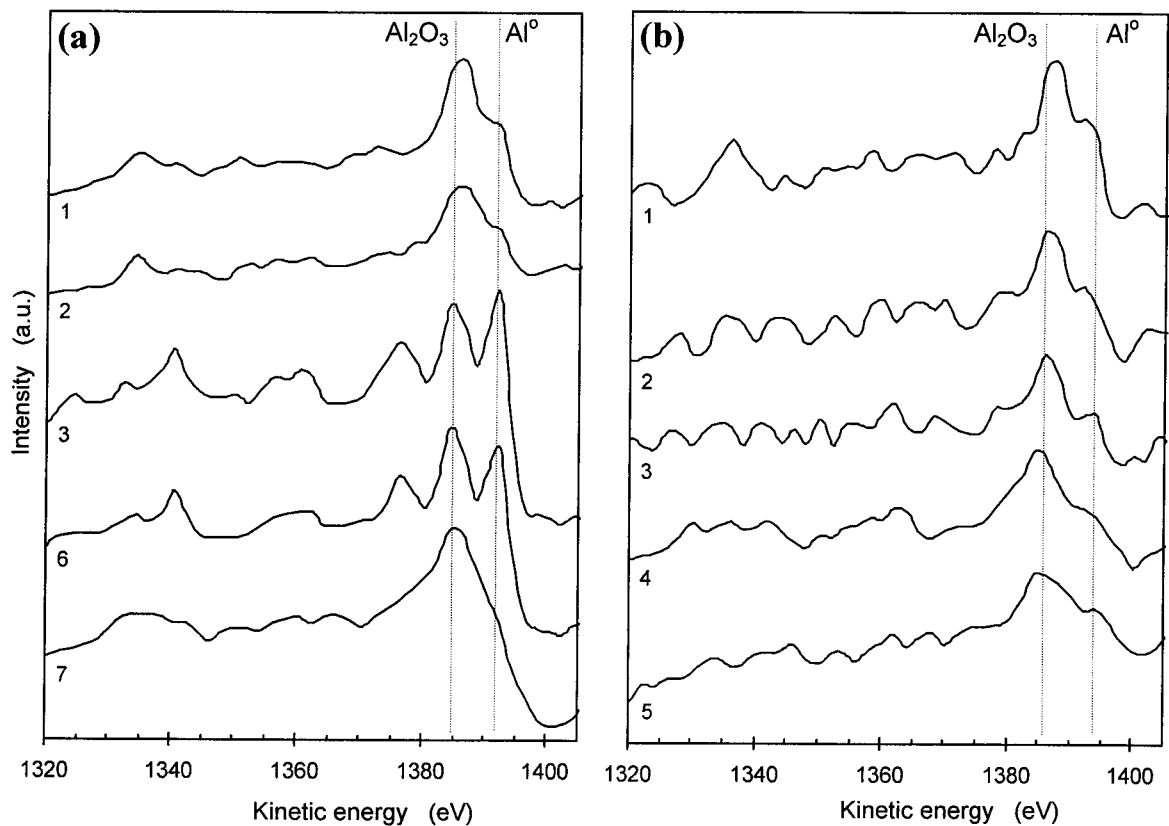


Figure 7.4 Al KLL Auger spectra measured from different regions of 2024-Al alloy after CCC treatment. Those in (a) are after 5 s treatment from: (1) central part of intact Al-Cu-Fe-Mn particle; (2) central part of intact Al-Cu-Mg particle; (3) Al matrix; (6) nodule on matrix; (7) halo surrounding severely dealloyed Al-Cu-Mg particle. Spectra in (b) are after 30 s treatment from: (1) intact Al-Cu-Fe-Mn particle; (2) intact Al-Cu-Mg particle; (3) Al matrix; (4) severely dealloyed Al-Cu-Mg particle; (5) halo in vicinity of particle in (4).

Figure 7.4(a) compares Auger Al KLL spectra from the same locations (and same labels) as for the spectra shown over a wide energy range in Figure 7.2, except the spectra (4) and (5) are not included in Figure 7.4(a) because of very low intensities. The vertical lines in Figure 7.4(a) indicate positions of structure characteristic of Al in its metallic and oxygen-bonded forms, and it is clear that both are present within the top layers probed (<10 nm), although the oxidized component is likely to be partly hydrated. More oxide is indicated in spectrum (6) than in spectrum (3), and this supports the earlier conclusion that the nodules observed after the 5 s immersion especially involve oxidized Al. This conclusion is also apparent for the alloy matrix, where similar overall compositions detected by Auger electron spectroscopy were indicated by comparing spectra (6) and (3) in Figure 7.2. The smaller metallic Al components observed in spectra (1) and (2) of Figure 7.4(a), belonging to the unaltered second-phase particles, apparently result from the thicker chromium oxide coatings over them, as compared to the matrix and nodules, but the existence of oxidized Al at the film-particle interface is still indicated. The appreciable oxidized-Al component in spectrum (7) of Figure 7.4(a) is fully consistent with the strong O signal in spectrum (7) of Figure 7.2.

In summary for this section, after 5 s of chromate immersion, the 2024-Al surface has received a discrete coating, with most CCC being located on top of those second-phase particles that appear intact. This finding supplements previous reports by Brown and Kobayashi [136] and by Campestrini *et al.* [135] who also concluded that the film initiation occurs over the intermetallic particles, but that was based on atomic force microscopy and energy dispersive X-ray analysis, rather than on the more direct surface analytical technique used here. Moreover, oxidized Al is apparent both on the uncoated alloy matrix (which was exposed to air) and on the coated second-phase particles, with its amount varying across the whole 2024-Al surface. It should also be noted that, although much more CCC was detected

over intact particles than over the alloy matrix, the surface of the Al-Cu-Fe-Mn particle in Figures 7.1(c),(d) looks much smoother than the Al matrix in Figure 7.1(f). It is possible that a denser CCC forms electrochemically on such a surface morphology, as has been reported previously [135]. Such a denser film over intermetallic particles could arise from the fast CCC deposition over the second-phase particles during the first stage of film growth [135,136].

7.3.1.1.2 Sample After 30 s Immersion

Figure 7.5 presents examples of typical features observed on the 2024-Al surface after the CCC treatment for 30 s. Although the contrast between various microstructural features is not as strong as after 5 s (Figure 7.1), the second-phase particles and Al matrix can be well distinguished. In Figure 7.5, part (a) is for a Al-Cu-Fe-Mn particle, (b) for a heavily dealloyed Al-Cu-Mg particle, (c) for an Al-Cu-Mg particle which has not changed according to SEM, and (d) is for the alloy matrix. Figure 7.6 compares Auger spectra collected from different second-phase particles and from the Al matrix after the 30 s chromate treatment. Spectra are reported from intact Al-Cu-Fe-Mn (1) and Al-Cu-Mg (2) particles and from the Al matrix (3); the spectrum (4) is from a previously dealloyed Al-Cu-Mg particle, where traces of Cu are still detected, while (5) is from a halo-like structure surrounding the particle. All spectra in Figure 7.6 demonstrate relatively strong and comparable Cr signals.

After the 30 s immersion, the 2024-Al surface looks generally more porous, although the coating morphology varies with the underlying microstructure (compare Figures 7.1 and 7.5). The basically intact particles in Figures 7.5(a),(c) have different chemical composition but demonstrate similar behaviour, insofar as they are covered by CCC and no peripheral

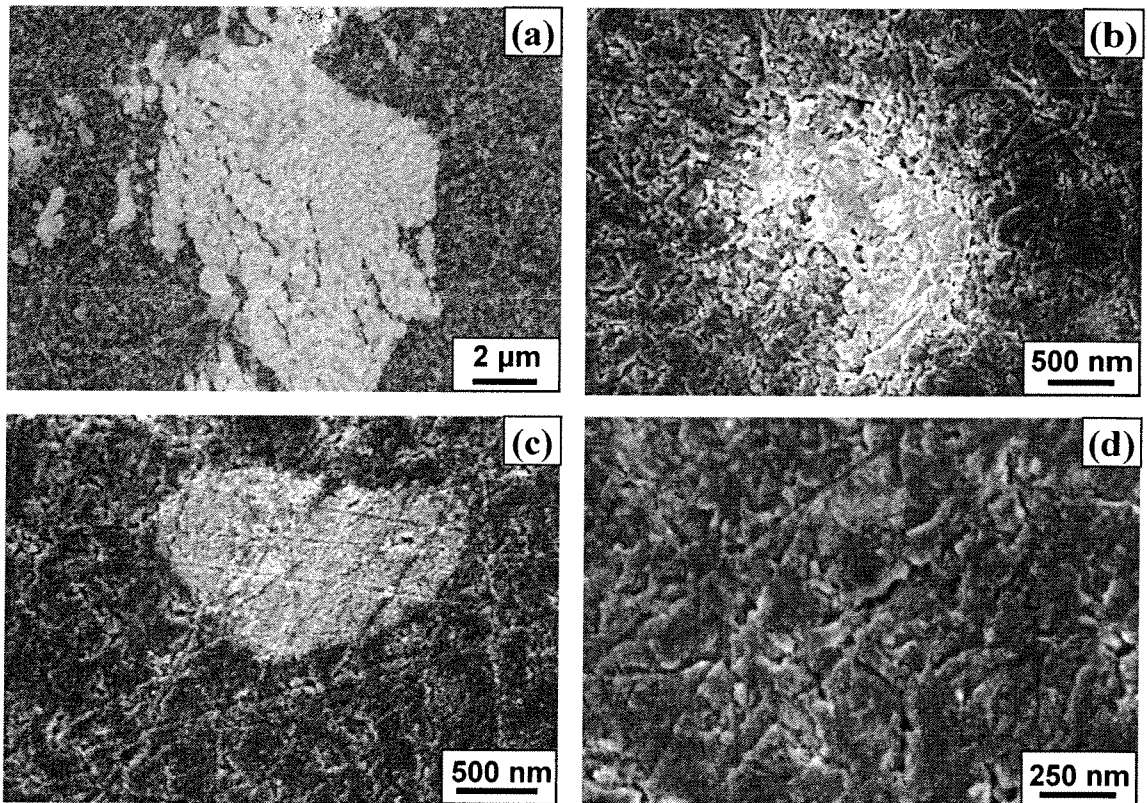


Figure 7.5 SEM images from different regions of 2024-Al alloy surface after 30 s CCC treatment: (a) Al-Cu-Fe-Mn particle; (b) Al-Cu-Mg particle that has undergone dissolution; (c) Al-Cu-Mg particle that has remained intact; and (d) Al matrix.

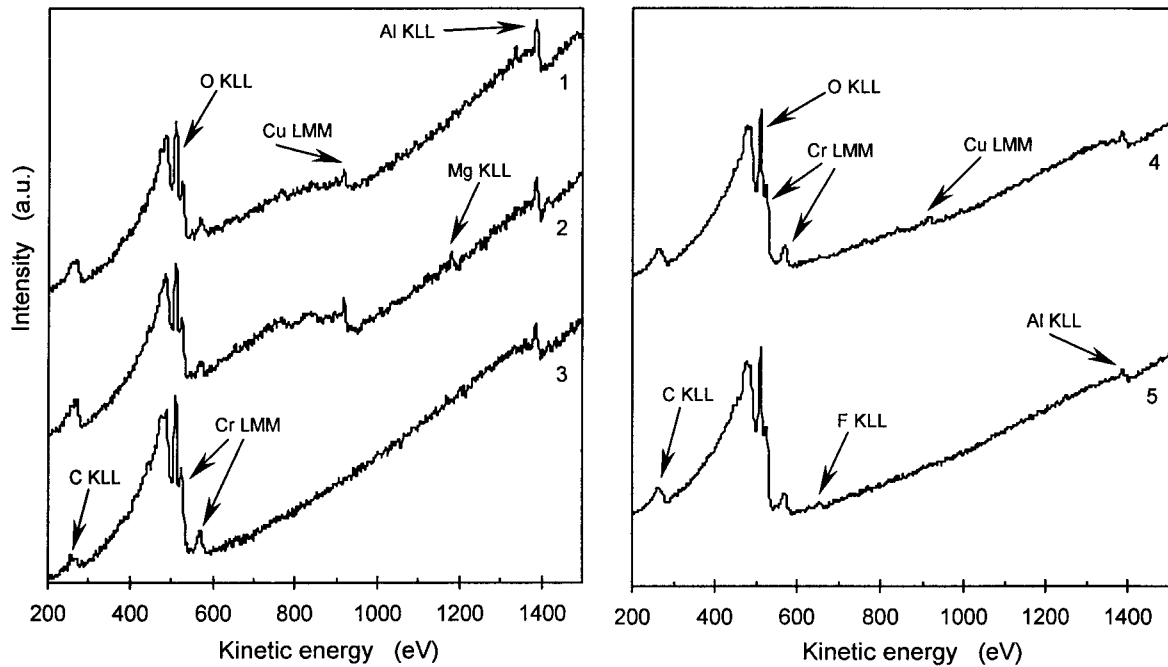


Figure 7.6 Point Auger spectra measured for 2024-Al after 30 s CCC treatment from: (1) intact Al-Cu-Fe-Mn particle; (2) intact Al-Cu-Mg particle; (3) Al matrix; (4) Al-Cu-Mg particle that has undergone severe dealloying; and (5) halo in vicinity of particle in (4).

trenches are observed. The Auger point spectra taken over these particles allow their origins to be distinguished: for example the Al-Cu-Mg particle still shows a weak peak of Mg (see spectrum (2) in Figure 7.6). The Auger point spectrum ((4) in Figure 7.6) confirms that the formerly dissolved Al-Mg-Cu particle with a halo-like vicinity is coated by CCC, and it appears porous (Figure 7.5(b)). The rapid CCC growth over dissolved particles between 5 and 30 s of chromate immersion probably results from the surface becoming porous by the dealloying and by the more cathodic nature of the remnant Al-Cu-Mg particle after dealloying.

Figure 7.5(d) shows a surface image of the alloy matrix after 30 s coating. Comparing that with after 5 s (Figure 7.1(f)) confirms there are a smaller number of nodules after the longer immersion time, which is consistent with their Al_2O_3 nature. The more pronounced porosity of the matrix surface is assumed to result from both the further acid etching and more deposition of amorphous Cr oxide. Also many Auger spectra measured after the 30 s immersion demonstrate weak F peaks, which were not detected from the sample treated for 5 s (compare Figures 7.2 and 7.6). Apparently the extra Al^{3+} in solution after 30 s may have led to the local solubility of AlF_3 being exceeded.

Figure 7.4(b) presents Al KLL Auger spectra corresponding to the locations measured in Figure 7.6. The allocation of structure emphasized by metallic and oxidized Al (as in Figure 7.4(a) for 5 s) reveals that less metallic Al is detected within the surface region of the sample after the 30 s treatment, as expected with a thicker CCC. A possible factor contributing to the oxide part of the Al KLL structure in Figure 7.4(b) might be hydrated species incorporating into the growing film. However, as was reported by Xia *et al.* [158], who scraped off a CCC and analyzed by inductively-coupled plasma spectroscopy, the Al/Cr ratio in such coatings is only of the order of 0.01. Therefore it appears most likely that the Al-

oxide components after 30 s originate more from the coating-substrate interfacial regions, with such contributions applying over the entire sample.

Figure 7.3 (filled symbols) reports the distribution of measured Cr/Al ratios over the intact second-phase particles and the adjacent alloy matrix after 30 s immersion in the CCC bath. The sample is now fully coated and more uniformly distributed. However, the CCC thickness is not constant, and the interfaces between the underlying second-phase particles and the alloy matrix are still detected insofar as the Cr/Al ratios demonstrate discrete change at their location. Since the Cr deposition after 5 s is especially on the particles, it is clear that fast CCC growth occurs over the Al matrix during the 5 s to 30 s period of coating. Also after this time of coating, the dealloyed second-phase particles are coated with a CCC layer similar to the intact particles.

7.3.1.2 Behaviour of Intermetallic Particles

Based on the behaviour of the intermetallic particles previously reported in a number of corrosion tests applied to 2024-Al alloy [7,105,159,160], it was not unexpected that similar behaviour would be demonstrated during the initial period of CCC growth. With immersion of 2024-Al in the chromate solution, the cathodic (Cr(VI) to Cr(III)) reaction takes place over Al-Cu-Fe-Mn particles, and the deposition of Cr(III) oxide occurs along with anodic dissolution of Al from the matrix immediately adjacent to the particles (as observed in Figure 7.1(d)). The Al-Cu-Fe-Mn particles are always noble with respect to the Al matrix, and hence are expected to demonstrate pitting (matrix dissolution) along their perimeter from galvanic coupling [136,43]. This is shown in Figure 7.1(d), where a trench forms at the perimeter of part of an irregular Al-Cu-Fe-Mn particle. Interestingly, a less-developed dissolution of Al matrix at the vicinity of another irregular particle is suggested by the reduced value of the

Cr/Al ratio at the particle-matrix interface (Figure 7.3(a), open diamonds), although that is not directly observable in the SEM image (Figure 7.1(a)). The more intense Al dissolution close to the particle apparently suppresses the Cr oxide deposition, thereby reducing the Cr/Al ratio over a range of ~500 nm from the particle. This suggests that the only difference between the peripheries of the particles in Figures 7.1(a) and 7.1(c),(d) is the degree of Al dissolution and trench development. The latter can be governed by a range of factors including initial oxide thickness, mechanical stress and cracking, and local composition. Also the deposited Cr oxide can limit further matrix pitting at the periphery by electronic insulation or by restricting diffusion of cathodic reactants [7]. Such factors can lead to the Al-Cu-Fe-Mn particle in Figure 7.1(c) demonstrating different degrees of pitting along its periphery.

More complex behaviour was demonstrated by the Al-Cu-Mg particles; only some of them initially acted as anodic sites and dissolved during the first 5 s of chromate treatment. The others appeared to have not appreciably dealloyed, and they acted more like the Al-Cu-Fe-Mn particles. Such a dual electrochemical behaviour of Al-Cu-Mg particles, with respect to the alloy matrix, when in a corrosive solution has been mentioned previously [136,7]. It is generally accepted that the Al-Cu-Mg particles are initially active, thereby releasing Mg and Al into solution [136,7,105] but, after a sufficient enrichment of Cu by dealloying, these particles change their galvanic relationship by becoming more noble. Such Cu-enriched particles are expected to induce peripheral matrix dissolution, analogous to that formed around initially noble particles [136,7].

Buchheit *et al.* [7] observed two types of concurrent behaviour for Al-Cu-Mg particles in corrosive NaCl solutions, and mentioned that there is no obvious metallurgical or microstructural factors that influence whether peripheral matrix pitting or selective particle dissolution occurs. They also reported that the two types of pitting behaviours result from

electrochemical activity of the particles with respect to the Al matrix. The dealloying, which leaves Cu-rich remnants, can occur in two ways. In the first, the remnants are basically intact and, being ennobled by dealloying, they produce pitting in the matrix at their periphery. In the second, Cu remnants detach from the surface and are removed from the pit formed by solution. While the Auger point analysis reported here generally supports the second model of behaviour (Cu clusters from dealloyed remnants could redeposit, e.g. (7) in Figure 7.2), this analysis is less consistent with the first model, as the Al-Cu-Mg particles which did not appear to have been selectively dissolved (e.g. Figure 7.1(b)) demonstrated Mg peaks in their Auger spectra after both 5 s and 30 s chromate treatments (spectra (2) in Figures 7.2 and 7.6).

Based on the results presented above for the “intact” Al-Cu-Mg second-phase particles, one can conclude that such particles, unlike those selectively dissolved during the few first seconds of immersion, acted as cathodic sites on which CCC formed before its growth on the alloy matrix. For the behaviour of intermetallic particles which are expected to be less noble with respect to the Al matrix, there may be effects due to compositional heterogeneity [159,160], for example due to surface depletion from earlier processes within the particle. This could lead to a surface that is depleted in Mg, thus making it noble, even though the more-regular composition is maintained below the surface. Such Al-Cu-Mg particles will act as cathodic sites, similar to the Al-Cu-Fe-Mn particles, and unlike the Al-Cu-Mg particles without a Mg-depleted surface. However, more needs to be known about the contrasting situations for these particles.

The detection of Mg from the “intact” Al-Cu-Mg particles is consistent with the report of Kolics *et al.* [105], who also used SAM and found Mg, along with a Cr-rich coating, on Al-Cu-Mg particles after a 2024-Al surface was exposed for 90 min to a solution of NaCl and Na₂CrO₄, at pH values of 3 and 6. Moreover, it was found that the CCC formed on the Al-Cu-

Mg particles prevented their dealloying, which did take place in solutions without the Na_2CrO_4 . It was proposed that the particles dealloyed during the initial exposure, before the CCC formed [105]. That does not appear to be the dominant effect for some of these particles in our experiments, perhaps because the higher chromate concentration used here results in faster CCC growth over the particles, so blocking further Mg release from them.

The serious dealloying of some Al-Cu-Mg particles observed in our study is consistent with the AFM observations of Waldrop and Kendig [139], who reported much slower CCC nucleation on Al-Cu-Mg particles after 10 s immersion at 5°C. Indeed, at the very early stage, as seen in Figures 7.1(e) and 7.2, some Al-Cu-Mg particles lose Mg and Al by dissolution, and probably some Cu clusters are mechanically washed away from the porous structure which is forming. These phenomena are expected to retard the deposition of Cr_2O_3 on such particles, as seen in Figure 7.2, where spectra (4) and (5) reveal less Cr than for the situation covered by spectrum (2).

7.3.2 Permanganate Coatings

7.3.2.1 Coating Chemical Composition

XPS spectra of the samples were collected in order to assess how the surface chemical composition changes with time. The evolution of the metallic elements detected by XPS for permanganating times from 1 to 210 min is shown in Figure 7.7. The dominant metallic component over time is Mn, as expected from previous reports [142], and the amount of Al detected steadily decreases as the substrate is covered. For coating at 25°C, the underlying Al is no longer recognized after about 150 min. However, for coating times greater than 50 min, there is clear evidence for Mg^{2+} , K^+ and Na^+ being incorporated into the growing PCCs (Figure 7.7(b)). In addition, samples coated for 1-5 min demonstrated trace

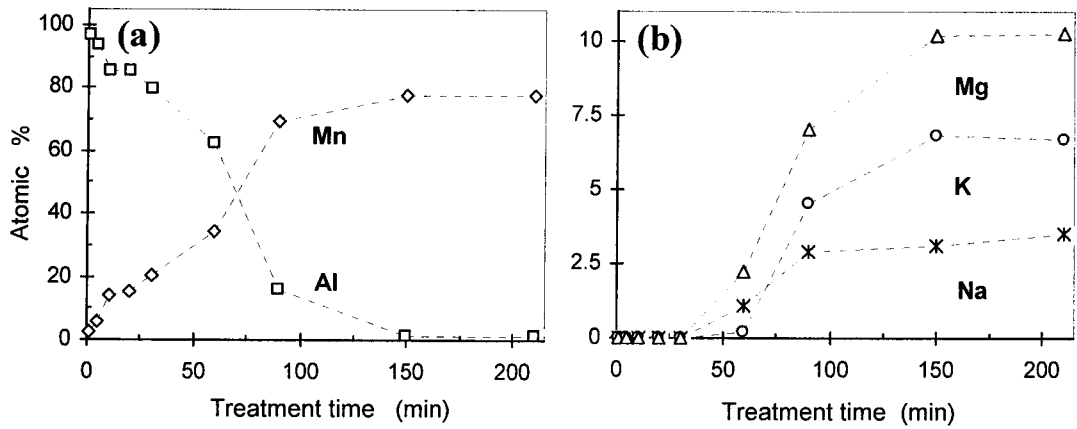


Figure 7.7 Relative amounts from XPS of major (a) and minor (b) metallic components in the surface layer of growing PCCs as a function of treatment time at 25°C. The dashed lines are given to guide the eye.

amounts of Cu in their XPS spectra. Since Cu was not detected for immersions longer than 5 min, we assume that these peaks at the early growth stage were mainly from the 2024-Al substrate (including the substrate-coating interface), and that no significant amount of Cu was incorporated into the coating at the later stages of growth. No B, originating from the borate in the solution, was detected in the coating by XPS.

Quantitative analyses of the XPS spectra for samples PCC-treated for 3 min at 50°C and at 68°C demonstrated surface compositions similar to those samples prepared at 25°C for 90 and 210 min respectively. Morphologically, the samples prepared at elevated temperatures were also similar to those prepared at room temperature with the immersion times mentioned. These trends are broadly similar to observations for temperature effects made by Bibber [145], who reported that PCCs with similar properties can be prepared by immersing Al alloys into basic KMnO₄ for 1 min at 68°C, 1.5-2 min at 57-63°C, or for ~60 min at 25°C.

According to the Pourbaix diagram for Al [161,16], the surface oxide is unstable at the pH used (~9.1), and its etching is expected to follow:



Then reactions at the freshly exposed Al surface can follow the half-reactions:



with the overall formation reaction for PCCs on Al in basic solution given as:



XPS analysis did not detect Al species from the thicker PCCs, implying that any incorporation of aluminate into the coatings must be small (after rinsing).

In principle, when Al is released into solution according to reactions 7.1 and 7.4, some alloying elements (e.g. Mg, Cu, Fe and Mn in 2024-Al) could also be released. The only such element that is clearly represented in the coating is Mg but, as noted in Figure 7.7(b), K and Na, from the permanganating bath, do incorporate at the later stages of the coating process.

7.3.2.2 Early Stages of Coating Growth

Figure 7.8 shows examples of SEM images of 2024-Al samples which have been permanganate treated at 25°C for different periods of time: 1 min (a,b) and 20 min (c,d). While the alloy matrix of 2024-Al still demonstrates polishing scratches, and thus looks etched rather than coated after 1 min of the permanganate immersion (Figure 7.8(b)), the intermetallic particles in Figure 7.8(a) look relatively intact and topographically pronounced compared with the surrounding alloy matrix. This could result either from a slower etching of the particles or from a greater deposition on them within this time of treatment.

After the 20 min treatment, the intermetallic particles (e.g. Figure 7.8(c)) appear even more topographically pronounced, thus supporting the idea that further deposition has occurred over them, and the observed “zones of influence” [162] around some particles is a signature of their electrochemical activity. For instance, the zone extending for $\sim 2 \mu\text{m}$ from the particle in Figure 7.8(c) is likely a result of more intense electrochemical processes, including etching and deposition, in the vicinity of the particle caused by its cathodicity and much smaller size relative to the surrounding matrix. At the same time, the Al matrix also shows change in the sense that the polishing scratches have become less dominant, and hillock-like islands (most likely deposits) occur in Figure 7.8(d). The topography of the PCC over the alloy matrix after 20 min treatment (round hillock-like structures) is consistent with

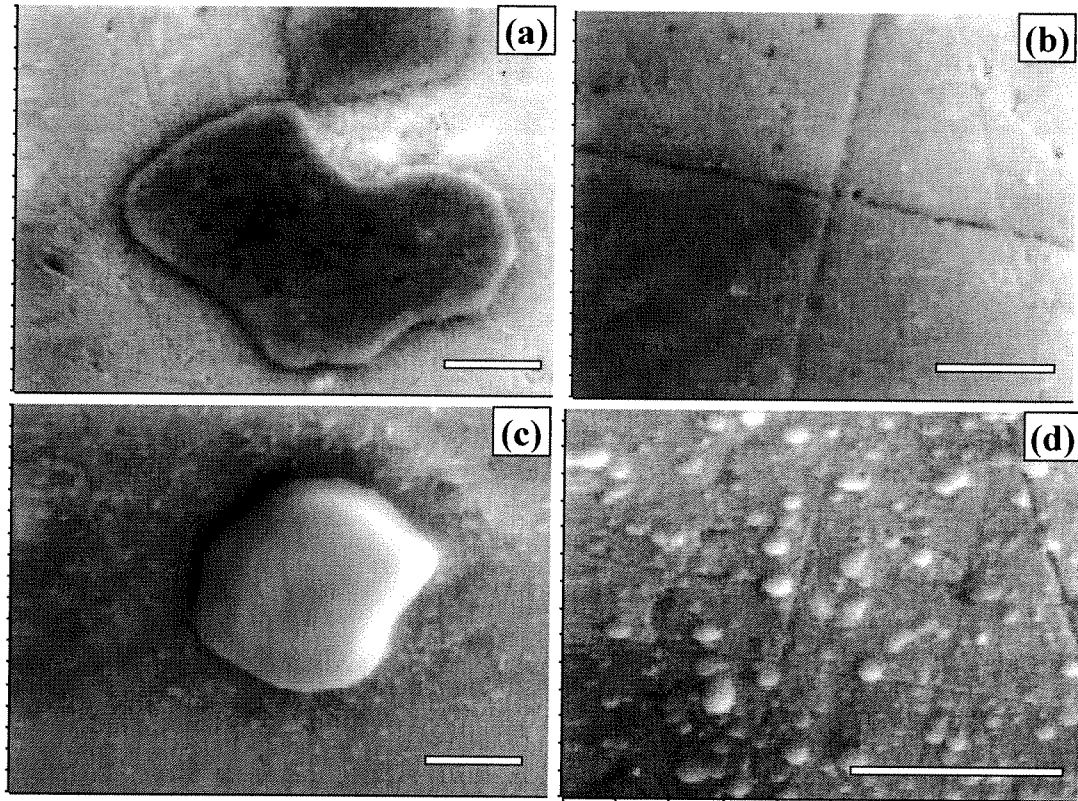


Figure 7.8 SEM images from different regions of 2024-Al samples after PCC-treatment at 25°C for different coating times: (a) both types of second-phase particle after 1 min; (b) alloy matrix after 1 min; (c) Al-Cu-Mg particle after 20 min; (d) alloy matrix after 20 min. Each scale bar indicates 2 μm .

that reported by Danilidis *et al.* for their PCC prepared by a ‘no-rinse’ procedure [142]. No obvious particle dealloying was seen by SEM in this work for the samples permanganated for 1-20 min and, except for a few pits, the second-phase particles looked unchanged (with a dense and relatively uniform coating). This is in contrast to CCCs (Section 7.3.1) where particle dealloying has been observed [135,136]. The coating bath conditions are less severe for PCCs (pH ~9 compared to ~2 for CCCs), resulting in less dissolution of Mg and Al from the Al-Cu-Mg particles.

Figure 7.9 shows some typical Auger spectra collected from different surface locations after the PCC treatment for 1 min (a) and 5 min (b). The spectra in Figure 7.9(a) allow the conclusion that Mn is present over both the Al-Cu-Mg (1) and Al-Cu-Fe-Mn (2) types of second-phase particles, while no Mn is detected over the alloy matrix. This is consistent with conclusions surmised from Fig. 7.8(a),(b) about topography at the intermetallic particles compared to the matrix. As a weak peak of Fe is observed in spectrum (2) (Figure 7.9(a)), one can conclude that the MnO₂ coating thickness on the Al-Cu-Fe-Mn particle is less than 10 nm, which is consistent with the presence of a fairly strong Al signal. Consistently with the above conclusions about relative coating thickness at different microstructural areas, the Al signal in spectrum (3), from the alloy matrix, is strong and much greater than that in spectrum (1) from the Al-Cu-Mg particle, where the coating is thicker.

Although the particles analyzed demonstrated some individuality in coating thickness, the spectra in Figure 7.9(a) demonstrate the inhomogeneous nature of the coating distribution over the 1 min sample: while all former intermetallic particle regions are well covered by PCC, no detectable Mn is seen over the matrix regions. Interestingly, there was no difference between Auger spectra taken from polishing scratches and from the relatively

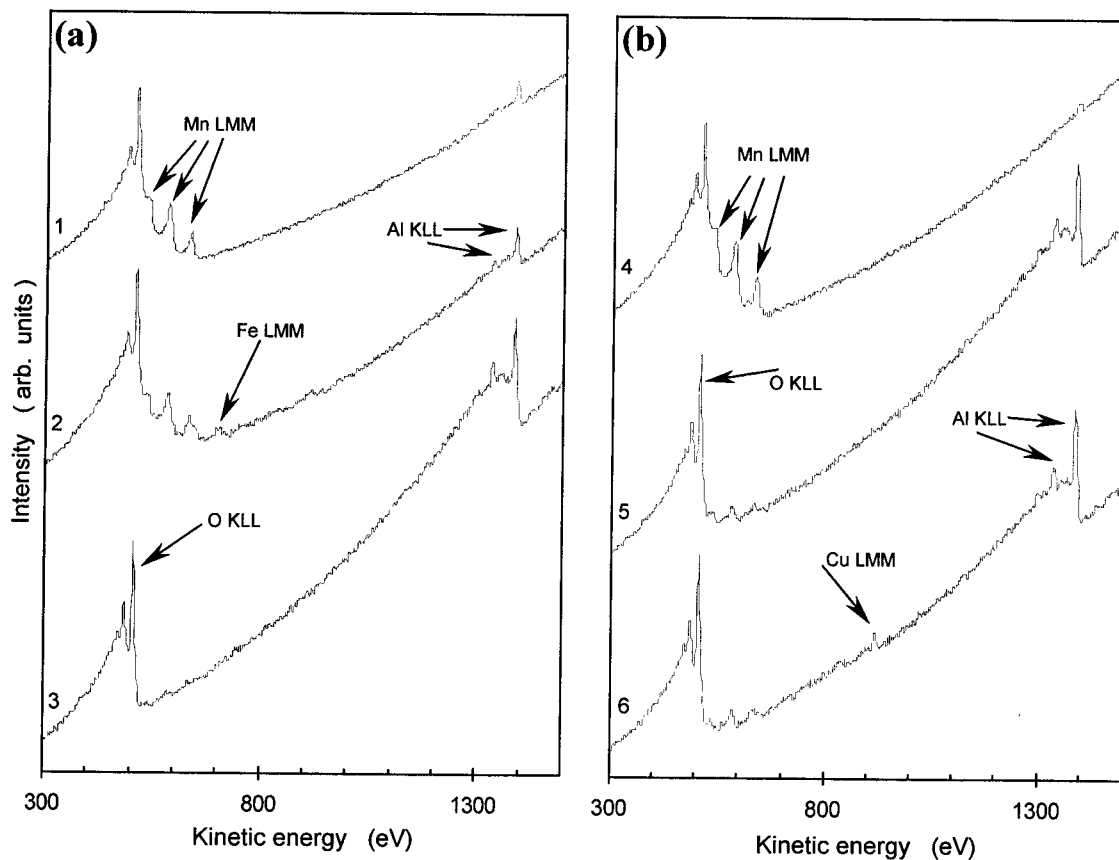


Figure 7.9 Auger point spectra measured from 2024-Al samples after PCC-treatment at 25°C for different coating times. (a) 1 min: (1) Al-Cu-Mg particle, (2) Al-Cu-Fe-Mn particle, (3) alloy matrix; (b) 5 min: (4) Al-Cu-Fe-Mn particle, (5) alloy matrix well removed from intermetallic particles, and (6) alloy matrix close to an Al-Cu-Fe-Mn particle. The arrows identify the most intense peaks in the elemental KLL or LMM series.

flat regions, implying that surface etching was dominating over all the alloy matrix during the first 1 min of permanganate immersion at 25°C.

In comparison to those in Figure 7.9(a), the Auger spectra in Figure 7.9(b) (for a sample after the 5 min immersion) clearly show the initiation of Mn deposition on the Al matrix (spectra (5) and (6)). Spectrum (4) presents a very small Al peak and no structure for Fe, which implies that the PCC over the Al-Cu-Fe-Mn particle is 10 nm or more thick (a similar spectrum, not shown, was measured for the Al-Cu-Mg particle after the 5 min immersion). Spectrum (6) demonstrates that Cu precipitates could be found on the alloy matrix near to the second-phase particles, where a “zone of influence” is established, as demonstrated in Figure 7.8(c). This implies some particle dissolution, with Cu clusters washed away and reprecipitated, and supports the belief that the electrochemical character of PCC growth on 2024-Al has a somewhat similar mechanism to that for CCC formation on 2024-Al (described in Section 7.3.1), specifically with respect to preferential deposition on cathodic regions [135,136]. It should be added that cathodic sites on the 2024-Al surface are not only confined to the large second-phase particles; they can also be present on the Al matrix due to heterogeneities, including those associated with alloying elements [136]. Electrochemical activity of such sites could be responsible for PCC deposition over the metal matrix surface.

Auger spectra taken on the Al matrix for samples treated for 10 and 20 min confirm an increase in intensity of Mn signals and hence further growth of the PCC; this supports the assumption stated above based on Figure 7.8(c),(d). Taken all together, this evidence shows the PCC grows on the second-phase particles during the first five minutes, and then nucleates with growth over the alloy matrix especially during the period 5-20 min.

XPS provides more chemical information to supplement the observations from point Auger analysis. The metallic components in Al 2p spectra were only observed for samples immersed for 1 or 5 min. This suggests that the PCC and any Al oxide which may survive after the treatment at 25°C is thicker than 10 nm after the 10 min immersion. Then, in parallel, Cu 2p peaks were seen only for samples PCC-treated for 1 and 5 min, the element being presumably from the substrate (intermetallic particles and alloy matrix). At the 10 min treatment, those peaks were no longer detected, so supporting the conclusion that the PCCs continuously covered the substrate, with a thickness (including any remaining Al oxide) of greater than ~10 nm.

The above observations for the initial growth of PCC with respect to the substrate microstructure suggest a mechanism of coating nucleation which is similar to that of CCCs (Section 7.3.1). This follows the similar electrochemical nature for deposition in both types of system, even though different pH values are used.

7.3.2.3 Thicker Coating Formation

Figure 7.10 shows some surface images for samples after PCC growth for 90 and 150 min at 25°C. In contrast to samples permanganated for shorter times (Figure 7.8), no polishing scratches can now be seen, and this is indicative of the surfaces being well covered by PCC when the treatments are for these longer times. The surface of the alloy matrix (Figure 7.10(c)) is fully covered by a relatively uniform and crack-free coating with hillock-like morphology, whereas the particles are coated with PCC that appears dense and featureless (Figure 7.10(a),(b),(d)). As shown in Figure 7.10(b), most of the bigger Al-Cu-Fe-Mn second-phase particles demonstrate cracked coating, which could result from the drying of relatively thick films on top of the particles, analogous to observations for thick

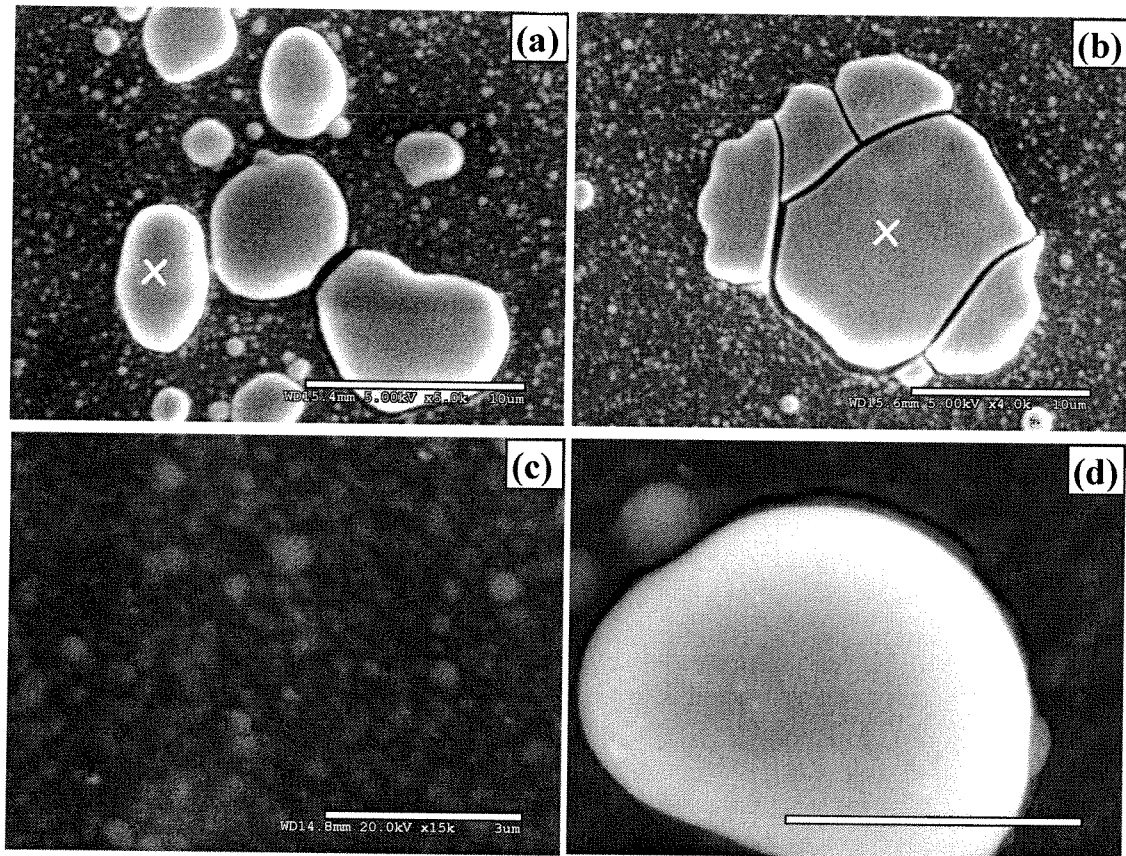


Figure 7.10 SEM images from different regions of 2024-Al samples after PCC-treatment at 25°C for different coating times: (a) cluster of Al-Cu-Mg particles with uniform coating after 90 min; (b) Al-Cu-Fe-Mn particle with cracked coating after 90 min; (c) hillock-like structure on alloy matrix after 150 min; (d) Al-Cu-Mg particle with peripheral trench after 150 min. Scale bars indicate 10 μm for (a,b), 3 μm for (c,d).

CCCs [135]. This phenomenon seems less apparent for the Al-Cu-Mg particles. The difference may depend on the particles' nature, or it may follow more from the bigger size and irregular shape for the Al-Cu-Fe-Mn particles. The deep trenches seen around the heavily coated Al-Cu-Mg particles (Figure 7.10(d)) could be caused either by electrochemical dissolution at the adjacent alloy matrix, or by a large difference in PCC thickness between the particles and their surroundings; the former would be most consistent with the experience for CCC formation [135].

The thicker PCCs are too insulating to be probed by Auger point analysis, and therefore their characterization was made by EDX in selective area analysis. Assuming a chemically uniform coating over a second-phase particle, or over the matrix at a particular area, the atomic ratio of Mn in the coating to the sum of all major metals (M = Al, Cu, Mg, Fe, Mn) in the substrate (i.e. $Mn_{\text{coating}}/\sum M_{\text{substrate}}$) should provide a guide to the relative PCC thickness at the region of interest. Since EDX characterizations show that Mn is present in 2024-Al at the same regions and at approximately the same level as Fe, this ratio can be estimated in practice as

$$R = (X_{\text{Mn}} - X_{\text{Fe}})/(X_{\text{Al}} + X_{\text{Cu}} + X_{\text{Mg}} + 2X_{\text{Fe}}), \quad (7.5)$$

where X_M represents the amount of M (in at%) detected by EDX from a local region.

Equation 7.5 can thus be applied equally to the Al-Cu-Fe-Mn second-phase particles (with $X_{\text{Mn}} \approx X_{\text{Fe}}$), as well as the Al-Cu-Mg particles and the matrix (where $X_{\text{Mn}} \approx X_{\text{Fe}} \approx 0$).

The sample treated for 90 min at 25°C demonstrated a quite uniform Mn oxide coating over the alloy matrix, with the ratio R equal to about 0.008 from all selected areas (diameter ~1 μm). (Incidentally the ratio was also found to be between 0.008 and 0.009 for matrix regions of the sample treated for 3 min at 50°C, which is consistent with observations from XPS for these two samples.) For comparison, EDX selective area analyses for the

particles marked with crosses in Figure 7.10(a),(b) gave R values equal to ~ 0.04 and ~ 0.05 respectively (approximately five times greater than R values for the matrix). Thus, it is clear that the Mn oxide deposits are significantly greater over the particles in the sample permanganated for 90 min, and the same statement holds for samples treated for longer times (samples treated for 3 min at 50 or 68°C also show the same trend).

The alloy matrix for samples permanganated for 150 and 210 min at 25°C demonstrated R values of ~ 0.009 - 0.01 for both coating times, indicating that the growth had essentially self-limited by about 150 min, and the same statement holds for coating on the particles. The self-limiting time observed in this work is longer than that reported by Bibber (~ 60 min at 25°C) [145], and the difference possibly relates to variations in surface pre-treatment prior to immersion in the permanganating bath.

Bibber reported for Al alloys with high Cu or Zn contents that a sealing procedure needs to be applied on a PCC in order to provide adequate protection in a corrosive environment [143-147]. The high cathodic activity of the Cu-containing second-phase particles in 2024-Al results in defects appearing on the surface after the PCC treatment, and this includes cracks in coatings over large particles and peripheral trenches (Figure 7.10(b),(d)). That the smaller Al-Cu-Mg particles did not demonstrate observable PCC cracks suggests there is a size dependence as well as a tendency for the defect formation to be associated with the noble character (cathodicity) of alloy inclusions. This work therefore demonstrates ways in which the more noble inclusions in the 2024-Al alloy lead to weaknesses in a prepared PCC, thereby opening the need for further sealing.

7.4 Concluding Remarks

7.4.1 Chromate and Permanganate Conversion Coatings

This chapter describes investigations of the initiation and subsequent evolution of chromate conversion coatings (CCCs) and permanganate conversion coatings (PCCs) on the different microstructural regions of a 2024-Al alloy surface.

The initial growth of CCCs is closely determined by the local microstructure. After a 5 s immersion, the coating occurs especially on the cathodic second-phase particles of Al-Cu-Mg and Al-Cu-Fe-Mn types, which did not undergo severe dealloying or etching, while little or no CCC formed on the alloy matrix. Auger measurements on the discrete nodules seen on the matrix at the earliest stages of coating indicate that they correspond to oxidized Al. Following the initial coating on the “intact” second-phase particles, their cathodicity decreases and the film growth continues on the alloy matrix. After the 30 s immersion, the coating is relatively more uniform over the whole surface.

Varying behaviours are indicated for the Al-Cu-Mg particles. While some are cathodic and coat from the start, others undergo significant dealloying during the initial exposure to the chromating bath at pH ~ 1.8 . This leads to a sponge-like Cu-rich surface, with remnants or pits, over which the CCC subsequently grows fast, apparently helped by the high porosity.

The CCC deposition on the alloy matrix appears to follow the mechanism proposed by Brown *et al.* where local galvanic couples are formed across the matrix by the various structural defects present [136,163,164]. The potential differences between these local regions are smaller than those between matrix and second-phase particles, but they still contribute to coating inhomogeneity on the matrix. A more porous coating forms on the alloy matrix compared to the second-phase particles.

Analysis of the Al $KL_{2,3}L_{2,3}$ Auger spectra after both the 5 s and 30 s chromate treatments is consistent with the coating-alloy interface containing hydrated Al oxide at both the alloy matrix and the second-phase particles. Thus it appears that the natural oxide is not completely removed by acid etching; others have assumed that electron tunneling takes place through such a layer during CCC growth [136].

For PCC coatings MnO_2 deposition occurs first over the intermetallic second-phase particles driven by their cathodicity with respect to the alloy matrix. The subsequent film nucleation and growth occurs on the Al matrix. The process is slow at room temperature and self-limits after about 150 min. Within the temperature range studied (25-68°C), comparable film morphologies and coatings were observed, with the PCC process being faster at the higher temperatures.

Al, Cu and B could not be detected by XPS in thicker coatings, but inclusions of Mg, K and Na were recognized at the later growth stages. The mechanism for incorporation of these inclusions during permanganating remains unclear.

The coatings formed over second-phase particles are considerably thicker than over the alloy matrix throughout the range of immersion time investigated at 25°C. Cracks are observed in thick PCC films covering the larger second-phase particles, but not on the alloy matrix, where the coating is relatively uniform and significantly thinner. These observations of morphology show a difference from the CCCs, since the latter are thicker over the alloy matrix and form cracks over all the surface after drying [135]. Therefore different failure mechanisms in corrosion protection can be expected for PCCs compared with the CCCs.

7.4.2 Comparison with Zinc Phosphate Coatings

The CCC distribution after 5 s of immersion (more deposition on the second-phase particles compared to the matrix) resembles the coating pattern for ZPO coatings containing Ni^{2+} (Chapter 5). On the other hand, the coating distribution is similar for the CCC (30 s immersion) and the ZPO coating containing Mn^{2+} , where there is a more even coating distribution across the different microstructural regions. When there is a smaller amount of coating deposition (CCC-5s, ZPO-Ni) the precipitation occurs mainly at the second-phase particles. When more coating deposition occurs (CCC-30s, ZPO-Mn) on the second-phase regions, less metal is exposed to the coating solution so diminishing the pH-increasing reduction reactions and rate of coating deposition. There is no equivalent retardation in coating deposition at the matrix because the coating coverage is less extensive. The cumulative result is a more even coating distribution across the surface. While CCCs and ZPO coatings have similar patterns of growth, PCCs differ: throughout the coating process the amount of deposition over second phase particles is greater compared to the alloy matrix. In this case the slowing of reduction reactions at the second phase regions would not drastically retard coating deposition because the basic conditions required for precipitation are maintained by the high pH of the coating solution.

Chapter 8

Concluding Remarks

8.1 New Results

There is a need to develop a replacement for chromate conversion coatings. To this end, it is necessary to have fundamental knowledge in order to design new coating methods that are effective and environmentally benign. An overall aim of this program was to develop understanding of the processes involved in the zinc phosphating of aluminum and its alloys, a subject that is poorly understood. One major objective of the work presented in this thesis was to explore the roles of the additive ions Ni^{2+} and Mn^{2+} in the coating baths and chemical reactions for the phosphating process on the 2024-Al alloy.

Ni^{2+} has a significant effect on macroscopic coating properties: it reduces the grain size for coatings on both 2024-Al alloy and high-purity Al, and improves the corrosion resistance for coatings on 2024-Al, in spite of an accompanying decrease in coating thickness. Substantial changes are observed in coating morphology and stability against corrosion as the amount of Ni^{2+} in the coating solution increases through the 0-2000 ppm range.

The Ni^{2+} additive has two main roles in the zinc phosphating process on 2024-Al. First, the rate of increase in local solution pH is limited by the slower kinetics of reactions involving Ni^{2+} compared to Zn^{2+} , leading to thinner ZPO coatings when Ni^{2+} is present in the coating solution. Second, most Ni^{2+} deposition occurs during the later stages of the coating process (i.e. between 30 s and 2 min). This deposition involves the formation of a Ni-rich oxide (referred to as NiAl_2O_4) on the alloy surface and nickel phosphate deposition. XPS and SAM support the presence of NiAl_2O_4 and SAM also indicates that NiAl_2O_4 deposition occurs especially at cathodic sites. The increased corrosion resistance of ZPO coatings

containing Ni^{2+} is most likely due to the presence in coating pores of NiAl_2O_4 , which is more resistant to degradation than aluminum oxide.

The XPS observations for the early stages of coating indicate that AlF_3 precipitates first during the coating process. This indicates that F^- incorporates into the coating in addition to its intended role of remaining in solution as AlF_6^{3-} . This is followed by the precipitation of aluminum phosphate. Subsequently a layer of ZnO (perhaps with $\text{Zn}(\text{OH})_2$ and/or ZnAl_2O_4) deposits, followed by precipitation of zinc and nickel phosphates.

SAM gave new information about the composition of ZPO coatings at different microstructural regions. When Ni^{2+} is present in the coating solution, the chemical composition of the coating above the Al-Cu-Fe-Mn particle is different from the coating on the rest of the surface as ZnO rather than ZPO predominates; that is apparently due to the slower etching rate at the Al-Cu-Fe-Mn particle. The coating pattern (thickness and composition) across the 2024-Al surface differs depending on the coating solution composition. When Ni^{2+} is added, the Al-Cu-Mg particles are coated more thickly than the Al-Cu-Fe-Mn particles, while there is no clear difference in the extent of coating when Ni^{2+} is absent. This is a consequence of the slowing of the coating rate caused by 2000 ppm Ni^{2+} , which permits more Mg and Al from the Al-Cu-Mg particle to dissolve, so leaving more local cathodic sites on the surface; in turn this facilitates the coating precipitation.

Mn^{2+} added to a ZPO solution for coating 2024-Al alloy also has a significant effect on macroscopic coating properties: it causes a decrease in crystal size and coating thickness. Both Ni^{2+} and Mn^{2+} additives act to decrease the size of the coating crystals, but Mn^{2+} causes a more significant reduction. The coating formed with the bath containing Mn^{2+} is thicker than that formed with Ni^{2+} in the coating bath, although thinner than the coating formed with

neither Ni^{2+} nor Mn^{2+} present. The last case is however less favorable because of the larger crystals that form the coating.

For longer immersion times the coating starts to dissolve as the etching reduces and the pH decreases at the coating-solution interface. In general, the coating process also varies with position across a heterogeneous Al-alloy surface, but the analysis with SAM shows that the Mn^{2+} additive acts to improve the evenness of coating distribution (compared with the Ni^{2+} additive) across the different microstructural regions of a 2024-Al surface. Throughout, the deposition patterns across a surface are affected significantly by additives in the ZPO coating solution, which also affect composition within the coating. Thus while Mn^{2+} deposits during the earlier stages of the coating process, the precipitation of Ni^{2+} occurs most in the later stages.

A second objective of this thesis was to explore the influences of surface oxides and the metal near the alloy-oxide interface on zinc phosphate coating formation at different microstructural areas. SAM measurements indicate that mechanical polishing in water causes the Al-Cu-Mg particle surface to become rich in metallic Cu, while the covering oxide subsequently formed predominantly involves Al and Mg. The oxide on the Al-Cu-Mg particle has a composition that is more easily etched, compared with the Al-Cu-Fe-Mn and matrix regions, where Al oxide is the main component. As a result, when dipped in the acidic coating solution, the Al-Cu-Mg particles are the first locations on the whole surface where metal contacts the solution, triggering reactions leading to coating deposition. The Cu-rich metal layer beneath the surface oxide is more cathodic than the other microstructural areas and is another factor causing increased coating deposition at the Al-Cu-Mg particle. It was determined that the oxide compositions at the matrix and Al-Cu-Fe-Mn particle surfaces are very similar, although the ZPO coating characteristics at these two regions are quite

different. That gives further direct support to the prevalent idea that electrochemical properties of the underlying metal substrate have a dominant influence on coating formation.

A third objective of this thesis was to explore degradation at different micro-regions on a 2024-Al surface which has been ZPO-coated and then exposed to a corrosive solution. Immersion of such a surface in the corrosive NaCl solution for 3 h results in partial dissolution of the ZPO and precipitation of Zn-Ni oxide, accompanied by oxidation of Al metal. Phosphate at the Al-Cu-Fe-Mn and matrix regions dissolves, but some phosphate coating remains at the Al-Cu-Mg region. However, as a result of the extended exposure for 48 h, phosphate is completely removed from all regions on the surface, and a layer containing Al and Zn oxides forms on the alloy. Corrosion occurs first at the matrix region on the coated surface. The ZPO coating provides more protection to the second-phase particles compared to the matrix, due to the different characteristics (e.g. morphology, composition) of the coating at each microstructural area.

A fourth objective of this thesis was to compare ZPO coating formation across the 2024-Al microstructure with chromate and permanganate types of conversion coatings. For the permanganate type, throughout the coating process the amount of deposition over second phase particles is greater compared to the alloy matrix. This differs from the chromate and ZPO patterns of growth where, for thicker coatings, the depositions are more even across the surface. This difference may depend on the basic coating solution involved in permanganating compared to the acidic solutions used for the chromate and ZPO coating processes.

Knowledge on the phosphating of multiphase systems has been very limited and that indicates the potential importance of the types of microstructural studies undertaken in this work. Since the second phase regions have an important influence on the alloy corrosion

resistance it is especially important to develop understanding of their behaviours under a variety of conditions.

8.2 Future Directions

The work in this thesis has been more exploratory and qualitative, but ultimately there will be a need to model the processes involved on a more quantitative basis. For that, as well as accounting for the changing natures of the solid phases, it is also necessary to have basic knowledge for the changing nature of the solution, particularly near the solid interface. This thesis presented initial experiments involving titration-type measurements that were designed to probe the coating solution chemistry, and more extensive solution characterization (using techniques such as Raman and UV spectroscopy) would be useful to probe the nature of the complexes in solution and how they change as the pH varies (this is particularly relevant to the solution pH rise which occurs during the coating process). There are a number of reactions occurring including several of the hydrolysis type, which can result in subtle effects. There are a few reports about the reactions occurring in other conversion coating solutions [134,165], but generally this is an area that needs development. Sum frequency generation and other vibrational spectroscopies (e.g. FTIR) should be used to explore the chemistry in the thin layer of coating solution at the alloy-solution interface [166]. Variations in the reactions occurring across the microstructure during the coating process could be measured in-situ using scanning electrochemical microscopy (SECM). It would also be useful to measure the solution pH above different micro-regions using a microscale pH meter.

In the experiments described in this thesis, 2024-Al was mechanically polished prior to coating; however, in industrial contexts, Al surfaces are generally cleaned with acidic solutions prior to dipping in a coating bath. The effect of the acidic pre-treatment on the

alloy microstructure and the initially-formed ZPO coating should be studied. It would also be useful to investigate the effects of exposing 2024-Al to a basic solution in order to develop a better understanding of the effects of such solutions (as in the permanganating process) on the alloy microstructure.

Atom probe tomography (APT) is a relatively new technique that can generate three-dimensional maps of chemical composition with resolution on the Å scale [167]. Insights on the effects of conversion coating solutions on the regions below the surface can in principle be obtained using this technique, as well as further probes of structure within coated layers. Such studies could be complemented by the use of synchrotron X-ray tomography for non-destructive imaging of second phase regions [168] as well as transmission electron microscopy (TEM) for morphological characterization [57].

Preliminary work was done in this thesis for corrosion at micro-regions on 2024-Al surfaces coated with Ni²⁺-containing ZPO. That work needs extension, including for tests on sealants for ZPO coatings. A recent review suggested that effective substitutes for chromate coatings may involve combining a phosphating bath with other conversion coating approaches involving cerium, zirconium, and vanadium compounds [16], hence the importance of investigating the formation and behaviour of such coatings. That suggests that the work undertaken in this thesis needs wider extension to systems containing a larger number of components. One advantage of the chromating approach is the self-healing phenomenon reported in their coatings [21], but more understanding is required. Finally, as well as the need for comparative studies on other Al alloys, extensive work is needed to develop new protective coatings on the more recently developed Mg alloys [169].

References

1. J.R. Davis, Ed., Corrosion of Aluminum and Aluminum Alloys, ASM International, Materials Park, Ohio, 1999.
2. D.G. Altenpohl, Aluminum: Technology, Applications, and Environment, Aluminum Association, Washington, D.C., 1998.
3. J.R. Davis, Ed., Aluminum and Aluminum Alloys, ASM International, Materials Park, Ohio, 1993.
4. W.D. Callister, Materials Science and Engineering: An Introduction, Wiley, New York, 2000.
5. L.F. Mondolfo, Aluminum Alloys: Structure and Properties, © Butterworth & Co. Ltd., London, 1976.
6. M. Gao, C.R. Feng, R.P. Wei, Metall. Mater. Trans. 29A (1998) 1145.
7. R.G. Buchheit, R.P. Grant, P.F. Hlava, B. McKenzie, G.L. Zender, J. Electrochem. Soc. 144 (1997) 2621.
8. T. Suter, R.C. Alkire, J. Electrochem. Soc. 148 (2001) B36.
9. N. Birbilis, R.G. Buchheit, J. Electrochem. Soc, 152 (2005) B140.
10. M. Pourbaix, Atlas of Electrochemical Equilibria in Aqueous Solutions, National Association of Corrosion Engineers, Houston, 1974.
11. C. Blanc, S. Gastaud, G. Mankowski, J. Electrochem. Soc. 150 (2003) B396.
12. A. Tonejc, M. Stubičar, A. M. Tonejc, K. Kosanović, B. Subotić, I. Smit, J. Mat. Sci. Lett. 13 (1994) 519.
13. Y. Liu, M.A. Arenas, P. Skeldon, G.E. Thompson, P. Bailey, T.C.Q. Noakes, H. Habazaki, K. Shimizu, Corros. Sci. 48 (2006) 1225.
14. <http://aluminium.matter.org.uk>
15. M.W. Kendig, R.G. Buchheit, Crit. Rev. Corr. Sci. Eng. 59 (2003) 379.
16. A. Nylund, Aluminum Trans. 2 (2000) 121.
17. P. Campestrini, H. Terryn, A. Hovestad, J.H.W. de Wit, Surf. Coat. Technol. 176 (2004) 365.

18. I. Danilidis, J. Hunter, G. M. Scamans, J.M. Sykes, *Corr. Sci.* 49 (2007) 1559.
19. J.H. Nordlien, J.C. Walmsley, H. Osterberg, K. Nisancioglu, *Surf. Coat. Technol.* 153 (2002) 72.
20. H. Guan, R.G. Buchheit, *Corrosion* 60 (2004) 284.
21. K. Ogle, R.G. Buchheit, in: M. Stratmann, G.S. Frankel (Eds.), *Corrosion and Oxide Films, Encyclopedia of Electrochemistry*, vol. 4, Wiley-VCH, Weinheim, 2003, p.460.
22. T.S.N. Sankara Narayanan, *Rev. Adv. Mater. Sci.* 9 (2005) 130.
23. K. Ogle, M. Wolpers, in: *Corrosion: Fundamentals and Protection, ASM Handbook*, Vol. 13A, ASM International, Materials Park, Ohio, 2003, p.712.
24. B.Y. Johnson, J. Edington, A. Williams, M.J. O'Keefe, *Mater. Characterization* 54 (2005) 41.
25. B.Y. Johnson, J. Edington, M.J. O'Keefe, *Mater. Sci. Eng. A* 361 (2003) 225.
26. A.O. Ita, *Metal Finish.* 98 (2000) 87.
27. D.B. Freeman, *Phosphating and Metal Pre-treatment*, Woodhead-Faulkner, Cambridge, England, 1986.
28. S. Wernick, R. Pinner, P.G. Sheasby, *The Surface Treatment and Finishing of Aluminum and its Alloys*, Finishing Publications Ltd., Teddington, Middlesex, England, 1987, Ch. 5.
29. W.A. Roland, *Galvano-Organic* 68 (1999) 194.
30. T. Sakauchi, T. Kumamoto, K. Yamamoto, *JSAE Rev.* 12 (1991) 12.
31. G.D. Cheever, in: P. Weiss, G.D. Cheever (Eds.), *Interface Conversion for Polymer Coatings*, American Elsevier Publishing Co., New York, 1968, p.150.
32. A. Whitaker, *Acta Cryst.* B31 (1975) 2026.
33. N. Sato, T. Minami, H. Kono, *Surf. Coat. Technol.* 37 (1989) 23.
34. W.-Y. Wu, X.-Q. Liang, Y.-Z. Li, *Acta Cryst.* E 61 (2005) i108.
35. P.-E. Tegehall, *Colloids Surf.* 49 (1990) 373.
36. N. Toshiko, S. Seiichiro, *World Intellectual Property Organization Patent* 2,007,013,626 (2007).
37. I. Van Roy, H. Terryn, G. Goeminne, *Colloids Surf. A* 136 (1998) 89.

38. W.H. Kok, X. Sun, L. Shi, K.C. Wong, K.A.R. Mitchell, T. Foster, *J. Mater. Sci.* 36 (2001) 3941.
39. J. Fang, P.C. Wong, K.A.R. Mitchell, T. Foster, *J. Mater. Sci.* 33 (1998) 1541.
40. D. Susac, C.W. Leung, X. Sun, K.C. Wong, K.A.R. Mitchell, *Surf. Coat. Technol.* 187 (2004) 216.
41. X. Sun, W.H. Kok, K.C. Wong, R. Li, K.A.R. Mitchell, T. Foster, *ATB Metall.* 40/41 (2000) 503.
42. X. Sun, D. Susac, R. Li, K.C. Wong, T. Foster, K.A.R. Mitchell, *Surf. Coat. Technol.* 155 (2002) 46.
43. D. Susac, X. Sun, R.Y. Li, K.C. Wong, P.C. Wong, K.A.R. Mitchell, R. Champaneria, *Appl. Surf. Sci.* 239 (2004) 45.
44. J.C. Rivière, S. Myhra, Ed., *Handbook of Surface and Interface Analysis*, Marcel Dekker, Inc., New York, 1998.
45. J.C. Vickerman, Ed., *Surface Analysis: The Principal Techniques*, Wiley, West Sussex, 1997
46. D. Briggs, M.P. Seah, *Practical Surface Analysis (Vol. 1)*, John Wiley & Sons, Chichester, 1990.
47. J.F. Moulder, W.F. Stickle, P.E. Sobol, K.D. Bomben, *Handbook of X-ray Photoelectron Spectroscopy*, Physical Electronics, Inc., Eden Prairie, Minnesota, 1995.
48. <http://www.uksaf.org/tech/uhv.html>
49. J.C. Rivière, *Surface Analytical Techniques*, Oxford University Press, 1990.
50. D.A. Shirley, *Phys. Rev. B* 5 (1972) 4709.
51. P. Auger, *Ann. Phys.* 6 (1926) 183.
52. K.J. Kim, D.W. Moon, C.J. Park, D. Simons, G. Gillen, H. Jin, H.J. Kang, *Surf. Interface Anal.* 39 (2007) 665.
53. D. Susac, *Surface Science Studies of Organosilane and Zinc Phosphate Coatings on 2024-T3 Aluminum Alloy*, Ph.D. thesis, University of British Columbia (2003).
54. *VG Scientific Auger Handbook*, VG Scientific Limited, East Grinstead, England, 1989.
55. *Thermo VG Scientific, Microlab 350 Operating Manual*, West Sussex, 2002.

56. L. Reimer, *Scanning Electron Microscopy: Physics of Image Formation and Microanalysis*, Springer-Verlag, Berlin, 1985.
57. S.L. Flegler, J.W. Heckman, K.L. Klomparens, *Scanning and Transmission Electron Microscopy: An Introduction*, W.H. Freeman, New York, 1993.
58. J.C. Russ, *Fundamentals of Energy Dispersive X-ray Analysis*, Butterworths, Boston, 1984.
59. L.M. Pidgeon, *Encyclopedia of Materials Science & Engineering*, Vol. 4, Pergamon Press, 1986.
60. J.I. Goldstein, D. Newbury, D. Joy, C. Lyman, P. Echlin, E. Lifshin, L. Sawyer, Michael, *Scanning Electron Microscopy and X-ray Microanalysis*, Kluwer Academic, New York, 2003.
61. A.C. Fisher, *Electrode Dynamics*, Oxford University Press, Oxford, 1996.
62. A.J. Bard, L.R. Faulkner, *Electrochemical Methods: Fundamentals and Applications*, Wiley, New York, 2001.
63. K.R. Trethewey, J. Chamberlain, *Corrosion for Science and Engineering*, Longman, Harlow, England, 1995.
64. N.A. Perekhrest, K.N. Pimenova, V.D. Litovchenko, L.I. Biryuk, *Prot. Met.* 28 (1992) 108.
65. G.D. Cheever, *J. Paint Technol.* 39 (1967) 1.
66. N. Helliwell, D.R. Gabe, M.O.W. Richardson, *Trans. Inst. Met. Finish. (UK)* 54 (1976) 185.
67. A.V. Lad, K.I. Vasu, *J. Electrochem. Soc. (India)* 29 (1980) 11.
68. N. Satoh, *Surf. Coat. Technol.* 30 (1987) 171.
69. N. Satoh, T. Minami, *Surf. Coat. Technol.* 34 (1988) 331.
70. P.E. Tegehall, N.G. Vannerberg, *Corros. Sci.* 32 (1991) 635.
71. J.W. Schultze, N. Muller, U. Konig, R. Krumm, in: R.G. Kelly (Ed.), *Proceedings of the Symposium on Critical Factors in Localized Corrosion III*, Electrochemical Society Inc., Pennington, New Jersey, 1999, p. 31.
72. R.W. Miller, M. Petschel Jr., R.G. Hart, *Met. Finish.* 92 (1994) 13.
73. J. Donofrio, *Met. Finish.* 100 (2002) 89.

74. M.G. Fontana, *Corrosion Engineering*, McGraw-Hill, New York, 1986, Ch. 9.
75. I.G. Casella, M.R. Guascito, M.G. Sannazzaro, *J. Electroanal. Chem.* 462 (1999) 202.
76. P.F. Luo, T. Kuwana, D.K. Paul, P.M.A. Sherwood, *Anal. Chem.* 68 (1996) 3330.
77. K.S. Kim, W.E. Baitinger, J.W. Amy, N. Winograd, *J. Electron. Spectrosc. Relat. Phenom.* 5 (1974) 351.
78. A.M. Venezia, R. Bertoncetto, G. Deganello, *Surf. Interface Anal.* 23 (1995) 239.
79. Z. Song, X. Bao, M. Muhler, *Appl. Surf. Sci.* 148 (1999) 241.
80. X. Sun, R. Li, K.C. Wong, K.A.R. Mitchell, T. Foster, *J. Mater. Sci.* 36 (2001) 3215.
81. A. Davidson, J.F. Tempere, M. Che, H. Roulet, G. Dufour, *J. Phys. Chem.* 100 (1996) 4919.
82. A.M. Beccaria, Y.Z. Wang, G. Poggi, *Surf. Interface Anal.* 21 (1994) 442.
83. A.N. Rider, D.R. Arnott, A.R. Wilson, I. Danilidis, P.J.K. Paterson, *Surf. Interface Anal.* 24 (1996) 293.
84. D.R. Arnott, B.R.W. Hinton, N.E. Ryan, *Mater. Perform.* 26 (1987) 42.
85. C.D. Wagner in: D. Briggs, M.P. Seah (Eds), *Practical Surface Analysis*, Wiley, New York, 1990, p. 595.
86. M. Handke, A. Stoch, S. Sulima, P.L. Bonora, G. Busca, V. Lorenzelli, *Mat. Chem.* 7 (1982) 7.
87. D. Zimmermann, A.G. Munoz, J.W. Schultze, *Electrochimica Acta* 48 (2003) 3267.
88. K. Ogle, A. Tomandl, N. Meddahi, M. Wolpers, *Corros. Sci.* 46 (2004) 979.
89. A. Tomandl, M. Wolpers, K. Ogle, *Corros. Sci.* 46 (2004) 997.
90. D.C. Harris, *Quantitative Chemical Analysis*, W.H. Freeman, New York, 1998.
91. *CRC Handbook of Chemistry and Physics*, Chemical Rubber Co., Cleveland, OH, 2000.
92. K.-H. Stellnberger, M. Wolpers, T. Fili, C. Reinartz, T. Paul, M. Stratmann, *Faraday Discuss.* 107 (1997) 307.

93. G. Lorin, *Phosphating of Metals: Constitution, Physical Chemistry, and Technical Applications of Phosphating Solutions*, Finishing Publications, Hampton Hill, 1974.
94. B. Cheng, S. Ramamurthy, N.S. McIntyre, *J. Mater. Eng. Perform.* 6 (1997) 405.
95. W. Rausch, *The Phosphating of Metals*, ASM International, Metals Park, Ohio, 1990.
96. N.S. McIntyre, T.E. Rummery, M.G. Cook, D. Owen, *J. Electrochem. Soc.* 123 (1976) 1164.
97. P. Lorenz, J. Finster, G. Wendt, J.V. Salyn, E.K. Žumadilov, V.I. Nefedov, *J. Electron Spectroscopy Relat. Phenom.* 16 (1979) 267.
98. R.B. Shalvoy, B.H. Davis, P.J. Reucroft, *Surf. Interface Anal.* 2 (1980) 11.
99. A. Velon, I. Olefjord, *Oxidation Metals* 56 (2001) 415.
100. D. Shriver, P. Atkins, *Inorganic Chemistry*, W.H. Freeman, New York, 1999, Ch. 7.
101. J. Kragten, *Atlas of Metal-Ligand Equilibria in Aqueous Solution*, E. Horwood, Chichester, 1978.
102. A.E. Martell, R.M. Smith, *Critical Stability Constants*, Plenum Press, New York, 1974.
103. C.F. Baes, R.E. Mesmer, *The Hydrolysis of Cations*, Wiley, New York, 1976.
104. P. Schmutz, G.S. Frankel, *J. Electrochem. Soc.* 145 (1998) 2285.
105. A. Kolics, A.S. Besing, A. Wieckowski, *J. Electrochem. Soc.* 148 (2001) B322.
106. S. Palraj, M. Selvaraj, P. Jayakrishnan, *Prog. Org. Coat.* 54 (2005) 5.
107. W.J. van Ooij, A. Sabata, *J. Coat. Technol.* 61 (1989) 51.
108. N.S. McIntyre, R.D. Davidson, I.Z. Hyder, in: J.C. Rivière, S. Myhra (Eds.), *Handbook of Surface and Interface Analysis*, Marcel Dekker, New York, 1998, p.654.
109. B.Y. Jibril, *Ind. Eng. Chem. Res.* 44 (2005) 702.
110. C.V.K. Sharma, C.C. Chusuei, R. Clérac, T. Möller, K.R. Dunbar, A. Clearfield, *Inorg. Chem.* 42 (2003) 8300.
111. B.R. Strohmeier, D.M. Hercules, *J. Phys. Chem.* 88 (1984) 4922.
112. V. Di Castro, G. Polzonetti, *J. Electron Spectrosc. Relat. Phenom.* 48 (1989) 117.
113. A. Aoki, *Jpn. J. Appl. Phys.* 15 (1976) 305.

114. CRC Handbook of Chemistry and Physics, CRC Press, Cleveland, Ohio, 2006.
115. S.J. Markich, P.L. Brown, R.A. Jeffree, *Sci. Total Environ.* 275 (2001) 27.
116. I.V. Rudii, N.M. Antraptseva, *Russ. J. Inorg. Chem.* 36 (1991) 1565.
117. G.M. Treacy, G.D. Wilcox, *Appl. Surf. Sci.* 157 (2000) 7.
118. P. Campestrini, H. Terryn, J. Vereecken, J.H.W. de Wit, *J. Electrochem. Soc.* 151 (2004) B370.
119. C. Blanc, A. Freulon, M.-C. Lafont, Y. Kihn, G. Mankowski, *Corros. Sci.* 48 (2006) 3838.
120. J. Kim, P.C. Wong, K.C. Wong, R.N.S. Sodhi, K.A.R. Mitchell, *Appl. Surf. Sci.* 253 (2007) 3133.
121. H. Habazaki, K. Shimizu, P. Skeldon, G.E. Thompson, G.C. Wood, X. Zhou, *Trans. IMF* 75 (1997) 18.
122. C. Chen, S.J. Splinter, T. Do, N.S. McIntyre, *Surf. Sci. Lett.* 382 (1997) 652.
123. T. Do, S.J. Splinter, C. Chen, N.S. McIntyre, *Surf. Sci.* 387 (1997) 192.
124. R.P. Wei, C.-M. Liao, M. Gao, *Metall. Mater. Trans.* 29A (1998) 1153.
125. L. Kozma, I. Olefjord, *Mater. Sci. Technol.* 3 (1987) 860.
126. N.S. McIntyre, R.D. Davidson, I.Z. Hyder, A.M. Brennenstuhl, in: *Handbook of Surface and Interface Analysis*, Marcel Dekker, Inc., New York, 1998.
127. D. Zhu, W.J. van Ooij, *Corros. Sci.* 45 (2003) 2163.
128. F.W. Lytle, R.B. Gregor, G.L. Bibbins, K.Y. Blohowiak, R.E. Smith, G.D. Tuss, *Corros. Sci.* 37 (1995) 349.
129. A.E. Hughes, R.J. Taylor, B.R.W. Hinton, *Surf. Interface Anal.* 25 (1997) 223.
130. P.L. Hagans, C.M. Haas, *Surf. Interface Anal.* 21 (1994) 65.
131. J. Zhao, L. Xia, A. Sehgal, D. Lu, R.L. McCreery, G.S. Frankel, *Surf. Coat. Technol.* 140 (2001) 51.
132. O. Lunder, J.C. Walmsley, P. Mack, K. Nisancioglu, *Corros. Sci.* 147 (2005) 1604.
133. M. Jaime Vasquez, G.P. Halada, C.R. Clayton, J.P. Longtin, *Surf. Interface Anal.* 33 (2002) 607.

134. P. Campestrini, G. Goeminne, H. Terryn, J. Vereecken, J.H.W. de Wit, J. Electrochem. Soc. 151 (2004) B59.
135. P. Campestrini, H. Terryn, J. Vereecken, J.H.W. de Wit, J. Electrochem. Soc. 151 (2004) B359.
136. G.M. Brown, K. Kobayashi, J. Electrochem. Soc. 148 (2001) B457.
137. D. Chidambaram, C.R. Clayton, G.P. Halada, M.W. Kendig, J. Electrochem. Soc. 151 (2004) B605.
138. D. Chidambaram, C.R. Clayton, M.W. Kendig, G.P. Halada, J. Electrochem. Soc. 151 (2004) B613.
139. J.R. Waldrop, M.W. Kendig, J. Electrochem. Soc. 145 (1998) L11.
140. W.R. McGovern, P. Schmutz, R.G. Buchheit, R.L. McCreery, J. Electrochem. Soc. 147 (2000) 4494.
141. L. Juffs, A.E. Hughes, S. Furman, P.J.K. Paterson, Corros. Sci. 44 (2002) 1755.
142. I. Danilidis, J.M. Sykes, J.A. Hunter, G.M. Scamans, Surf. Eng. 15 (1999) 401.
143. J.W. Bibber, Proc. Corrosion 95: the NACE International Annual Conference and Corrosion Show. March 1995, Orlando, FL, NACE International, Paper 392.
144. J.W. Bibber, Plating Surf. Finishing 90 (2003) 40.
145. J.W. Bibber, U.S. Patent 4,755,224 (1988).
146. J.W. Bibber, U.S. Patent 4,878,963 (1989).
147. J.W. Bibber, U.S. Patent 4,988,396 (1991).
148. L. Xia, R.L. McCreery, J. Electrochem. Soc. 145 (1998) 3083.
149. M. Takaya, Jpn. Inst. Light Met. 45 (1995) 713. (In Japanese)
150. H. Umehara, S. Terauchi, M. Takaya, Mater. Sci. Forum 350-351 (2000) 273.
151. H. Umehara, M. Takaya, S. Terauchi, Surf. Coat. Technol. 169-170 (2003) 666.
152. C.S. Lin, C.Y. Lee, W.C. Li, Y.S. Chen, G.N. Fang, J. Electrochem. Soc. 153 (2006) B90.
153. M. Zhao, S.S. Wu, J.R. Luo, Y. Fukuda, H. Nakae, Surf. Coat. Technol. 200 (2006) 5407.

154. D. Hawke, D.L. Albright, *Met. Finish.* 93 (10) (1995) 34.
155. K.Z. Chong, T.S. Shih, *Mater. Chem. Phys.* 80 (2003) 191.
156. R.G. Buchheit, M. Cunningham, H. Jensen, M.W. Kendig, M.A. Martinez, *Corrosion* 54 (1998) 61.
157. V. Guillaumin, G. Mankowski, *Corros. Sci.* 41 (1999) 421.
158. L. Xia, R.L. McCreery, *J. Electrochem. Soc.* 145 (1998) 3083.
159. G.S. Frankel, *J. Electrochem. Soc.* 145 (1998) 2186.
160. P. Schmutz, G.S. Frankel, *J. Electrochem. Soc.* 145 (1998) 2295.
161. M. Pourbaix, *Atlas of electrochemical equilibria in aqueous solutions*, Pergamon Press, 1966, p.171.
162. D. Susac, X. Sun, K.A.R. Mitchell, *Appl. Surf. Sci.* 207 (2003) 40.
163. G.M. Brown, K. Shimizu, K. Kobayashi, G.E. Thompson, G.C. Wood, *Corros. Sci.* 33 (1992) 1371.
164. G.M. Brown, K. Shimizu, K. Kobayashi, G.E. Thompson, G.C. Wood, *Corros. Sci.* 35 (1993) 253.
165. F. Scholes, C. Soste, A.E. Hughes, S.G. Hardin, P.R. Curtis, *Appl. Surf. Sci.* 253 (2006) 1770.
166. F. Vidal, A. Tadjeddine, *Rep. Prog. Phys.* 68 (2005) 1095.
167. M.K. Miller, *Atom Probe Tomography*, Kluwer Academic, New York, 2000.
168. A.G. Peele, H.M. Quiney, B.B. Dhal, A.P. Mancuso, B. Arhatari, K.A. Nugent, *Radiation Phys. Chem.* 75 (2006) 2067.
169. J.E. Gray, B. Luan, *J. Alloys Compd.* 336 (2002) 88.